Experimental and Simulation-Based Investigation of the Influence of Freezing and Annealing on the Microstructure in Lyophilisates

Doctoral Thesis

Submitted in partial fulfilment of the requirements for
the degree of doctor of natural sciences
of the Faculty of Mathematics and Natural Sciences

at Kiel University, Germany

by

Tigran Levonovic Kharatyan

Kiel, 2024

Printed with the permission of the Faculty of Mathematics and Natural Sciences of Kiel University.

This work was carried out from May 2019 until April 2023 at the Department of Pharmaceutical Development of Daiichi Sankyo Europe GmbH, Pfaffenhofen an der Ilm, Germany. The thesis was prepared under supervision of Prof. Dr. Regina Scherließ. In this thesis, DeepL Write has been used to identify and correct language mistakes (grammar and spelling).

1st Referee:	Prof. Dr. Regina Scherließ
2nd Referee:	Dr. Nora A. Urbanetz
Submission of the PhD application:	21.05.2024
Date of examination:	06.09.2024
Dean:	Prof. Dr. Frank Kempken

– Dedicated to my family –

Publications

The dissertation includes text and figures from the publications of the authors listed below.

I. *Quantitative Analysis of Glassy State Relaxation and Ostwald Ripening during Annealing Using Freeze-Drying Microscopy* by Tigran Kharatyan, Srikanth R. Gopireddy, Toru Ogawa, Tatsuhiro Kodama, Norihiro Nishimoto, Sayaka Osada, Regina Scherließ and Nora A. Urbanetz in *Pharmaceutics* (Volume 14, Issue 6, June 2022, 1176)

II. *Impact of post-freeze annealing on shrinkage of sucrose and trehalose lyophilisates* by Tigran Kharatyan, Shunya Igawa, Srikanth R. Gopireddy, Toru Ogawa, Tatsuhiro Kodama, Regina Scherließ and Nora A. Urbanetz in *International Journal of Pharmaceutics* (Volume 641, June 2023, 123051)

Table of contents

Introduction **1**

Objectives **2**

1 General background **3**

1.1 Freeze-drying in the pharmaceutical field 3

1.2 Freeze-dryer unit 4

1.3 Pharmaceutical formulations in freeze-drying 5

1.4 Process steps in a freeze-drying cycle 7

1.4.1 Freezing 9

1.4.1.1 Heterogeneous and homogeneous nucleation 10

1.4.1.2 Freeze-concentration of the matrix phase 12

1.4.2 Annealing during the freezing phase 15

1.4.3 Primary drying 17

1.4.4 Secondary drying 20

1.5 Microstructure formation in an aqueous solution during freezing 21

1.6 Coarsening of the ice crystal phase during annealing 23

1.7 Morphological assessment of the microstructure in a lyophilisate 25

1.8 Numerical simulations and phase-field methods in the pharmaceutical field 27

2 Materials and methods **31**

2.1 Materials 31

2.1.1 D-(+)-sucrose 31

2.1.2 D-(+)-trehalose 32

2.2 Methods 32

2.2.1 Lyophilisation 32

2.2.2 Freeze-drying microscopy 33

2.2.3 Polarised light microscopy 35

2.2.4 Differential scanning calorimetry 36

2.2.5 Phase-field computation and visualisation 36

2.2.6 Image analysis 37

3 Results and discussion **38**

3.1 Microstructure formation during freezing 38

3.1.1 Recalescence and crystallisation in samples during freezing 38
3.1.2 Characterisation of the thermal profile during freezing..... 41
3.1.3 Height-dependent recalescence and crystallisation in lyophilisation vials 48
3.1.4 Assessment of the microstructure in a frozen solution..... 52
3.1.5 Impact of thermal history during freezing on the microstructure 62
3.1.6 General discussion – importance of recalescence and crystallisation 66
3.2 Microstructure evolution during annealing 67
3.2.1 Methodological framework to investigate the microstructure..... 68
3.2.2 Implementation and calibration of the phase-field model 72
3.2.2.1 Formulism of the multiphase-field model 72
3.2.2.2 Experimental determination of relevant calibration parameters..... 74
3.2.2.2.1 Mass fractions during annealing 75
3.2.2.2.2 Volume fractions during annealing/maximum freeze-concentration 78
3.2.2.2.3 Recrystallisation rates during annealing 80
3.2.3 Initial conditions for two-dimensional and three-dimensional simulations 86
3.2.4 Calibration of input parameters for the phase-field simulations..... 95
3.2.4.1 Adjustment of the area and volume fractions of the particulate phase 95
3.2.4.2 Coarsening parameters for the two-dimensional phase-field model..... 101
3.2.5 Advancement of the phase-field simulation to three-dimensional 107
3.2.6 Final adjustment of particle volume fractions..... 110
3.2.7 Morphological properties in the three-dimensional phase-field model 111
3.2.7.1 Description of morphological properties in a porous microstructure..... 112
3.2.7.2 Ice crystal size distribution 116
3.2.7.3 Conjunction area of ice crystals 120
3.2.7.4 Surface area of the matrix phase 126
3.2.8 General discussion – pore size determination in lyophilisates 129

4 Future applications 134

4.1 Reorganisation kinetics during recalescence and crystallisation 134
4.2 CFD simulations through the porous microstructure..... 135

5 Appendices 137

Appendix A – Validation and stability analysis for the phase-field simulation 137
i. Gibbs-Thomson (capillarity) effect on composition 137
ii. Energy barrier coefficient on interfacial free energy..... 138

iii. Gradient energy coefficients on interfacial width and interfacial energy 140
Appendix B – Complete data from Chapter 3.1.2 143
Appendix C – List of abbreviations 145
Appendix D – Formula symbols 145
Appendix E – Materials 149
References 150
Abstract i
Zusammenfassung iii
Acknowledgements v
Statement in lieu of an oath vii

Introduction

In the pharmaceutical industry, freeze-drying, also known as lyophilisation, has become an essential method for stabilising products for storage and extending their shelf life. Despite the process being both time-consuming and costly, the advantages of removing water from sensitive products at low temperatures far outweigh these drawbacks. Excipients commonly used in freeze-drying include stabilisers like carbohydrates, which form amorphous, porous structures when freeze-dried. These microstructures are not formed randomly but result from complex physicochemical processes influenced by the freezing conditions of the pharmaceutical product. The characteristics of these microstructures significantly impact both the drying process and the properties of the final product.

Recent advances have substantially enhanced the understanding of the lyophilisation process. The adoption of advanced techniques such as micro-computed tomography in pharmaceutical development has become more prevalent, facilitating the assessment of the effects of process conditions and formulation excipients on lyophilisation. Moreover, numerical modeling is increasingly utilised to simulate aspects of the process that are challenging or impossible to investigate experimentally. Despite these advancements, the morphological properties of the porous microstructures formed during lyophilisation remain relatively unexplored, primarily due to the complexity of data collection and analysis. A major challenge is that structural changes like shrinkage and cracking occur in the lyophilised product during the drying phase, meaning that the original state of the microstructure in the frozen solution is not accurately represented in post-process analyses. Furthermore, the interpretation of measurement data and the definition of morphological properties, such as pore size, often vary depending on the analytical method used.

This lack or uncertainty of experimental data underscores the need for innovative methods to study the development and evolution of the microstructure in a lyophilisate. This need is a key motivation for this work, as future research could accelerate the establishment of robust lyophilisation cycles and help ensure the consistent quality of the final product. Moreover, developing and implementing simulation methods is particularly valuable, as research and development in the field of freeze-drying are highly demanding endeavours.

Objectives

The aim of this work is to examine the formation and evolution of the porous microstructure in a water-disaccharide system during freezing and annealing. Initially, an experimental investigation will focus on the formation of the microstructure during freezing. This will clarify the initial conditions before the annealing step and illuminate the factors influencing the microstructure in a lyophilisate when no annealing is performed. Subsequently, the impact of annealing on this microstructure will be examined. Current measurement techniques, however, fall short in accurately detecting and describing the morphological properties of the porous microstructure in a lyophilisate. The boundaries between individual pores, often in the sub-micron range, cannot be precisely measured by techniques such as computed tomography. Moreover, inferring three-dimensional characteristics from two-dimensional images, as attempted with scanning electron microscopy, presents significant challenges.

To overcome these obstacles, this thesis adopts an interdisciplinary approach. Factors influencing microstructure formation are experimentally investigated and quantified wherever possible. However, some measurements necessitate observing the microstructure in an artificially thin layer, which may alter its formation and evolution due to the experimental setup. To address this issue, a phase-field simulation will be implemented. This simulation will act as a digital counterpart to the experiment, allowing for the subsequent reconstruction of the thin experimental layer into a domain free from spatial constraints. Additionally, the simulation model will enable a more detailed characterisation of the microstructure, providing insights into the temporal evolution of morphological features, such as the narrowest gaps within the porous framework, which are unattainable through empirical methods alone.

The application and methodology of the phase-field model proposed in this thesis represent a novel approach within the pharmaceutical sector. This aligns with the increasing trend of integrating simulations to study specific sub-processes, particularly in the context of lyophilisation. In summary, this thesis focuses on two main areas: (1) investigating the process variables and their influence on the formation of the microstructure in a frozen disaccharide solution, and (2) developing a numerical simulation approach to predict the morphological properties of the resulting porous microstructure during annealing in a three-dimensional domain.

1 General background

1.1 Freeze-drying in the pharmaceutical field

Freeze-drying, also known as lyophilisation or cryodesiccation, is a widely used method in the pharmaceutical industry for enhancing the stability and shelf life of formulations containing sensitive molecules [1–3]. Over half of the more than 300 biopharmaceutical products approved by the FDA are freeze-dried formulations [4,5].

This drying technique aims to remove a solvent from a solution without harming sensitive molecules, such as therapeutic proteins, by utilising the principle that solvent molecules can sublimate directly from solid to gas at low temperatures and pressure, bypassing the liquid phase. The result is a solid block with a porous microstructure, often referred to as a lyo cake or lyophilisate, which consists of the non-sublimated components of the formulation. Most lyophilised pharmaceutical products are prepared from aqueous solutions, using water as the solvent [6]. Depending on the process, the water content of the lyophilisate can be reduced to less than 1 % [2,7]. For successful sublimation, the pressure during the drying process must be maintained below the triple point of the solvent, as demonstrated in Figure 1.1 for water.

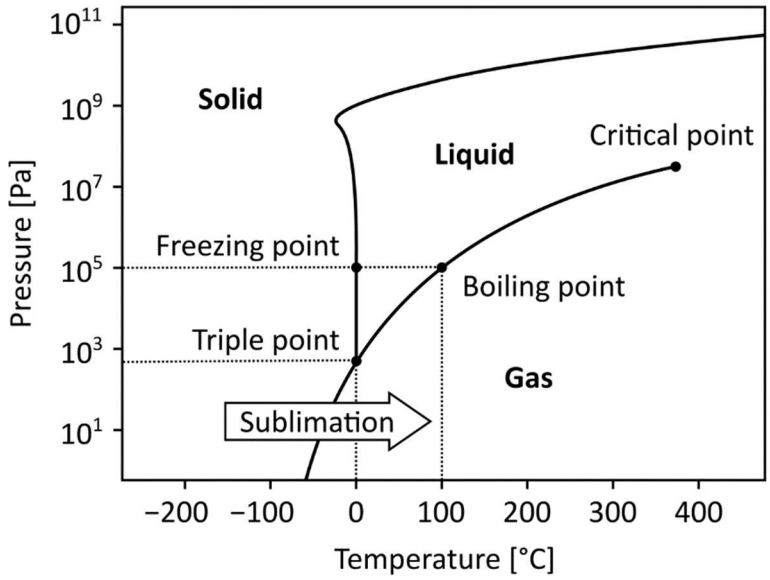

Figure 1.1: Phase diagram of water depicting its physical states depending on temperature and pressure. The triple point of water is at 0.01 °C and 611.7 Pa. Modified from [8].

Biopharmaceutical products are often unstable in solution due to their susceptibility to physical, chemical, or biological reactions such as aggregation, glycation, or proteolysis.

However, these products generally degrade more slowly after undergoing freeze-drying [3,9–11]. Once the pharmaceutical has to be administered and is needed in its liquid form, the porous microstructure of the lyophilised product, which has a high specific surface area, allows rapid reconstitution by the addition of a solvent [2]. Despite these benefits, lyophilisation remains a complex, costly, and time-consuming process, requiring significantly more time than merely removing water through evaporation [12]. Additionally, freeze-dryers used in the pharmaceutical industry are subject to batch size limitations and can exhibit inhomogeneous process conditions based on the type and size of the equipment [13,14]. Freeze-drying processes are also prone to failures due to specific process conditions and formulations, which can lead to defects like the collapse of the lyophilised product [15].

1.2 Freeze-dryer unit

The essential requirements of a freeze-dryer can be summarized as follows. The equipment must be capable of maintaining low temperatures during the freezing phase and high temperatures during the sublimation phase, while also sustaining reduced pressures within the drying chamber to facilitate sublimation. Additionally, a freeze-dryer must effectively trap the sublimated solvent to remove it from the product. The basic structure of a freeze-dryer is depicted in Figure 1.2. However, depending on the manufacturer and model, additional functional components may be incorporated.

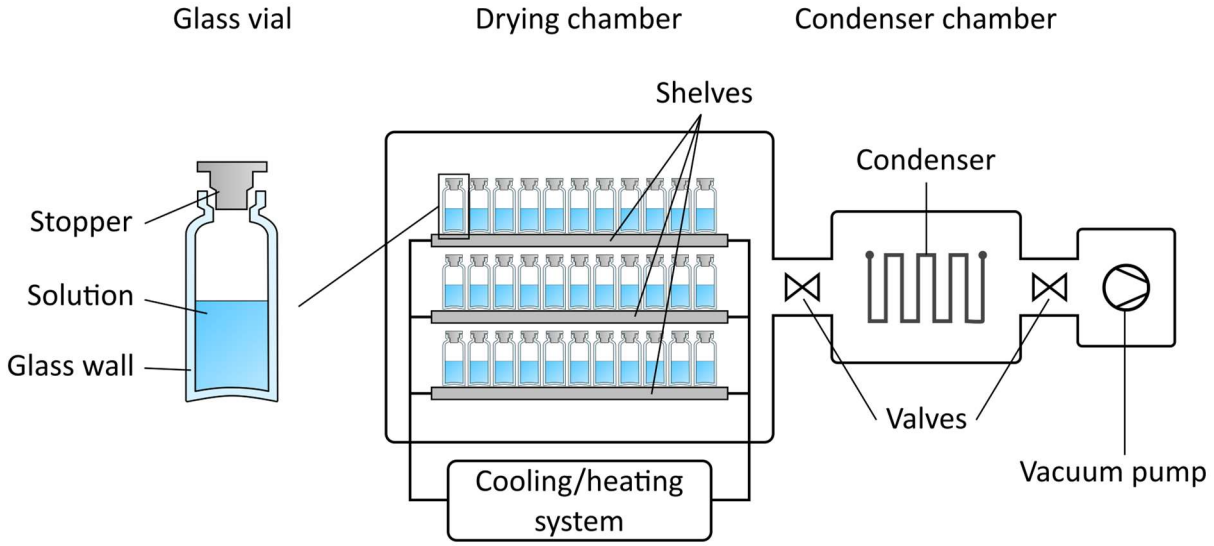

Figure 1.2: Basic components of a freeze-dryer. The stopper in the glass vial is used to seal the gas composition in the sample once the drying process is complete. Modified from [16].

The solution intended for drying is placed in containers such as glass vials, which are available in various sizes and materials. For instance, amber glass vials are used for products sensitive to UV radiation [17]. Before drying, the product must be thoroughly frozen at temperatures typically ranging from -50 °C to -80 °C. This ensures maximum phase separation within the sample due to freezing, a process that will be detailed later. Consequently, a cooling system connected to the shelves where the vials are placed is essential. Some freeze-dryers lack an integrated cooling system, requiring products to be pre-frozen outside the dryer.

To facilitate sublimation, the pressure within the drying chamber must be reduced to at least below the triple point of the solvent, making a vacuum system indispensable. The drying chamber is connected to a condenser chamber and a vacuum pump through valves, with the vacuum pump regulating the pressure by removing non-condensable gases [16]. The condenser, kept at temperatures lower than the shelves, enables the transition of water vapor into ice via deposition/resublimation. The driving force behind the freeze-drying process is the temperature difference between the product and the condenser. This difference creates varied saturation vapor pressures of ice at the sublimation front in the product and at the ice on the condenser, thereby establishing a pressure gradient that facilitates the transfer of water molecules from the product to the condenser [18]. Additionally, these condensers are designed with high surface areas to enhance their capacity for accumulating ice [2]. The vials are heated via the shelves in order to expedite the sublimation process by further increasing the temperature difference between the product and the condenser [19].

1.3 Pharmaceutical formulations in freeze-drying

Freeze-drying is typically utilised for Active Pharmaceutical Ingredients (APIs) where gentle drying processes and stabilisation are crucial [3]. This is particularly the case for biopharmaceutical APIs such as monoclonal antibodies, therapeutic proteins and vaccines, which are prone to loss of functionality, expensive to produce, and require meticulous downstream processing [5,20]. Furthermore, temperature-sensitive small molecule drugs such as antibiotics or antivirals are also subject to freeze-drying in order to preserve their functionality. Some examples of freeze-dried pharmaceuticals are listed in Table 1.1.

Besides the API, freeze-dried pharmaceutical products contain inactive excipients, defined by the FDA as “any component of a drug product other than an active ingredient” [21].

Approximately 67 % of lyophilised small molecule pharmaceuticals and nearly all biotechnology-derived products contain excipients [22,23]. Lyophilisation excipients are classified according to their functions as stabilisers, buffers, surfactants, or bulking agents [4]. Certain substances may fulfil multiple roles in a formulation. For example, disaccharides such as sucrose may be used as stabilisers and bulking agents at the same time [24].

Table 1.1: Examples of freeze-dried pharmaceuticals with FDA approval [25].

Drug name (FDA approval year)	API	Category/Indication	Manufacturer
Enbrel® (1998)	Etanercept	Rheumatoid arthritis, Psoriasis	Amgen Inc.
Enhertu® (2019)	Trastuzumab deruxtecan	Breast/gastric cancer	Daiichi Sankyo Company, Limited
Avonex® (1996)	Interferon beta-1a	Multiple sclerosis	Biogen
Orencia® (2005)	Abatacept	Rheumatoid arthritis	Bristol-Myers Squibb
Botox® (1991)	Daxibotulinumtoxin A	Various	Allergan
Dantrium® (1979)	Dantrolene sodium	Muscle relaxant	The Procter & Gamble Company
Cosmegen® (2009)	Dactinomycin	Antibiotic oncologic	Merck KGaA

Stabilisers serve to protect APIs from aggregation or structural changes during freezing or drying, acting as cryoprotectants or lyoprotectants [4,26–28]. Examples of stabilisers include disaccharides such as sucrose and trehalose, along with synthetic polyethers such as polyethylene glycol and polyvinylpyrrolidone. The mechanisms through which stabilisers operate include vitrification and water replacement [29]. Vitrification involves the immobilisation of the API in an amorphous matrix phase, which prevents interactions between API molecules. Water replacement describes the substitution of hydrogen bonds between the API and water with bonds between the stabiliser and the protein. As the stabiliser is not removed during drying, the API is less likely to be forced out of its native form upon desorption of unfrozen water.

Buffers can be incorporated into a formulation to regulate pH and maintain the solubility and stability of the API. For instance, proteins typically have the lowest solubility at their isoelectric point due to the neutral net charge on their surface, which leads to interactions between

proteins rather than between proteins and dipolar water molecules [30]. However, the selection of a suitable buffer is crucial, as phosphate buffers, for example, can lead to significant pH shifts during freezing, resulting in protein denaturation and precipitation [31,32]. Buffers commonly used in lyophilisation, such as citrates and histidine buffers, are less prone to crystallisation and exhibit a smaller temperature-dependent pH range [4].

Surfactants, such as polysorbate 80 and lecithin, are amphiphilic and effective at lowering the surface tension of water. In pharmaceutical formulations, surfactants bind to the hydrophobic regions of proteins, decreasing aggregation. Furthermore, surfactants raise the energy required for proteins to unfold, thereby stabilising their native structure [33,34].

Bulking agents are added to formulations when the API is present in small amounts per dose due to its high potency, therefore increasing the total mass of the pharmaceutical product [35]. Frequently utilised bulking agents for biopharmaceuticals include disaccharides like sucrose and trehalose, or sugar alcohols such as xylitol and mannitol, which form either amorphous or crystalline phases upon freezing [2,36,37]. As bulking agents may constitute a significant portion of a lyophilisate, their behaviour during freezing and drying is important for the overall process.

1.4 Process steps in a freeze-drying cycle

A freeze-drying cycle is divided into three main process steps: freezing, primary drying, and secondary drying. During each stage, the pharmaceutical solution or lyophilisate undergoes physicochemical changes on both the micro- and macroscale, as illustrated in Figure 1.3.

The subprocesses of a lyophilisation cycle are regulated by the shelf temperature and chamber pressure. The initial freezing step involves lowering the temperature of the samples until the solution solidifies completely, resulting in the formation of a microstructure composed of dispersed individual ice crystals within a continuous matrix phase. Solutions containing glass-forming solutes freeze over a wide temperature range. For example, a solution might start as a slush around -10 °C and solidify around -30 °C to -40 °C, depending on the solute [38]. Therefore, to thoroughly freeze such a solution, temperatures well below the triple point of the solvent are necessary. An optional annealing subprocess can be included in the freezing step, where the temperature is slightly raised but kept below the melting point of the solution to prevent thawing.

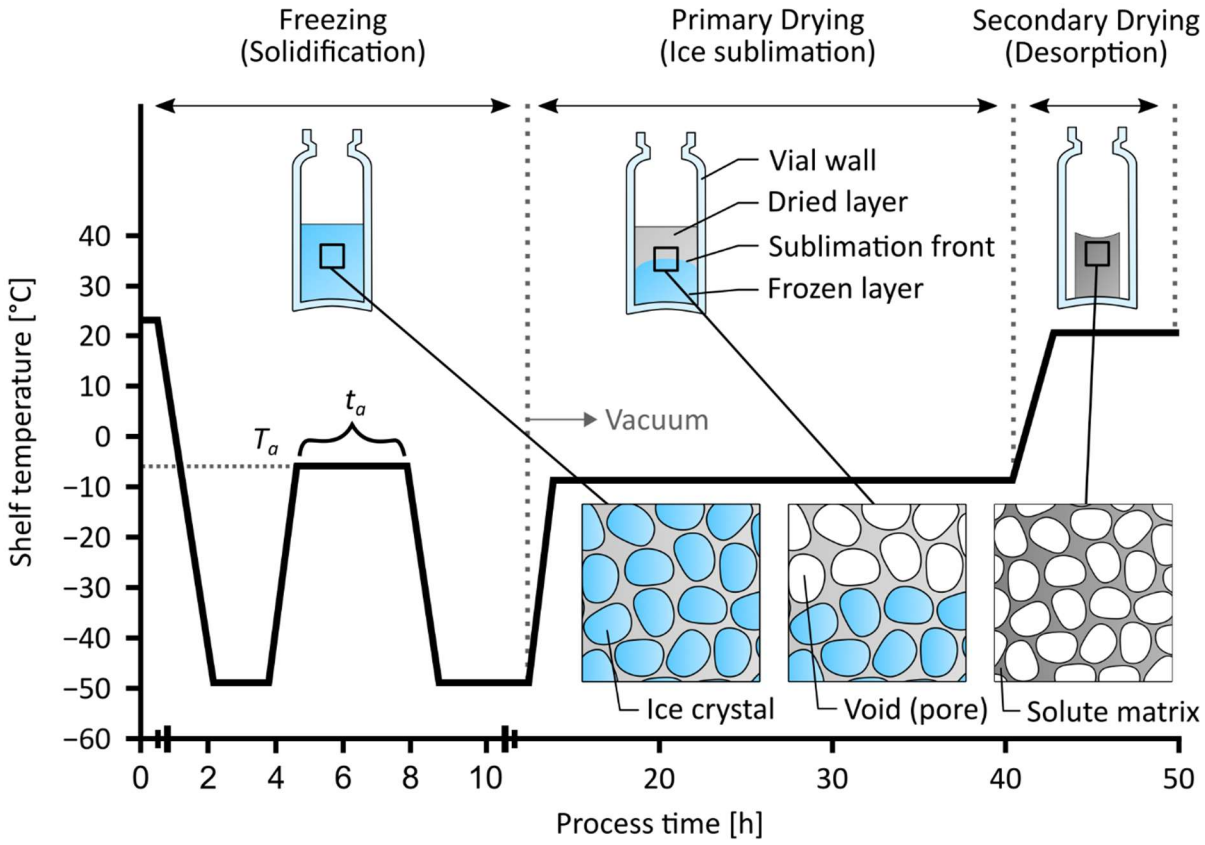

Figure 1.3: Illustration of a freeze-drying process including an annealing step during freezing. This phase is shown in greater detail to highlight the annealing temperature (T_a), annealing time (t_a), and the rates of freezing and cooling.

In primary drying, most of the water, in the form of ice crystals, is removed from the vials by reducing the chamber pressure to at least below the triple point of the solvent. Since sublimation is an endothermic phase transition, the temperature inside the vials decreases during this stage. To counteract this cooling and accelerate sublimation, the samples are heated via the shelves. During this phase, only the ice in direct contact with the gas phase undergoes the phase transition, creating a sublimation front that progresses from the surface of the frozen solution towards the bottom of the vial. To complete the drying process, it is necessary to remove the residual water from the matrix phase. This is typically achieved by further increasing the shelf temperature, which causes water molecules to diffuse and desorb from the matrix phase, reducing the water content in the lyophilisate to the target range of usually around 1 % (w/w) to 3 % (w/w) for freeze-dried biological products [2]. Once the desired water content is reached, the vials are sealed, often with an inert gas, to prevent moisture from the air from wetting the lyophilisate.

1.4.1 Freezing

In the freezing step, the shelf temperature is lowered with the goal of ensuring that most of the solvent, such as water, crystallises. This leads to partial phase separation, commonly referred to as freeze-concentration, which is crucial for the subsequent removal of the solvent through sublimation in later stages of the process. This phase includes several subprocesses, which are illustrated in Figure 1.4.

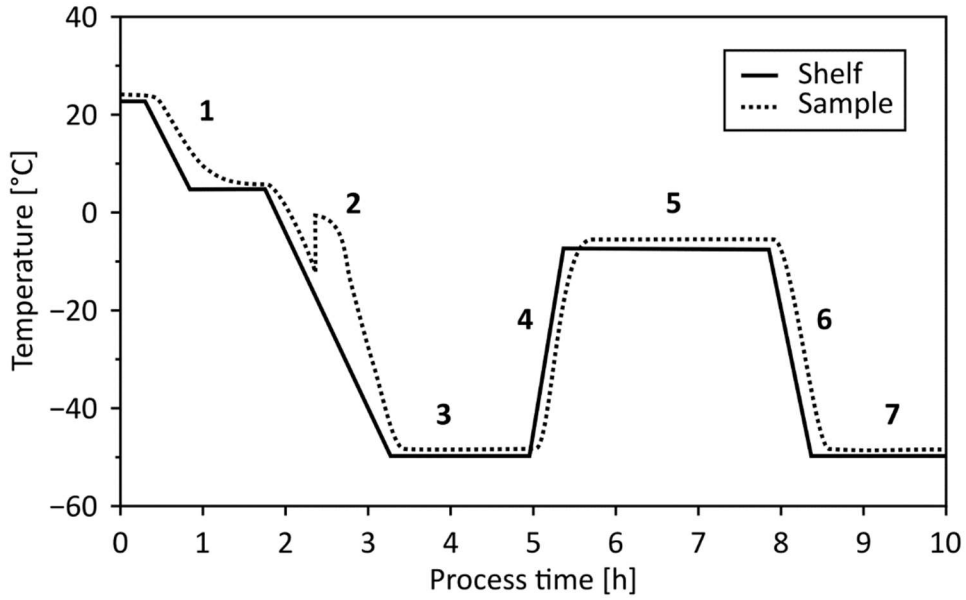

Figure 1.4: Temperature profile of sample and shelf during the freezing step: precooling (1), freezing/crystallisation (2), freezing plateau (3), annealing ramp (4), annealing (5), refreezing (6), refreezing plateau (7).

After an optional precooling step aimed at equalizing the conditions across vials in the freeze-dryer to approximately 5 °C, the shelf temperature is further decreased to typically between -40 °C and -50 °C to freeze the samples. During this process, a notable increase in the sample's temperature occurs after reaching 10 °C to 15 °C below its equilibrium freezing/melting point, i.e., the temperature at which a frozen solution with the same components would completely melt. This temperature increase signals an exothermic phase transition, specifically the crystallisation of water to ice. Just before the temperature begins to rise, the solution remains liquid despite being below its equilibrium freezing temperature, thereby becoming supercooled. A supercooled solution is not in equilibrium and is only meta-stable [39]. The greater the degree of supercooling, the more the solution becomes oversaturated with respect to the solvent, which in turn increases the probability of nucleation [13]. Once

nucleation begins, exothermic crystallisation rapidly occurs throughout the entire sample. This rise in temperature during solidification is known as recalescence, occurring when the heat released during the transition exceeds the rate at which heat can dissipate from the material [40]. This phenomenon, depicted in Figure 1.5, is essential for understanding the impact of freezing conditions on the lyophilisation process.

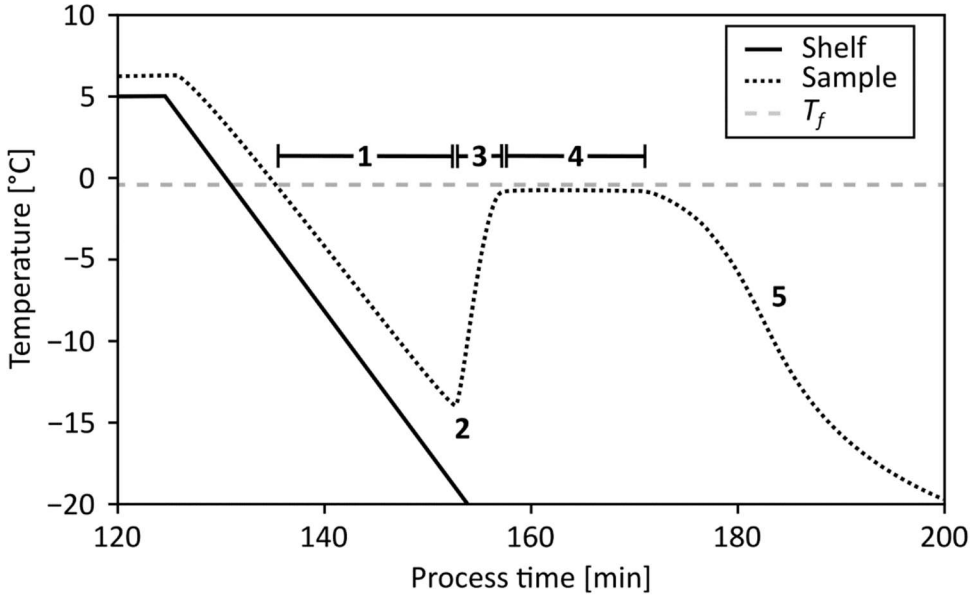

Figure 1.5: Schematic temperature profile of a solution during freezing: supercooling (1), nucleation (2), recalescence (3), freeze-concentration (isothermal crystallisation) (4), end of solidification (5). The equilibrium freezing temperature (T_f) is shown as a grey dashed line. Modified from [41].

Once the sample temperature nearly reaches its equilibrium freezing temperature, it remains steady for period of time. Meanwhile, water continuously crystallises, releasing heat that must be removed from the sample by the cooling shelves. A detailed description of the phenomena contributing to the typical temperature profile of the sample during freezing will be presented in the following sections. Additionally, an in-depth examination of recalescence and the subsequent crystallisation will be explored in the Results section of this work. This focus is motivated by the often underestimated impact of the temperature increase during freezing on the microstructure of the lyophilisate.

1.4.1.1 Heterogeneous and homogeneous nucleation

The onset of crystallisation requires the formation of initial nucleation points, known as nuclei, where water molecules start to precipitate and form larger ice crystals [42]. Nucleation does

not necessarily occur at the equilibrium freezing temperature but can happen at much lower temperatures, influenced by process conditions and material properties. For instance, pure water, with a melting point at 0 °C, can remain unfrozen at temperatures as low as -42 °C [43]. However, the presence of impurities might initiate nucleation at temperatures closer to the equilibrium freezing point, such as -5 °C [44,45]. These impurities could include particulate contaminants or large molecules like proteins, acting as interfaces to facilitate nucleation [46]. This phenomenon is explained by classical nucleation theory, which differentiates between homogeneous and heterogeneous nucleation, and is illustrated in Figure 1.6.

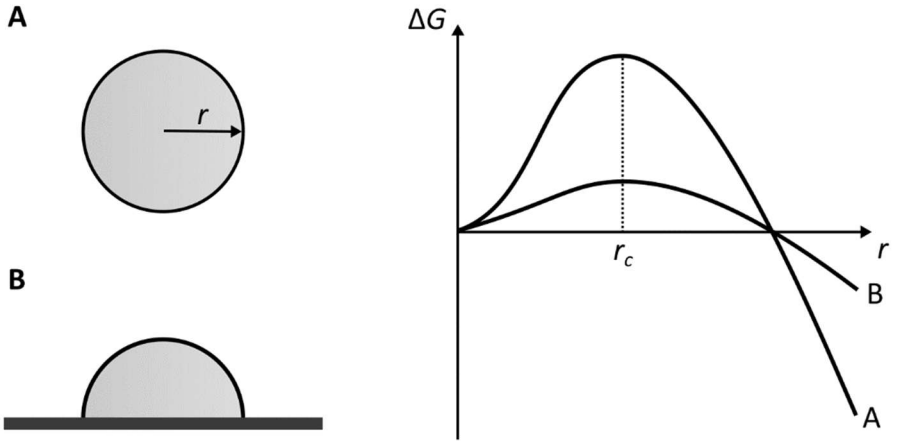

Figure 1.6: Size-dependent free energy of homogeneous (A) and heterogeneous (B) nucleation. Modified from [47].

In homogeneous nucleation, small nuclei form as a solid phase within the oversaturated solution. These nuclei are clusters of water molecules arranged and bonded similarly to ice. Their formation, driven by Brownian motion within the bulk volume, is stochastic in nature, yet the probability of formation increases as the temperature decreases [48]. The energy required to form and sustain a nucleus depends on its size, with the Gibbs free energy (ΔG) comprising surface free energy and bulk free energy components. Surface free energy increases with nucleus size, while bulk free energy has a stabilising effect, reducing the system's free energy as the nucleus grows [49]. Therefore, the stability of a nucleus hinges on its surface area to volume ratio, or simply its radius in the case of a spherical nucleus. The free energy peak indicates the critical particle size (r_c) that must be surpassed for larger ice crystals to grow from the nucleus. Failing to exceed this size, the system's free energy can only decrease by reducing the surface area of the nuclei, potentially leading to their complete break up. In heterogeneous nucleation, the new solid phase forms on an existing interface,

such as the surface of an impurity, which reduces the required energy for nucleus stabilisation due to a smaller surface area compared to homogeneous nucleation for the same radius, thereby making heterogeneous nucleation more prevalent [50]. In freeze-drying, various techniques are utilised to influence the nucleation temperature during the freezing step. These include the ice fog technique, quench freezing, electro freezing, ultrasound-controlled ice nucleation, vacuum-induced surface freezing, high-pressure shift and depressurisation, and the addition of nucleation agents [44].

1.4.1.2 Freeze-concentration of the matrix phase

Once stable nuclei with radii above the critical size are formed, water molecules from the supercooled liquid phase can attach to their surfaces and start to form ice crystals [51]. In the conditions of a freeze-dryer, ice typically forms in the I_h phase, also known as normal hexagonal crystalline ice. Within a solution, the dense structure of hexagonal ice prevents most solutes from being incorporated into the crystalline lattice, leading to the formation of a nearly pure ice phase and a solute-enriched matrix phase [16]. This reversible process, known as freeze-concentration, is governed solely by temperature. The lower the temperature, the more water precipitates from the solution into the existing ice crystals, as illustrated in Figure 1.7. However, this process can only continue until the matrix phase reaches its maximum freeze-concentrated state, which varies depending on the solute in the aqueous solution [52].

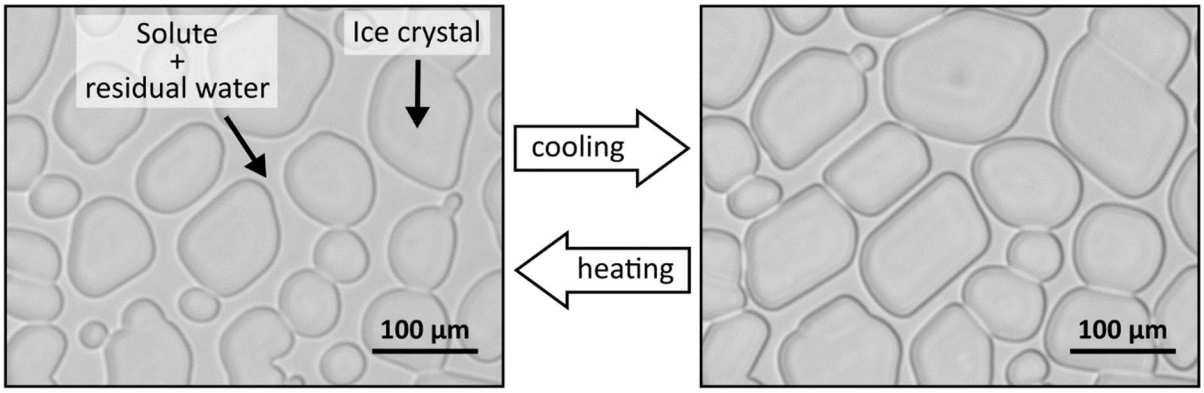

Figure 1.7: Freeze-drying microscopy of a partially frozen 10 % (w/w) sucrose solution at -4 °C (left) and at -10 °C (right).

The freezing behaviour of a matrix phase can be classified as crystallising or vitrifying and the choice of excipients in the formulation will determine which of these behaviours is present or

whether a combination of both is observed. Crystalline systems are typically characterised by the formation of a eutectic mixture upon freezing, as illustrated in the phase diagram for a two-component system shown in Figure 1.8.

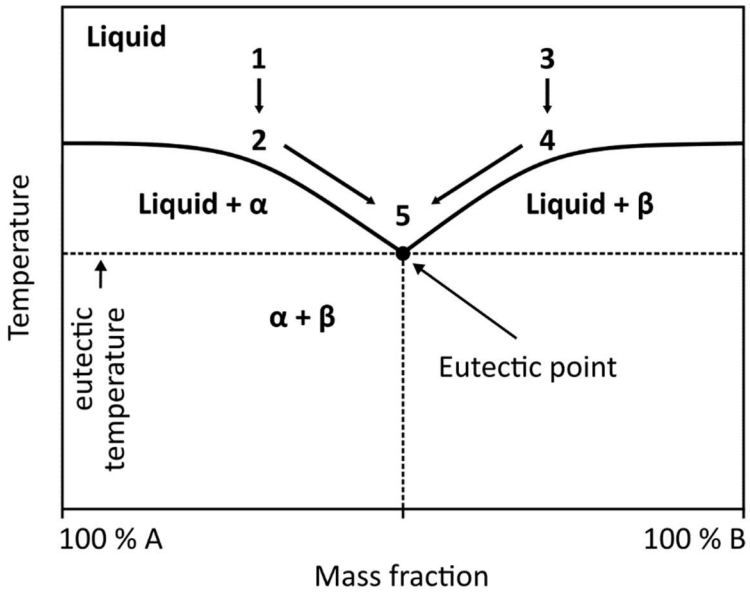

Figure 1.8: Phase diagram of a binary system with crystallising components A and B. Modified from [16].

A eutectic mixture has a lower freezing point than any other mixing ratio of its components. This means that the mixture abruptly freezes at the eutectic temperature (T_{eu}), and the components, A and B, form a fine structure of individual crystalline phases, illustrated in Figure 1.8 as α and β. Non-eutectic mixtures, either hypoeutectic or hypereutectic, begin to form a precipitate of the excess component as the temperature decreases. A hypoeutectic mixture remains entirely liquid until it reaches the equilibrium freezing temperature, also known as the liquidus line. At this point, component A begins to precipitate (1→2). This process continues along the liquidus line until the eutectic point (5), where a portion of component A forms a eutectic mixture with all of component B. Upon further cooling, this eutectic mixture crystallises. A hypereutectic mixture follows a similar path (3→4→5). Upon solidification, such eutectic systems may form microscopic arrangements, where one phase is embedded as lamellar or globular structures within the other phase [53,54].

Many pharmaceutical formulations contain major components that do not crystallise upon freezing but instead remain in a rubbery phase and undergo glass transition upon sufficient cooling. During freezing of a solution with a glass-forming component, precipitation of water

and ice formation follow the liquidus line once nucleation occurs, similar to a crystallising system. However, instead of forming a eutectic mixture, i.e., a mixture with a single melting point, more water crystallises over a broad temperature range. This process continues until the amorphous phase cannot be further concentrated by temperature reduction. At this point, the system is referred to as maximally freeze-concentrated and is characterised by the onset temperature for ice melting T_m' and the solute concentration in the matrix phase c_g' [38]. The phase diagram in Figure 1.9 illustrates the freezing behaviour of such solutions.

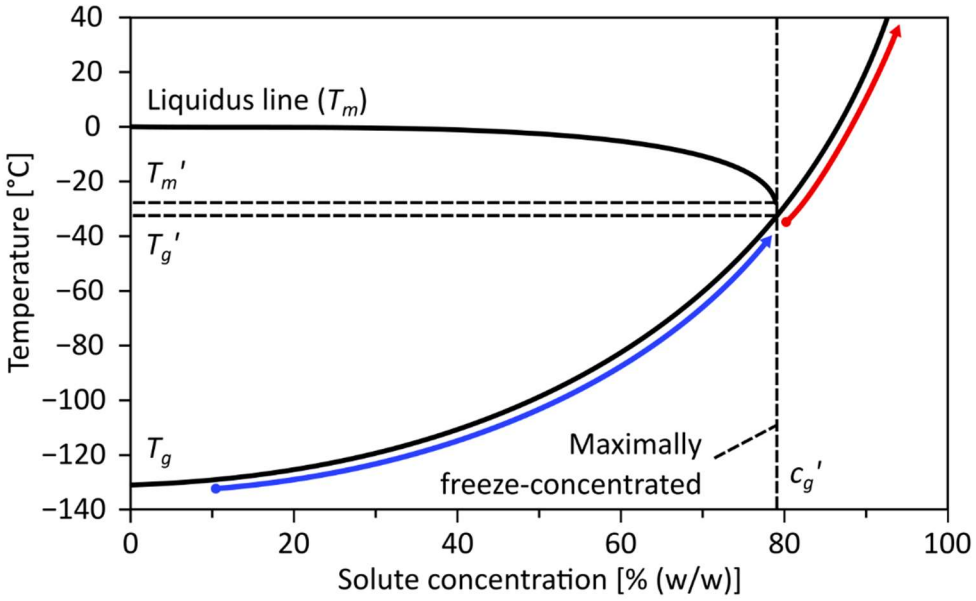

Figure 1.9: Phase diagram of an aqueous system with a glass-forming solute. The glass transition temperature of the solute-enriched phase (T_g) changes during freeze-concentration (blue) and desorption of unfrozen water (red). Modified from [55,56].

In case of glass-forming disaccharides, the formation of hydrogen bonds between solute and water as well as between solute molecules exhibits comparable energy and configuration [57]. A decrease in temperature shifts the chemical potential (μ) of these hydrogen bonds. Once the matrix phase becomes maximally freeze-concentrated, the μ of hydrogen bonds between the solute and water falls below the μ of water-water interactions, thus inhibiting further crystallisation of water [38]. Roos (1991) showed that approximately 20 % (w/w) of residual water remains in a maximally freeze-concentrated matrix of a frozen sucrose solution. Further investigation by Seifert et al. (2020) determined that the residual water content in sucrose ranges between 22.6 % and 24.6 % (w/w).

At the glass transition temperature T_g', the matrix phase vitrifies from a rubbery to a glassy state with a steep increase in its viscosity in the order of 10^{12} Pa to 10^{14} Pa [60,61]. More precisely, T_g' is used to describe a maximally freeze-concentrated material. The glass transition temperature (T_g) varies depending on the composition of the matrix phase. Notably, the higher the water content, the lower the T_g. This viscosity increase reduces molecular mobility within the amorphous phase, thereby slowing down crystallisation to the extent that no additional water can be removed through freeze-concentration [60]. This phenomenon is crucial for the subsequent drying process, as the moisture content, which influences the viscosity of the amorphous phase, plays a critical role in determining the mechanical stability of the microstructure and, consequently, the integrity of the resulting lyophilized cake [62].

In summary, the key distinction between crystallising and glass-forming excipients during freezing is in their matrix phases. In eutectic crystallisation, a fine distribution of individual ice and solute crystals forms, allowing complete removal of water during the primary drying stage [63]. For amorphous substances, the water associated with the non-crystallised (vitrified) solute molecules must be removed by desorption, necessitating a secondary drying step.

1.4.2 Annealing during the freezing phase

Once the solution has solidified, an optional annealing step can be performed. Annealing is a heat treatment that modifies the physical and/or chemical properties of a material to enhance its ductility, soften it, and alleviate internal stresses [64]. In a frozen aqueous solution, annealing allows water to dissolve back from ice crystals into the matrix phase, reversing the freeze-concentration to the temperature-dependent matrix composition. This means that the matrix phase is more plasticised with water during annealing, which contributes together with the increase of the sample temperature to a reduction in the viscosity of the matrix phase [65]. This reduction is accompanied by enhanced molecular mobility within the matrix phase, facilitating relaxation processes that will be detailed later.

Theoretically, during annealing, the sample temperature must be increased to values between the glass transition temperature of the matrix phase at maximum freeze-concentration (T_g') and the melting point of the entire solution (T_m). Exceeding T_g' causes a steep decrease in the viscosity of the matrix phase, enabling changes in the material, which will be detailed below. However, surpassing T_m results in the dissolution of all crystalline structures, rendering the

annealing step pointless. This temperature range can be quite broad, depending on the solution. For instance, T_g' and T_m for a 10 % (w/w) sucrose solution are approximately -30 °C and -0.6 °C, respectively [66,67]. Typically, annealing temperatures for freeze-drying are set to ensure that the solution does not completely thaw, while minimising process time, as the impact of annealing is dependent on the annealing temperature [67,68]. Practical recommendations can be found for annealing temperatures of -15 °C to -10 °C [69], however studies often employ higher annealing temperatures of up to -5 °C to accelerate the annealing process [70–72].

As a side note, the term “melting temperature" has to be used carefully for an aqueous solution containing a glass-forming solute because the change in temperature primarily affects the solubility of the solute in water, rather than inducing a distinct phase transition. This means that the process involved is not a phase transition in the traditional sense, such as ice melting into water at a specific temperature, but rather a continuous shift in the amount of solvent that precipitates/dissolves over a wider temperature range.

The changes occurring in the material during annealing include relaxation processes that lower the system’s free energy, such as Ostwald ripening and glassy state relaxation [38,70]. Ostwald ripening is a coarsening process where small particles (in this context: ice crystals) dissolve and larger particles grow by the diffusion of molecules from smaller to larger particles. This process reduces the total number of particles and increases the average particle size. The underlying force of Ostwald ripening is the difference in curvature between smaller and larger particles. Smaller particles possess higher curvature, which lowers their melting points/solubility due to increased vapour pressure [73]. Glassy state relaxation refers to the relaxation of the internal stress and structural changes that occur in an amorphous material when heated above T_g' [70,74].

Both relaxation processes affect the subsequent drying of the frozen solution. During the drying process, pores form in the lyophilisate as the ice crystals sublimate and leave voids behind. Ostwald ripening, which increases the average pore size, reduces resistance to the movement of water vapour through those channel-like pores during sublimation, potentially speeding up the drying process [75,76]. Conversely, glassy state relaxation can alter the composition of the matrix phase by reducing the residual water content even before drying begins [38,70]. The reduction in water content leads to an increase in the glass transition

temperature of the solute phase [77]. Here, T_g' indicates that the material cannot be further freeze-concentrated under current conditions, i.e., a temperature reduction does not alter the composition of the matrix phase. However, an annealing step has been shown to raise T_g' [67]. This means that dependent on the treatment of the sample, freeze-concentration ceases at varying matrix compositions during the freezing/refreezing step. Furthermore, the collapse temperature $T_{c,}$ defined as the lowest sample temperature during drying where loss of the initial frozen microstructure takes place, has been shown to alter with an annealing step [78]. A higher T_c allows drying at higher temperatures with a reduced risk of structural collapse, thus decreasing drying time [79]. Consequently, this means that there must have been an excessive amount of water in the freeze-concentrated matrix before annealing, otherwise annealing (and refreezing) would not be able to reduce the residual water content in the amorphous phase. This phenomenon can be attributed to the fact that the viscosity in the system has risen so sharply after nucleation of the supercooled liquid that molecules were prevented from rearranging thoroughly into the corresponding phases [80]. In this state, the matrix phase possesses a higher enthalpy than it would in equilibrium. Several factors influence this non-equilibrium freezing of aqueous solutions, including solute concentration and type, cooling and heating rates, and the presence of impurities. These factors can affect the physical and chemical properties of the frozen material, such as microstructure, crystallinity, and stability [81].

Furthermore, it was shown that protein aggregation could be reduced by the addition of an annealing step [82]. A possible explanation for this phenomenon could be that aggregation of proteins occur at the ice/freeze-concentrate interface [83]. Ostwald ripening reduces the overall interfacial area as a result of ice crystal coarsening, and therefor decreases the area at which aggregation can take place.

1.4.3 Primary drying

After the annealing step is completed, the sample is cooled down again to allow the amorphous phase to reach its maximum freeze-concentrated state before the drying step commences. The main objective of primary drying is to remove the bulk water present in the ice phase via sublimation. For this purpose, the pressure within the drying chamber is set and consistently maintained between 50 mTorr (≈ 0.07 mbar) and 200 mTorr (≈ 0.27 mbar) using

a vacuum pump [69]. Furthermore, the shelves are heated to provide additional energy in order to speed up the drying process. Here it is important that the partial vapour pressure in the gas phase is lower than the saturation vapour pressure of the ice in the sample so that sublimation takes place, but higher than the saturation vapour pressure of the ice at the condenser so that the water molecules from the gas phase deposit at the condenser. Sublimation is an endothermic phase transition, which can be observed in the sample temperature as illustrated in Figure 1.10.

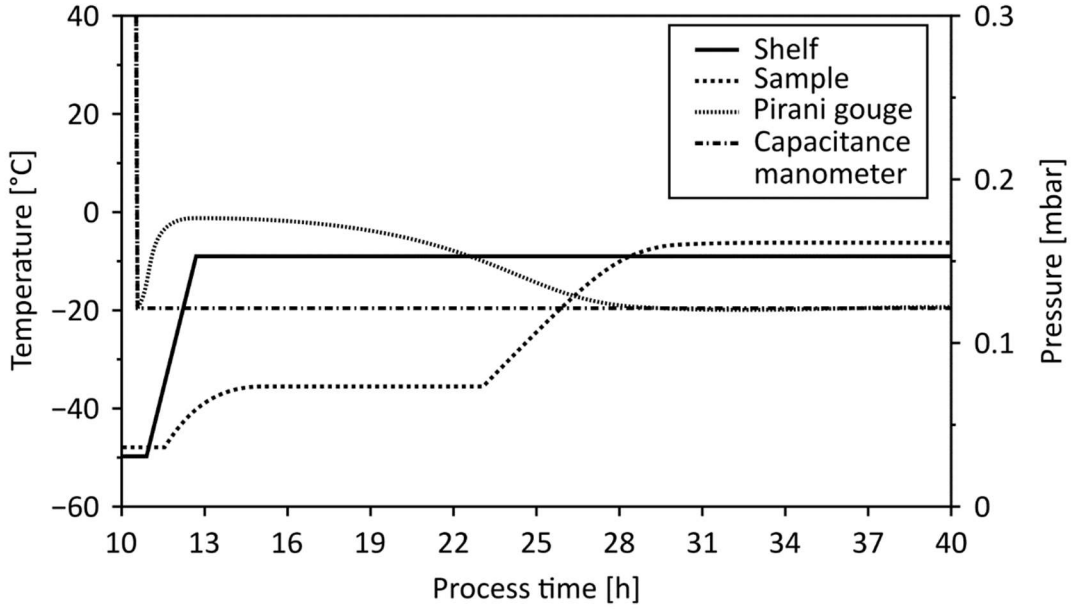

Figure 1.10: Temperature profile of a sample and shelf as well as pressure profile via Pirani gouge and capacitance manometer during primary drying.

Notably, the sample temperature is not equal to the shelf temperature during primary drying but is reduced due to the endothermic sublimation of ice crystals. This is particularly important because the frozen samples should not be heated arbitrarily in primary drying. Specifically, the sample temperature must not exceed the eutectic point T_{eu} for crystalline excipients or the collapse temperature T_c for amorphous substances. Generally, T_c ranges between 1 °C to 5 °C warmer than T_g' for a glass-forming solute [84,77]. Exceeding these temperature thresholds at the sublimation front can lead to structural damage in the matrix phase: in crystalline excipients, the eutectic mixture melts, while in amorphous substances, the matrix phase softens to the point where it cannot support its own weight and collapses [85,86]. The duration of primary drying is tied to the sublimation rate, which is determined by the shelf temperature. Increasing the product temperature by about 5 °C can halve the drying time.

Therefore, finding a balance between speeding up the process and preventing structural damage to the lyophilisates is essential when setting the shelf temperature for primary drying [87].

During primary drying, water vapour migrates from the samples to the condenser chamber, where it undergoes a phase change on the cold surface of the condenser, depositing directly as ice. The condenser functions as a water trap, with its capacity contingent on its surface area [77]. This migration of water molecules from the samples to the condenser is driven by the difference in saturation vapor pressure between the ice at the sublimation front in the sample and the ice on the condenser [18], which is mainly influenced by the temperature of each ice phase. Sublimation continues as long as the saturation vapor pressure at the sublimation front in the sample exceeds the partial vapor pressure in the chamber's gaseous phase, specifically above the sublimation front. Furthermore, deposition occurs as long as the partial vapor pressure within the gaseous phase of the condenser chamber exceeds the saturation vapor pressure of the ice on the condenser. Thus, the drying process relies on both the temperature difference between the sample and the condenser and the partial vapor pressure within the freeze-dryer. When endothermic sublimation occurs, it reduces the sample temperature, which in turn decreases the saturation pressure difference between the sample and the condenser. By heating the sample, this saturation pressure difference is increased, thereby accelerating the sublimation of bulk water from the frozen sample.

Various methods can be employed to determine the endpoint of primary drying. For instance, the temperature profile in samples, measured using thermocouples or wireless sensors, can be utilised to identify when the sample and shelf temperatures converge. Since sublimation is an endothermic phase change, it can be concluded that the bulk water has been removed at this point [16]. Alternatively, the pressure profile in the freeze-dryer can be used to determine when primary drying is complete. The total pressure in the drying chamber is monitored by a capacitance manometer. Additionally, a Pirani gauge, which measures the thermal conductivity of the gas phase, is also used. However, its readings are influenced by the gas composition. Specifically, a Pirani gauge will indicate an erroneously high pressure in the presence of water vapor, since water vapor has approximately 1.6 times the thermal conductivity of nitrogen, the main component of air. Once both pressure sensors are calibrated in a dry freeze-dryer, the alignment of readings from both the capacitance

manometer and the Pirani gauge during primary drying can indicate the absence of water vapour, thus signalling the end of the sublimation process [88].

1.4.4 Secondary drying

The water that has not precipitated into ice crystals during freeze-concentration remains closely associated with the solute molecules and must be removed during a secondary drying step. To facilitate this, the shelf temperature is typically increased, which accelerates the desorption of these bound water molecules.

However, care must be taken with the drying temperature during the transition from primary to secondary drying. The material typically has a relatively low glass transition temperature due to its high residual moisture content. This becomes particularly problematic if the temperature ramp between primary and secondary drying is steep, and water cannot desorb quickly enough to increase T_g. In the worst case, this can result in the collapse of the lyophilisate. However, primary drying and secondary drying cannot be completely separated from each other since desorption already takes place during the former [89]. Desorption occurs locally as soon as pores form due to the sublimation of bulk water, and the sublimation front migrates downwards, exposing areas of the matrix phase to the gaseous phase. Therefore, T_g of the matrix phase will already increase if sufficient time is allowed during primary drying.

During desorption, stresses induced by drying build up within the lyophilisate, which are relieved either by cracking and/or shrinkage of the material [90]. These phenomena are distinct from collapse, which occurs purely as a result of exceeding T_c [85]. The extent and ratio of cracking to shrinkage depend on various factors. For instance, materials like trehalose are more prone to cracking than sucrose, which could be due to the higher adhesion of trehalose to the glass vial. This adhesion restricts shrinkage as the primary mechanism of stress relief during drying, leading to cracking [91]. As solute concentrations increase, cracking tends to increase while shrinkage decreases. It is generally observed that stress relief is finite, i.e., an increase in cracking is always accompanied by a corresponding decrease in shrinkage and vice versa [92]. These behaviours are linked to the tensile fracture toughness of the material [93]. The volume change of the lyophilisate, or shrinkage, is slightly influenced by drying conditions but is closely related to the amount of residual water in the maximum

freeze-concentrated matrix before drying [67,94]. The conditions and duration of secondary drying allow the desired residual moisture in the lyophilisate to be achieved. This is important because APIs are not necessarily best stabilised when the residual moisture is as minimal as possible [95–97].

1.5 Microstructure formation in an aqueous solution during freezing

The literature on the properties of the porous microstructure in lyophilisates generally agrees that pore size and number are influenced by two key physical phenomena: nucleation and Ostwald ripening. The nucleation temperature is crucial as it affects the number of stable nuclei that form and subsequently grow into ice crystals. A lower nucleation temperature results in a greater number of stable nuclei [13,16,86,98]. This is further supported by molecular simulations, which indicate that for homogeneous ice nucleation at 15 °C below the equilibrium freezing temperature, the critical size of a nucleus is approximately 8000 molecules, corresponding to a critical radius of 4 nm. This critical size decreases to 1.7 nm with a greater degree of supercooling of 35 °C [99].

The volumetric nucleation rate B_0 describes the number of stable nuclei that form in a given volume per unit time and is defined by Colucci et al. (2020) as:

$$B_0 = k_b\left(T_f - T_n\right)^b, \qquad \text{(Eq. 1)}$$

where k_b and b are kinetic parameters, T_f is the equilibrium freezing temperature, and T_n is the nucleation temperature. The kinetic parameters in this model can be adjusted over a range of values until an acceptable fit is achieved between the model predictions and experimental data. The experimental data for this purpose can be determined by examining images of the dried lyophilisate with a scanning electron microscope (SEM) and quantifying the number of pores.

According to Equation 1, the critical factor determining the number of stable nuclei is the difference between the equilibrium freezing temperature of the mixture and the actual nucleation temperature. However, this does not imply that nuclei form uniformly across the entire sample volume at the moment of nucleation. Instead, nucleation typically begins with the formation of at least one primary nucleus, likely through heterogeneous nucleation. From this initial site, the ice crystal front advances, with new nuclei forming via secondary

nucleation, often simply referred to as crystallisation, throughout the entire supercooled volume of the sample [86].

The rate of crystallisation, or more specifically, the secondary nucleation front velocity or the propagation rate of the ice front, is influenced by the degree of supercooling with greater supercooling resulting in a faster propagation rate [2,100]. Empirical equations have been formulated to depict the relationship between the propagation rate of the ice front and the nucleation temperature. For instance, at an average nucleation temperature of -10 °C ± 3 °C for water for injection, the propagation rate of the ice front is approximately 5.2 cm/s. However, this rate significantly increases to about 23.7 cm/s at a lower nucleation temperature of -20 °C [16]. When a solute is present, the propagation rate of the ice front slows down to the order of mm/s and varies depending on the solute concentration in the solution [101,102].

Once primary and secondary nuclei have formed, water molecules precipitate from the supercooled solution into these stable nuclei, forming ice crystals. Although this process does not change the number of crystals, it does increase their size. These ice crystals have crystallographic orientations that prevent them from coalescing when there is a mismatch between the orientations of neighbouring crystals [103]. The volume of water that precipitates is solely dependent on the ambient temperature, and this process continues until the maximum freeze-concentrated composition of the solute-enriched matrix phase is achieved [59]. Assuming that no additional nucleation occurs once the stable primary and secondary nuclei are present, the size of the resulting ice crystals primarily depends on the initial number of these nuclei, as illustrated in Figure 1.11. This rationale also underpins the methodology used to determine the parameters for Equation 1, where each individual pore is attributed to a corresponding individual ice crystal and, by extension, to a preceding individual stable nucleus.

In their study, Colucci et al. (2020) measured pore sizes in a freeze-dried 5 % (w/w) sucrose solution using scanning electron microscopy (SEM), finding sizes ranging from approximately 25 µm to 50 µm based on axial position within the lyophilisate. Thomik et al. (2022) reported pore sizes of 23.73 µm ± 11.13 µm in a similar 5 % (w/w) sucrose solution, measured using micro-computed tomography (µ-CT). Additionally, Fang et al. (2020) employed low-pressure mercury intrusion porosimetry and Brunauer-Emmet-Teller (BET) analysis to determine

average pore sizes ranging from 20 µm to 60 µm in their study of a similar solution. Although the freezing protocols and equipment varied across these studies, the results consistently showed a similar magnitude with the minimum pore size around 20 µm.

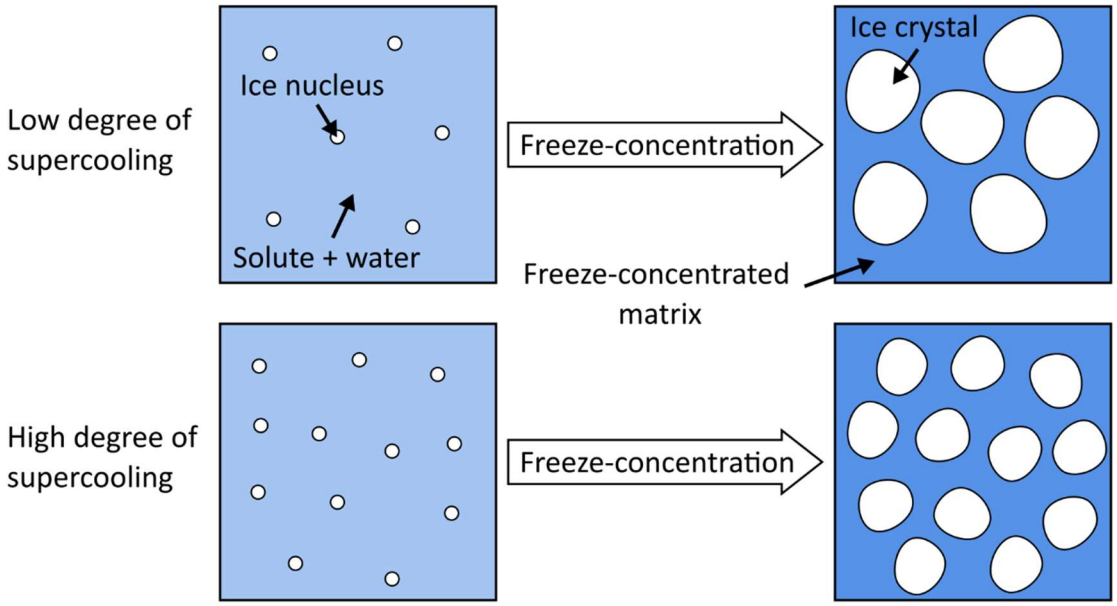

Figure 1.11: Schematic depiction of the influence of supercooling on the size of ice crystals in a frozen solution.

These findings assume that size and number of pores in non-annealed samples are solely influenced by nucleation kinetics when no additional annealing step is included. However, this explanation simplifies the formation of microstructures in aqueous solutions during freeze-drying. The phase transition during freezing generates latent heat of crystallisation, which raises the sample temperature and results in a complex thermal history throughout the freezing stage of a lyophilisation cycle. In summary, it is assumed that the number of stable nuclei formed during freezing dictates the number of individual ice crystals in the frozen solution, and consequently, the number of pores in the dried lyophilisate. This work, however, seeks to clarify the impact of the latent heat of crystallisation during recalescence and the subsequent crystallisation phase on the microstructural formation in solutions intended for freeze-drying.

1.6 Coarsening of the ice crystal phase during annealing

An annealing step can be incorporated into the process post-freezing to coarsen the disperse ice phase, as depicted in Figure 1.12. Nakagawa et al. (2018) demonstrated that a 20 % (w/w)

sucrose solution, initially with an average pore size of approximately 60 µm after 1 hour of annealing at -5 °C, expanded to about 150 µm after 6 hours of annealing. Similarly, in the study by Thomik et al. (2022), a 5 % (w/w) sucrose solution annealed for 11 hours at -5 °C showed an increase in pore size from 23.73 µm ± 11.13 µm to 33.04 µm ± 26.95 µm.

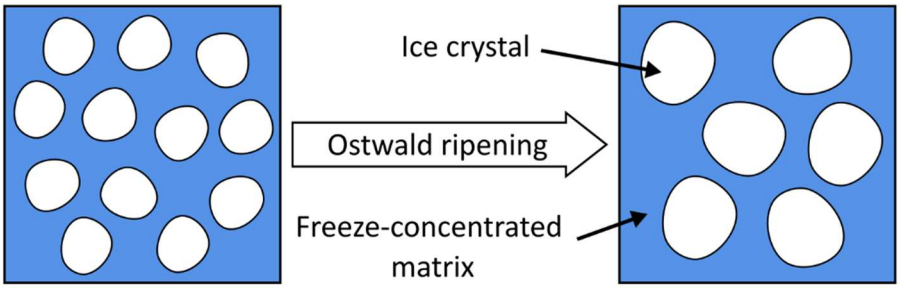

Figure 1.12: Schematic depiction of the influence of annealing on the size of ice crystals in a frozen solution.

As described in Chapter 1.4.2, the phenomenon that occurs during annealing is called Ostwald ripening, and it is driven by the reduction of the system's free energy. This effect is mathematically expressed by the classical Lifshitz-Slyozov-Wagner (LSW) theory of Ostwald ripening, which describes the coarsening behaviour of particles (here: ice crystals) or droplets in a matrix phase or solution. It is often used in the context of material science, especially for metal alloys, when characterising the growth of the average particle size over time. In the work of Niethammer (2008), a detailed description of assumptions and limitations regarding the LSW theory are given. The LSW theory assumes that the particles are spherical and exhibit initially a uniform size distribution. Additionally, the distance between particles is considered large compared to the individual particle size, so that diffusion of molecules from the particulate phase is the dominant mechanism for particle growth. Furthermore, the concentration in the surrounding medium or matrix phase is assumed to be constant, i.e., no concentration gradients are present in the matrix phase. The mathematical expression for the temporal change of particle radius *r* due to dissolution and redeposition is given by [105]:

$$\frac{dr}{dt} = \frac{D}{r}\left(\Delta - \frac{\varepsilon}{r}\right), \qquad \text{(Eq. 2)}$$

where *D* is a system-dependent diffusion constant, Δ is the difference between concentration at the particle surface and the equilibrium concentration in the liquid phase, ε is a term

containing surface tension, atomic volume of the solute, solubility, the ideal gas constant, and temperature.

Under the assumption that diffusion of molecules through the liquid phase is the rate limiting factor, the following equation describing the change of the mean particle size can be derived [106]:

$$\bar{r}(t)^3 = r_0^3 + kt\,, \qquad \text{(Eq. 3)}$$

where $\bar{r}$ is the mean particle radius, r_0 is the initial particle size, and k is the isothermal recrystallisation rate, given by [105]:

$$k = \frac{8\sigma c_\infty v^2 D}{9RT}, \qquad \text{(Eq. 4)}$$

where σ is the surface tension, c_∞ is the solubility of the particle material, v is the molar volume of the particle material, D is the diffusion coefficient of the particle material, R is the ideal gas constant, and T is the absolute temperature.

According to Equation 3, the mean particle size increases with time, and the rate of increase is proportional to the cube of the particle radius. In an ideal system that fulfils all the requirements of LSW theory, Equation 4 can be used to calculate the recrystallisation rate, i.e., the rate at which the particulate phase in the system coarsens, from first principles. In such a case, the rate of Ostwald ripening can be deduced from the physical and chemical properties of the system.

1.7 Morphological assessment of the microstructure in a lyophilisate

Various techniques are employed in the literature to assess the impact of annealing in a frozen disaccharide solution or the dried lyophilisate. Lyophilisates shrink due to desorption of the unfrozen water content in the maximum freeze-concentrated matrix phase during primary and secondary drying [91,67]. Although shrinkage primarily reflects a reduction in the bulk volume of the lyophilisate, it also implies changes in the internal microstructure. In the simplest scenario, a proportional reduction occurs in the individual structures, i.e., if the bulk volume decreases by approximately 20 %, the individual pores are similarly reduced in their volume. In other scenarios, internal structures may collapse to compensate for the overall reduction in bulk volume. Therefore, it is crucial to specify whether the discussion pertains to ice crystals in the frozen solution or pores in the dried lyophilisate.

Freeze-drying microscopy is commonly used to determine the collapse temperature of a solution during the primary drying step and was used in this work to investigate the impact of freezing and annealing on the initial formation and the subsequent evolution of the microstructure in frozen disaccharide solutions. Nakagawa et al. (2018) used a different approach to investigate the microstructure, where cross-sections of frozen rhodamine dye-stained solutions were cut using a microtome, followed by measurement of ice crystal size with a light microscope. Alternatively, scanning electron microscopy (SEM) can be utilised to analyse the microstructure after drying [107,108]. Advancements in this field include scanning electron cryomicroscopy (cryo-SEM), which enables direct observation of frozen and undried samples [109,110]. Additionally, X-ray microtomography was employed by Thomik et al. (2022) to assess the pore size distribution in freeze-dried samples.

However, each of these methods presents certain drawbacks when characterising and quantifying the microstructure that forms as a result of freezing and evolves during annealing. Freeze-drying microscopy, for instance, confines the sample between two glass plates rather than in a larger bulk volume, which can affect the coarsening of the ice crystal phase. Techniques requiring the slicing of samples, such as microtome use, yield results that depend on the fracture or slice plane in the frozen solution or lyophilisate. Since ice crystals or pores are exposed at random and varying positions, differentiation becomes challenging if only the narrowest or widest parts of an ice crystal or pore are visible, making all measured parameters imprecise. Similarly, SEM and cryo-SEM analyses produce two-dimensional data from a three-dimensional structure due to the opacity of the sample surface, limiting observations to an area rather than a volume. Techniques that require dried samples also pose problems, as the removal of water may alter the structure within the matrix phase. Additionally, conducting an entire lyophilisation cycle just to test a single annealing condition can be excessively time-consuming. Moreover, the resolution of methods like X-ray microtomography may not be sufficient to capture all fine structures within the lyophilisate. This limitation was illustrated by Thomik et al. (2022), who reported varying porosities for annealed versus non-annealed samples. This finding is contrary to expectations since annealing should increase the average pore size, yet the total volume of the matrix phase, and consequently the porosity, should remain largely unchanged.

Due to the limitations mentioned above, current methods for determining the microstructure in a frozen solution or in a dried lyophilisate are insufficient to conclusively assess the impact of freezing and annealing conditions on the microstructure. Consequently, a different approach is necessary. This approach should not be limited to experimental methods alone but should also incorporate computational techniques. These computational methods can simulate phenomena that are not directly observable or measurable, providing a more comprehensive understanding of the processes involved.

1.8 Numerical simulations and phase-field methods in the pharmaceutical field

Numerical simulations are computational techniques that are used to model phenomena or entire systems as they evolve over a period of time. By solving algorithms and equations on a computer, these simulations make predictions about the system of interest [111,112]. These *in silico* methods can be used complementary to experimental findings, i.e., experimental data can be used to calibrate simulations, but processes can also be simulated when the acquisition of experimental data is not feasible. Overall, simulation techniques can provide valuable insights into complex systems and phenomena, but their meaningful use depends on appropriate consideration of limitations and assumptions [113,114].

In general, simulation models can be classified into two types: first-principle and phenomenological models. First-principle models, also known as *ab initio* (“from the beginning") models, are built directly on fundamental physical or chemical laws and principles. This means that the underlying equations represent the most basic, irreducible elements of these laws. The advantage of first-principle approaches is their utility in exploring areas with limited data availability, providing insights based on theoretical foundations. On the other hand, phenomenological models are empirical, developed based on observations and experimental data. These models mathematically describe phenomena, such as the rate of change of a parameter, and are calibrated to replicate observed behaviour as accurately as possible. While typically simpler than first-principle models, phenomenological models rely more heavily on assumptions, which may affect the reliability of their predictions.

Various simulation techniques exist, each with its advantages and disadvantages depending on the application area and the system under investigation. These simulations can model physical, chemical, biological, and other types of systems, and are extensively used across

scientific research, engineering design, and numerous other fields. For instance, computational fluid dynamics (CFD) is widely employed to simulate the flow behaviour of fluids in three-dimensional spaces. CFD simulations are grounded in the fundamental laws of physics, as they derive from the conservation laws of mass, momentum, and energy, and do not depend on empirical relationships or assumptions. Applications of CFD in the field of lyophilisation include optimising the design of freeze-dryers [115] or condensers [116], as well as investigating the heat transfer within freeze-dryers [117,118], or the mass flux in vials [119]. Furthermore, the scale-up of processes is also supported by CFD analysis [120].

Simulation methods other than three-dimensional modeling are often employed to describe parts of the freeze-drying process. For instance, Colucci et al. (2020) developed a one-dimensional population balance model that predicts the pore size in a lyophilisate based on its axial position within the vial. Similarly, Chun et al. (2020) proposed a mathematical model that correlates primary drying times with the size of ice crystals in frozen solutions. Additionally, Arsiccio et al. (2017) utilised a mechanistic model to predict the distribution of ice crystal sizes after freezing. While detailed information on three-dimensional simulations of ice crystals in pharmaceutical solutions during annealing is scarce, the formation of similar microstructures, which consist of particulate and matrix phases, and their coarsening is well-established in other fields such as metallurgy. Phase-field models, especially for alloys, are used in metallurgy to better understand microscopic evolution and changes in the material, as evidenced by recent studies by Geslin et al. (2015), Radhakrishnan et al. (2018), and Ansari et al. (2021).

The phase-field method is a numerical simulation technique used to describe phase boundaries and microstructures within materials. Phase-field models are a powerful tool in materials science, physics, medicine, biology, and earth sciences for simulating morphological changes in materials. These simulations use numerical methods to represent the spatial and temporal evolution of individual phases, including their interfacial motions, and can consider different characteristics such as chemical compositions and crystallographic orientations. The microstructure results from the shape and volume of the individual phases, which in turn are formed by diffusive, mechanical, thermal, electrochemical or magnetic driving forces [126].

Phase-field models first gained prominence in the 1970s and 1980s when scientists explored phase transformations, specifically focusing on solidification and microstructure evolution.

Pioneers like J.W. Cahn and J.E. Hilliard made significant contributions, laying the foundational groundwork for understanding the mathematics of phase separation and transitions. In the 1990s, researchers such as W.J. Rappel and A. Karma expanded these studies to include solidification and dendritic growth. With recent advancements in high-performance computing, phase-field models now enable detailed simulations, leading to technological progress through new mathematical models, algorithms, and a broadening range of applications.

A defining characteristic of phase-field models is their ability to depict distinct phases within a system using an order parameter. This parameter generally ranges from 0 to 1, with 0 representing one phase, 1 representing another, and values between 0 and 1 indicating the interface that separates these phases. The interface demonstrates diffusivity, creating a gradual transition across a finite area. This inherent diffusivity enables a realistic representation of phase changes as they occur. Additionally, phase-field models streamline the depiction of complex interfacial motions, such as merging, dissolution, and breakup, by reconstructing the interface through a set of continuous field variables. The basic principle of a phase-field model is depicted in Figure 1.13.

In a phase-field model, the driving force is characterised by the free energy functional. Different components of the free energy can be included, each incorporating distinct terms tailored to the specific aspects of the energy balance that need representation in the simulation. In general, the free energy functional can be defined as follows [126]:

$$F = \int_V \left[f_c + f_g + f_m + f_e \right] dV, \qquad \text{(Eq. 5)}$$

where f_c is the chemical free energy density, f_g is the gradient free energy density, f_m is the mechanical free energy density, and f_e is the external free energy density.

The chemical free energy density, also known as homogeneous or bulk free energy density, promotes phase separation in the absence of an interface, while the gradient energy density penalises the formation of sharp interfaces by imposing penalties. The mechanical free energy density includes contributions from elastic displacements caused by stress and strain. Additionally, all external forces, such as electrostatic or magnetic influences, are incorporated into the external free energy density. During simulations, concerted efforts are made to minimise the system's free energy, which leads to changes in the phases within the system.

Additionally, phase-field models also have the capacity to describe multiple phases concurrently as multi-phase systems.

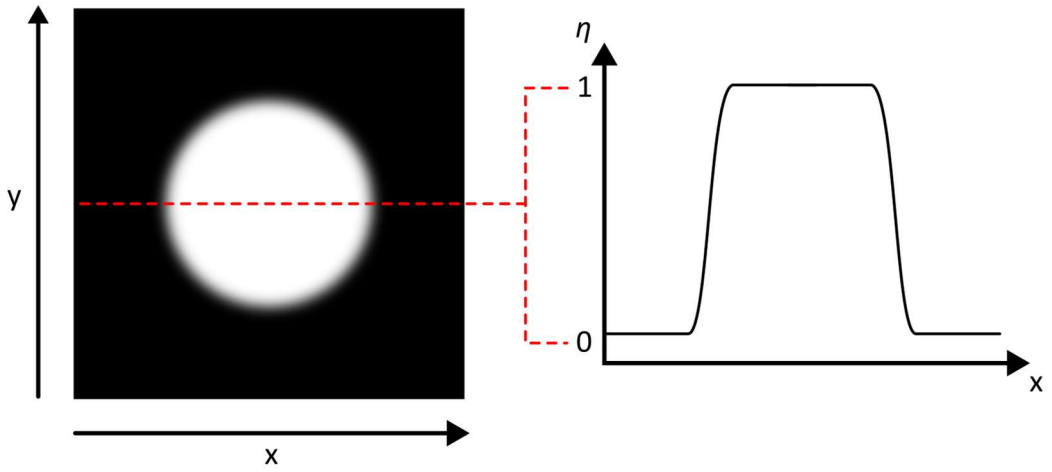

Figure 1.13: Principle of the order parameter (η) in phase-field modeling. The phases are captured by values between 0 (black) and 1 (white). Modified from [127].

The relevance of phase-field models in the pharmaceutical environment is increasingly evident, with a growing body of literature addressing the microscopic behaviour of substances within this context. Van der Sman (2016) enhanced a two-dimensional phase-field model with theories on thermodynamics and diffusion kinetics to simulate ice crystal growth in a sugar solution during freezing. Similarly, Fan et al. (2018) developed a sophisticated two-dimensional phase-field model to describe the phenomenon of freeze-concentration during freezing, based on first-principle assumptions. Li and Fan (2020) modelled macroscopic freezing in a cylindrical vessel, while Li et al. (2022) applied phase-field modeling to explore dendritic morphologies and ice crystal growth inhibition in a sucrose solution. The investigations in this work are based on the model used by Mukherjee et al. (2009), which was originally used by the authors to elucidate the effect of misfit strain and interface curvature on the growth of a single precipitate in a supersaturated matrix. A detailed description of the model can be found in the Results section of this work.

2 Materials and methods

2.1 Materials

The characteristics of main materials used in this work are described below. A full list of materials and sources/suppliers can be found in Appendix E.

2.1.1 D-(+)-sucrose

D-(+)-sucrose (β-D-fructofuranosyl-α-D-glucopyranoside), commonly known as table sugar or saccharose, has a molecular weight of 342.3 g/mol and is a non-reducing disaccharide composed of a glucose molecule linked to a fructose molecule by a glycosidic bond. The structural formula is shown in Figure 2.1.

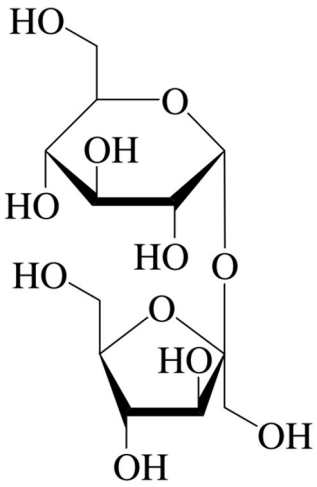

Figure 2.1: Chemical structure of D-(+)-sucrose [66].

Sucrose occurs naturally in various plant sources, particularly sugar cane and sugar beet, and is known for its sweetness, making it a common choice as a sweetener in the food and beverage industry. In the human body, the enzyme sucrase catalyses the hydrolysis of sucrose into its constituent monosaccharides. In pharmaceutical applications, sucrose is valued for its ability to form an amorphous glass during lyophilisation, which acts as a stabilising agent in pharmaceutical formulations. Moreover, sucrose does not undergo the Maillard reaction with amino acids, a process that can degrade active pharmaceutical ingredients. During primary drying, sucrose has been shown to be more effective for preserving the secondary structure of proteins than the disaccharide trehalose [37].

2.1.2 D-(+)-trehalose

D-(+)-trehalose (α-D-glucopyranosyl-α-D-glucopyranoside), with a molecular weight of 342.3 g/mol, is a non-reducing disaccharide containing two molecules of glucose linked via a glycosidic bond. Its structural formula is depicted in Figure 2.2.

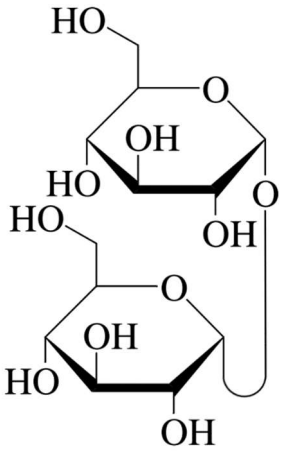

Figure 2.2: Chemical structure of D-(+)-trehalose [66].

Trehalose, derived from plants, fungi, and yeast, is less sweet than sucrose. It is metabolised in the body by the enzyme trehalase to produce two glucose molecules. In the pharmaceutical sector, trehalose plays a similar role to sucrose, mainly due to its ability to form an amorphous glass during lyophilisation, which contributes to its role as a stabiliser in pharmaceutical formulations. Trehalose does not break down proteins or peptides by reacting with amino acids, and research has suggested that it is more efficient to preserve protein structure during long-term storage than sucrose [37].

2.2 Methods

2.2.1 Lyophilisation

In this work, a pilot-scale freeze-dryer was used to record the temperature profiles of samples during the freezing and annealing steps. The components of this freeze-dryer are detailed in Table 2.1. Temperature profiles were monitored using thermocouples and wireless temperature sensors. To ensure uniform conditions for the samples, only the middle shelf of the three available in the freeze-dryer was used, as temperatures varied between the shelves. To minimise heat conduction and radiation between samples due to the latent heat of crystallisation, samples were spaced with two empty vials between them. The loading scheme

can be seen in Figure 2.3. Samples were pre-cooled to 5 °C for 30 minutes in the freeze-dryer to equalise the starting conditions for all samples. Details of the freezing steps involved are provided in the Results section for each experiment.

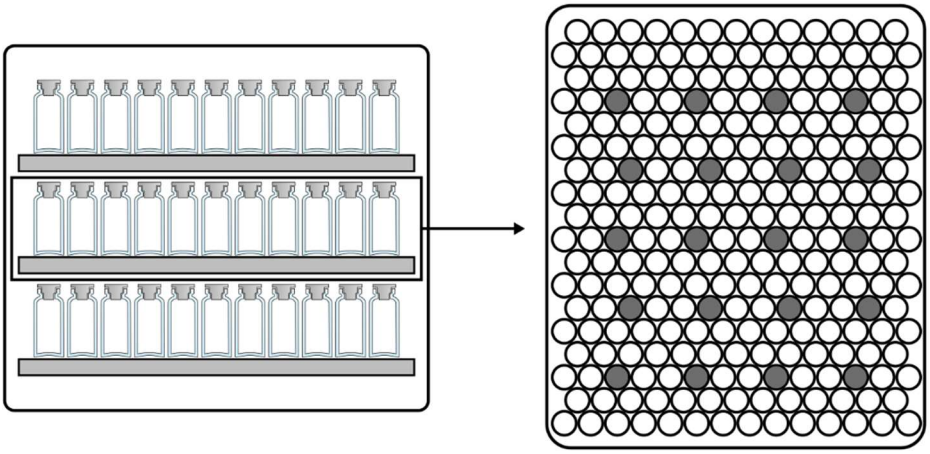

Figure 2.3: Loading scheme of the freeze-dryer for all experiments in this work. In the top view (right) the filled vials are shown in grey and empty vials in white.

Table 2.1: Components of the freeze-dryer used in this work.

Component	Description	Supplier
Freeze-dryer	Epsilon 2-10D LSCplus	Martin Christ, Osterode am Harz, Germany
Camera	LyoCam	Martin Christ, Osterode am Harz, Germany
Wireless temperature sensor	WTMplus 2.0	Martin Christ, Osterode am Harz, Germany
Software	LPCplus	Martin Christ, Osterode am Harz, Germany

2.2.2 Freeze-drying microscopy

Freeze-drying microscopy (FDM) is a conventional method for determining the collapse temperature T_c of a formulation designated for freeze-drying. FDM employs a specialised freeze-drying stage system that allows to mimic the temperature and pressure conditions of a freeze-dryer. In this setup, the sample is placed between two glass plates, which are separated by a spacer. These plates sit on a thermally conductive silver block that can be either electrically heated or cooled with liquid nitrogen. The entire freeze-drying stage system is hermetically sealed, allowing the creation of a vacuum with a vacuum pump. To determine the T_c of a formulation, the temperature is gradually increased during the drying process until

structural changes, such as collapse, are observed at the sublimation front. The components of the freeze-drying microscope are shown in Figure 2.4 and listed in Table 2.2.

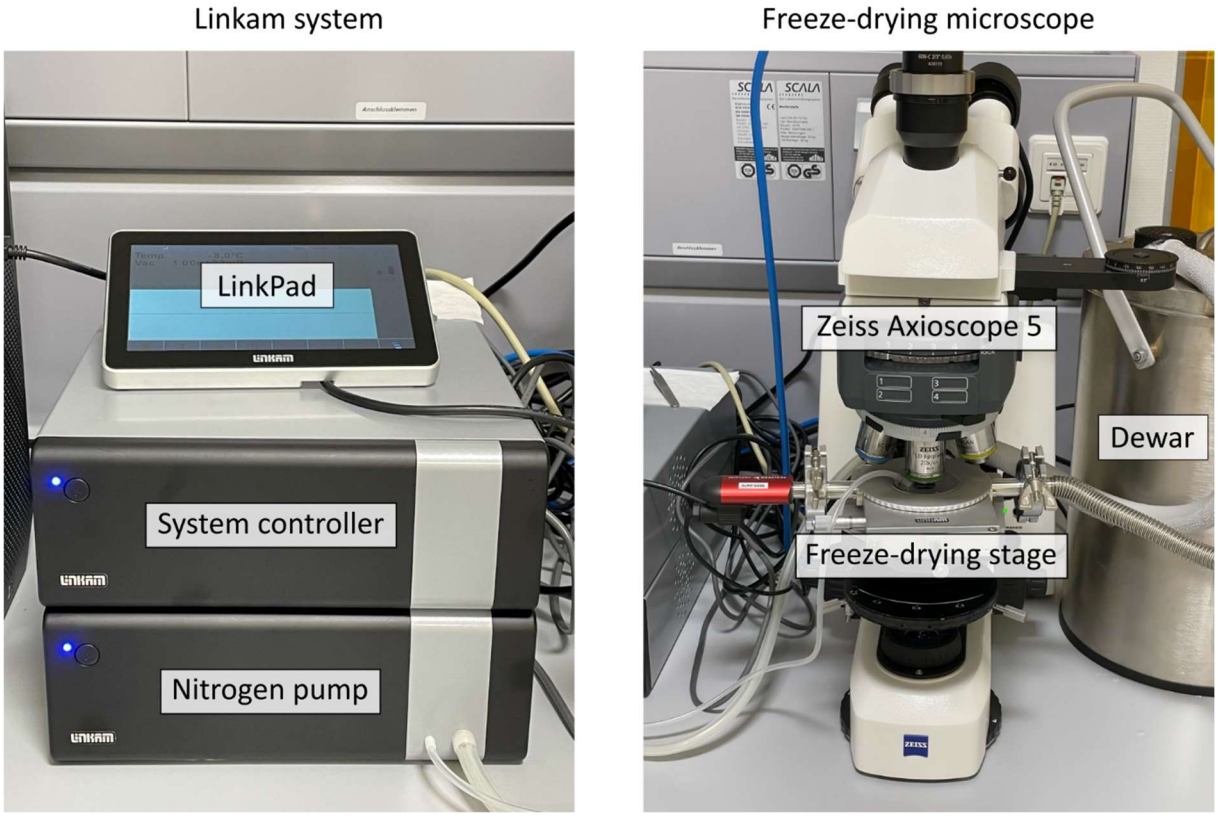

Figure 2.4: Freeze-drying microscope (right) with the Linkam control system (left).

Table 2.2: Components of the FDM system used in this work.

Component	Description	Supplier
Freeze-drying stage	FDCS196	Linkam Scientific Instruments Ltd., Salfords, UK
Microscope	Axioscope 5	Carl Zeiss, Oberkochen, Germany
Polariser	Polarisator D	Carl Zeiss, Oberkochen, Germany
Camera	Axiocam 305 color	Carl Zeiss, Oberkochen, Germany
Liquid nitrogen pump	LNP96	Linkam Scientific Instruments Ltd., Salfords, UK
System Controller/LinkPad	T96	Linkam Scientific Instruments Ltd., Salfords, UK
Software	ZEN core v3.1	Carl Zeiss, Oberkochen, Germany

In this work, the freeze-drying microscope was utilised to observe microstructural changes in a (partially) frozen solution during the annealing process. To achieve this, the temperature profile was controlled to initially freeze the sample thoroughly, followed by heating and maintaining it at specific annealing temperatures. The specifics for each experiment are provided in the relevant Result sections.

2.2.3 Polarised light microscopy

The freeze-drying microscope was also used in this work for polarised light microscopy. Polarisation of light is frequently used in various fields such as mineralogy, biology, and material sciences, and its principles are explained below and illustrated in Figure 2.5.

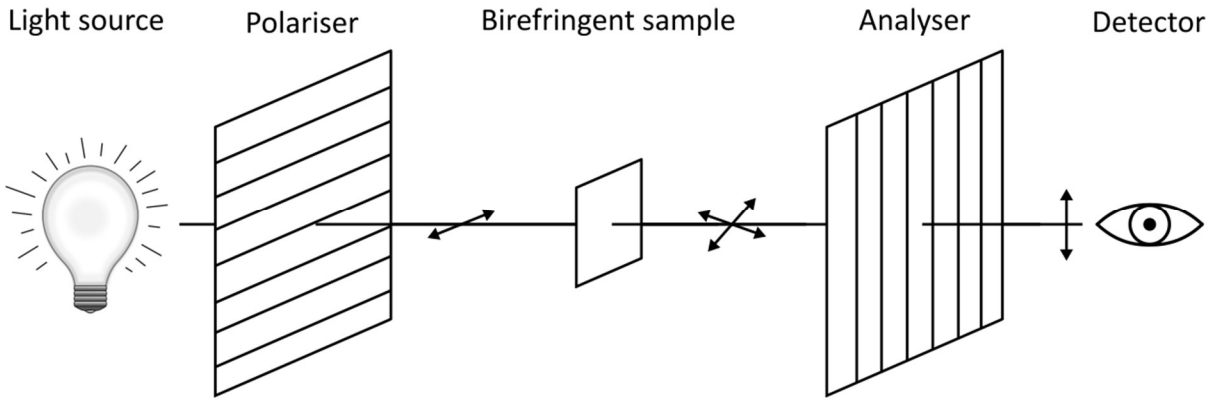

Figure 2.5: Principle of polarisation microscopy on a birefringent sample. Modified from [133].

The polariser filters the incoming light, allowing only the light waves that oscillate in one direction to pass. This produces polarised light which then interacts with the sample. Materials with anisotropic properties can change the polarisation state of the light passing through them because their optical properties vary with the direction of vibration of the light. This can either cause a change in the direction of vibration or split the light into two beams vibrating perpendicular to each other, a phenomenon known as birefringence. The modified light then passes through the analyser, which is oriented perpendicular to the polariser. The analyser further filters the light so that only those components of the light that have been modified by the sample (e.g., by birefringence) can reach the detector.

If an isotropic sample, which has uniform optical properties in all directions, is placed under the microscope, it generally appears dark. Such materials do not alter the polarisation direction or cause a phase difference in the light wave. When the polariser and analyser are

perpendicular, light passing through an isotropic sample remains unchanged, preventing it from passing through the analyser to the detector.

When observing crystals, which are typically birefringent, under a polarisation microscope, the magnitude of birefringence and variations in crystal orientation can be visualized. This is crucial for understanding the material properties and behaviours.

2.2.4 Differential scanning calorimetry

The thermal profile of disaccharide-water systems was determined using a dual furnace differential scanning calorimeter (DSC). For each sample, 10 µl of solution was added to an aluminium pan and sealed. The samples were cooled from ambient temperature to -50 °C at a cooling rate of 10 °C/min and held for 1 minute to ensure complete solidification. The samples were then heated to 25 °C at a rate of 10 °C/min. The melting temperature of the solution was determined by detecting the melting peak in the endothermic heat flux. The DSC was calibrated with indium at a rate of 10 °C/min. All measurements were performed in triplicate. The components of the DSC system are listed in Table 2.3.

Table 2.3: Components of the DSC system.

Component	Description	Supplier
Differential scanning calorimeter	DSC 8500	PerkinElmer, Waltham, USA
Cooler	IP-100	PolyScience, Niles, USA
Software	Pyris	PerkinElmer, Waltham, USA

2.2.5 Phase-field computation and visualisation

A two-dimensional and three-dimensional multiphase-field model was implemented and computed using MATLAB R2022b (TheMathworks Inc, Natick, USA). A detailed description of the model, including the governing equations, initial conditions and simulation parameters, is given in the Results section. The calculations were performed on desktop workstations. However, comparable computation times were also achieved using conventional personal computers. On average, about 1 week of computing time was required to simulate 6 hours of annealing for a simulation domain size of 240x208x196 grid points. Validation and stability

analyses were also carried out and are included in Appendix A. The simulation results were visualised using the open-source data analysis software ParaView (Sandia National Laboratories, Kitware Inc, Los Alamos National Laboratory).

2.2.6 Image analysis

To determine recrystallisation rates in annealing experiments as well as investigate the freezing behaviour of disaccharide solutions, individual ice crystals on FDM images were marked in the open-source scalable vector graphics editor Inkscape (Inkscape Community). The automatic counting function in Inkscape was then used to determine the number of ice crystals in each image. This process is shown in Figure 2.6.

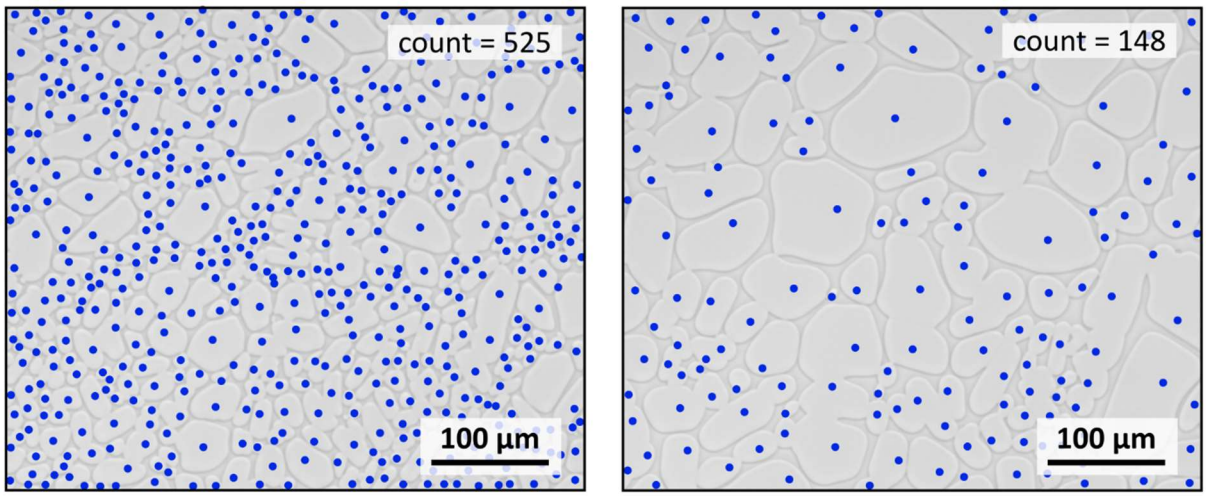

Figure 2.6: Counting of individual ice crystals from an FDM image section of a 10 % (w/w) trehalose solution during annealing at -6 °C for 10 min (left) and 60 min (right). The blue dots were manually placed to mark each individual ice crystal.

3 Results and discussion

The findings of this thesis are presented in the following sections. As described in the Objectives chapter, the main aspects can be summarised as follows. The first part focuses on the investigation of the microstructure consisting of a particulate (here: ice crystal) and matrix phase during freezing of an aqueous disaccharide solution. In the second part, a phase-field simulation was implemented and calibrated with experimental data to model the coarsening behaviour of the microstructure in the frozen solution during annealing. The final step of this work was to compare and discuss data obtained from the literature with data generated from the phase-field simulations.

3.1 Microstructure formation during freezing

In Chapter 1.5, the formation of microstructure during the freezing of an aqueous solution, as often discussed in the literature, was explained. It was also noted that samples develop a complex thermal history during the freezing process, namely, the temperature of the sample does not merely follow the shelf temperature (see Chapter 1.4.1). This raises the question of how much the thermal history, derived from the measured temperature profile during freezing, influences the formation of the microstructure. To assess this, the temperature profiles of samples during freezing in a lyophiliser were analysed, followed by an investigation of the impact of thermal history on the microstructure in a frozen sucrose solution using a freeze-drying microscope. Given that disaccharide solutions ranging from 5 % to 20 % (w/w) are commonly used in the field of lyophilisation [70,83,71], a 10 % (w/w) sucrose solution was employed for this work.

3.1.1 Recalescence and crystallisation in samples during freezing

To investigate the thermal history of samples during freezing, vials were filled with a 10 % (w/w) sucrose solution and placed in a lyophiliser. Thermocouples were positioned close to the glass bottom inside the samples to record the temperature. After a short precooling phase to equilibrate the sample temperature to approximately 5 °C, the shelves were cooled to -40 °C at a rate of 1.2°C/min. Images of the filled vials were taken continuously during this process. The results are shown in Figure 3.1.

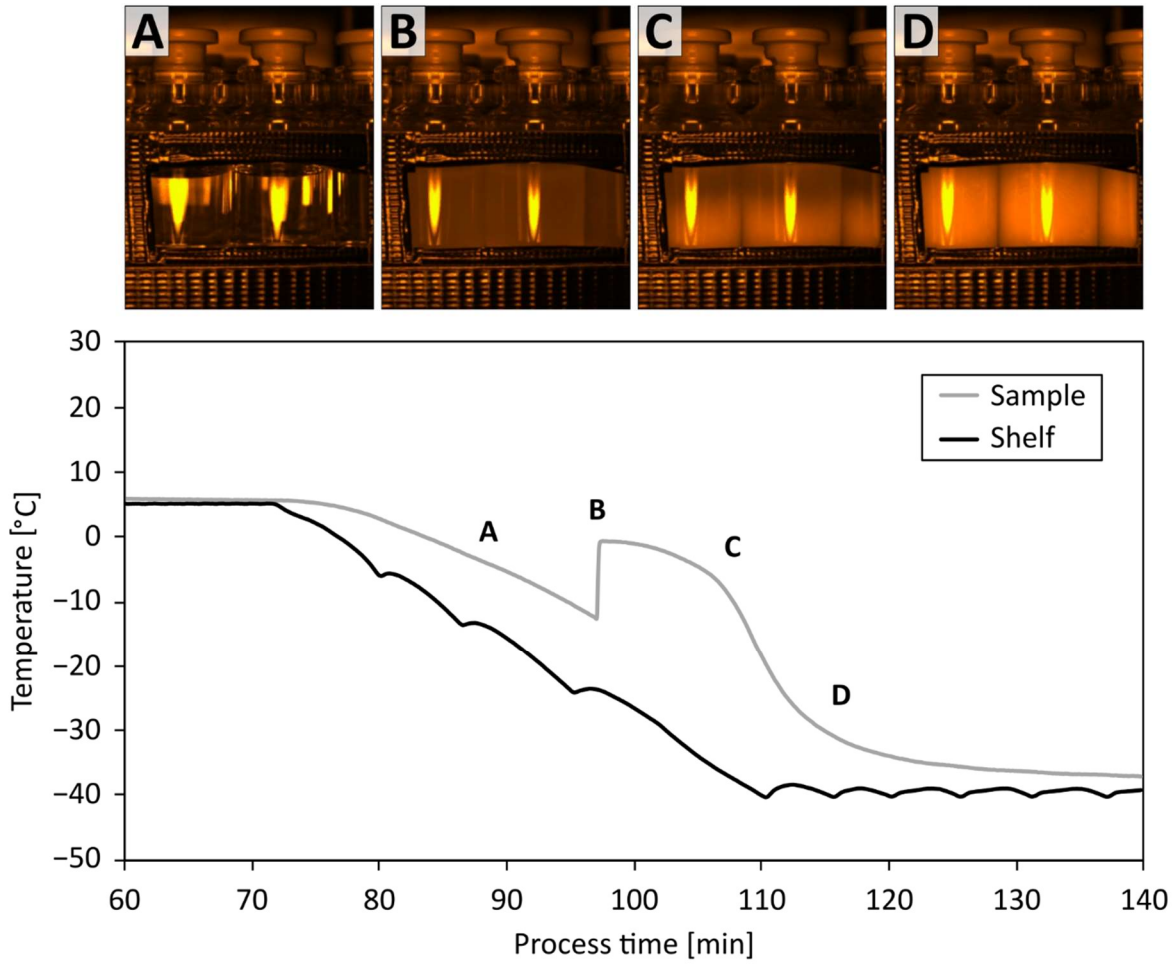

Figure 3.1: Shelf and sample temperature during freezing at 1.2 °C/min. The sample temperature was measured near the bottom of the vial. Pictures were taken of samples at different stages: supercooling (A), nucleation and recalescence (B), crystallisation (C), and complete solidification (D).

During the cooling of the shelves, the temperature inside the samples also decreased. Notably, a delay between shelf and sample temperature became apparent due to the imperfect conduction of heat and the placement of the thermocouple with a small distance of approximately 5 mm from the bottom of the vial. The sample temperature decreased to nearly -13 °C without freezing, which means that the solution became supercooled once falling below its equilibrium freezing temperature (A). Upon the formation of stable nuclei in the supercooled solution, the initiation of ice crystal growth lead to a sudden increase in the sample temperature as a result of the heat of crystallisation (B). Once the sample reached its maximum temperature during recalescence (B), the temperature remained elevated for a period of time (B→C). This is due to the heat balance between the latent heat generated by the freezing water in the sample and the heat removed by the cooling shelf of the lyophiliser,

as will be explained in the following. The total amount of latent heat generated by water during freezing is approximately 79.7 cal/g [66]. This means that about 79.7 calories of heat are generated to completely freeze one gram of water. In the experiment, however, this heat was not immediately removed from the samples. Instead, the supercooled sample took up only a portion of that heat, which in turn raised its temperature close to its equilibrium freezing temperature (B→C). Depending on the degree of supercooling, approximately 15 cal/g of heat are nearly immediately taken up by the sample as sensible heat [2]. This indicates that only a portion of the water was rapidly frozen once nucleation occurred. Subsequently, the temperature of the sample was continuously reduced via the cooling shelves, which in turn allowed more water to crystallise and generate more latent heat. In order to completely solidify the sample, the totality of latent heat of ice crystallisation (79.7 cal/g) had to be removed via the cooling shelves of the freeze-dryer throughout the entire freezing step once nucleation had occurred (B→C→D). As soon as the water content available for freezing was completely crystallised, and no additional heat could be generated, the sample temperature decreased and converged almost to the shelf temperature (D). In summary, the “freezable” water in the sample did not freeze directly but necessitated the removal of the heat it generated while further crystallising. The time required to achieve this caused a delay in the sample temperature drop relative to the shelf temperature. This delay resulted in a certain time the sample remained above its nucleation temperature (B→C).

This entire process was also observed via a camera in the freeze-dryer. As a side note, the placement of the samples for the image recording did not follow the scheme previously shown in Chapter 2.2.1. Instead, the samples were positioned (without any thermal sensors) directly in front of the camera in order to take pictures. The supercooled and transparent sample (A) became slightly opaque once nucleation occurred (B). Over the course of freezing a gradual increase in opaqueness was observed from the bottom to the top of the vial (C), until the sample became completely opaque after complete solidification (D). It can be inferred that the opaqueness of the sample is dependent on the amount of ice in the sample. More specifically, the liquid phase and the crystalline ice phase have different refractive indices, which means that the total surface area of ice crystals, where refraction of light occurs, defines the opaqueness of the sample. During recalescence, the volume fraction of the crystalline phase is lower than in a completely solidified sample due to the increased sample

temperature. Therefore, the total surface area of the crystalline phase is also lower than in a completely solidified sample. Furthermore, the gradient of opaqueness during freezing (C) can be explained by the directional removal of heat from the sample (and therefore further crystallisation) at the bottom of the vial by the cooling shelves. This phenomenon is particularly of interest, because it indicates that the temperature conditions in the sample are not uniform but rather dependent on the distance to the cooling shelf.

3.1.2 Characterisation of the thermal profile during freezing

The temperature profile shown in Figure 3.1 is typical of lyophilisation samples, and it is often used to describe the phenomenon of supercooling during freezing [2,16,44,86]. Several studies have been carried out to investigate the thermal evolution of samples during lyophilisation, focusing on the influence of the temperature ramp of the shelves and the nucleation temperature of the samples [86,134–136].

These studies typically compare the detected nucleation temperature and freezing rate with primary drying times. The underlying assumption is that the nucleation temperature determines the number of stable nuclei that will grow into ice crystals and later form the pores in the lyophilisate (see Chapter 1.5). This seems reasonable since the amount of water available for freezing is finite, which means that the higher the number of ice crystals, the smaller the average ice crystal size must be. It is also assumed that this pore size will affect the drying time of the sample. Specifically, smaller pore sizes should result in increased resistance to vapour flow through the lyophilisate, thus reducing the rate of sublimation during drying.

However, these studies tend to overlook the fact that during lyophilisation the samples are exposed to elevated temperatures due to both recalescence and the subsequent crystallisation phase until the total heat of crystallisation is removed from the sample. For the purposes of this work, the time during which the temperature of the samples is increased as a result of recalescence and crystallisation is referred to as the residence time (t_r). The residence time can be defined for different temperature limits, i.e., when does the sample temperature exceed or fall below a certain temperature, as shown in Figure 3.2. In addition, the area under the curve (AUC) can be derived from the temperature profile and the corresponding temperature limit of the residence time. It should be noted that neither the

residence time nor the AUC for the respective residence time are physical values intended for any kind of thermodynamic quantification, but serve in this work as a measure to evaluate the effect of freezing on the exposure of the sample to elevated temperatures.

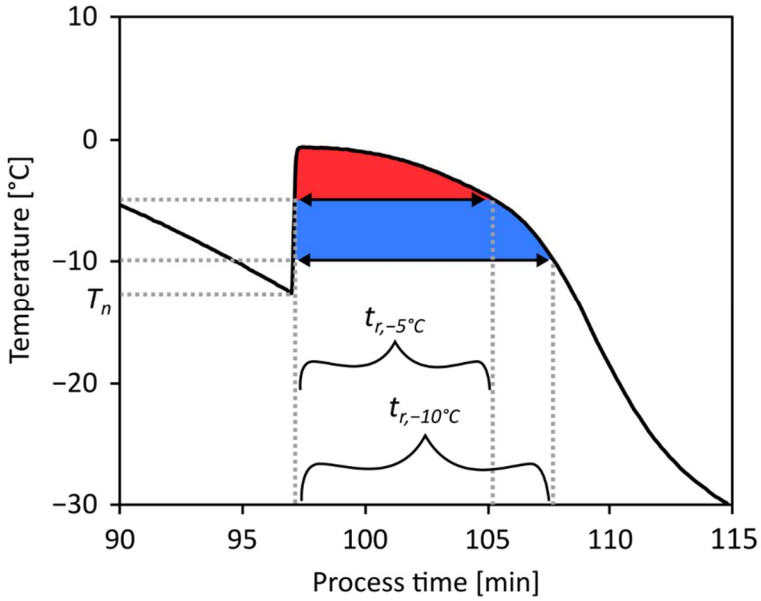

Figure 3.2: Temperature profile of a 10 % (w/w) sucrose solution during freezing with nucleation temperature (T_n) and residence times (t_r) for temperature limits of -5 °C and -10 °C. The area under the curve (AUC) is also shown for temperature limits of -5 °C (red) and -10 °C (red and blue).

To investigate the residence time during freezing, vials were filled with 3 ml of a 10 % (w/w) sucrose solution and placed in the lyophiliser. Two empty vials were left between each sample to reduce heat transfer between samples, as discussed in Chapter 2.2.1. Thermocouples and wireless temperature sensors were placed approximately 1 mm above the bottom of each sample vial to ensure comparability of individual measurements, as a thermal gradient is expected in the samples due to cooling from the bottom of the vials. It should be noted that the use of thermocouples/wireless temperature sensors introduced additional surfaces where nucleation could occur. However, this could not be avoided as the only way to measure temperature in this work was by this invasive method. The samples were pre-cooled to approximately 5 °C and then frozen to -40 °C using two different freezing rates. The first rate was 1.2 °C/min, which is close to the upper limit possible with the freeze-dryer in this work, while the second rate of 0.1 °C/min served as a very slow freezing rate. The nucleation temperature was first determined for each measurement and is shown in Figure 3.3.

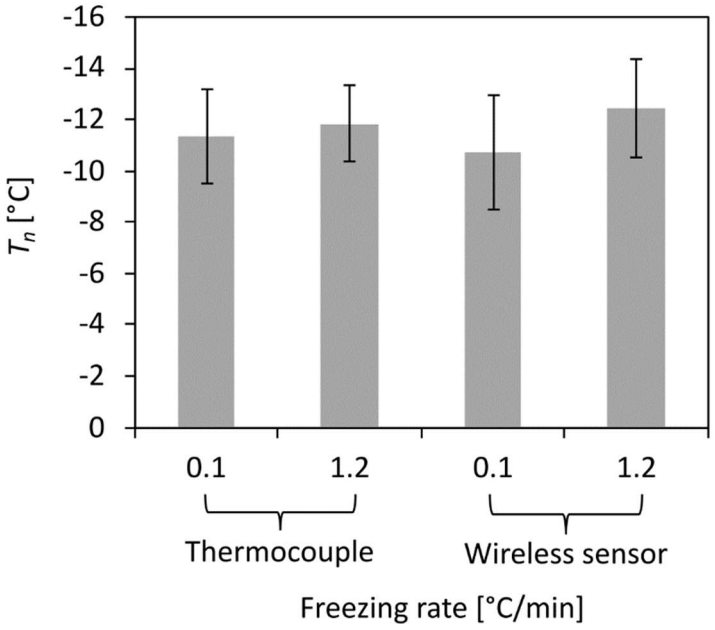

Figure 3.3: Effect of freezing rate on nucleation temperature (T_n) in a 10 % (w/w) sucrose solution. Standard deviations (error bars) were determined for thermocouples with n = 8 and wireless sensors with n = 16.

The nucleation temperature did not show a significant dependence on the freezing rate for both thermocouple and wireless sensor measurements ($p > 0.05$). This is consistent with the findings of Searles et al. (2001), who reported no effect of freezing rate on nucleation temperature in the range of 0.05 °C/min to 1 °C/min. It can be concluded that the higher freezing rate was not sufficient to lower the temperature fast enough to affect nucleation. Instead, the supercooled samples all became unstable at around -11.9 °C ± 2.1 °C and started to form the first stable nuclei.

The residence time was then examined in relation to the freezing ramp and is shown in Figure 3.4. For this purpose, temperature limits between -2 °C and -10 °C were chosen and the corresponding residence times were extracted from the temperature profiles. The lower temperature limit of -10 °C was chosen for the current study because it is close to the average nucleation temperature of the 10 % (w/w) sucrose solution in the freeze-dryer, while the upper limit of -2 °C is only slightly below the equilibrium freezing temperature of the solution. In addition, temperature intervals of 2 °C were chosen to more accurately capture the temperature profile observed during recalescence and crystallisation. It should be noted that this approach is only an attempt to characterise the thermal profile and does not include any thermodynamic considerations regarding the freezing solution.

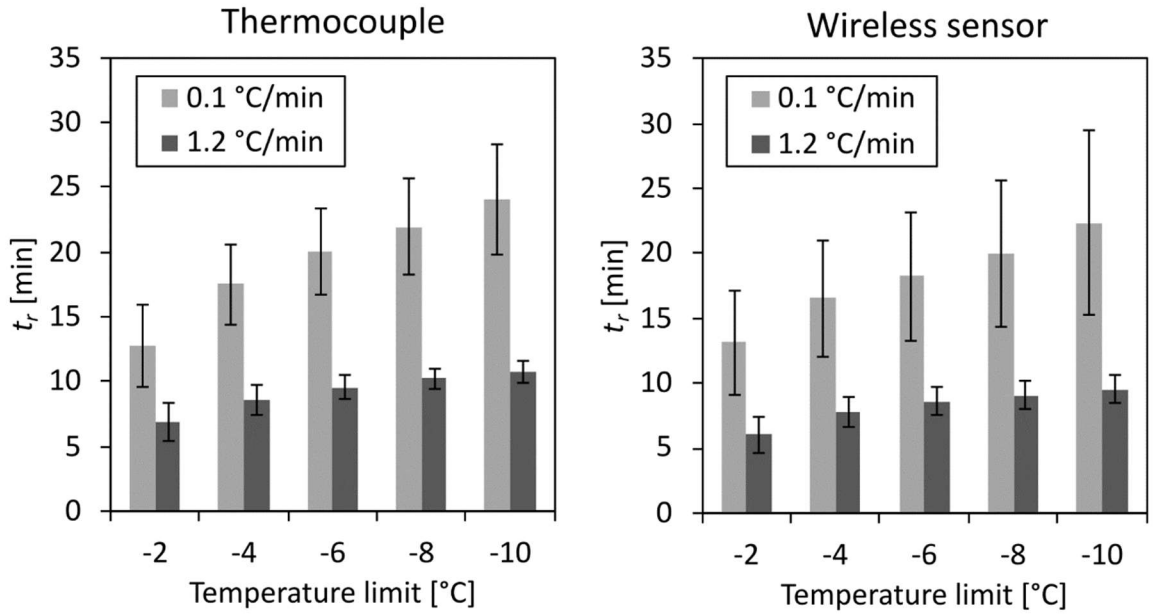

Figure 3.4: Effect of freezing rate on residence times (t_r) in a 10 % (w/w) sucrose solution. Standard deviations (error bars) were determined for thermocouples with n = 8 and wireless sensors with n = 16.

Significant differences in residence times were observed between freezing ramps of 0.1 °C/min and 1.2 °C/min for each temperature limit ($p < 0.05$). At the highest freezing rate of 1.2 °C/min, which is close to the maximum capacity of the equipment and therefore represents the upper limit of heat removal possible in a lyophiliser, the residence time was between 6.3 min ± 3.7 min and 9.5 min ± 1.1 min, depending on the temperature limit. The lower freezing rate of 0.1 °C/min resulted in residence times between 13.0 min ± 3.7 min and 23.0 min ± 6.1 min, also dependent on the temperature limit. It can be concluded that the freezing ramp can be used to influence the residence times of the samples during freezing.

An alternative method of assessing the effect of freezing on the exposure of the sample to elevated temperatures was by determining the AUC of the recalescence and crystallisation phase using the same temperature limits of -2 °C and -10 °C. This approach considers the non-linear nature of the temperature profile during freezing, and might therefore capture details better than the residence time. The results of the evaluation are shown in Figure 3.5.

Significant differences were observed between the freezing ramps of 0.1 °C/min and 1.2 °C/min ($p < 0.05$), except for a temperature limit of -2 °C ($p > 0.05$). The AUC showed similar trends to the evaluation of the residence time. However, the AUC exhibited a linear increase with decreasing temperature limit, whereas the residence time showed a flattened profile.

This difference can be attributed to the non-linear temperature profile during recalescence and crystallisation

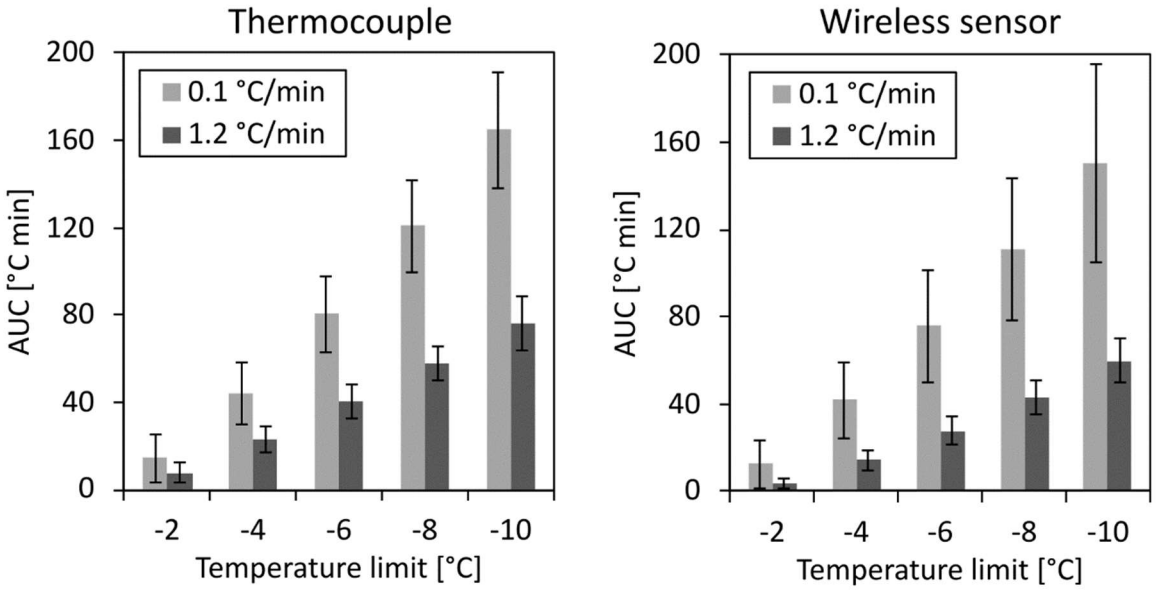

Figure 3.5: Effect of freezing rate on the area under the curve (AUC) of the thermal profile of a 10 % (w/w) sucrose solution during freezing. Standard deviations (error bars) were determined for thermocouples with n = 8 and wireless sensors with n = 16.

In the field of lyophilisation, there is a consensus that the nucleation temperature affects the primary drying time [86,137–140]. Specifically, higher nucleation temperatures are associated with shorter primary drying times due to fewer stable nuclei and consequently larger average ice crystal sizes. This observation aligns with classical nucleation theory, which explains the relationship between nucleation temperature and nucleation rate (see Chapter 1.5). However, previous studies have largely overlooked the role of the recalescence and crystallisation phase, focusing instead on attributing ice crystal size prior to drying to nucleation kinetics. The goal of this work is not to dispute classical nucleation theory but to explore whether the temperature increase from the latent heat of crystallisation impacts the microstructure and if its significance has been underestimated.

This first raises the question whether nucleation temperature has an impact on the thermal profile of a sample during freezing. To investigate this, the residence times and AUC from the freezing experiments were plotted against the nucleation temperatures for each sample. The results are shown in Figure 3.6. For clarity, only data pertaining to a temperature limit of -6 °C with wireless sensors are displayed. Additional data can be found in Appendix B.

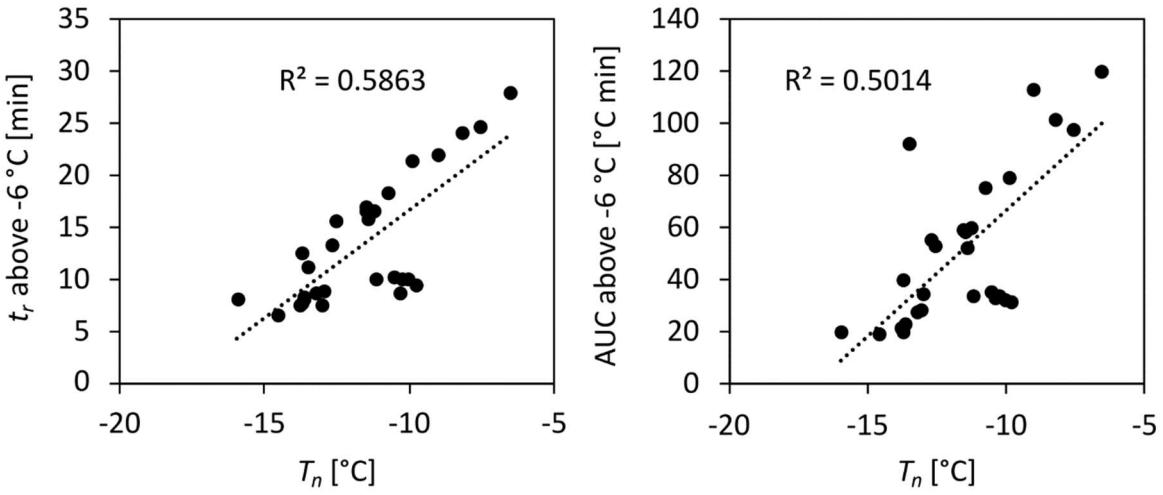

Figure 3.6: Comparison of residence time (t_r) and area under the curve (AUC) of the recalescence and subsequent crystallisation phase with the nucleation temperature (T_n) during freezing of a 10 % (w/w) sucrose solution measured with wireless temperature sensors.

The residence time and the AUC of the recalescence both exhibited a positive correlation with the nucleation temperature. Although the coefficient of determination R^2 is rather low, it has to be considered that uniform temperature conditions cannot be guaranteed in a freeze-dryer, and that the vials were distributed over nearly the entire shelf (see Chapter 2.2.1). Nevertheless, the quality of the data is comparable to other works in this field [86]. The observed dependence between recalescence and subsequent crystallisation, here quantified by residence time and the AUC, and the stochastic nucleation temperature supports the following hypothesis about the formation of the microstructure in a frozen solution.

In the following, a hypothesis will be made that explains the relationship between the thermal profile of a sample during freezing and the nucleation temperature. During the freezing step, samples typically become supercooled as described in Chapter 1.4.1. As soon as nucleation occurs, latent heat of crystallisation is generated during the recalescence and crystallisation phase and must be removed by the cooling shelf. However, the amount of latent heat released immediately after nucleation depends on the degree of supercooling. This phenomenon is illustrated in Figure 3.7.

The initial uptake of the latent heat of crystallisation by the sample is only possible until the sample temperature nearly reaches its equilibrium freezing temperature (T_f). Exceeding this temperature would mean that crystallisation could produce enough heat to melt the crystalline phase completely, which would be absurd from a thermodynamic point of view.

Therefore, the temperature difference (ΔT) depends on the nucleation temperature (T_n) and the equilibrium freezing temperature.

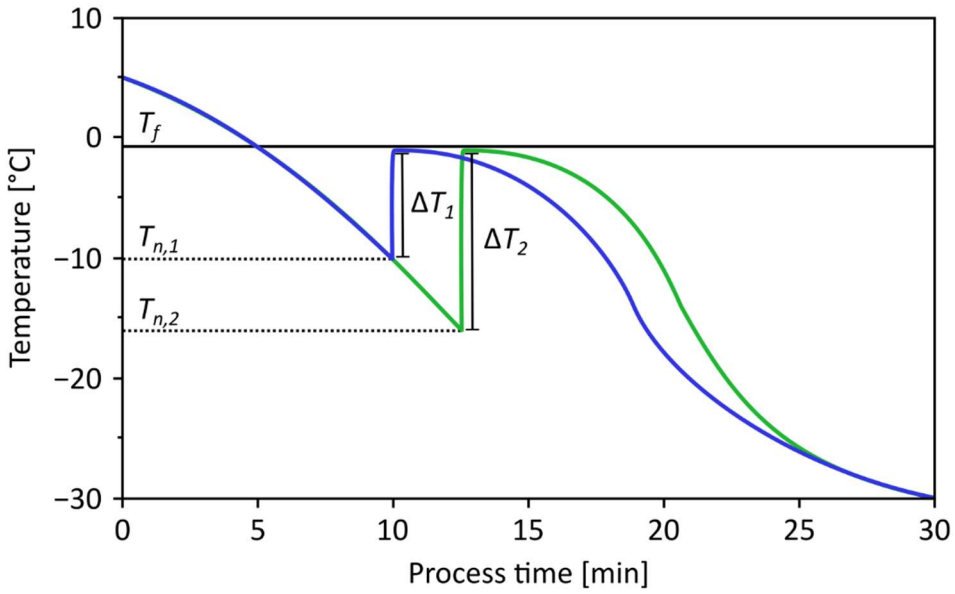

Figure 3.7: Schematic temperature profile of two samples with different nucleation temperatures (T_n) during the freezing step in a lyophiliser.

It can be concluded that a lower nucleation temperature results in a higher temperature difference, thus increasing the amount of heat removed from the supercooled sample immediately after nucleation. This observation does not imply a change in the overall energy balance but indicates that the timing and quantity of heat released during crystallisation can vary based on the nucleation temperature. Additionally, when the sample reaches its equilibrium freezing temperature, it is likely that more water has crystallised in the sample with the lower nucleation temperature, as the temperature difference reflects the amount of latent heat of crystallisation produced until reaching the equilibrium freezing temperature. Consequently, for the continuous crystallisation that occurs as the solution approaches its maximum freeze-concentrated state, less latent heat of crystallisation will be generated if a significant temperature difference was already present at the point of nucleation.

This is logical because the total latent heat of crystallisation comprises the heat generated immediately after nucleation and the heat generated during the continuous crystallisation of the solution. Therefore, as the nucleation temperature decreases, both the residence time and the AUC of recalescence and crystallisation phase tend to decrease as well.

This hypothesis is supported by the experimental results presented in Figure 3.6, which demonstrate a positive correlation between the nucleation temperature and both the residence time and the AUC of recalescence and crystallisation phase.

Based on the experiments conducted, three major conclusions can be drawn:

- The nucleation temperature in vials is independent of the freezing rate in a typical lyophiliser.
- The nucleation temperature correlates positively with the residence time and the AUC of the recalescence and subsequent crystallisation phase.
- An increase in the freezing rate leads to a decrease of both the residence time as well as the AUC.

These findings provide new insights into previous research and suggest that the relationship between nucleation temperature and, for example, the reduction in primary drying times, which was previously attributed to the influence of the nucleation temperature on ice crystal sizes, may also be explained by the temperature increase from the recalescence and crystallisation phase during freezing. A microscopic investigation of this hypothesis will be conducted in Chapter 3.1.4.

3.1.3 Height-dependent recalescence and crystallisation in lyophilisation vials

In the previous chapter, temperature measurements were taken from a single point near the bottom of the vial. However, as detailed in Chapter 3.1.1, solidification progresses directionally from bottom to top as heat is removed from the bottom of the vial by the cooling shelves. This process is illustrated in Figure 3.1, where a gradient of opacity throughout the sample can be observed, indicating that temperature conditions are not uniform across the sample but vary with proximity to the cooling shelf. Consequently, a thermal gradient develops during the freezing step, moving from the bottom to the top of the sample until solidification is complete.

To determine the temperature conditions at different positions in the vial, samples of 3 ml and 6 ml of a 10 % (w/w) sucrose solution were prepared. Three thermocouples were then positioned in each vial (see Figure 3.8) to ensure consistent nucleation conditions for each measurement. The axial position in the vial was of interest, as differences in solidification were mainly observed in height.

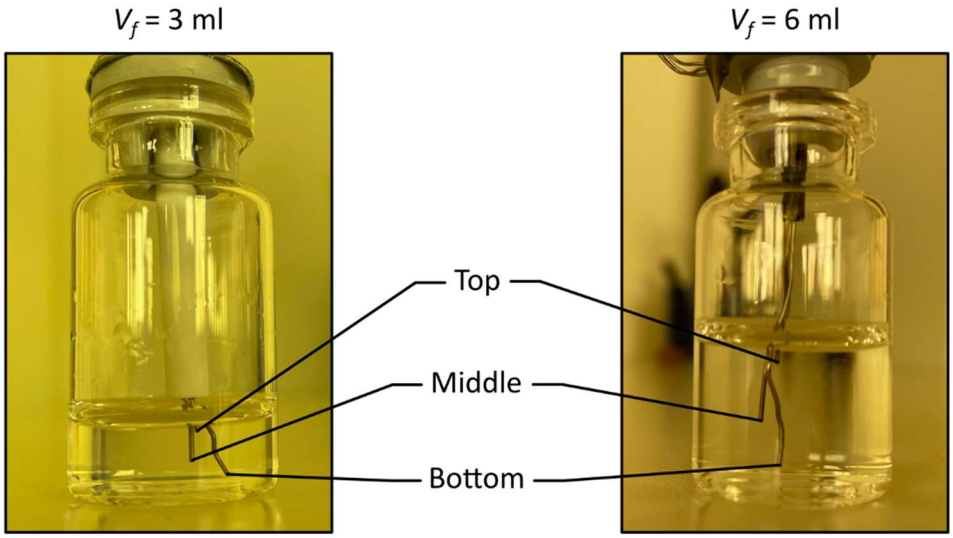

Figure 3.8: Positioning of thermocouples in vials with filling volumes (V_f) of 3 ml (left) and 6 ml (right).

Similar to previous experiments, the thermocouples also acted as additional nucleation surfaces. However, given the rapid advance of the secondary nucleation front due to supercooling (discussed in Chapter 1.5), it is likely that the entire sample crystallised quickly. Therefore, the specific location of nucleation was not critical for this part of the study. These vials were placed in the centre of the middle shelf of the freeze dryer with two empty vials between each sample. Different temperature ramp settings (1.2 °C/min, 0.8 °C/min, 0.4 °C/min) were then applied during the freezing process. The resulting data are shown in Figure 3.9.

In general, the typical temperature profile discussed in Chapter 1.4.1 was observed in all cases. However, there were also clear differences between the temperature ramps and filling volumes. The small filling volume of 3 ml showed a shorter recalescence and crystallisation phase compared to the larger filling volume of 6 ml. Simultaneously, the lower the thermocouple was positioned in the vial, the faster the temperature decreased. Furthermore, the faster the freezing rate, the shorter the recalescence and crystallisation phase. It should be noted that the distance of the bottom, middle and top thermocouples to the bottom of the vial was not identical between the two filling volumes. This means for example that the thermocouple at the top position of the two filling volumes had different distances to the cooling shelf. Therefore, the results should be evaluated qualitatively as an indication for the varying temperature conditions in a vial during freezing.

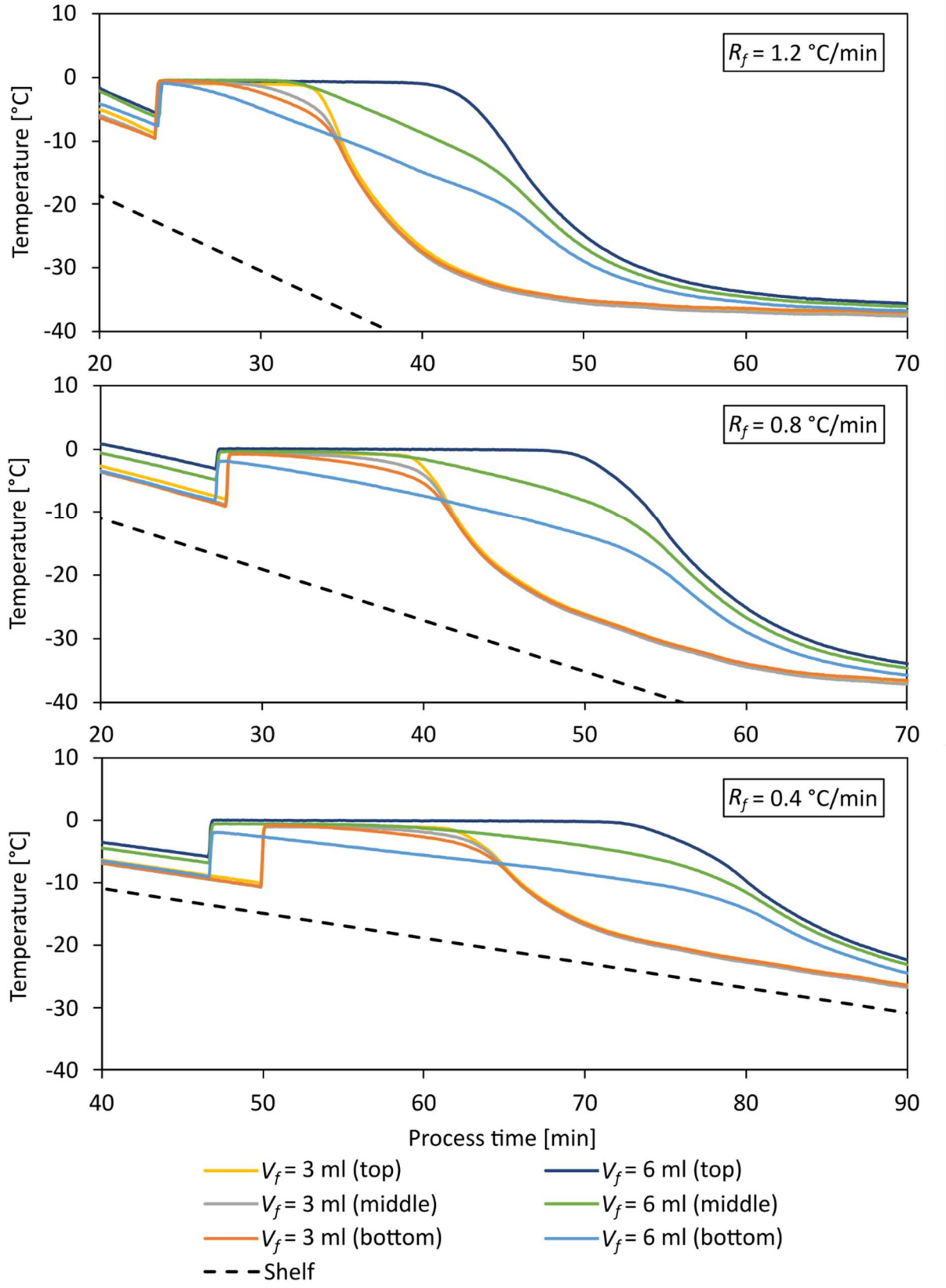

Figure 3.9: Temperature profile at three positions in a vial with different filling volumes (V_f) and various freezing rates (R_f).

Similarly to the evaluation in Chapter 3.1.2, the residence time was determined with a temperature limit of -6 °C, i.e., for what duration did the sample remain above -6 °C after nucleation occurred. The AUC of the recalescence and crystallisation phase could have been used as well, however, residence time showed slightly better R^2 when fitting the regression line. The data are shown in Figure 3.10.

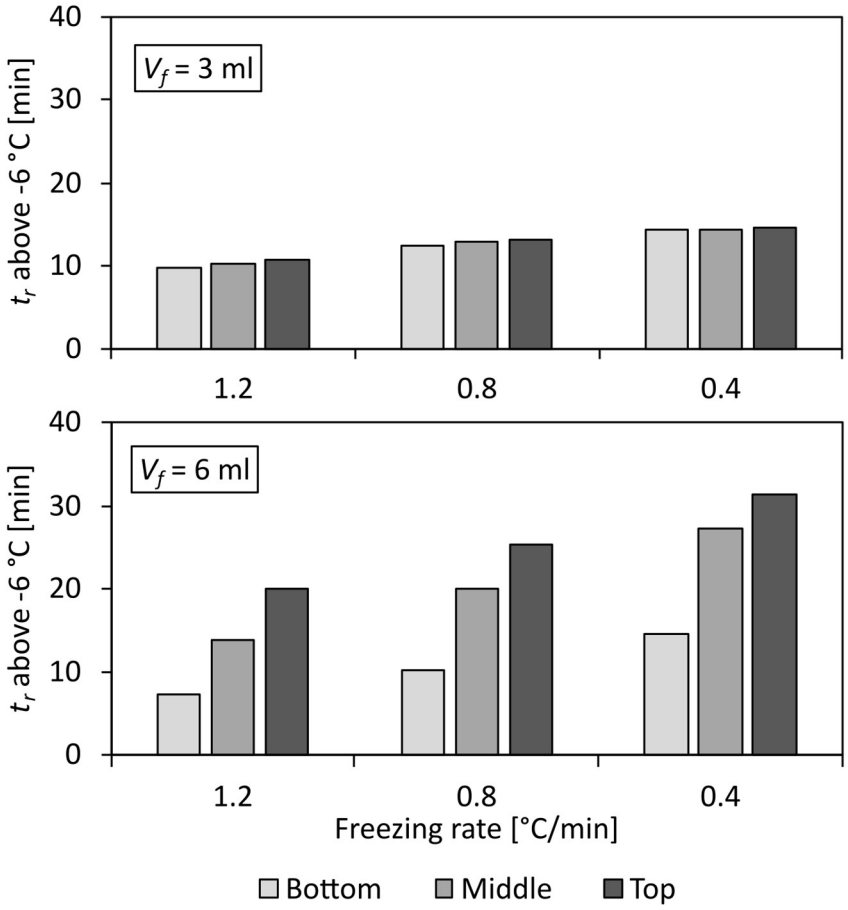

Figure 3.10: Comparison of residence time (t_r) for different positions in the vial and freezing rates for filling volumes (V_f) of 3 ml (top) and 6 ml (bottom).

Generally, the residence time increased with decreasing temperature ramps. However, when comparing the filling volumes, the impact of the temperature ramp on the residence time was more pronounced in the case of the higher filling volume of 6 ml. To reiterate, the residence time serves as the key metric for quantifying recalescence and the subsequent crystallisation phase. This phenomenon can be explained by the fact that a larger filling volume contains more total mass, resulting in a greater release of exothermic heat of crystallisation. At the same time, the contact surface with the cooling shelf remains constant for both filling volumes. As the temperature of the sample is primarily reduced by the shelf, it follows that

the larger volume would exhibit a longer recalescence and subsequent crystallisation phase, particularly in the middle and upper positions of the vial.

These observations can provide valuable insight into the height dependent variations within a lyophilisate. The experimental results show that the temperature conditions in the freezing solution depend on the filling volume and the freezing ramp, but also on the axial position within the vial. As a next step, the effect of these temperature conditions on the microstructure during the recalescence and crystallisation was investigated in order to assess the importance of the temperature increase during freezing step.

3.1.4 Assessment of the microstructure in a frozen solution

In order to determine the influence of the recalescence and subsequent crystallisation phase during the freezing step on the morphological properties in a lyophilisate, it was necessary to study the temporal changes of the microstructure in the frozen solution at the microscopic level. Typically, the microstructure of a dried lyophilisate is analysed by scanning electron microscopy or X-ray microtomography. However, these approaches are not feasible for this work due to the problems previously explained in Chapter 1.5. The main challenges include the use of dry samples that may have undergone additional structural changes during the drying process such as shrinkage, and the insufficient resolution of most methods to accurately detect the thin walls of the porous microstructure in a lyophilisate. Moreover, even with the fastest freezing ramps in a freeze-dryer, the temperature rise due to crystallisation cannot be completely avoided, making it impossible to observe a sample without a substantial recalescence and crystallisation phase.

To overcome these limitations, freeze-drying microscopy (FDM) was used to observe the microstructure formation of a 10 % (w/w) sucrose solution exposed to different temperature conditions. The key advantage of FDM in this context is that it allows the sample temperature to be adjusted almost instantaneously, reducing effects such as recalescence to negligible levels. This rapid adjustment is feasible because the ratio of sample volume of 1 µl to the contact area with the heating/cooling block of approximately 200 mm² is over 1000 times smaller compared to a typical vial set up in a lyophiliser. There, standard filling volumes are around 3 ml with contact areas of about 450 mm². Notably, vials used in lyophilisation often

have a concave bottom, which results in contact with the cooling shelf only at the outer edge of the vial, further reducing the contact area.

For the subsequent experiments, 1 µl of a 10 % (w/w) sucrose solution was pipetted onto a glass plate, covered with a second glass plate, and placed into the freeze-drying stage of the microscope (refer to Chapter 2.2.2). The temperature of the cooling block was rapidly reduced to -40 °C at a rate of 50 °C/min to freeze the sample. This steep freezing rate and the low volume-to-contact area ratio were aimed at minimising changes in the microstructure that could be enabled by a rise in the sample temperature due to heat of crystallisation, thereby addressing the issues of temperature gradients and heterogeneity typical of a vial setup. Experiments were performed with and without a spacer between the glass plates to determine the most suitable sample preparation. Once completely frozen, the temperature was raised to -5 °C at a rate of 10 °C/min and maintained to anneal the samples, simulating the temperature conditions during the recalescence and the subsequent crystallisation phase. The results of these experiments are shown in Figure 3.11.

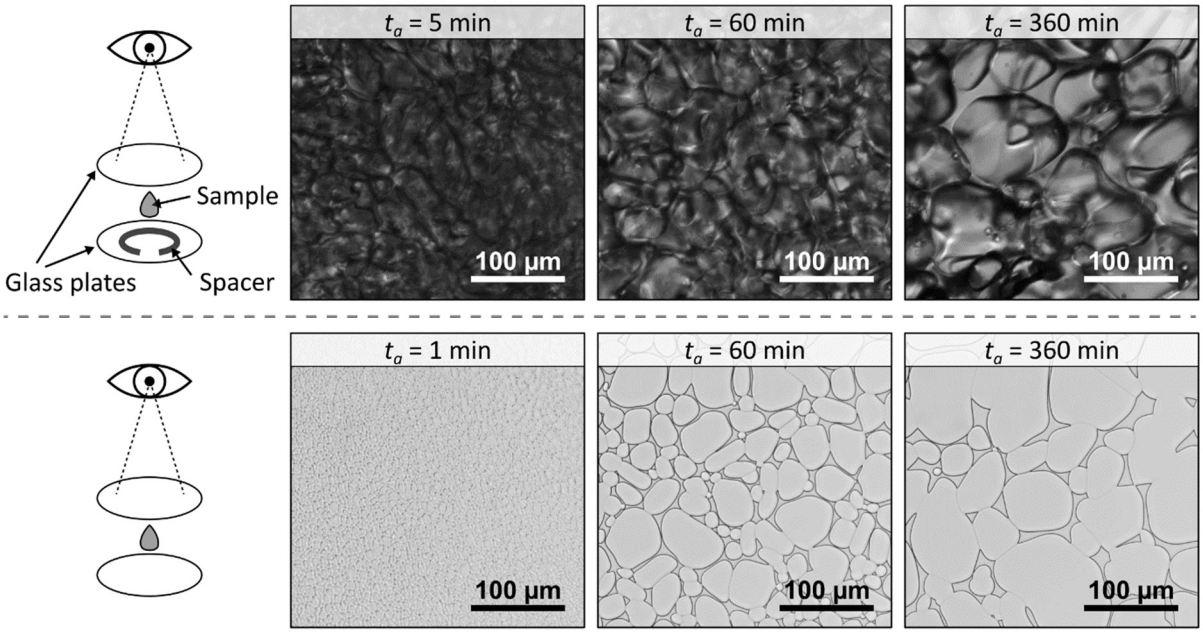

Figure 3.11: Freeze-drying microscopy of a 10 % (w/w) sucrose solution with (top) and without (bottom) a spacer after annealing at -5 °C for various annealing times (t_a). The spacer increased the sample height to approximately 70 µm.

The frozen sucrose solution showed a lack of well-defined structures under the freeze-drying microscope when a spacer was used. Even after a short annealing phase of 5 minutes, during which the particulate ice phase was expected to coarsen due to Ostwald ripening, the

identification of individual structures remained speculative. In contrast, omitting the spacer facilitated the formation of a thin layer, with a calculated sample height of approximately 5 µm. This setup allowed for the identification of distinct ice crystals with grain-like shapes. This concept is further illustrated in Figure 3.12.

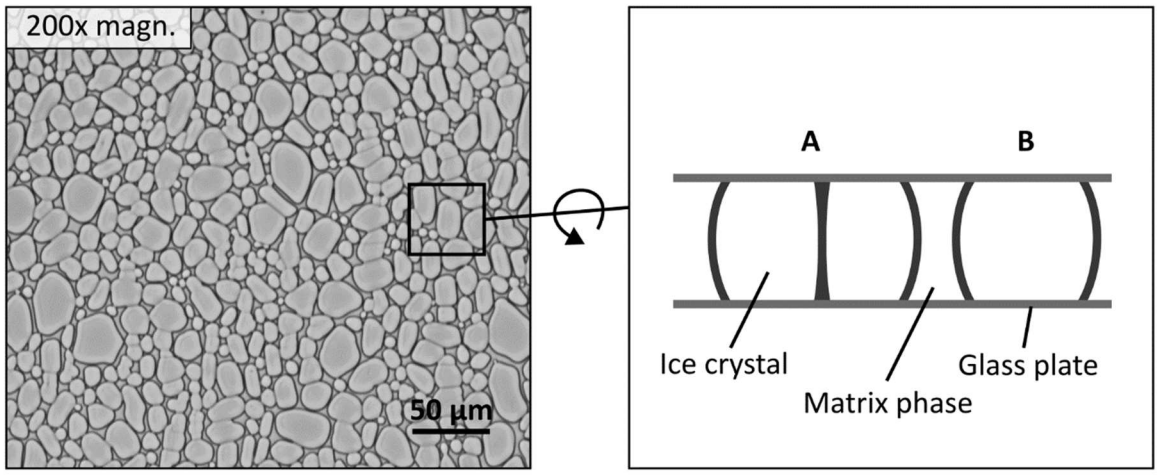

Figure 3.12: Freeze-drying microscope image of a 10 % (w/w) sucrose solution after annealing at -6 °C for 10 min (left) and schematic depiction of the cross section of the sample (right) with bordering ice crystals (A) or ice crystals separated by the matrix phase (B).

The clear visibility of individual ice crystals can be attributed to their simultaneous contact with both the lower and upper glass plates. This arrangement causes the phase boundary between the ice crystal and the amorphous matrix to extend across the entire distance from one glass plate to the other. In cases where ice crystals are sufficiently small to allow multiple crystals to fit between the glass plates, phase boundaries would form parallel to the plates, hindering the identification of individual ice crystals. Notably, when the frozen sample was not subjected to an additional annealing step, even without a spacer, the visual characteristics of the solution immediately after freezing did not align directly with the presence of grain-like ice crystals as observed after the annealing process, as shown in more detail in Figure 3.13. Instead, a fine texture was observed, and the determination of its microstructural properties was not possible due to the insufficient magnification of the freeze-drying microscope.

The images of non-annealed samples shown in Figure 3.13 prompt an investigation into the arrangement of the crystalline and amorphous components within the frozen sample. Two hypotheses can be considered. The first suggests that, similar to the annealed samples, grain-like ice crystals might be present within a continuous matrix phase, but significantly smaller in

size. The overlap of these small ice crystals, in addition to their small size, may hinder their clear observation using a freeze-drying microscope. Alternatively, it is plausible that the ice crystals in non-annealed samples form differently, not appearing as grain-like structures. Alternatively, it is plausible that the ice crystals in non-annealed samples are present in a different form rather than grain-like ice crystals. This phenomenon is intriguing because of the significant size difference between the structures observed in non-annealed samples under the freeze-drying microscope and the pores typically found in lyophilised products. As mentioned in Chapter 1.5, different studies using different methods have reported average pore diameters of approximately 20 µm to 60 µm in non-annealed 5 % (w/w) to 20 % (w/w) sucrose samples [70,83,98,71]. This order of magnitude is comparable to that observed in annealed samples from the freeze-drying microscope (see Figure 3.13). However, this does not hold true for non-annealed samples with their fine structures.

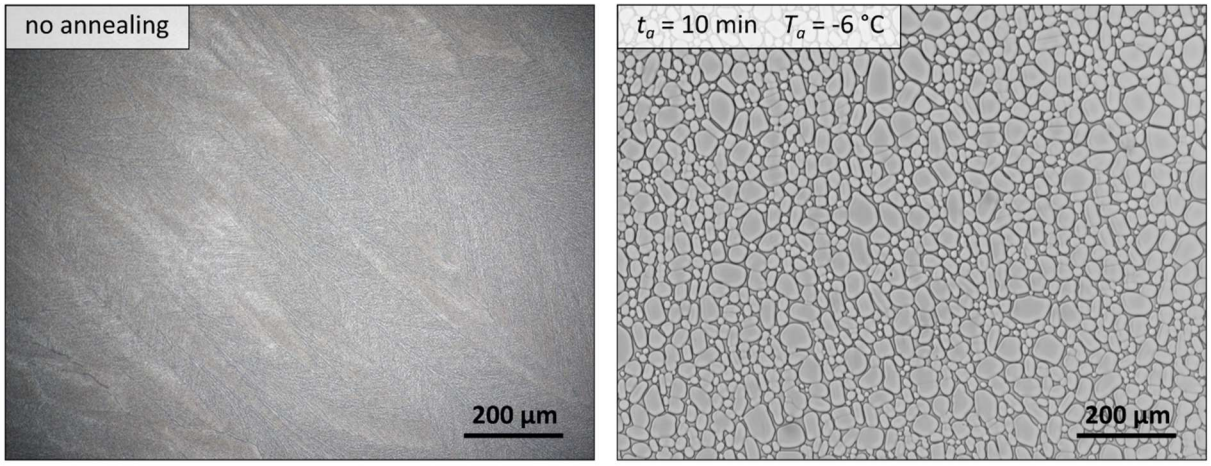

Figure 3.13: Freeze-drying microscopy of a 10 % (w/w) sucrose sample without (left) and after 10 minutes of annealing at -6 °C (right). The freezing temperature was approximately -17 °C.

The next step involved testing different freezing ramps in the freeze-drying microscope to identify at what temperature nucleation occurred and whether the nucleation temperature could be affected by the freezing ramp in this experimental setup. Nucleation temperatures were determined by capturing images as the sample cooled until crystallisation was visible. This transition was observed in the camera view as texture-like fine structures began to form, as depicted in Figure 3.13. Due to camera limitations at rapid freezing rates, images were captured every 1 °C, resulting in a nucleation temperature data resolution of 1 °C. Figure 3.14 displays the nucleation temperatures for different freezing rates observed with the freeze-drying microscope.

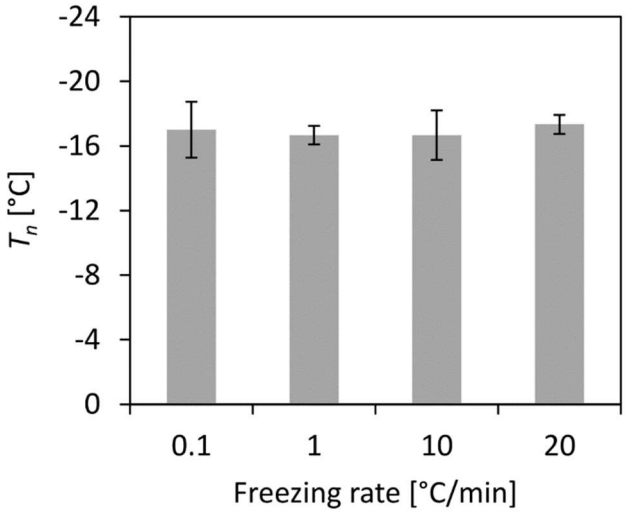

Figure 3.14: Effect of freezing rate on nucleation temperature (T_n) in a 10 % (w/w) sucrose solution under a freeze-drying microscope. Standard deviations (error bars) were determined from triplicates.

The average nucleation temperature in the freeze-drying microscope was determined to be -16.9 °C ± 1.1 °C. No significant differences in nucleation temperatures were observed between freezing ramps from 0.1 °C/min to 20 °C/min ($p > 0.05$). In contrast to the freezing ramps used in the lyophiliser, steeper ramps were tested in the freeze-drying microscope to determine whether the highest possible freezing ramp in a lyophiliser of 1.2 °C/min was simply insufficient to affect the nucleation temperature. Consequently, the freezing ramp was found to be ineffective in influencing the nucleation temperature in both lyophiliser and freeze-drying microscopy experiments.

However, the nucleation temperature in the lyophiliser was found to be -11.9 °C ± 2.1 °C, which significantly differed from the values in the freeze-drying microscope ($p < 0.05$). To ensure comparability between freeze-drying microscopy and lyophilisation experiments, the nucleation temperature in the freeze-drying microscope had to be adjusted accordingly. Efforts were made to induce nucleation at approximately -12 °C, including attempts to hold the temperature for a prolonged time, abruptly reducing and increasing the pressure in the freeze-drying stage, and oscillating temperature within ± 1 °C of the desired nucleation temperature. The most reproducible results were obtained when nucleation was induced by repeated gentle taps on the sample holder while maintaining the sample temperature at -12 °C. Further examination of the samples was carried out in the freeze-drying microscope using polarised light, as shown in Figure 3.15 for frozen and non-annealed samples. The

principles of polarisation and birefringence have already been described in Chapter 2.2.3. The samples were cooled to -12°C and nucleation was induced by tapping the sample holder. The samples were then cooled to -40°C at 10°C/min and images were taken.

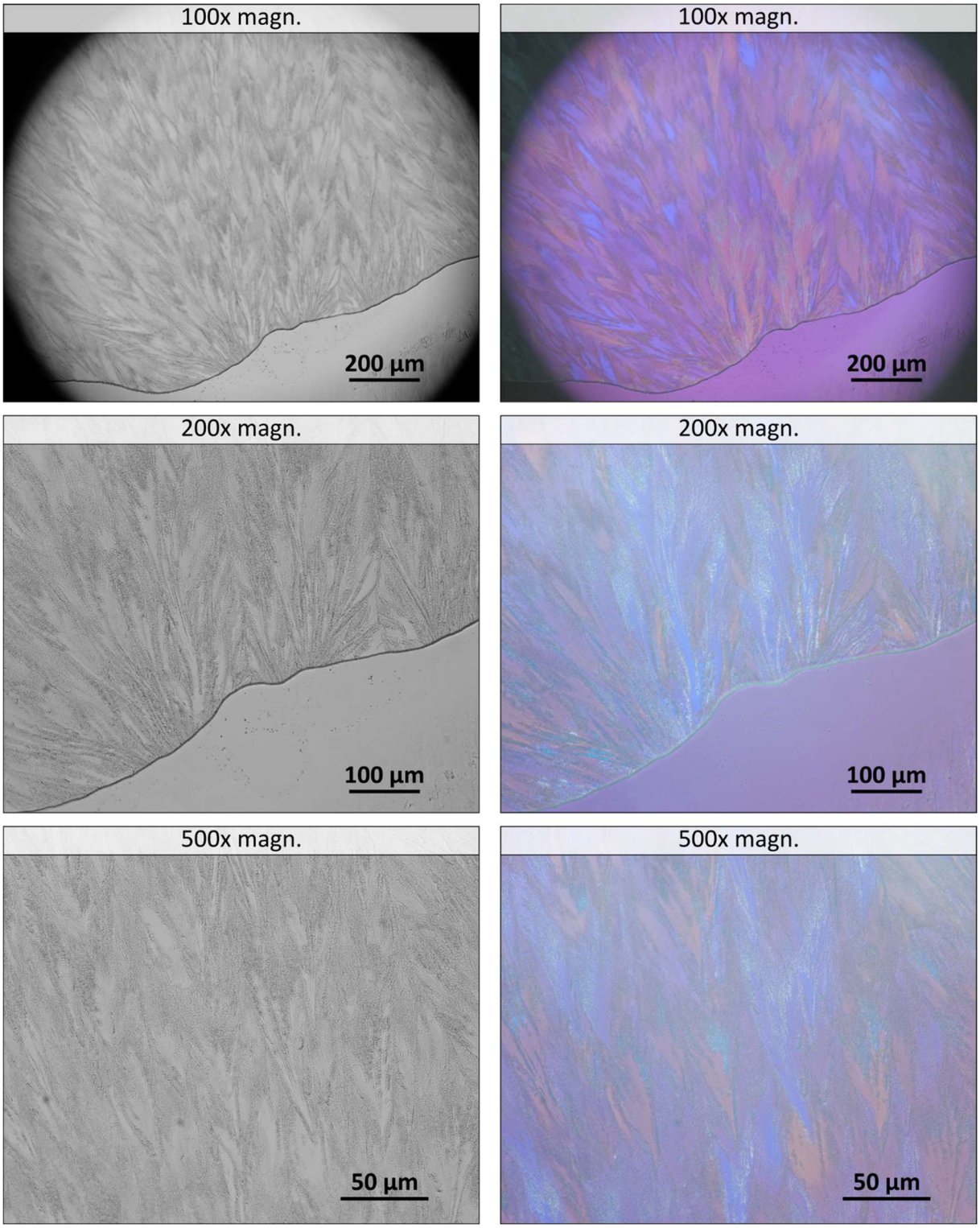

Figure 3.15: Freeze-drying microscopy of a 10 % (w/w) sucrose sample with (right) and without (left) polarisation at -40 °C with preceding nucleation at around -12 °C.

The freeze-drying microscope images show identical sections with and without polarised light. In addition, the outer edge of the frozen sample was deliberately included in the 100x and 200x magnifications (bottom right-hand corner of each image). Due to the high freezing rate of 10 °C/min, the samples were cooled to -40°C within 3 minutes of nucleation. No separate annealing step was performed for these samples. The polarised light microscopy images also indicate the presence of feather-like structures without a clear pattern similar to an ice flower on a window. Additionally, the structures seem to have originated and spread out from the phase boundary of the solution. To investigate the transition from ice crystals in non-annealed samples to grain-like ice crystals, the sample was heated from -40 °C to -6 °C at 10 °C/min and annealed for 120 minutes. The corresponding images are shown in Figure 3.16. Irregular structures were observed in the non-annealed sample at the top of Figure 3.16, while single grain-like ice crystals became visible after short annealing times (t_a = 10 min). Each individual ice crystal appeared to have a single uniform colour. It is also noticeable that neighbouring ice crystals often exhibited the same colouration. These clusters of ice crystals of the same colour were often located where irregular structures of a similar colour had previously been present.

In order to further investigate the effect of the recalescence and crystallisation phase on the microstructure in a frozen solution, the annealing step in the freeze-drying microscope was designed to mimic the conditions experienced by the samples in the lyophilisation experiments from Chapter 3.1.2.

However, the temperature profile of the sample in the lyophiliser during freezing was not linear or stepwise, so it would not have been feasible to implement such a profile in the freeze-drying microscope. In addition, care must be taken to ensure that the sample temperature does not exceed the equilibrium freezing temperature of the solution, as this would result in complete thawing of the sample. Some temperature fluctuations are to be expected in the freeze-drying microscope and therefore it would have been too risky to use a set temperature slightly below the equilibrium freezing temperature for a 10 % (w/w) sucrose solution of about -0.6 °C [66]. Therefore, in the following experiments, an annealing temperature of -6 °C was chosen, which, based on previous experience, clearly demonstrated the effect of annealing on the microstructure, but was sufficiently far from the equilibrium freezing temperature to prevent the complete thawing of the sample. The residence times in the lyophilisation experiments from Chapter 3.1.2 were taken into account for the annealing time for the freeze-

drying microscopy experiments. For a temperature limit of -6 °C, the residence times for freezing ramps of 1.2 °C/min and 0.1 °C/min were rounded off to 10 minutes and 20 minutes, respectively.

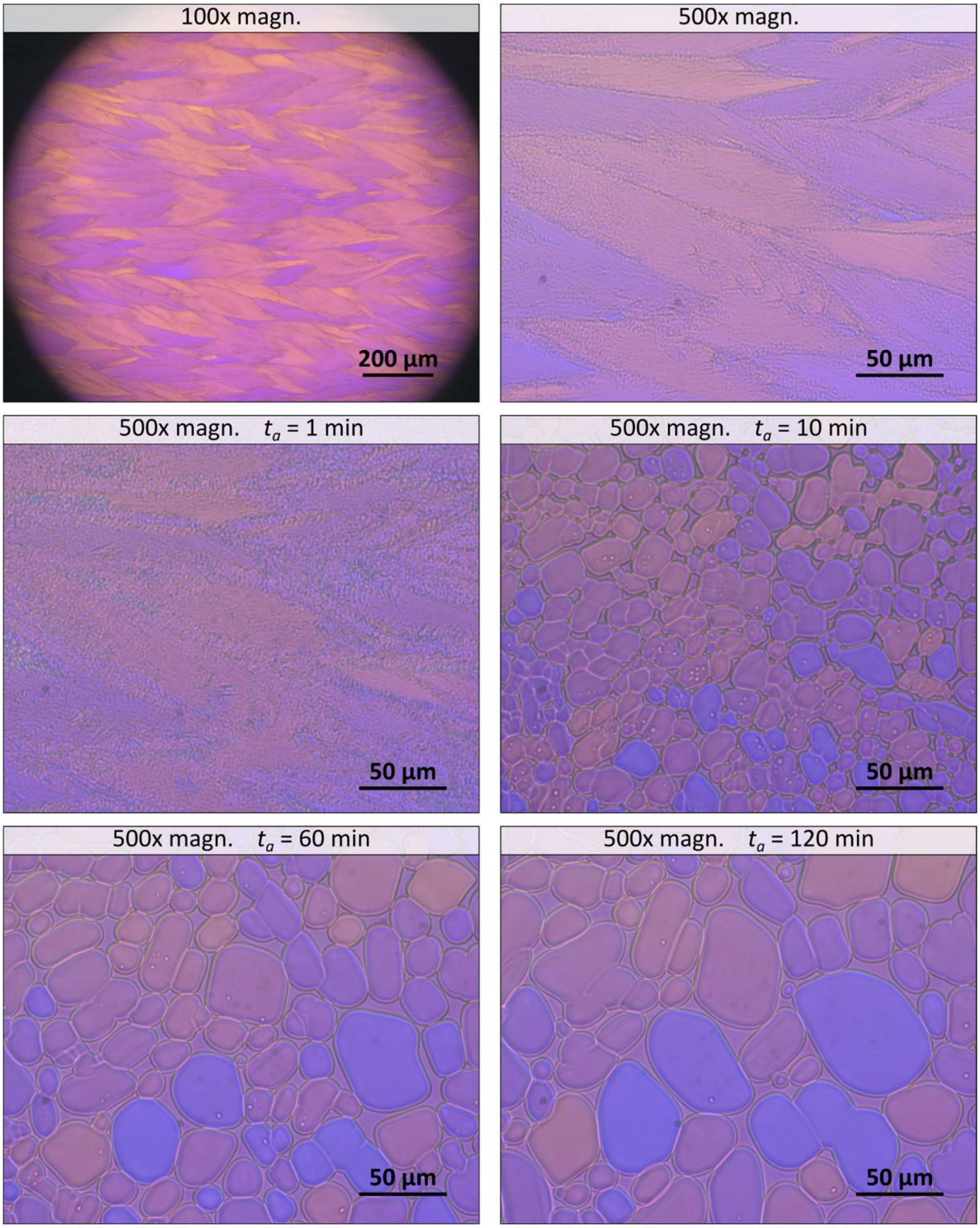

Figure 3.16: Freeze-drying microscopy with polarised light of a 10 % (w/w) sucrose sample during annealing at -6 °C.

The microstructure of a frozen solution was assessed by counting individual ice crystals after mimicking the temperature conditions of the recalescence and crystallisation phases experienced during freezing in a lyophiliser. As previously discussed in Chapter 1.5, the number of ice crystals serves as an indicator of the eventual pore size after drying. This is because the freezable water in the solution is distributed among all the ice crystals formed during freeze-concentration, i.e., a larger number of ice crystals corresponds to smaller average ice crystal sizes. For this evaluation, samples were either cooled using different freezing ramps until nucleation occurred or nucleation was induced at -12 °C. Following nucleation, the samples were rapidly cooled to -40 °C at a rate of 50 °C/min to minimise structural changes that might occur above the glass transition temperature. The samples were then heated to an annealing temperature of -6 °C at 10 °C/min and held for 20 minutes. Images were taken after 10 minutes and 20 minutes, corresponding to residence times of freezing ramps of 1.2 °C/min and 0.1 °C/min in a freeze-dryer. The number of ice crystals was quantified through image analysis, as detailed in Chapter 2.2.6, across a viewing area of approximately 1.12×10^3 µm². The results are shown in Figure 3.17.

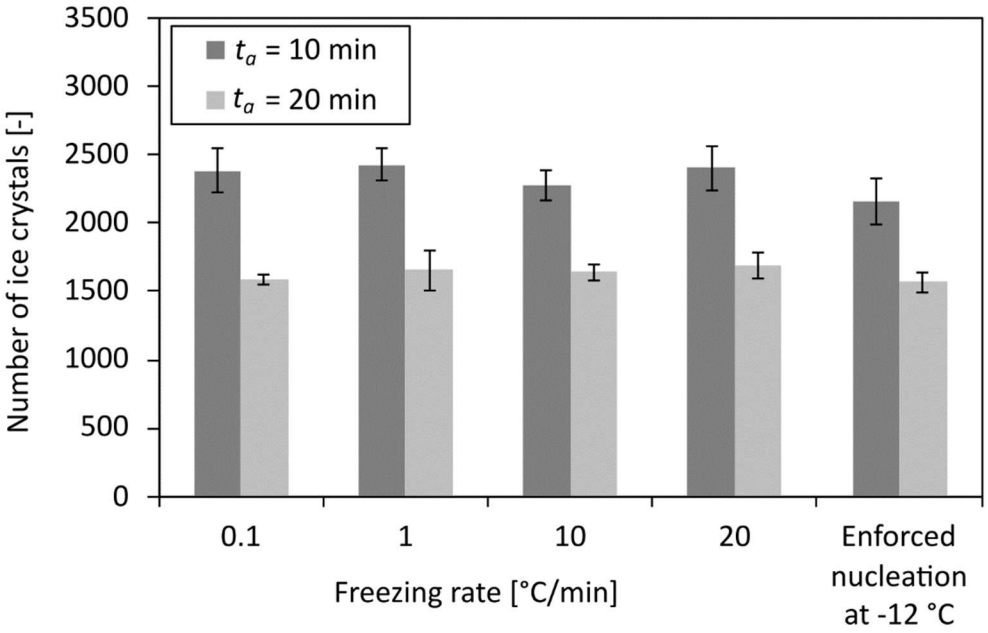

Figure 3.17: Effect of freezing rate and annealing time (t_a) on the number of ice crystals in a 10 % (w/w) sucrose solution. Standard deviations (error bars) were determined from triplicates.

For all freezing ramps, as well as for enforced nucleation at -12 °C, no significant difference was observed in the number of individual ice crystals ($p > 0.05$), indicating that under uniform

annealing conditions, the coarsening of the crystalline phase occurred independently of the preceding freezing conditions. However, a significantly lower number of ice crystals was counted after 20 minutes of annealing compared to 10 minutes, across all freezing ramps and enforced nucleation conditions ($p < 0.05$).

The relationship between the number of ice crystals and the nucleation temperature is illustrated in Figure 3.18. It is important to note that the nucleation temperature for each measurement was determined with an accuracy of 1 °C, due to limitations in capturing more images with the camera during the steep freezing ramps.

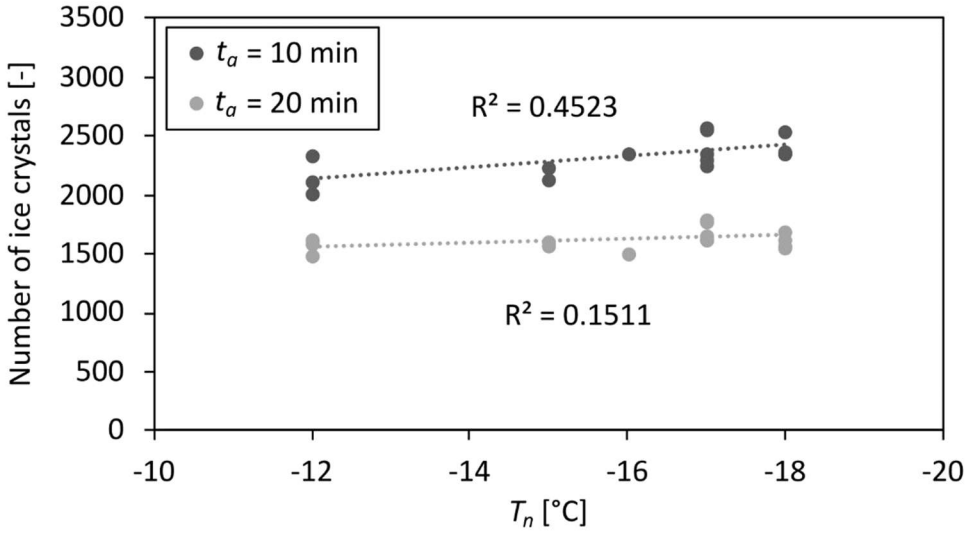

Figure 3.18: Effect of nucleation temperature (T_n) and annealing time (t_a) on the number of ice crystals in a 10 % (w/w) sucrose solution.

These results also show that over a range of nucleation temperatures from -12 °C to -18 °C, the resulting number of individual ice crystals did not change significantly after the samples were exposed to either 10 minutes or 20 minutes of annealing ($p > 0.05$). However, there was a significant difference between the datasets corresponding to the two different annealing times at any given nucleation temperature ($p < 0.05$), similar to the results from Figure 3.17.

The results of the annealing experiments in the freeze-drying microscope can be summarised as follows:

- Freezing a small volume of sample while preventing the temperature from rising due to recalescence and crystallisation leads to the formation of fine feather-like structures.

- If these structures are composed of small individual ice crystals, then these ice crystals are one or more orders of magnitude smaller than any pore found in a lyophilisate.
- When these frozen samples are annealed in a freeze-drying microscope under conditions that mimic typical residence times in a lyophiliser, individual grain-like ice crystals with sizes comparable to pores in a dry lyophilisate are formed.
- The quantity (and therefore size) of these ice crystals depends mainly on the conditions during the recalescence and crystallisation phases, and not on the nucleation temperature.

It is important to note that the reduction in sample thickness can impact the rate of Ostwald ripening of ice crystals during annealing. The spatial confinement between glass plates alters the shape of ice crystals by flattening them, as illustrated previously in Figure 3.12. Ostwald ripening, described in Chapter 1.4.2, is a curvature-dependent process and may decelerate when fewer curved surfaces are present. Therefore, it is crucial to clarify that the objective of these experiments is not to determine an exact pore size based on freezing and annealing conditions. Rather, the goal is to assess the qualitative effect of recalescence and the subsequent crystallisation phase on the morphological changes within the microstructure of the frozen solution.

3.1.5 Impact of thermal history during freezing on the microstructure

The following hypothesis is proposed to interpret the experimental data from previous chapters, with additional context on the freezing of a glass-forming disaccharide solution.

The growth of ice crystals from a nucleus in a solution can be classified into three main types: dendrites, irregular dendrites, and spherulites, influenced by factors such as freezing rate, solute composition, and concentration [48]. Regular dendrites form when there is sufficient time for ice crystal growth, while faster crystallisation leads to the development of irregular dendrites and spherulites [2]. Given that the samples experienced supercooling both in the freeze-drying microscope and in the lyophiliser, it is likely that the crystallisation process occurred relatively quickly after nucleation. This rapid formation is evident in Figure 3.15, where the structures appear less organized than, for instance, a snowflake, which exemplifies dendritic ice crystal growth. Structures like dendrites, irregular dendrites, and spherulites are

characterised by high surface-to-volume ratios due to their elongated, branching, and spear-like shapes, as illustrated in Figure 3.19.

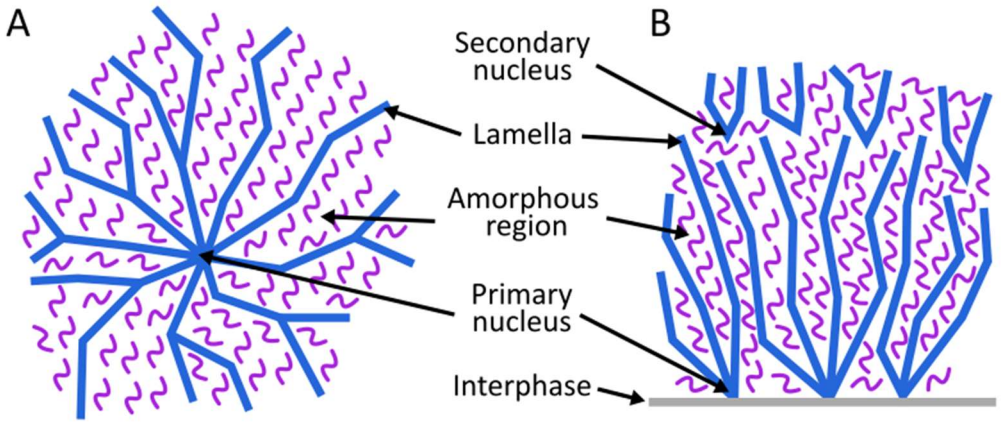

Figure 3.19: Spherulites from homogeneous nucleation (A) and dendrites from heterogeneous nucleation (B). Modified from [141,142].

The arrangements of ice crystals and amorphous regions in non-annealed samples were visible as feather-like structures, as described in Chapter 3.1.4. Furthermore, the directionality of these structures seems to indicate that they originated from an interface, as shown conceptually in Figure 3.19 and experimentally in Figure 3.15. It could be inferred that heterogeneous nucleation, which is the most common type of nucleation (see Chapter 1.4.1.1), took place at the boundary between the liquid and gaseous phases (small air bubble or outer edge of the solution in contact with air) during freezing. The liquid phase then began to crystallise directionally from the interface, producing irregular dendrites throughout the bulk volume. Notably, the latent heat of crystallisation was rapidly removed from the sample by the cooling block, meaning that the structural changes of the irregular dendrites were small compared to those observed in a freezing solution within a vial. This explanation is consistent with observations from several publications, which describe the rapid freezing of a supercooled solution producing irregular dendrites [2,44,48].

Irregular dendrites exhibit a higher interfacial energy than grain-like ice crystals due to their greater surface-to-volume ratio. The initial formation of these structures can be attributed to the non-equilibrium freezing process as a result of supercooling. Water molecules were incorporated into the ice crystals more randomly compared to the crystals that grow more slowly and form more ordered shapes, such as snowflakes. Moreover, the rapid reduction in temperature associated with supercooling prevented these dendrites from transitioning to

lower enthalpy forms by inhibiting processes such as Ostwald ripening. Consequently, the frozen system remained in a state of increased enthalpy.

This description applies to the freeze-drying microscope experimental setup because the sample temperature did not increase due to recalescence and crystallisation. However, when the temperature conditions during recalescence and the subsequent crystallisation phase from the lyophiliser were mimicked in the freeze-drying microscope, the ice crystals underwent reorganisation and adopted structures with a lower volume to surface ratio, such as grain-like ice crystals. By raising the temperature of the sample above its glass transition temperature, the molecular mobility of the system was increased to the point where the reorganisation of the ice crystals could be observed in real time under the freeze-drying microscope. The reorganisation of the frozen solution was demonstrated by the blurring of the fine feather-like structures (see Figure 3.16, t_a = 1 min). Such structural transitions are complex and probably result from capillary (surface energy) effects [40]. In addition, the colouring of the images in polarised light microscopy provides information about the distribution of the crystalline phase by visualising the crystallographic orientation of ice crystals [143], as shown in Figure 3.20.

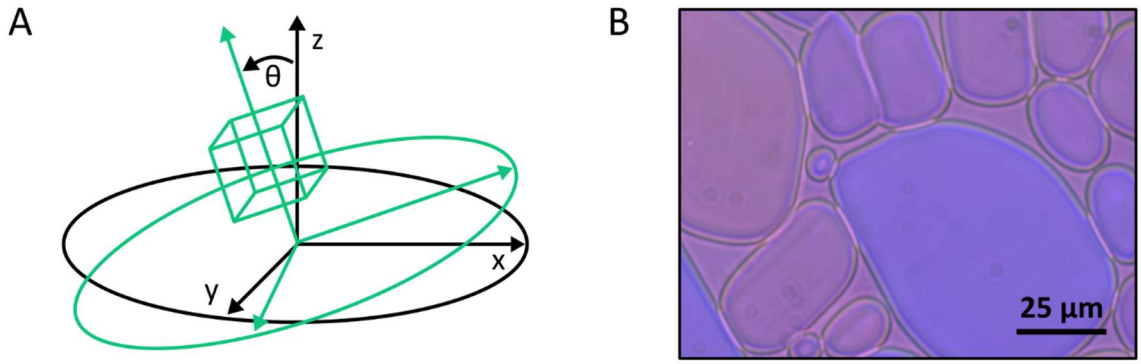

Figure 3.20: Concept of crystal orientation with a cube rotated in relation to the x,y,z-plane (A), and freeze-drying microscopy with polarised light of a 10 % (w/w) sucrose solution after annealing at -6 °C for 120 minutes (B). Modified from [144].

Crystal orientation refers to the alignment of the crystal lattice, or crystallographic axis, in space. In microscopy, the path of light traveling vertically through the sample serves as the reference point. When the electric field vectors of the polarised light interact with the birefringent crystal, the orientation of the crystal determines how the interference colours and their intensity appear by altering the birefringence experienced by the passing light.

It is notable that the individual grain-like ice crystals in the frozen sucrose solution appear uniform in color. This uniformity suggests that each “grain” constitutes a single crystal, characterised by a lattice that is uniformly oriented in a single direction. During the Ostwald ripening process, these ice crystals exchanged water molecules, which were then incorporated into their respective crystal lattices. This exchange led to the coarsening of the crystalline phase, resulting in fewer ice crystals overall, but with an increased average size of each individual crystal. From the observations in Figure 3.16, it is noticeable that in the non-annealed samples, the patches appearing as branched areas within the feather-like structures also exhibited uniform colouring. This suggests that these patches were actually irregular dendrites, originating from a single stable nucleus upon freezing, and therefore shared the same orientation of their crystal lattice. When the temperature was increased during the annealing step, these patches began to blur, and subsequently grain-like ice crystals became visible. A summary of this hypothesis is shown in Figure 3.21.

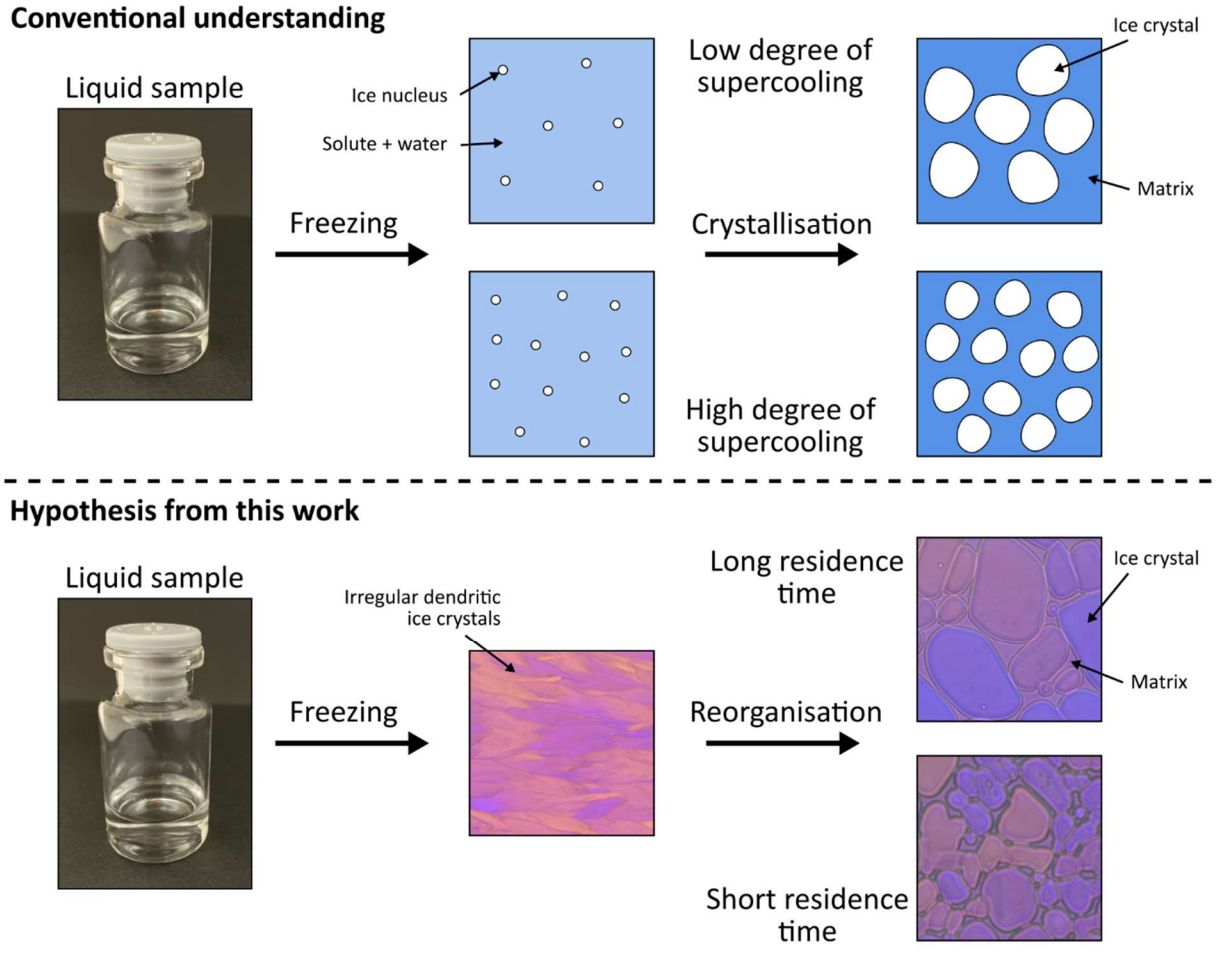

Figure 3.21: Differences in the conventional understanding of the dependence of supercooling and ice crystal sizes (top) the hypothesis based on the results of this work (bottom).

It is important to note that when samples are rapidly frozen using methods like immersion in liquid nitrogen or dry ice/isopropanol before freeze-drying, the primary drying rate tends to slow down [86], and the ice crystal surface area increases [145] compared to samples frozen under regular conditions. This observation aligns with the hypothesis that the recalescence and crystallisation phase in rapidly frozen samples is shorter due to the quick removal of heat during freezing. Consequently, there is less opportunity for Ostwald ripening to occur, resulting in smaller ice crystals, which in turn leads to slower primary drying rates.

3.1.6 General discussion – importance of recalescence and crystallisation

The findings of this work underscore the significance of the recalescence and subsequent crystallisation phase in ice crystal formation during freezing. In the field of freeze-drying, it is widely believed that the nucleation temperature primarily influences the number and size of ice crystals, which subsequently impact the resistance to vapor flow during primary drying. This perspective is grounded in classical nucleation theory, which links the number of stable nuclei to the nucleation temperature, and is supported by empirical data on pore sizes in dried lyophilisates and primary drying times.

However, the results of this work challenge the prevailing notion by demonstrating that the temperature conditions during recalescence and crystallisation significantly influence the formation of grain-like ice crystals and, consequently, the microstructure of the lyophilisate. This conclusion is supported by the lack of a significant correlation between nucleation temperature and the number and size of ice crystals when the recalescence and crystallisation phases were mimicked in the freeze-drying microscope. Importantly, this hypothesis does not refute classical nucleation theory. Instead, it suggests that nucleation kinetics and the final microstructure of the lyophilisate are decoupled by the recalescence and crystallisation phenomenon during freezing. This means that the statement "a stable nucleus subsequently results in a pore in the lyophilisate" is, according to the observations in this work, incorrect. These conclusions rely on the reasonable assumption that the freezing phenomena observed in the freeze-drying microscope and in the lyophiliser are comparable.

Regarding the height-dependent temperature conditions during recalescence and crystallisation (discussed in Chapter 3.1.3), the findings of this work qualitatively align with other studies that have shown pore size variations dependent on the axial position within the

vial. Colucci et al. (2020) developed a mathematical model to predict height-dependent pore size variations in lyophilisates. For example, the SEM data revealed significant differences in pore sizes, ranging from approximately 27 µm at the bottom of the vial to over 50 µm at the top. This phenomenon can be explained by the variations in residence times across different regions of the vial. The results in Chapter 3.1.3 indicate that the upper positions in the vial experience higher residence times, allowing for prolonged Ostwald ripening compared to the lower regions, and consequently, larger pores are formed after drying.

In the academic field, these findings could be applied to the development of nucleation models for lyophilisation. Expanding on this work, it is essential to incorporate the recalescence and crystallisation phases, specifically the reorganisation from irregular dendritic to grain-like ice crystals as influenced by temperature and other factors such as solute concentration. Such models could then be validated using existing methods, such as SEM imaging of dried lyophilisates, since a detected pore would have originated from a grain-like ice crystal, a byproduct of reorganisation during recalescence and crystallisation.

In practical terms, the results of work can refine the determination of critical process parameters for lyophilisation. For instance, the collapse temperature, which seems to be influenced by annealing [78], can be more accurately determined if the sample in the differential scanning calorimeter is treated under the same temperature conditions that a sample in a vial would experience due to recalescence and crystallisation.

3.2 Microstructure evolution during annealing

In the previous chapter it was shown that the sample temperature during freezing had a significant effect on the size of ice crystals formed in a frozen sucrose solution. Upon nucleation, the increase in temperature due to the latent heat of crystallisation caused the ice to reorganise from dendritic structures to single grain-like ice crystals. These ice crystals then coarsened due to Ostwald ripening as long as the temperature of the sample remained elevated. Both the nucleation temperature and the freezing ramp were shown to influence the residence time, i.e., the time that the sample temperature was raised during the recalescence and crystallisation phase.

In lyophilisation, a separate annealing step can also be used to modify the properties of the frozen solution and the subsequent drying process. Chapter 1.4.2 provides an overview of the

current understanding of the effect of the annealing step in the literature. Typically, experiments are carried out with different annealing conditions to assess their influence on the process parameters during drying and on the final product. There, the sample temperature is used to determine when sublimation is complete in individual vials, or the pressure in the lyophiliser can be utilised as an indicator for the entire batch (see Chapter 1.4.3). However, these approaches treat the sample in the vial as a black box since *in vitro* observations of the microstructure formation are not possible with current equipment. Consequently, the exact relationship between ice crystal size and primary drying time remains unclear. While the simple determination of drying times reduction and annealing conditions may aid in process optimisation, understanding the temporal evolution of microstructural properties in frozen solutions can provide valuable insights into the importance of process conditions during the freezing and annealing steps in freeze-drying.

The experimental methods listed in Chapter 1.7 and their limitations do not allow for a sufficiently detailed characterisation of the microstructure in the dried or frozen samples. Therefore, the influence of annealing on the microstructure cannot be reliably investigated. To overcome these problems, an alternative methodology is proposed below. The approach is an *in silico* strategy using numerical simulation to study the coarsening behaviour of ice crystals during annealing. The selection of an appropriate simulation method is crucial to capture all relevant phenomena, followed by calibration to ensure accurate representation of the phenomena. Coarsening is influenced by two key factors, namely the volume fractions of the crystalline and amorphous phases, and the recrystallisation rate, which describes the reduction in the number of ice crystals over time.

3.2.1 Methodological framework to investigate the microstructure

In this work, a phase-field model was used to simulate the temporal evolution of the microstructure in three-dimensional space. The details of the phase-field model are explained in the following chapter. However, the direct determination of the recrystallisation rate was problematic due to the limitations of the measurement methods discussed in Chapter 1.7. Therefore, an alternative methodology was applied in this work by exploiting the similarities in curvature planes between a two-dimensional phase-field simulation and the experimental

setup of a freeze-drying microscope. The concept of planes of curvature is illustrated in Figure 3.22.

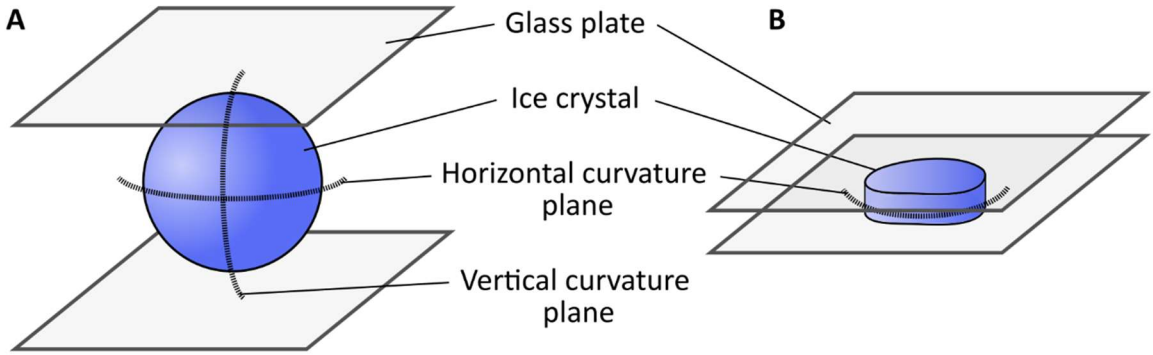

Figure 3.22: Schematic representation of the morphology of ice crystals between two spatial boundaries. If the distance between the boundaries is sufficiently large, spherical ice crystals with two planes of curvature are formed (A), whereas if the distance is small, cylindrical ice crystals with only one plane of curvature are present (B).

Ice crystals in three-dimensional space without any boundaries exhibit two curvature planes, namely a horizontal and a vertical plane. However, when the distance between the boundary surfaces that limit the ice crystals becomes smaller than the diameter of the ice crystals, then the ice crystals start to deform until they assume cylindrical shapes that only have a single curvature plane.

The driving force behind Ostwald ripening, the phenomenon that is of interest for this work, is based on the Gibbs-Thomson effect, which refers to the dependence of vapour pressure or chemical potential on the interfacial energy/curvature of a surface [146]. As explained in Chapter 1.4.2, the saturation vapour pressure deviates from a purely temperature-dependent material property when the material is present in sufficiently small particles such as microscopic ice crystals. A mathematical relationship can be established between curvature and the deviation in saturation vapour pressure, which is described in Appendix A for phase-field models. If a circle (two-dimensional) and a sphere (three-dimensional) with radius r are considered, the mean curvature is $1/r$ and $2/r$, respectively. This means that the deviation in saturation vapour pressure doubles when a circle is expanded into a sphere, i.e., another plane of curvature is added (see Equation App. 1). Accordingly, phenomena such as Ostwald ripening would also proceed at a different rate for a circle and a sphere of the same radius.

In freeze-drying microscopy experiments, the sample volume is confined to a thin film between two glass plates. The distance between the two glass plates can be controlled using a spacer. If no spacer is used, the distance between the two glass plates will adjust according to the sample volume (see Chapter 3.1.4). When the distance between the glass plates is sufficiently small compared to the size of the ice crystals, the ice crystals are forced into a cylindrical shape (see Figure 3.22). Subsequently, the plane of curvature in the vertical direction becomes negligible, reducing the system to a single plane of curvature. In this state, annealing still causes Ostwald ripening to occur, but the curvature-dependent coarsening of the ice crystals is expected to be altered due to the reduction of the system to a single plane of curvature.

Precisely this property was utilised to carry out a simulation-based investigation of the coarsening, because two-dimensional simulations are representative of the freeze-drying experiments due to the single curvature plane, while three-dimensional simulations with their two curvature planes reflect the ice crystals in a lyo vial. Phase-field modelling was chosen as the simulation type for the following reasons. Phase-field models can be easily extended from two-dimensional to three-dimensional, while the overall mathematical basis and simulation parameters remain identical. In addition, phase-field models inherently incorporate the concepts of curvature (interfacial energy) and saturation vapour pressure (composition/chemical potential). They provide a straightforward way of describing the temporal evolution of phases in such a system and are often used to predict coarsening phenomena. The simulation strategy is illustrated in Figure 3.23 and explained below.

First, samples for freeze-drying microscopy experiments were prepared with small volumes in order to reduce the sample height as much as possible. The aim was to reduce the vertical plane of curvature to such an extent that its contribution to the coarsening of the ice crystals became negligible. In Chapter 3.2.2.2.3, annealing experiments were carried out with these samples in the freeze-drying microscope to determine the recrystallisation rates for a single plane of curvature at different annealing temperatures. This experimental data was used to calibrate a phenomenological two-dimensional phase-field model in order to determine simulation parameters that would capture the coarsening behaviour as accurately as possible (see Chapter 3.2.4).

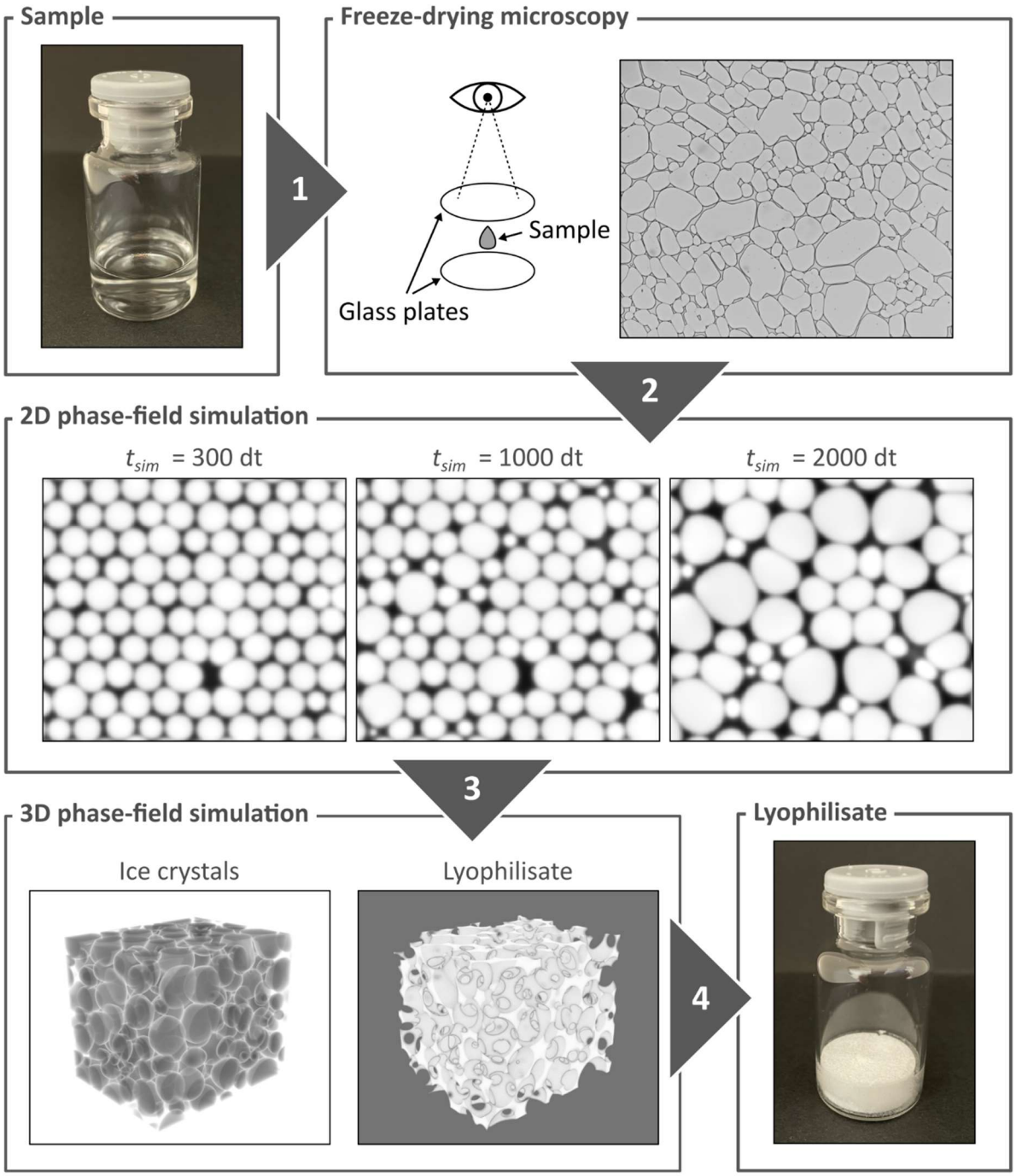

Figure 3.23: Approach to the prediction of morphological properties of the microstructure in a lyophilisate in this work: sample preparation for freeze-drying microscopy (1), calibration of a two-dimensional phase-field model (2), determination of simulation parameters (3), prediction of microscopic morphological parameters (4).

A three-dimensional phase-field simulation was then implemented using the simulation parameters determined from the two-dimensional simulation in Chapter 3.2.5. The aim of this step was to re-introduce the horizontal plane of curvature, thus reversing the reduction in the number of planes of curvature from the experimental setup. This would then allow

conclusions to be drawn for the impact of the annealing process on a frozen disaccharide solution in a lyo vial. Finally, with the three-dimensional extension, morphological parameters were predicted in their temporal evolution, such as the ice crystal size distribution, the surface area of the matrix phase and the conjunction area between ice crystals. The details of each morphological parameter are given in the relevant chapters.

3.2.2 Implementation and calibration of the phase-field model

In the following sections, a phase-field model was implemented as a numerical method to investigate the microstructural changes in a frozen solution during annealing, and experimental data were collected to calibrate the relevant model parameters.

3.2.2.1 Formulism of the multiphase-field model

The considered phase-field model is based on a particulate phase *p* (here: ice crystals) and a continuous matrix phase *m*. These phases are described in space **r** and time *t* by the order parameter $\eta(\mathbf{r},t)$ (crystalline ice phase = 1, amorphous matrix phase = 0) and their composition $c(\mathbf{r},t)$ (pure water = 1, pure solute = 0). The transition between the phases is represented in the phase-field model by a smooth interface with values between the corresponding minima and maxima.

The evolution of the microstructure in this phase-field model is governed by the Cahn-Hilliard diffusion equation for conserved field variables:

$$\frac{\partial c}{\partial t} = \nabla M \nabla \frac{\delta F}{\delta c}, \qquad \text{(Eq. 6)}$$

and the Allen-Cahn relaxation equation for non-conserved field variables:

$$\frac{\partial \eta}{\partial t} = -L \nabla \frac{\delta F}{\delta \eta}, \qquad \text{(Eq. 7)}$$

where *M* is the mobility coefficient, *L* is the relaxation coefficient and *F* is the free energy of the system [126].

Since Ostwald ripening is a diffusive process, particle-particle interactions such as coalescence must be inhibited. In nature, fusion of ice crystals is prevented through a mismatch of the crystallographic orientations of neighbouring crystals [103].

This concept can also be adopted in a phase-field model, where $\eta(\mathbf{r},t)$ is extended to the multiphase-field $\eta_i(\mathbf{r},t)$ and is given by:

$$\frac{\partial \eta_i}{\partial t} = -L\nabla \frac{\delta F}{\delta \eta_i(r,t)}, \tag{Eq. 8}$$

with $i = 1, 2, \ldots, n$ and the particulate phase is divided between the n elements of the phase fields. The free energy of the system F is composed of the bulk free energy and the contributions from the gradient free energies:

$$F(f,c,\eta_i) = \int_{\Omega} \left[f(c,\eta_i) + \kappa_c(\nabla c)^2 + \kappa_\eta(\nabla \eta_i)^2 d\Omega \right], \tag{Eq. 9}$$

where $f(c,\eta_i)$ is the bulk free energy density, and κ_c and κ_η are the gradient energy coefficients for composition and order parameter, respectively. The bulk free energy density $f(c,\eta_i)$ promotes phase separation whenever gradient and interfacial energies are not present and is given by:

$$\begin{aligned} f(c,\eta_i) = f^m(c)\left(1 - \sum_{i=1}^{n} W(\eta_i)\right) + f^p(c)\sum_{i=1}^{n} W(\eta_i) \\ + \sum_{i=1}^{n} P\eta_i^2(1-\eta_i)^2 + Q\sum_{i=1}^{n}\sum_{i\neq j}^{n} \eta_i^2\eta_j^2 , \end{aligned} \tag{Eq. 10}$$

where P is a coefficient for the magnitude of the energy barrier between the m- and the p-phase, Q is a coefficient for the magnitude of the energy barrier between the n particulate phases, and f^m and f^p are the free energies of the m- and the p-phase, respectively.

The interpolation function $W(\eta_i)$ is used in Eq. (7) and is defined as [147]:

$$W(\eta_i) = \begin{cases} 0; & \text{for } \eta_i < 0, \\ \eta_i^3(10 - 15\eta_i + 6\eta_i^2); & \text{for } 0 \leq \eta_i \leq 1, \\ 1; & \text{for } \eta_i > 1. \end{cases} \tag{Eq. 11}$$

The free energies f^m and f^p are given by:

$$f^m(c) = A(c - c_m^e)^2 , \tag{Eq. 12}$$

$$f^p(c) = B\left(c_p^e - c\right)^2 , \tag{Eq. 13}$$

where A and B are positive constants, and c_m^e and c_p^e are equilibrium compositions for the m- and the p-phase, respectively.

In this work, the recrystallisation rate in the model was calibrated using the simulation parameters *M* and *L*. Both values remained constant, i.e., when *M* was changed, *L* was adjusted to the same value, effectively only impacting the recrystallisation rate and not the morphological properties of the particles. If dissimilar values of *M* and *L* had been used in a simulation, the ratio of diffusion to relaxation of the particles would have changed, potentially affecting the morphology adopted by the particles during coarsening. The generation of the two-dimensional and three-dimensional initial conditions is discussed later in Chapter 3.2.3. The dimensionless simulation parameters for the phase-field model are listed in Table 3.1.

Table 3.1: Dimensionless parameters used in this work.

Parameter	Value
κ_c	1
κ_η	1
A	1
B	1
P	1
Q	2

A semi-implicit Fourier spectral scheme was implemented according to Chen and Shen (1998) by treating linear and second-order operators implicitly and residual terms explicitly. Some stability tests and parameter determination tests are provided in Appendix A.

3.2.2.2 Experimental determination of relevant calibration parameters

The phenomenological phase-field model employed to predict the effect of annealing on the microstructure of disaccharide solutions, both during annealing and in their maximally freeze-concentrated state, required calibration of relevant simulation parameters. Initially, experimental values were obtained for the volume fractions of ice crystals and the amorphous matrix phase, which vary with sample temperature and thus differ based on whether annealing is performed or if the solution reaches its maximally freeze-concentrated state. Recrystallisation rates during annealing, which are also temperature-dependent, were then determined experimentally. These experiments included both sucrose and trehalose solutions to also consider a second commonly used excipient in freeze-drying.

3.2.2.2.1 Mass fractions during annealing

As described in Chapter 1.4.1.2, the mass fractions of solute and solvent in the freeze-concentrated matrix phase of a frozen solution depend solely on the sample temperature. This is important because the temperature is increased during annealing above the onset temperature of melting T_m' at which water molecules dissolve from the crystalline phase into the matrix phase. Consequently, the ratio of solute and solvent in the amorphous phase changes. These mass fractions in the matrix phase follow the liquidus line of the solute-solvent system. For example, if a 30 % (w/w) sucrose solution becomes completely liquid at -1.6 °C, a freeze-concentrated matrix at this exact temperature (regardless of the initial concentration in the solution) will also contain a 30 % (w/w) ratio of sucrose to water. Therefore, the freezing point depression for different solute concentrations can be used to determine the temperature-dependent mass fractions in the freeze-concentrated matrix phase [60].

In the following, the melting temperature T_m of sucrose and trehalose solutions with concentrations between 30 % (w/w) and 55 % (w/w) was determined using differential scanning calorimetry (DSC) with the protocol from Chapter 2.2.4. An example heat flow is shown in Figure 3.24.

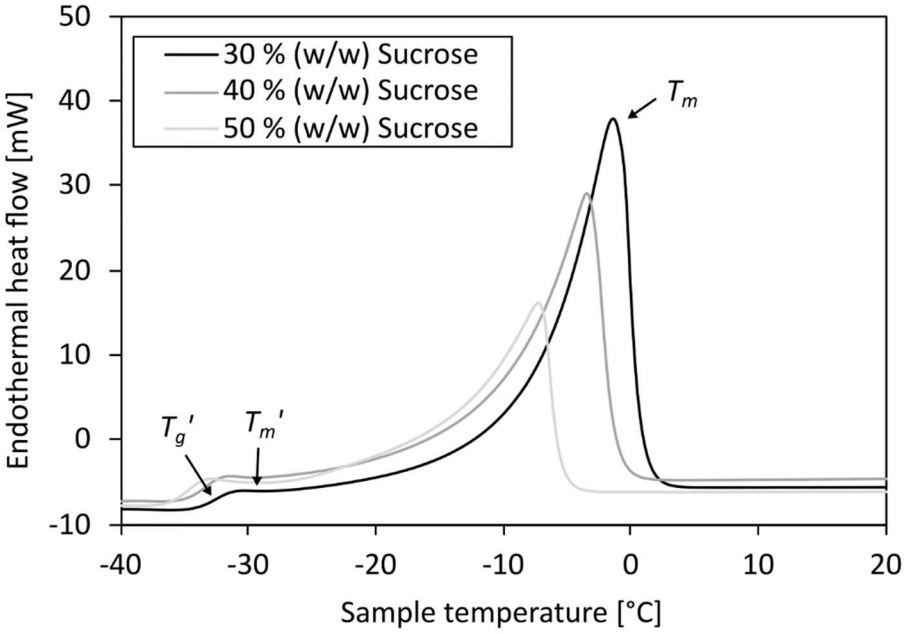

Figure 3.24: Exemplary thermograms of sucrose solutions with different solute concentrations during melting. The melting peak was used to determine the melting temperature (T_m) of the respective solution.

The glass transition during heating can be observed at approximately -33 °C by the shift in the heat flow from one plateau to another. According to Chapter 1.4.1.2, the glass transition temperature of a maximally freeze-concentrated solution (T_g') should theoretically be identical for all samples, as it is presumed independent of solute concentration. However, observed differences between the solutions can be attributed to the dissimilar thermal histories arising from varying solute concentrations. Given that nucleation temperature is influenced by solute concentration [46], and considering the demonstrated correlation between nucleation temperature and residence time due to recalescence and crystallisation (as shown in Chapter 3.1.2), it can be inferred that the samples underwent different conditions during freezing.

After the glass transition, all curves depicted in Figure 3.24 exhibited similar behaviour during heating, although with variations in peak positions and peak areas. These differences in peak area can be attributed to the varying amounts of water present in each solution. A sample with a lower solute concentration contains more water, thereby providing more ice for melting. Since melting is an endothermic phase transition, it appears as a positive heat flow in the thermogram. As mentioned in Chapter 1.4.2, care must be taken when using terms such as melting in the context of solutions. Melting is used here to describe the dissolution of precipitated ice into the matrix phase, which contains sucrose and water, and not the distinct phase change that occurs at a particular temperature when an entire substance changes phase. Specifically, the melting temperature T_m of the solution has been defined in this work as the temperature at which the heat flux peaks. The temperature of the melting peak, indicating the temperature at which the largest fraction of ice in the sample converts to water, is observed to decrease with increasing solute concentration. This relationship is critical for the calibration of the phase-field model and is detailed in Figure 3.25 for both solutes.

As the solute concentration increased, the melting temperature for the corresponding sucrose and trehalose solutions decreased. This is consistent with the phenomenon of freezing point depression, where the freezing temperature of the solution is negatively correlated with the amount of solute added to a solvent [149]. Furthermore, the recorded data are in agreement with values reported in the literature [72,150], with no significant difference between the liquidus lines for sucrose and trehalose solutions ($p > 0.05$).

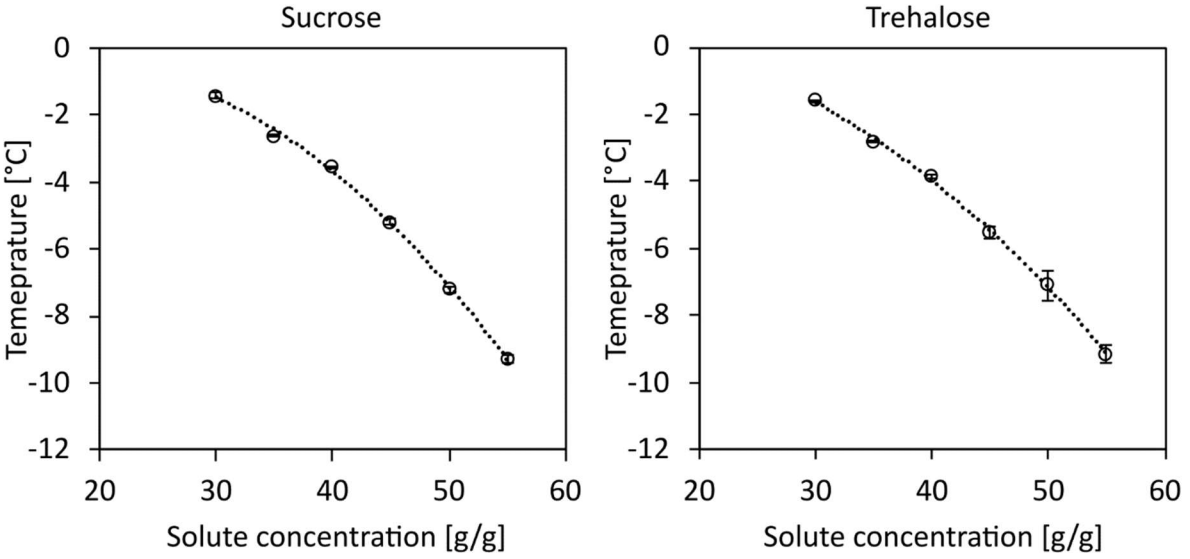

Figure 3.25: Liquidus line of a sucrose-water (left) and trehalose-water (right) system. The melting temperature of 30 % (w/w) to 55 % (w/w) solutions were measured via DSC. Standard deviations (error bars) were calculated from triplicates.

A second-degree polynomial trend line was fitted to the data and can be represented as:

$$y = -0.0062x^2 + 0.2188x - 2.4362\,, \qquad \text{(Eq. 14)}$$

where *y* is the melting temperature, and *x* is the solute concentration, with $R^2 = 0.9985$.

Equation 14 relates the solute mass fraction in the matrix phase to the ambient temperature for sucrose and trehalose solutions with concentrations ranging from 30 % (w/w) to 55 % (w/w). This experimental range corresponds to melting temperatures of -1.6 °C ± 0.0 °C and -9.3 °C ± 0.1 °C, respectively. Thus, Equation 14 can be used to determine the composition of the matrix phase at annealing temperatures within this range.

Next, appropriate annealing temperatures were selected to perform coarsening experiments for the calibration of the phase-field model. Annealing should always be performed above the glass transition temperature T_g' of the solution, otherwise changes in the microstructure will be in the order of mm/year due to the high viscosity of the material [60]. The rate of coarsening, or recrystallisation rate, of the ice phase is dependent on the annealing temperature, with higher temperatures resulting in faster coarsening [72]. However, while higher annealing temperatures shorten the process time, it is important to avoid setting the temperature too close to the melting temperature of the solution as even small temperature fluctuations in the equipment can lead to the complete thawing of the sample. As discussed

in Chapter 3.1.4, the melting temperature of a 10 % (w/w) sucrose solution is at approximately -0.6 °C, which, based on experience, allows annealing temperatures of around -2 °C in the freeze-drying microscope without risking the thawing of the sample.

Commonly, -5 °C is used in literature to study the effects of annealing on lyophilisate microstructure [70,71], providing a substantial buffer from the melting point while allowing short annealing durations to noticeably impact the microstructure. Therefore, annealing temperatures of -4 °C and -6 °C were chosen for further experiments and simulations, considering the process duration and at the same time maintaining realistic conditions comparable to published studies. In addition, two different annealing temperatures were chosen to demonstrate the temperature dependency of the process. Since -4 °C and -6 °C were within the range of the experimentally determined polynomial from Equation 14, and sucrose and trehalose solutions did not differ significantly in their freezing point depression, the solute to water mass fractions for both disaccharides at -4 °C and -6 °C were calculated to be 0.398 g/g and 0.461 g/g, respectively.

3.2.2.2.2 Volume fractions during annealing/maximum freeze-concentration

The next step involved converting the mass fractions into volume fractions for both the ice and matrix phases under annealing conditions and at maximum freeze-concentration. Due to the unavailability of direct measurements of the matrix phase density at -4 °C, -6 °C, and maximum freeze-concentration, literature data for the density of concentrated sucrose and trehalose solutions at 20 °C were utilised. Potential expansion or contraction of the matrix phase due to low temperatures was not considered. In the first-principles simulation work by Fan et al. (2018), the impact of temperature on the density change of the amorphous phase was limited to the contraction of the residual water content, which is particularly small compared to the solute mass fraction at maximum freeze-concentration. Therefore, any deviation in the volume fraction was deemed negligible in this context. The ice phase did not present this issue, as density data for ice under the specified freezing conditions in a lyophiliser were available (see Table 3.3). First, the water mass fractions in the maximum freeze-concentrated matrix phase for both sucrose and trehalose solutions were gathered from various literature sources and are summarised in Table 3.2.

Table 3.2: Water mass fraction in the maximum freeze-concentrated matrix phase (ω_w'), reported by different authors.

Excipient	ω_w' [g/g]	Reference
Sucrose	0.226 – 0.246	[59]
	0.180	[94]
	0.200 – 0.210	[151]
	0.200	[152]
Trehalose	0.188	[153]
	0.167	[154]
	0.184	[152]

Differences between data for the same excipient can be observed due to variations in measurement methods and freezing protocols. Therefore, the values listed in Table 3.2 were used to calculate the average mass fraction of water in the maximum freeze-concentrated matrix for both sucrose and trehalose solutions, which were found to be 0.210 g/g and 0.180 g/g, respectively.

The amount of water and solute present in the matrix phase of a 10 % (w/w) solution was determined with:

$$\frac{m_s}{m_w} = \frac{\omega_s}{\omega_w}, \qquad \text{(Eq. 15)}$$

where m_i is the mass of a component, and ω_i is the corresponding mass fraction. This was possible because the solute is exclusively present in the matrix phase due to the solute exclusion phenomenon (see Chapter 1.4.1.2).

The volume fractions of the ice and the matrix phase were subsequently calculated with:

$$\varphi_i = \frac{V_i}{V_i + V_j}, \qquad \text{(Eq. 16)}$$

where V_i and V_j are the volumes of the respective phases, and are defined as:

$$V_k = \frac{m_k}{\rho_k}, \qquad \text{(Eq. 17)}$$

where m_k is the mass and ρ_k is the density of the respective component.

All values related to mass and volume fractions used for the calculation and subsequent calibration of the phase-field model are listed in Table 3.3. It is noteworthy that a difference between sucrose and trehalose solutions was only observed at -40 °C, due to the different water mass fractions in the maximally freeze-concentrated matrix phase. Conveniently, this means no separate calibration of input parameters is necessary for sucrose and trehalose regarding their mass and volume fractions at both annealing temperatures.

Table 3.3: Effect of temperature (T) on solute mass fraction in the matrix phase (ω_s), water mass fraction in the matrix phase (ω_w), density of the ice/particulate phase (ρ_p), density of the matrix phase (ρ_m), volume fraction of the ice/particulate phase (φ_p) and volume fraction of the matrix phase (φ_m) in freeze-concentrated 10 % (w/w) sucrose and trehalose solutions.

Excipient	T [°C]	ω_s [g/g]	ω_w [g/g]	ρ_p [g/cm³]	ρ_m [g/cm³]	φ_p [cm³/ cm³]	φ_m [cm³/ cm³]
Sucrose	-4	0.398	0.602	0.918[1]	1.182[2]	0.793	0.207
	-6	0.461	0.539	0.918[1]	1.215[2]	0.828	0.172
	-40	0.790	0.210	0.924[1]	1.404[2]	0.913	0.087
Trehalose	-4	0.398	0.602	0.918[1]	1.182[2]	0.793	0.207
	-6	0.461	0.539	0.918[1]	1.215[2]	0.828	0.172
	-40	0.820	0.180	0.924[1]	1.423[2]	0.917	0.083

[1] Rumble (2021)

[2] Lescure (1995)

3.2.2.2.3 Recrystallisation rates during annealing

The rate of coarsening of the ice phase in the partially frozen sucrose and trehalose solutions during annealing was determined for annealing temperatures of -4 °C and -6 °C in order to calibrate the two-dimensional phase-field model. As previously explained in Chapter 1.6, the classical Lifshitz-Slyozov-Wagner (LSW) theory of Ostwald ripening can be used to determine the recrystallisation rate directly from the physical and chemical properties of the system. However, it is crucial to first confirm that the conditions required by the LSW theory are satisfied both in the disaccharide-water systems under study and within the experimental setup.

In Chapter 3.1.4, freeze-drying microscopy was employed to assess the number of ice crystals under various annealing conditions. The solution was spatially confined between two glass plates to form a thin film, allowing the clear observation of individual structures during annealing. The images captured by the freeze-drying microscope revealed that the particles were neither spherical nor circular, and they were mostly in contact with each other due to the low volume fraction of the matrix phase. Similar conditions are likely to be present in the experimental setup in a lyophiliser, where simply a larger volume of the same solution is filled into a vial. The thin layer of the sample and the low solute concentration in the solution prevented most of the assumptions of the LSW theory from being considered, notably due to particle-particle contact and the non-spherical nature of the ice crystals observed under the freeze-drying microscope.

Consequently, instead of employing the first-principles approach with Equation 4 to calculate the recrystallisation rate directly, an alternative strategy was utilised to describe the coarsening of the ice phase in this work. The ice phase represents the phase otherwise referred to as the particulate phase in coarsening systems. Therefore, in the context of the following chapters, ice crystal and particle as well as ice phase and particulate phase can be used synonymously. The recrystallisation rate was determined directly using Equation 3, by measuring changes in the mean particle radius over time. However, accurately determining the ice crystal area and the respective radii of individual particles proved challenging during the early stages of annealing due to their small sizes (as shown in Figure 3.26, t_a = 10 min). Therefore, the average particle size was derived from the number of ice crystals and the volume fractions of the particulate phase. The theoretical volume fractions were already calculated in Chapter 3.2.2.2.2, and the number of particles were determined with a similar setup to that described in Chapter 3.1.4, but with only 0.3 µl of 10 % (w/w) sucrose and trehalose solutions to further minimise the distance between the glass plates. This volume was sufficient to completely wet the area between the plates and resulted in a calculated sample height of approximately 1.49 µm. The samples were first cooled to -40 °C at 10 °C/min for 1 minute and then heated to the respective annealing temperatures of -4 °C and -6 °C for 360 minutes, with images taken at 10 minute intervals. Figure 3.26 shows an example of the annealing experiment images from the freeze-drying microscope.

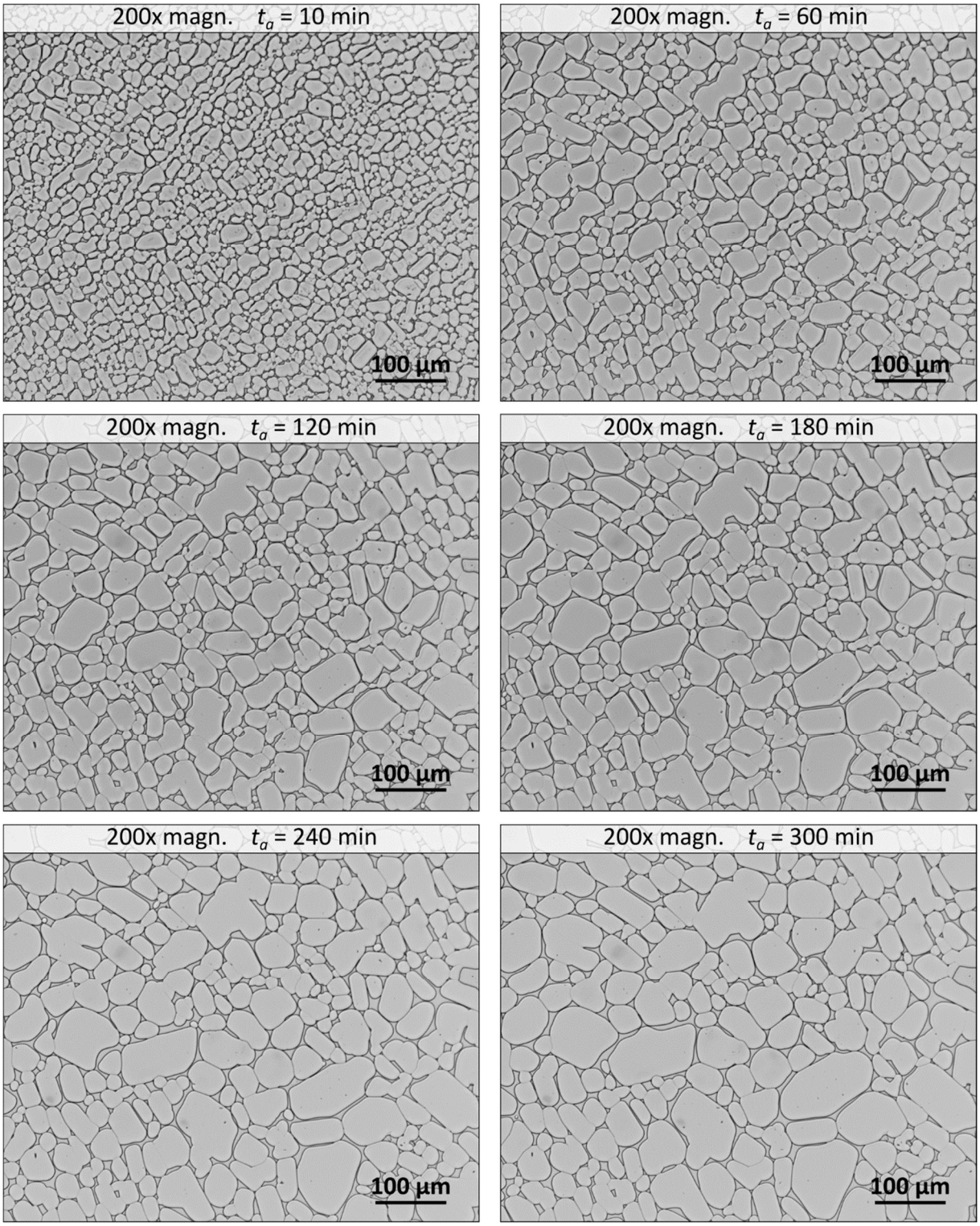

Figure 3.26: Freeze-drying microscopy of a frozen 10 % (w/w) sucrose solution during annealing. The sample was frozen with 10 °C/min and subsequently annealed at -6 °C.

A reduction in the number of ice crystals can be clearly seen during the annealing process. In order to quantify the coarsening of the particulate phase, individual ice crystals were counted manually according to Chapter 2.2.6, as automatic detection was not possible due to almost

transparent boundaries between some adjacent ice crystals. The results of this manual counting are presented in Figure 3.27.

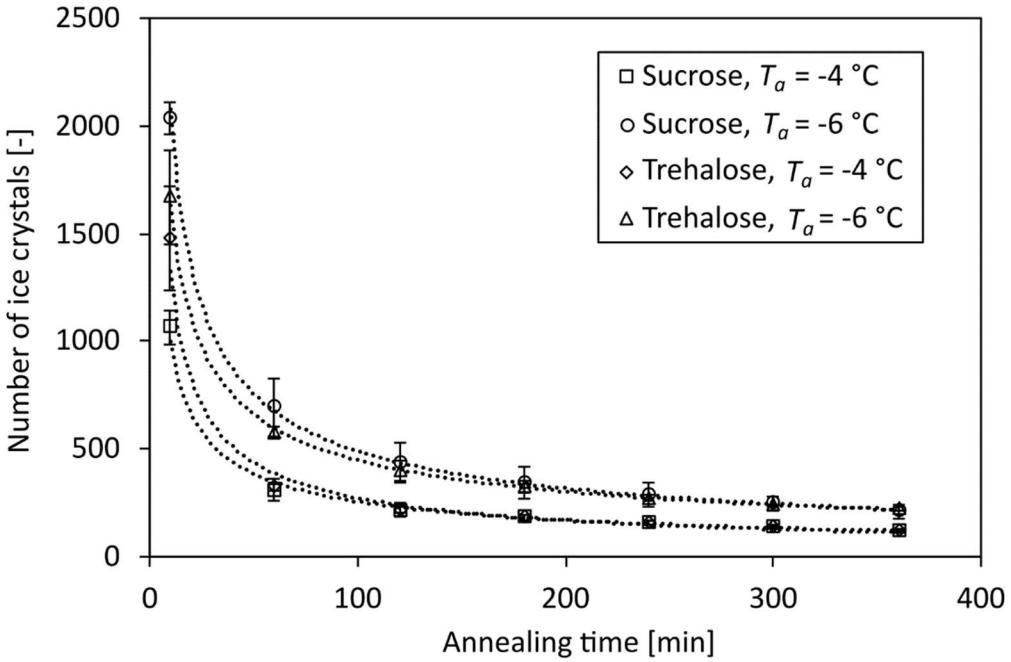

Figure 3.27: Effect of annealing on the number of individual ice crystals in 10 % (w/w) sucrose and trehalose solutions. Standard deviations (error bars) were calculated from triplicates.

The decrease in the number of ice crystals followed a power law for both solutions and annealing temperatures, as shown by the trend line fit. Notably, the standard deviation was particularly large in the early stages of annealing due to the difficulty in accurately determining the correct number of ice crystals. The average ice crystal area $\bar{A}$ was calculated with:

$$\bar{A} = \frac{A_{total} \cdot \varphi_p}{N_p}, \qquad \text{(Eq. 18)}$$

where A_{total} is the overall area of vision, φ_p is the volume fraction of the particulate phase, and N_p is the total number of particles per image.

It should be noted that area and volume fractions can be used interchangeably in the context of freeze-drying experiments and phase-field simulations. Area fraction is used because the microscopic view technically only allows for an area to be observed. However, in reality the sample still exhibits some height and is therefore present as a volume. Due to the cylindric shape of the ice crystals, the area fraction from the experiments, and the volume fraction from the calculations, are still considered to be equal.

At 200x magnification, the field of view of the freeze-drying microscope covered an area of approximately 37 mm². As mentioned, the volume fractions of the ice phase were previously determined in Chapter 3.2.3.2 for different annealing temperatures. Next, the circle equivalent radius of the average ice crystal was determined with:

$$r_e = \sqrt{\frac{\bar{A}}{\pi}}. \qquad \text{(Eq. 19)}$$

According to the growth law from Equation 3, the cube of the particle radius increases proportionally with annealing time. Therefore, the cube of the circle equivalent radius was calculated and is also shown in Figure 3.28.

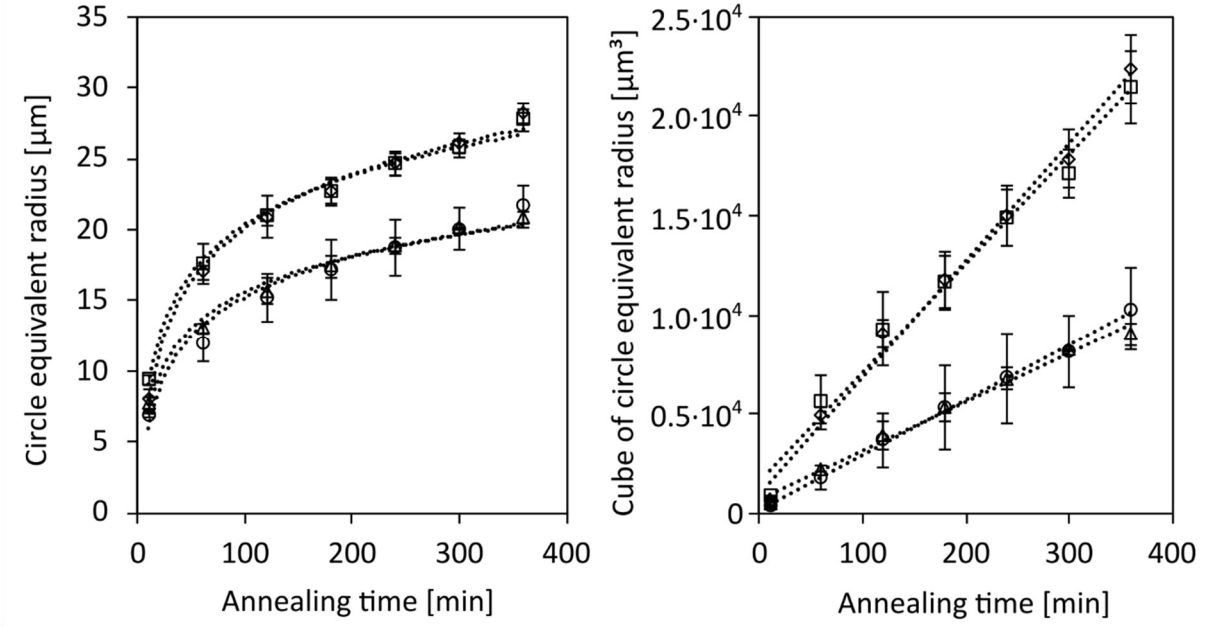

Figure 3.28: Effect of annealing on the circle equivalent radius (left) and cube of the circle equivalent radius (right) of ice crystals in 10 % (w/w) sucrose and trehalose solutions. Standard deviations (error bars) were calculated from triplicates.

The average circle equivalent radius of ice crystals exhibited a logarithmic curve profile, while the cube of the circle equivalent radius of ice crystals increased linearly with annealing time for sucrose and trehalose solutions. A statistically significant difference for the data sets between sucrose and trehalose solutions was neither for -4 °C nor for -6 °C observed ($p > 0.05$). Accordingly, no difference between the coarsening behaviour of frozen sucrose and trehalose solutions in the freeze-drying microscope was found in this work. This outcome is somewhat

surprising, as a difference in recrystallisation rate was previously found in a separate publication [68]. However, it should be noted that the aim of this preceding publication was not to determine an exact recrystallisation rate, but rather to assess Ostwald ripening and glassy state relaxation qualitatively. Accordingly, the annealing experiment was only performed and evaluated once for both solutes, and no standard deviation could be taken. Klinmalai et al. (2017) also found a slight difference between the two solutes during coarsening. However, the quality of the data is questionable as the standard deviation varies greatly depending on the series of measurements. In addition, it can also be observed from the microscopy images that non-cylindrical 3-dimensional crystals form in some experiments. This is particularly problematic as the radius of an ice crystal can no longer be reliably determined and the measurement now strongly depends on the layer thickness of the sample.

An increase in the annealing temperature resulted in a significant increase in the recrystallisation rate from an average for sucrose and trehalose of 26.13 µm³/min at -6 °C to 56.80 µm³/min at -4 °C ($p < 0.05$). The linear relationship observed between the cube of the circle equivalent radius and annealing time suggests that the coarsening behaviour of sucrose and trehalose solutions in the freeze-drying microscope follows the growth law of the LSW theory. However, this observation only validates Equation 3, as not all the conditions of the LSW theory are met within the experimental setup of the freeze-drying microscope. Therefore, the slopes derived from the linear fits in Figure 3.28 were used to directly determine the recrystallisation rate using Equation 3 instead of the first-principles approach from Equation 4. However, this is perfectly adequate as the phase-field simulation in this work is intended to be a phenomenological model anyway, i.e., the simulation should only quantitatively describe the respective phenomenon from the experiment and does not have to be derived from physical laws. All fitting parameters are summarised in Table 3.4.

The linear fit of the cube of the circle equivalent radius of ice crystals during the annealing experiment serves as the basis for calibrating the two-dimensional phase-field simulation. Although other fits were also determined, the use of the cube of the circle equivalent radius is a convenient choice as it is already established in the literature and allows for easy comparison between simulation and experiment due to its linear relationship.

Table 3.4: Fitting parameter of number of particles (NoP, power law fit), circle equivalent radius (CER, logarithmic fit) and the cube of the circle equivalent radius (CER³, linear fit) at different annealing temperatures (T_a).

Solution	T_a [°C]	NoP			CER			CER³	
		a [-]	*b* [1/min]	R²	*a* [µm]	*b* [µm]	R²	*k* [µm³/min]	R²
10 % (w/w) sucrose	-4	3895	-0.592	0.9958	4.943	-2.38	0.9919	54.74	0.9849
	-6	8815	-0.628	0.9997	4.024	-3.27	0.9695	27.74	0.9973
10 % (w/w) trehalose	-4	8482	-0.689	0.9940	5.433	-4.90	0.9930	58.86	0.9914
	-6	5970	-0.563	0.9994	3.685	-1.37	0.9862	24.52	0.9891

3.2.3 Initial conditions for two-dimensional and three-dimensional simulations

The specification of initial conditions is a crucial step for *in silico* methods, where relevant parameters must be defined as the starting point of the simulations. For the phase-field model used in this work, the initial placement and size distribution of the particles (=ice crystals) are essential to simulate the subsequent coarsening process. This section describes the method used to generate the distribution and positioning framework of the particulate phase for all two-dimensional and three-dimensional phase-field simulations.

Initially, a basic structure for the positioning of individual particles was established. For two-dimensional simulations, two simple geometric arrangements were considered: a square and a triangular lattice, as depicted in Figure 3.29. These configurations represent examples of close-packing that maximize the number of equal-sized particles in a given distribution. It is important to note that the choice of the basic geometric structure is not influenced by physical considerations but is instead chosen solely to establish a starting point for creating the initial conditions. The choice of close-packing structure affects the dimensions and particle area fractions. The triangular lattice results in a y-coordinate length of $Ny = \sqrt{3}/2 \cdot Nx$, due to the positioning of the particle centres. This structure also achieves a higher area fraction of the particulate phase, as it utilises the spaces between particles more efficiently. The area fraction for a square close-packed system is approximately 0.79, while for a triangular close-packed system it is about 0.91 [155].

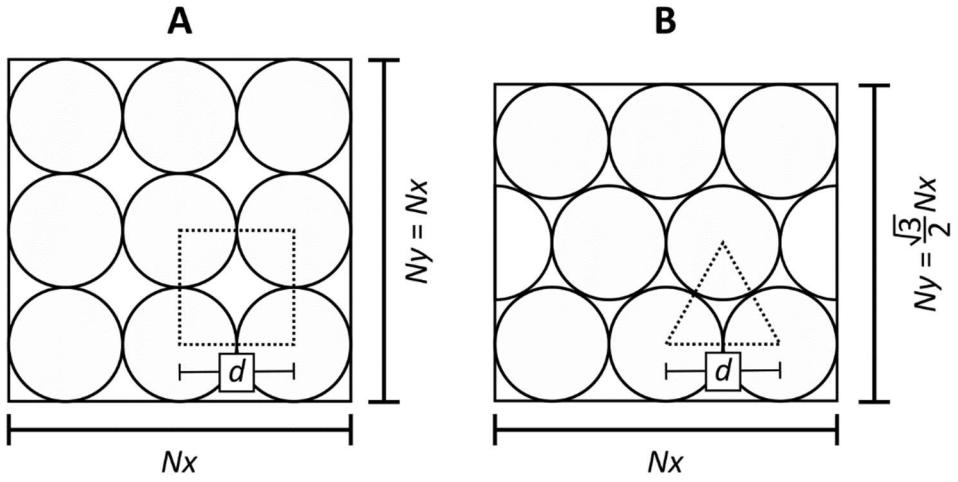

Figure 3.29: Illustration of the close-packing of circles in square (A) and triangular (B) lattices. Both arrangements exhibit an equidistant distribution regarding the centre of the particles.

To reiterate, volume and area fractions are used interchangeably for two-dimensional simulations, as they are assumed to be identical in the experimental setup due to the low layer thickness and cylindrical particle shape. This assumption would be invalid if the particles had too much curvature in the vertical height axis. The volume fractions of the particulate phase during annealing were calculated in Chapter 3.2.3.2 and amounted to an average of 0.793 and 0.828 for annealing temperatures of -4 °C and -6 °C, respectively. Therefore, the triangular lattice was chosen for the two-dimensional simulations in this work, as it is easier to reduce the area fraction of a close packing by simply reducing the particle size than by increasing the area fraction of the square lattice. The exact setting of the area fraction in two-dimensional simulations and the volume fraction in three-dimensional simulations will be discussed in the next chapter.

For the initial conditions of the three-dimensional simulations, the basic structure for particle distribution needed to be established as well. When extended into three dimensions, the two-dimensional triangular structure transitions into a tetrahedral distribution of particles. Two different close-packings based on a tetrahedral building block are possible, as depicted in Figure 3.30. Both close-packings in three-dimensional have similar packing fractions of approximately 0.74 [156]. Consequently, the choice is therefore not based on physical considerations or volume fractions, but rather on ease of implementation. The hexagonal close-packing has a more repetitive positioning and is therefore slightly easier to implement. Analogous to the reduction of the y-coordinate in the triangular two-dimensional case, the z-

coordinate also changes in the hexagonal three-dimensional case to $Nz = \sqrt{6}/3 \cdot Nx$. In summary, the particle positioning was chosen to be triangular for two-dimensional simulations and hexagonal for three-dimensional simulations to simplify the setup and implementation process.

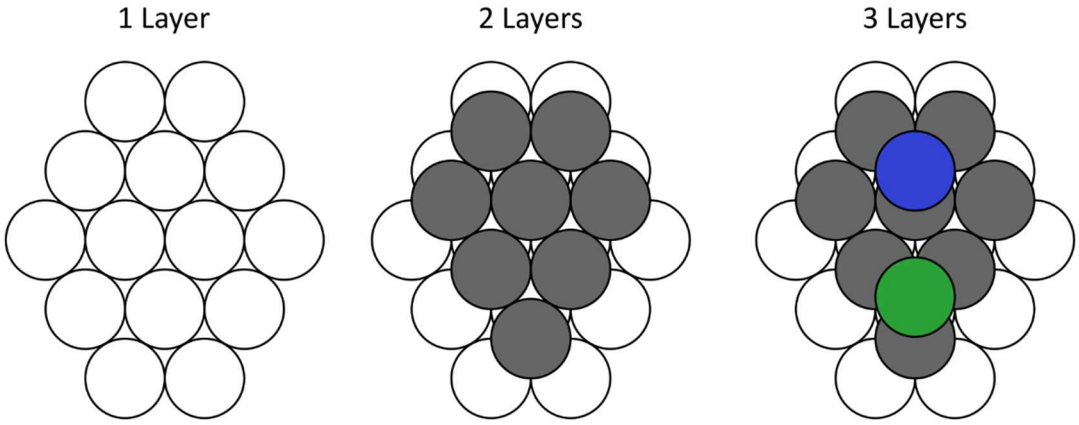

Figure 3.30: Arrangement of hexagonal and cubic close-packings in different layers. In the hexagonal system, the particles in the third layer are positioned exactly the same as in the first (blue), while in the cubic system the position is slightly shifted (green).

Next, the grid size of the simulation domain and the initial number of particles were established based on computational feasibility. The scaling of the total number of grid points in such a system is depicted in Figure 3.31.

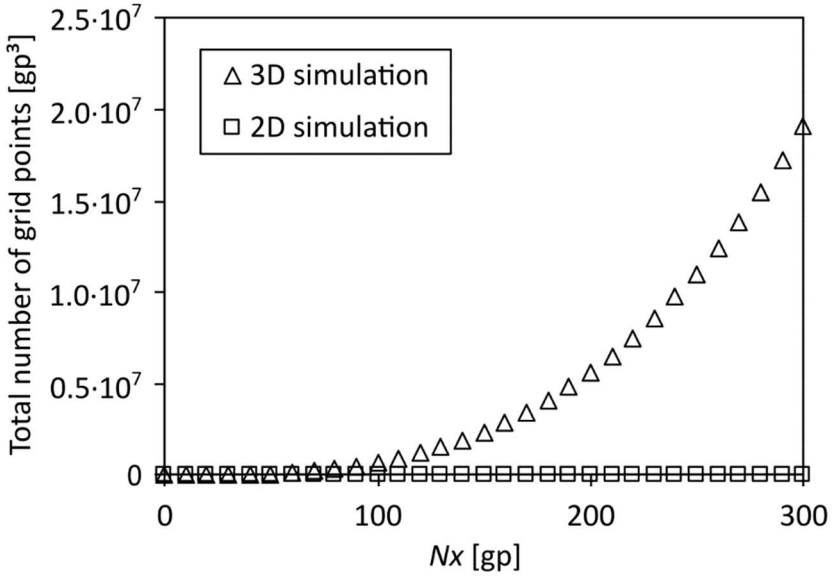

Figure 3.31: Scaling of the simulation grid size (*Nx* · *Ny* · *Nz*) with the hexagonal positioning of particles. The tetrahedral basic structure results in $Ny = \sqrt{3}/2 \cdot Nx$ and $Nz = \sqrt{6}/3 \cdot Nx$.

When determining the domain size, it was crucial to manage the number of grid points to prevent unreasonably long computation times. This consideration is especially important for three-dimensional simulations, where the number of grid points substantially increases due to the addition of the z-coordinate. Consequently, the total size of the three-dimensional domain was used to define the simulation domain. The base grid size was chosen based on experience with an upper limit of approximately 10 million grid points (gp). According to Figure 3.31, a base grid size of Nx = 240 gp was chosen, resulting in a total of just under 9.8 million grid points, with Ny = 208 gp and Nz = 196 gp.

The next stage of the process involved the selection of the number of particles to be used for the starting point of the simulation. In the case of two-dimensional simulations, a total of n particles were placed in each coordinate, resulting in a total of n^2 particles. In the three-dimensional setup with hexagonal positioning, a total of $4n^3$ particles were used. As with the grid size, an issue may arise when the number of particles becomes too large due to the need to increase the number of order parameters in the multiphase-field approach. To reiterate, the order parameter in the multiphase-field model is the equivalent to the crystallographic orientation of ice crystals. This approach allows a defined number of particles to be computed in a single iteration, provided that the particles in the same order parameter are not in close proximity to each other. If particles of the same order parameter come into contact with each other, unintentional interactions such as fusion of neighbouring particles will occur. Therefore, it is important that the initial particles are distributed over a sufficient number of order parameters in order to prevent contact-to-contact interactions between particles within the same order parameter. The advantage of placing multiple particles into the same order parameter is that this reduces the computational time by a factor equal to the average number of particles per order parameter. For example, placing 10 particles per order parameter reduces the computational time by approximately 10-fold. Therefore, the choice of how many particles are placed in each order parameter is a balance between preventing unwanted interactions while decreasing computational effort.

Based on experience, n was chosen to be 6 for three-dimensional simulations, resulting in 864 initial particles. All particles were distributed over 86 order parameters, with an average of 10 particles per order parameter. This means that a maximum of 86 iterations had to be calculated for a single time step instead of 864. The particles were generated with a large

spacing within the same order parameter to avoid unwanted interactions after slight coarsening. In the case of two-dimensional simulations, *n* was increased to 10 to have 100 initial particles in order to observe coarsening over a larger number of particles. Due to the short computational times of two-dimensional simulations, 100 order parameters were used, i.e., each particle was placed in its own order parameter.

To initiate coarsening in the phase-field simulation, irregularities in the initial particle size, shape, or position had to be introduced, as will be explained below. Figure 3.32 illustrates the process of constructing the initial condition for the two- and three-dimensional simulations.

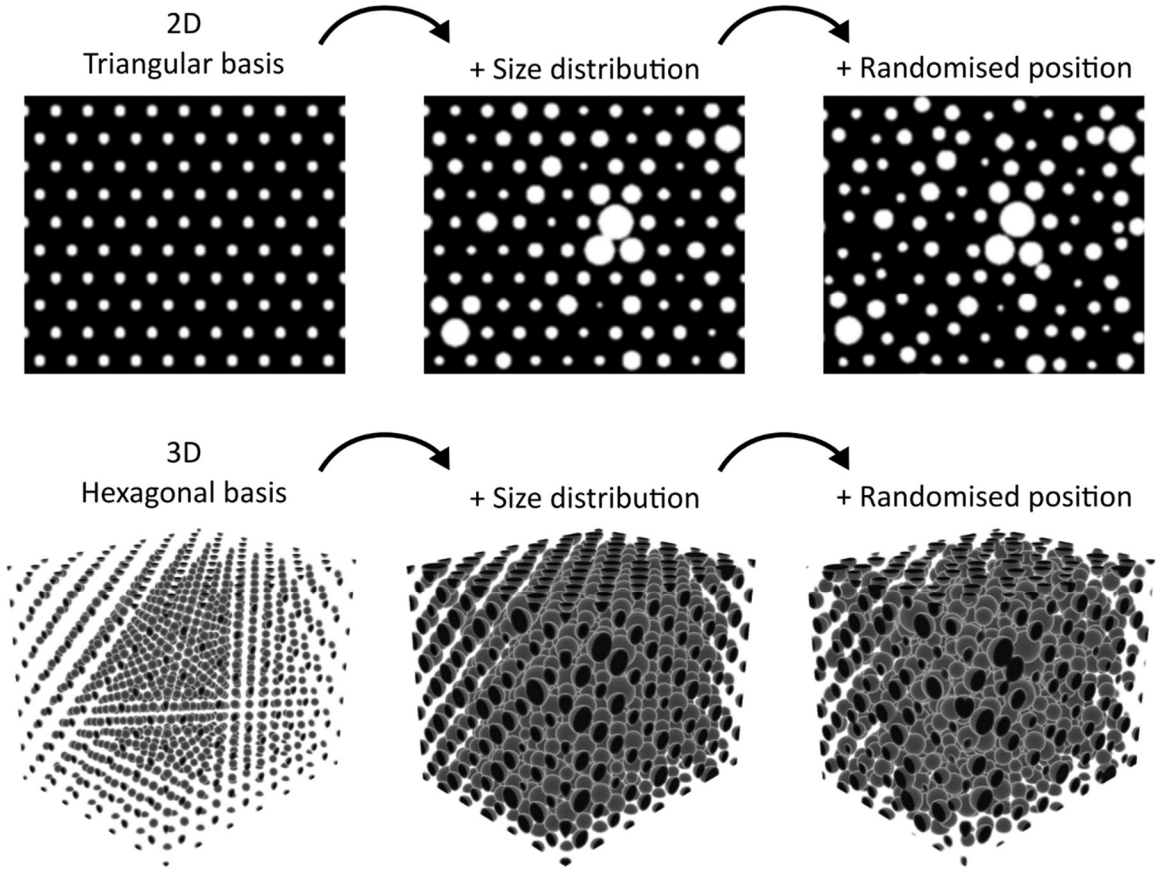

Figure 3.32: Generation of the initial conditions with a triangular base structure for two-dimensional simulations (upper row) and a hexagonal base structure for three-dimensional simulations (lower row).

A system with equidistant particles of similar size would not coarsen because the interfacial energy or curvature of all particle surfaces would be identical, thus lacking a driving force for change. Introducing irregularities leads to deviations from ideal packing, affecting the expected area and volume fractions. These deviations were, however, are of no consequence

as the natural packing fractions of triangular and hexagonal close-packings differed from the calculated fractions. This means that a separate adjustment of the area and volume fractions regardless of initial irregularities needed to be performed anyway. To introduce irregularity, the particle size was first changed from the densest packing, where adjacent particles are in contact, to a size distribution. A slight randomisation of particle positioning was then introduced, moderately varying the distances between particles while maintaining the basic triangular or hexagonal positioning.

The choice of *Nx*, *Ny* and *Nz* is based on the computational effort, as the grid size increases exponentially as shown in Figure 3.31. On the other hand, the distances between two grid points *dx*, *dy* and *dz* in the phase field simulations can be chosen more flexibly as they do not affect the computational effort. For the sake of simplicity, only *dx* will be referred to as the distance between two grid points, as the same value is usually used for *dx*, *dy* and *dz* in a simulation. Increasing *dx* will result in a larger physical domain of the simulation as the actual edge length of the simulation is calculated using $Nx \cdot dx$. However, setting *dx* to a high value may result in interfaces being covered by an insufficient number of grid points. This might lead to grid effects, where the angle of an interface affects its interfacial energy, causing numerical problems during the simulation. An example of this is shown in Figure 3.33.

An increase in the distance between grid points *dx* was accompanied by deformation of the particles when they were tilted (*dx* = 1.2) or even loss of curvature when *dx* became too large (*dx* = 1.5). As *dx* increased, so did the physical simulation domain, but the interfaces also became narrower and at a critical point it was no longer possible to accurately represent inclinations at the interfaces. The choice of *dx* was therefore a trade-off, as lower *dx* required higher *Nx* to capture the same physical space, while higher *dx* reduced accuracy and even led to errors. After careful consideration, a value of *dx* = 0.9 was chosen for all subsequent simulations, as this provided the largest physical domain size without noticeable grid effects. Additional tests were carried out to verify the phase-field simulation implementation and parameters. These tests included verifying the correct representation of the Gibbs-Thomson effect and ensuring that the interfacial energy was independent of the energy barrier coefficient. The results of the other tests to ensure the stability of the simulation are presented in Appendix A.

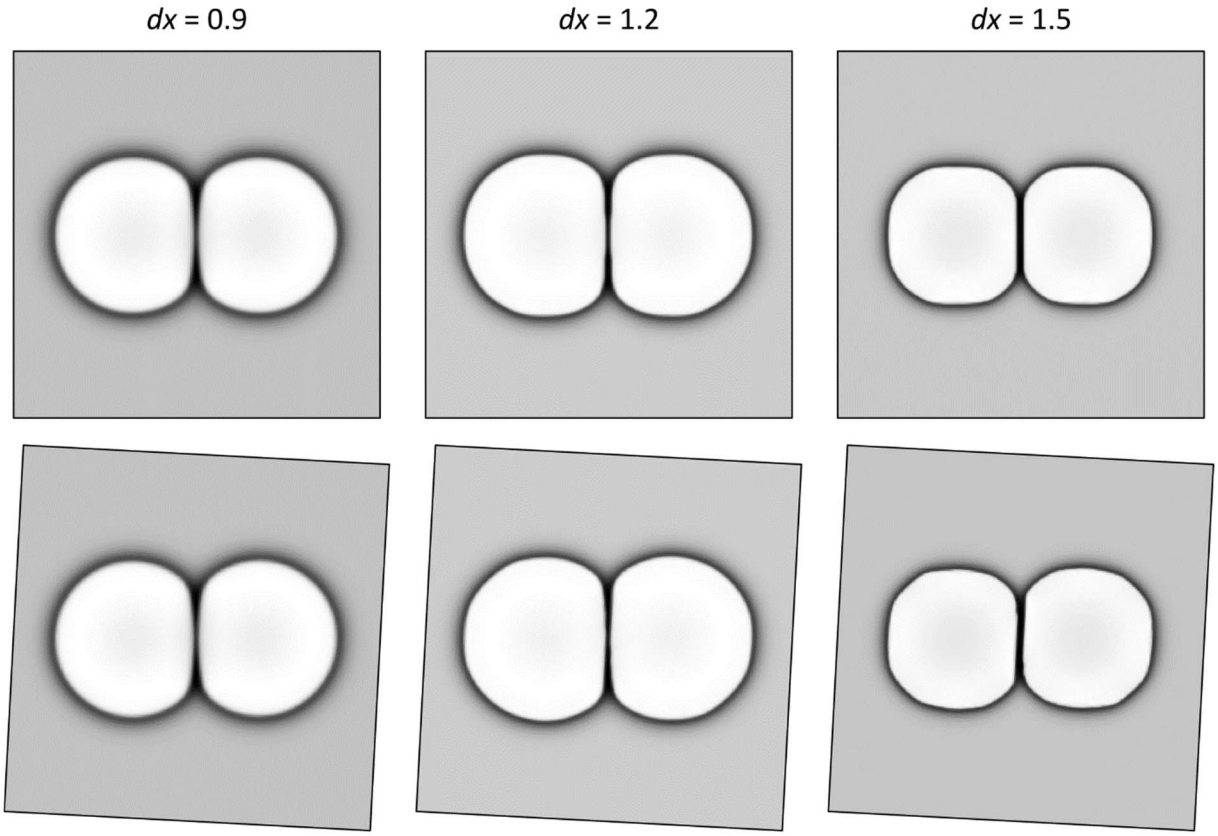

Figure 3.33: Grid effect in a two-dimensional phase-field simulation with two particles horizontally aligned (upper row) and slightly tilted (lower row). The tilted simulations are rotated to visualise the difference compared to the horizontally aligned simulations.

In the next step, the spatial discretisation was dimensionalised to give physical meaning to the space in the simulation domain. A conversion factor α was introduced to convert the distance between two grid points into a physical length. For example, a conversion factor of 1 µm/gp would imply that for Nx = 240 gp the x-coordinate corresponds to 240 µm. The method for deriving α will be explained in the following.

In this work, Nx = 240 gp and N_p = 864 were selected due to feasibility and computational constraints. Under this configuration, the particles reach an average size (defined here as the sphere equivalent radius) of 14.1 gp ± 1.7 gp when occupying the space in the simulation domain with volume fractions of the particulate phase of 0.915. This value represents the average ice crystal volume fraction of maximum freeze-concentrated 10 % (w/w) sucrose and trehalose solutions, as previously determined in Chapter 3.2.2.2.2. In Chapter 1.5, published data on pore sizes in non-annealed samples were presented. These pore sizes were the product of conventional freezing and drying and were converted to circle equivalent radii of

10.0 µm to 30.0 µm [83], 12.5 µm to 25.0 µm [98], and 11.9 µm ± 5.6 µm [71]. A wide range of pore sizes can be observed within the individual publications, which can be attributed to various factors such as a heterogeneous distribution of pore sizes, differences in pore sizes depending on the axial position in the vial [98], and measurement uncertainties associated with the methods used. Unfortunately, this means that there is no uniform value for experimentally determined pore sizes that can be used as a starting point for the phase-field simulations. Therefore, a range of initial pore sizes has also been considered in this work.

Due to the microscopic scale of the simulation domain, simulating a wide variety of initial particle sizes within a single simulation is impractical. Therefore, separate simulations were run for different initial particle sizes at the start of annealing. At this point, two setup options were considered:

- **Adapting the grid size:** The first option was to derive the conversion factor α and adjust *Nx* (and consequently *Ny* and *Nz*) for each initial particle size. However, this approach could result in a simulation domain that is either excessively large or so small that the interfacial width would become limiting, i.e., most of the simulation domain would be occupied by interface alone if *Nx* becomes too small as the interfacial width is more or less fixed.
- **Using different conversion factors:** The alternative was to vary the initial conditions using different conversion factors without altering the three-dimensional simulation domain. This meant maintaining the same number of initial particles and grid points across simulations but adjusting their physical meaning through the conversion factor.

In this work, the second option was chosen in order to avoid potential excessive computational times during the execution of the simulation. The conversion factor was defined as:

$$\alpha = \frac{r_{exp}}{r_{sim}}, \qquad \text{(Eq. 20)}$$

where r_{exp} is the experimentally determined circle equivalent radius, and r_{sim} is the sphere equivalent radius from three-dimensional simulations.

Three different initial particle sizes of 10.0 µm, 12.5 µm, and 15.0 µm were selected, based on the experimental data, and conversion factors were calculated to align the average particle

size in the three-dimensional simulation domain (14.1 gp ± 1.7 gp) with these physical sizes. For example, the conversion factor was calculated that would translate the initial physical particle size of 10.0 µm to the simulation particle size of 14.1 gp, in this case α = 0.68 µm/gp.

These conversion factors were then used to calculate the base grid size for two-dimensional phase-field simulations, ensuring alignment with FDM experimental data. For a conversion factor of α = 0.68 µm/gp, the particle size at the beginning of the simulation should be 9.2 gp. This is based on the experimental finding that particles had an average radius of 6.2 µm at the earliest quantifiable time point of 10 minutes after annealing began. In order to place 100 particles in the simulation domain, each with an average radius of 9.2 gp, the base grid size was determined to be Nx = 197.

In summary, this means that the conversion factors were used to determine the size of the two-dimensional simulation domains that could representatively describe 100 particles from FDM experiments. However, the various conversion factors themselves were previously calculated by comparing the established three-dimensional phase-field simulation and literature data on ice crystal sizes/pore sizes. This strategy allowed for adaptations only in the two-dimensional simulations, while the length scales of the more resource-intensive three-dimensional simulations were simply adjusted by the corresponding conversion factors. A summary of all data required to calculate the conversion factors and Nx for two-dimensional simulations is provided in Table 3.5.

Table 3.5: Determination of conversion factors (α) and base grid size for two-dimensional simulations (Nx_{2D}) for the experimentally determined circle equivalent radius of particles from freeze-drying microscopy after 10 minutes of annealing at -6 °C (r_{exp}), the initial sphere equivalent radius of particles in three-dimensional ($r_{sim,3D}$), and the initial circle equivalent radius for two-dimensional simulations ($r_{sim,2D}$).

r_{exp} [µm]	$r_{sim,3D}$ [µm]	$r_{sim,2D}$ [gp]	α [µm/gp]	Nx_{2D} [gp]
	10.0	9.2	0.68	197
6.2	12.5	7.4	0.85	157
	15.0	6.2	1.00	134

3.2.4 Calibration of input parameters for the phase-field simulations

In the previous chapter, initial conditions were generated that provided the basic structure of the particulate phase, including positioning and size distribution. However, the resulting area and volume fractions of the particulate phase were between 0.08 to 0.18 in two dimensions, depending on the grid size, and about 0.10 in three dimensions. These values did not align with the theoretical values discussed in Chapter 3.2.2.2.2. In the following chapter, the adjustment of the area and volume fractions to these theoretical values was carried out, and simulation parameters representative of the experimental recrystallisation rates from Chapter 3.2.2.2.3 were determined and implemented.

3.2.4.1 Adjustment of the area and volume fractions of the particulate phase

In the phase-field model, equilibrium compositions for the matrix phase (c_m^e) and the particle phase (c_p^e) can be set. These parameters dictate that the phases in the system adjust to their appropriate compositions regardless of initial conditions. If a phase starts supersaturated relative to its equilibrium composition, the area or volume fraction of the particulate and matrix phase will adjust until both phases reach their equilibrium states. For instance, if c_m^e = 0.1 is chosen and the composition in the matrix phase is initially set to 0.3, the composition of the matrix phase will gradually reduce to 0.1 over the course of the simulation. Consequently, the area or volume fraction of the particulate phase, representing the ice crystal phase in experiments, must increase to balance the reduction in the matrix phase composition. Essentially, the particles will grow until most of the grid points in the matrix phase achieve a compositional value of 0.1.

Conceptually, this adjustment is similar to changes in solubility during freezing in experimental setups. As the sample temperature decreases, the equilibrium with respect to solubility shifts, prompting a phase to precipitate and increasing the volume fraction of the precipitate phase. This mechanism is mirrored in the phase-field model, where particle growth is driven by initial supersaturation in the matrix phase. The initial matrix composition is defined as:

$$c_m^{initial} = c_m^e + c_m^{SS}, \qquad \text{(Eq. 21)}$$

where c_m^e is the equilibrium matrix composition, and c_m^{SS} is the supersaturation in the matrix phase.

The impact of supersaturation in the matrix phase on the phase-field simulation is depicted in Figure 3.34. When the initial matrix composition exceeds the equilibrium matrix composition, in addition to the adjustments of the area fraction, particle shapes efficiently adapt to utilise the available space within the matrix phase. As the particles grow and come into contact, the interfaces between adjacent particles inhibit further expansion, leading to particle deformation and filling of voids within the matrix phase.

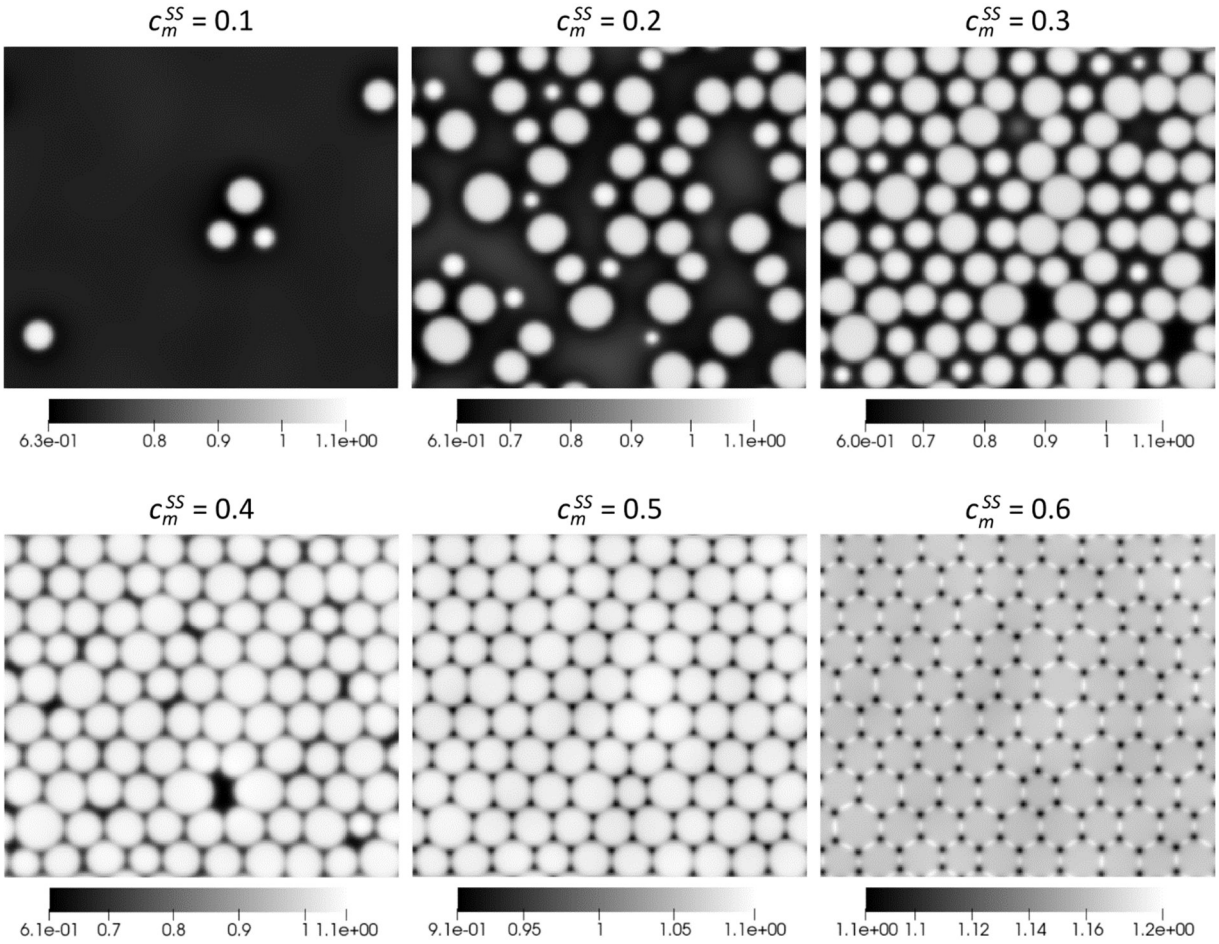

Figure 3.34: Adaptation of the compositional field to supersaturation of the matrix phase (c_m^{SS}) with c_m^e = 0.539 and *Nx* = 197 gp after 500 dt (time steps).

The adaptation of the area fraction to the initial supersaturation in this phase-field model can be classified into three types based on the degree of supersaturation. For low supersaturations up to 0.2, the number of particles decreased until the phases reached their respective equilibrium compositions. For a supersaturation between 0.3 and 0.5, the number of particles remained constant while the area fraction of the particles increased, and the particles deformed to occupy the available space in the matrix phase. At a supersaturation of

0.6, the particles became generally anisotropic, as evidenced by the formation of hexagonal shapes.

To quantify the volume fractions, all grid points where the values of the order parameters reached 1, indicating that the volume was occupied by the particulate phase, were summed. Specifically, a value of 1 in the order parameter means that the area or volume is occupied by ice crystals, whereas a value of 0 indicates the presence of the amorphous phase. It is important to understand that the order parameter indicates phase affiliation, while the composition parameter describes the mass fraction (of water) within a phase. When the system is allowed to reach equilibrium with respect to its compositional field, the spaces occupied by the matrix phase would have a composition equal to c_m^e and a value of 0 in the order parameter, while the grid points where particles are present would have a compositional value of c_p^e and a value of 1 in the order parameter.

Furthermore, to include the interface in this calculation, grid points with values greater than 0.1 were also considered part of the particulate phase. This threshold of 0.1 was chosen based on observations from the experimental setup, where a significant proportion of the visible interface consists of the ice phase, as illustrated previously in Figure 3.12. This scenario is particularly apparent when two ice crystals are in direct contact, forming an interface where the matrix phase is negligible. The areas or volume fractions of the particulate phase have been calculated using:

$$\varphi_p = \frac{N_{p,grid}}{N_{total,grid}}, \qquad \text{(Eq. 22)}$$

where $N_{p,grid}$ is the number of grid points occupied from the particulate phase, and $N_{total,grid}$ is the total number of grid points of the simulation domain.

Figure 3.35 shows an example of how the area fraction of the particulate phase in a two-dimensional simulation adjusts over time when the matrix phase is supersaturated in the beginning of the simulation. The area fractions of the particulate phase displayed different profiles depending on the degree of supersaturation. The initial particle area fraction was approximately 0.08 based on the number of particles and their size distribution from the initial conditions (see Chapter 3.2.3). In the absence of supersaturation, the area fraction gradually decreased until it reached zero. For a supersaturation of 0.1, the area fraction first increased

for a few iterations, then decreased and finally stabilised at a value lower than the initial value of 0.08. For a supersaturation of 0.2, the area fraction showed a slow increase but did not reach equilibrium even after a simulation time of t = 500 dt (time steps). However, at a supersaturation higher than 0.3, the area fraction of the particulate phase reached a plateau after approximately t = 100 dt. The height of the plateaus increased with supersaturation, indicating that greater supersaturation led to higher plateaus.

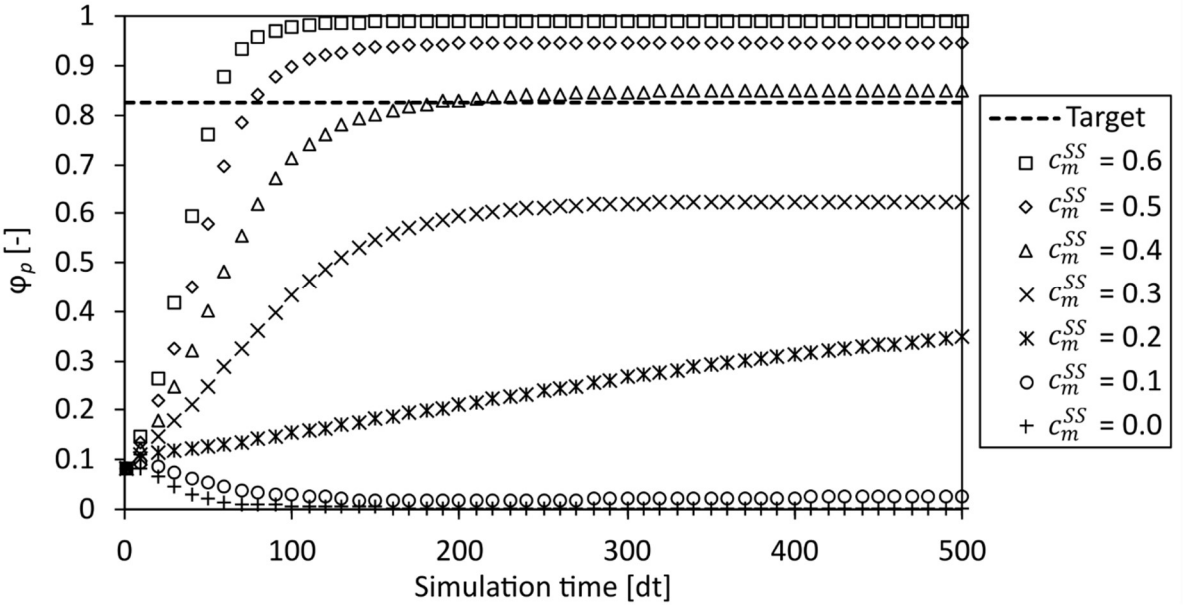

Figure 3.35: Adaptation of the particle area fraction (φ_p) in a two-dimensional phase-field simulation to the initial supersaturation of the matrix phase (c_m^{SS}) with c_m^e = 0.539 and *Nx* = 197 gp. The target area fraction of 0.828 was calculated from experimental data.

The behaviour at low supersaturations ($c_m^{SS} \leq 0.1$) can be explained by the fact that there is a critical particle size below which particles tend to dissolve completely, as detailed in Appendix A. The number of disappearing particles in this case is determined by the degree of supersaturation. As particles dissolve, the composition in the matrix phase increases, which in turn stabilises the remaining particles. However, if there is sufficient supersaturation at the beginning of the simulation, all particles in the system will be stabilised and the system will quickly reach equilibrium, as indicated by the plateaus in the area fractions.

For the initial conditions detailed in Table 3.5, simulations were conducted by incrementally increasing the initial supersaturation in the matrix phase. The objective was to determine the level of supersaturation necessary for the system to align with the physically correct volume fractions calculated in Chapter 3.2.2.2.2. Only simulations where the supersaturation was at

least 0.3 were included in the evaluation, as these reached equilibrium within a few iterations. The outcomes of the two-dimensional simulations are presented in Figure 3.36, while the results of the three-dimensional simulations are shown in Figure 3.37. To reiterate, area and volume fractions are used synonymously in this work because their values are identical within the simulation strategy employed.

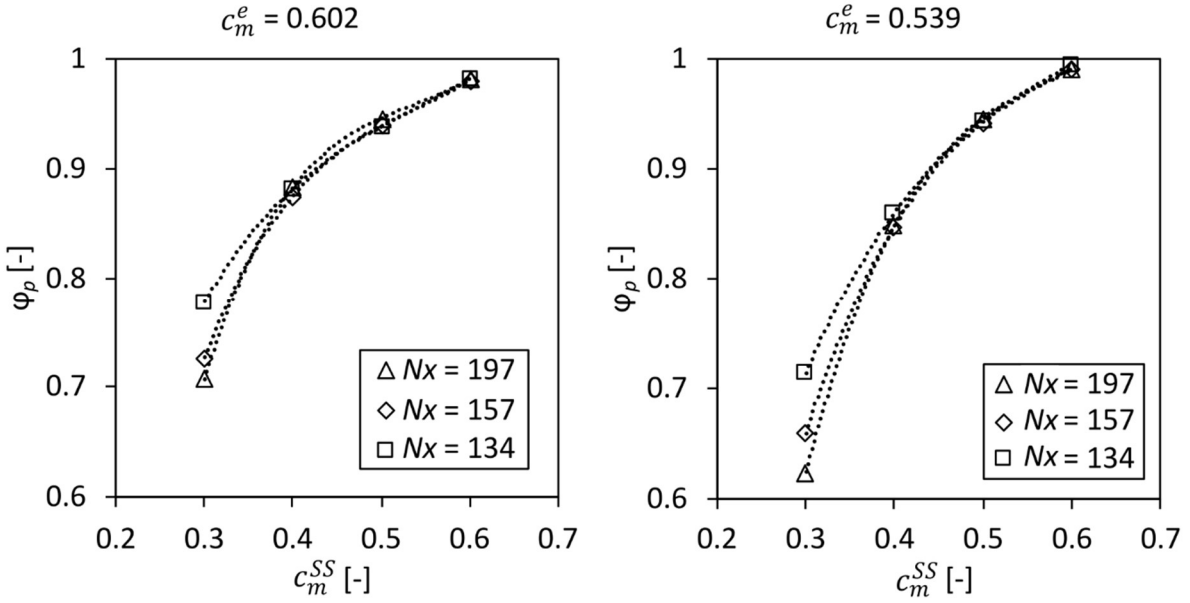

Figure 3.36: Impact of the initial supersaturation of the matrix phase (c_m^{SS}) on the area fraction of the particulate phase (φ_p) for two-dimensional phase-field simulations after t = 500 dt.

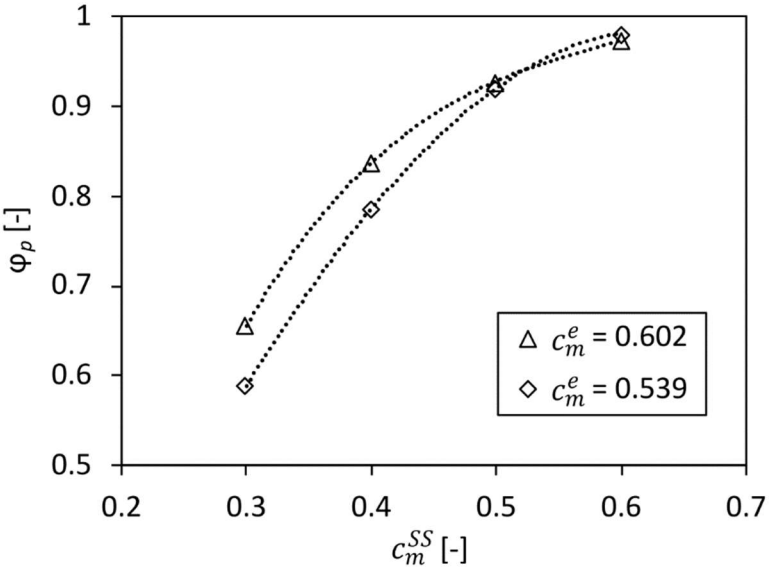

Figure 3.37: Impact of the initial supersaturation of the matrix phase (c_m^{SS}) on the volume fraction of the particulate phase (φ_p) for three-dimensional phase-field simulations after t = 500 dt.

The area fraction of the particulate phase increased with the initial supersaturation of the matrix phase, but this relationship was non-linear due to two effects. First, the matrix phase remained supersaturated at higher area fractions of the particulate phase, indicating that there was no more space for the particulate phase to grow and thus the matrix phase could not reach its equilibrium composition. This phenomenon is evident in the minimum values of the scales, which increase at higher initial supersaturations, shown in Figure 3.34. Second, the interfaces of the particles, mostly considered part of the particulate phase due to the threshold of 0.1 for the respective phase affiliation, contributed to this non-linearity. This means with more interfaces present more particle affiliation will be measured.

This impact of the interface on the area fraction of the particulate phase is also pronounced especially at lower supersaturations. The phase-field model maintains a constant interfacial width, regardless of the overall grid size. Consequently, a higher interfacial fraction is measured at lower grid sizes. This interfacial fraction then contributes excessively to the particle area fraction. However, this effect diminishes as the area fraction increases due to the decreasing ratio of interfacial area to particle area.

Analogous to the two-dimensional phase-field simulations, the volume fraction of the particulate phase in the three-dimensional simulations increased with supersaturation in a similar manner. In addition, a significant difference between the equilibrium compositions of the matrix phase was observed for supersaturations between 0.3 and 0.4. Specifically, the simulation with c_m^e = 0.602 required less supersaturation to achieve higher particle volume fractions. This can be explained by the fact that the interface also adopts $c_m^{initial}$ as its minimum value at the beginning of the simulation, and as supersaturation increases the values of the composition at the interface, the overall composition of the simulation domain increases, resulting in an increase in the volume fraction of the particulate phase.

As a next step, polynomials were calculated to capture the relationship between the initial supersaturation of the matrix phase and the area fraction for two-dimensional simulations and the volume fraction for three-dimensional simulations. The resulting polynomials for all two-dimensional and three-dimensional simulation conditions are listed in Table 3.6.

Table 3.6: Parameters for the calibration of the two-dimensional and three-dimensional phase-field model. The polynomial function for the initial supersaturation of the matrix phase (c_m^{SS}) was determined dependent on the area and volume fraction of the particulate phase (φ_p) and the base grid size of the simulation domain (*Nx*).

φ_p [-]	Dimensions [-]	*Nx* [gp]	Polynomial function	R^2 [-]	c_m^{SS} [-]
0.793	2D	197	$y = 14.133x^3 - 22.555x^2 + 12.313x - 1.3377$	1	0.338
		157	$y = 9.9716x^3 - 16.137x^2 + 9.0861x - 0.8157$	1	0.336
		134	$y = 5.4224x^3 - 8.8472x^2 + 5.226x - 0.1402$	1	0.313
	3D	240	$y = 7.5809x^3 - 13.627x^2 + 8.5475x - 0.8864$	1	0.369
0.828	2D	197	$y = 12.225x^3 - 21.028x^2 + 12.45x - 1.549$	1	0.386
		157	$y = 8.1264x^3 - 14.481x^2 + 9.0219x - 0.9637$	1	0.385
		134	$y = 5.073x^3 - 9.2468x^2 + 6.0656x - 0.4106$	1	0.372
	3D	240	$y = -1.7858x^3 - 0.9729x^2 + 3.3107x - 0.2685$	1	0.426

3.2.4.2 Coarsening parameters for the two-dimensional phase-field model

In the following, the simulation parameters for the two-dimensional phase-field simulations were determined which correspond to the experimental recrystallisation rates from Chapter 3.2.2.2.3. The objective was to adjust the mobility coefficient *M* and relaxation coefficient *L* simultaneously to match the temporal evolution of particle sizes between experiments and simulations. An example of coarsening in a two-dimensional phase-field simulation is depicted in Figure 3.38.

At the start of the simulation, the area fraction of the particulate phase increased rapidly until it plateaued at t_{sim} = 300 dt, indicating that the phases had reached their respective equilibrium compositions. The height of the plateau was adjusted by the initial supersaturation of the matrix phase as discussed in Chapter 3.2.4.1. In order to reduce the total number of particles in the system, complete dissolution of individual particles was required. However, at the start of the simulation the supersaturation of the matrix phase stabilised the small particles until the equilibrium compositions were reached. Therefore, as

long as the volume flux into small particles due to supersaturation was greater than that out of them due to Ostwald ripening, the number of ice crystals did not change. After equilibrium compositions were reached, the standard deviation of the average particle area steadily increased, indicating a broadening of the particle size distribution. Consequently, some particles fell below the critical particle size and dissolved, leading to an increase in local composition within the matrix phase and slight supersaturation. In response, neighbouring particles began to grow to reduce the supersaturation.

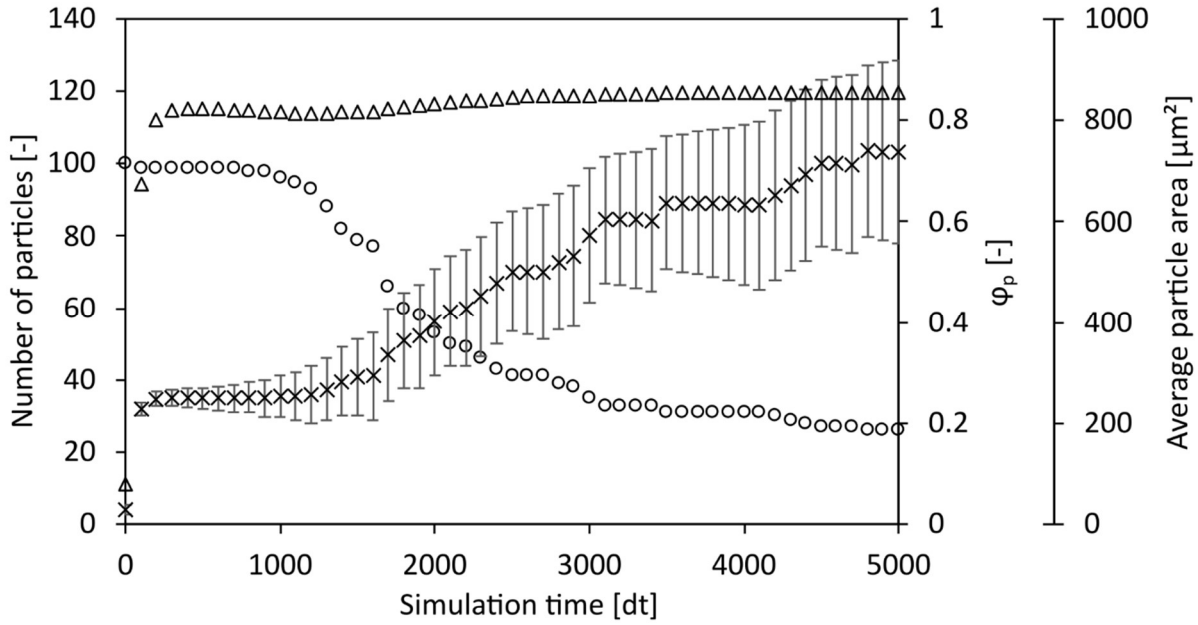

Figure 3.38: Temporal evolution of number of particles (○), area fraction of the particulate phase φ_p (Δ), and the average particle area (x) with standard deviation (error bars) in a two-dimensional phase-field simulation with *M* = 1, *L* = 1, c_m^e = 0.539, and *Nx* = 197 gp.

After a lag phase of t_{sim} = 1000 dt, the particle number started to decrease with a hyperbolic curve profile. Experimental data from freeze-drying microscopy do not show such a lag phase due to the presence of smaller particles at the time of observation (t_a = 10 min), which immediately fall below the critical radius and dissolve when the sample temperature is increased. This in turn immediately reduces the number of ice crystals from the start of the observation. From t_{sim} = 3000 dt, the decrease in the number of particles slowed down and approached an apparent plateau. The mean particle area and its standard deviation increased steadily from t_{sim} = 1000 dt, indicating coarsening. In addition, based on the Gibbs-Thomson effect (see Appendix A), a slight increase in the area fraction of the particulate phase was observed. The simulation results are visualised in Figure 3.39.

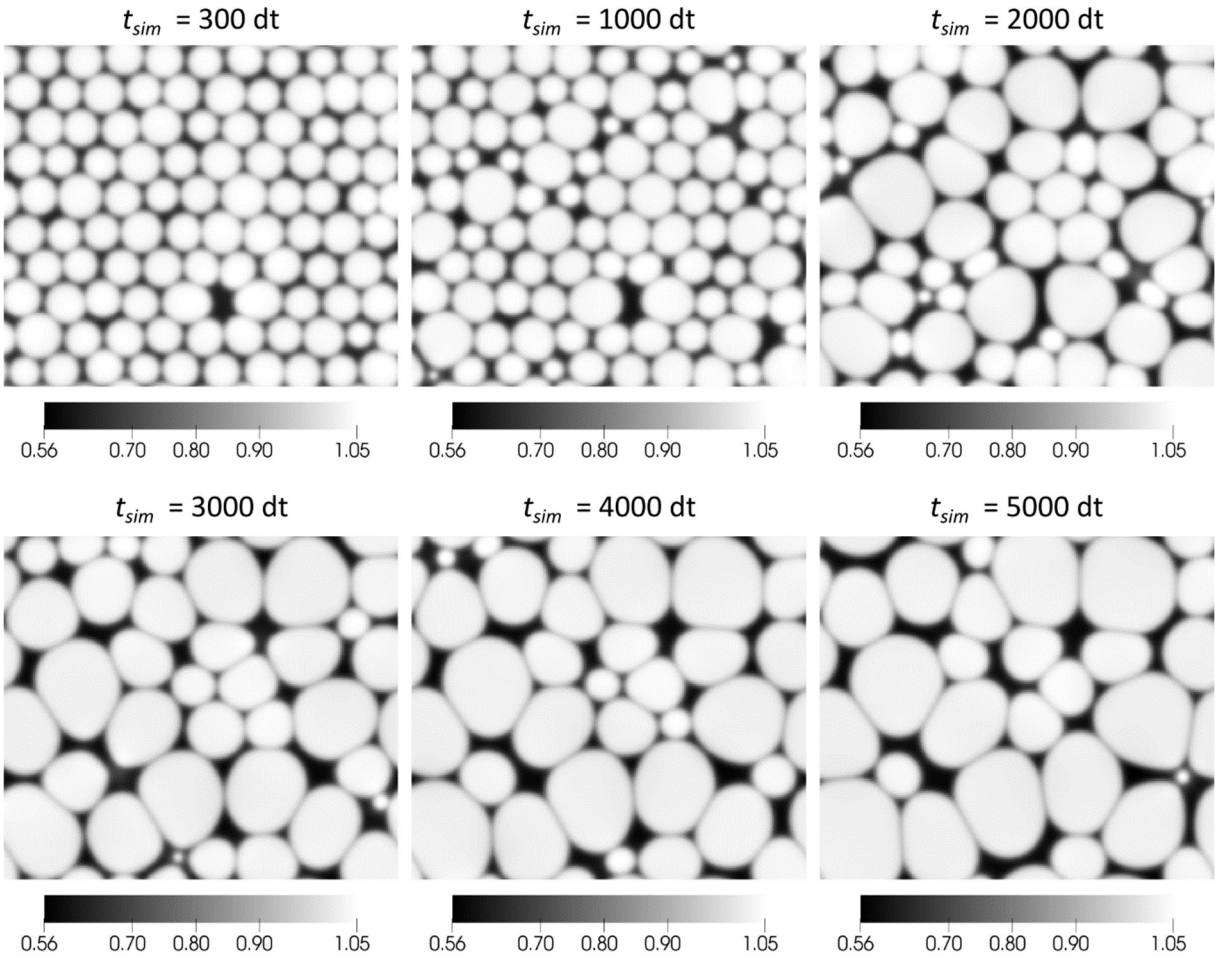

Figure 3.39: Visualisation of the composition field in a two-dimensional phase-field simulation with M = 1, L = 1, c_m^e = 0.539, and Nx = 197 gp.

The simulation results were visualised starting from t_{sim} = 300 dt, when the matrix phase reached its equilibrium composition. Between t_{sim} = 300 dt and t_{sim} = 1000 dt, the particulate phase underwent a redistribution resulting in a broader particle size distribution with the presence of both smaller and larger particles. From t_{sim} = 1000 dt to t_{sim} = 5000 dt, the number of particles visibly decreased, resulting in a coarsening of the particulate phase.

The next step was to assign physical meaning to the temporal discretisation of the simulation. This means that the time between two iterations in the simulation (*dt*) had to be defined in SI units. However, *dt* itself is a parameter used to ensure the stability of the simulation and to minimise inaccuracies and errors. If *dt* is set too high, the simulation may not be able to capture the temporal evolution correctly as excessive change occurs between iterations. If *dt* is set too low, more iterations will have to be calculated to simulate the same phenomenon, increasing computational time. For this work, a *dt* of 0.05 has proven optimal, as higher values

led to crashes and lower values to prolonged simulation times. The temporal scale, i.e., what each simulation iteration means in physical time, was then adjusted based on the coarsening profile in Figure 3.38, as will be explained in the following.

For M = 1 and L = 1, the estimated lag phase lasted about 1000 iterations and the number of particles remained relatively constant after 4000 iterations. In this work, M and L were chosen while the temporal conversion factor τ was determined. Technically, the temporal conversion factor could have been chosen first and then the appropriate M and L determined. Mathematically, the results would have been identical. As the experimental data covered 360 minutes of annealing and the actual coarsening occurred within simulations with M = 1 and L = 1 for about 3000 iterations, each simulation iteration was set to represent 0.1 minutes or 6 seconds. The temporal conversion factor was calculated with:

$$\tau = \frac{6s}{dt}, \qquad \text{(Eq. 23)}$$

and resulted in τ = 120 s for all simulations.

As previously mentioned, the recrystallisation rate in the phase-field simulations was manipulated by adjusting the values for M and L simultaneously. This approach allowed the recrystallisation rate to be modified while keeping the interfacial energy of the system constant. Altering the ratio of M and L would have affected the contributions of diffusion, dissolution and redeposition to the overall coarsening, which is outside the scope of this work. In order to investigate the relationship between M, L and the recrystallisation rate (including the temporal conversion factor), various simulations were carried out with incrementally changing M and L. The results are illustrated in Figure 3.40. It should be noted that the simulation data was not used until coarsening started to occur. This means that the starting point varied between simulations as higher values of M and L would result in a shorter lag phase.

Similar to the experimental data, the simulation results displayed a linear increase in the cube of the circle equivalent diameter as coarsening commenced. The curves may appear almost stepwise. However, this is a misconception. This appearance can be explained by the fact that when particles dissolve from one iteration to the next, the total number of particles changes, leading to erratic fluctuations in the calculated average cube of circle equivalent radius.

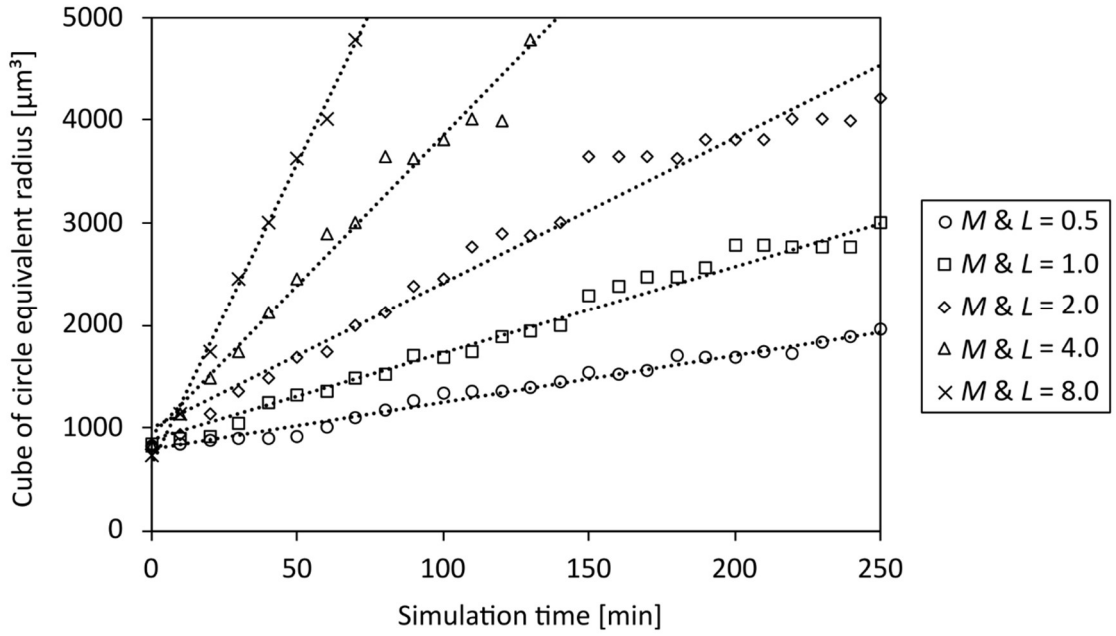

Figure 3.40: Impact of simulation parameters *M* and *L* on the coarsening behaviour of a two-dimensional phase-field simulation with c_m^e = 0.539 and *Nx* = 197 gp.

The slope of the regression increased with higher settings of *M* and *L*, indicating the successful increase of the recrystallisation phenomenon dependent on *M* and *L.* Following these observations, the conditions specified in Table 3.6 were used to conduct two-dimensional phase-field simulations. These simulations were aimed at determining recrystallisation rates based on the slopes of the cube of the circle equivalent radii. The results of these simulations are depicted in Figure 3.41.

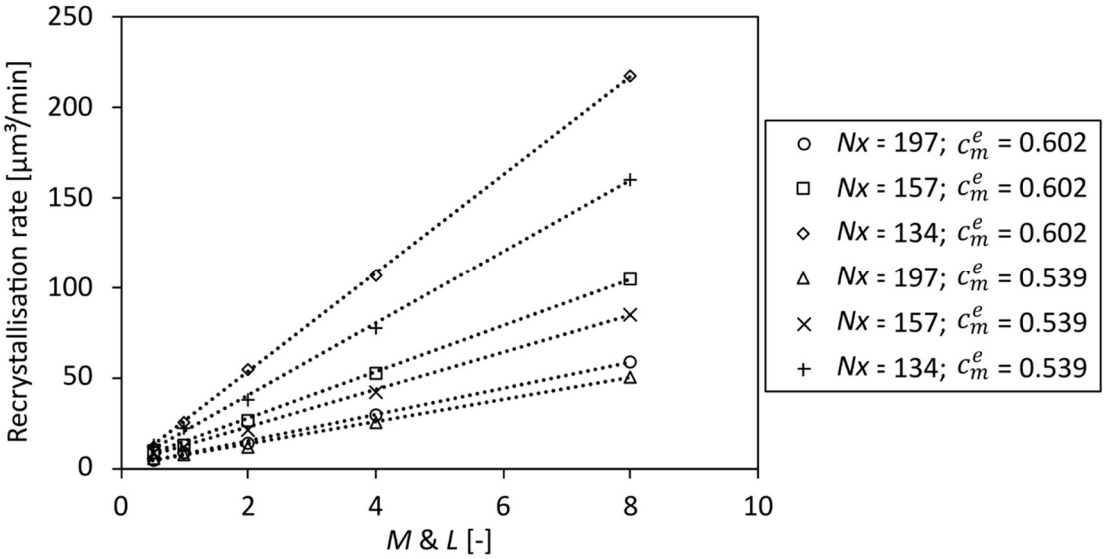

Figure 3.41: Impact of *M* and *L* on the recrystallisation rate in a two-dimensional phase-field simulation.

The recrystallisation rate exhibited a positive linear correlation with the simulation parameters *M* and *L*, as expected. This is because an increase in both *M* and *L* simultaneously equates mathematically to an increase in *dt*. This relationship can be simplified as follows In the simulations, it does not matter whether a process takes, for example, 10 minutes with a data point collected every minute, or if the process runs twice as fast with a data point collected every half minute. Ultimately, the amount of work done, and the output data remain identical.

It was also observed that the recrystallisation rate scales faster with *M* and *L* as the grid size decreases. The effect of *M* and *L* on the recrystallisation rate also increased with the equilibrium concentration of the matrix phase. Using the regression lines from Figure 3.41, the simulation parameters *M* and *L* corresponding to the experimental recrystallisation rates were determined and are shown in Table 3.7.

Table 3.7: Determination of simulation parameters mobility coefficient *M* and relaxation coefficient *L* dependent on experimental recrystallisation rate and base grid size (*Nx*).

Recrystallisation rate [µm³/min]	*Nx* [gp]	Polynomial function	R^2 [-]	*M* & *L* [-]
56.80	197	y = 7.2702x + 0.5562	0.9992	7.74
	157	y = 12.822x + 1.4688	0.9994	4.32
	134	y = 27.29x – 1.0529	0.9999	2.12
26.13	197	y = 6.0147x + 1.5804	0.9978	4.08
	157	y = 10.318x + 1.9271	0.9988	2.35
	134	y = 19.78x + 1.0279	0.9988	1.27

Next, the simulation parameters *M* and *L*, as determined in this chapter, were applied to three-dimensional phase-field simulations. These simulations aimed to predict the coarsening behaviour of frozen 10 % (w/w) sucrose and trehalose solutions at annealing temperatures of -4 °C and -6 °C with initial particle radii of 10 µm, 12.5 µm, and 15 µm.

3.2.5 Advancement of the phase-field simulation to three-dimensional

For the implementation of the three-dimensional phase-field simulation, all fields (e.g., composition, order parameters, etc.) were extended to include the z-coordinate. Spatial operators (∇) used for calculating gradients and divergences of these fields were accordingly modified to accommodate the additional dimension. The particle position and size distributions, as established in Chapter 3.2.3, served as the initial conditions. Volume fractions were also adjusted based on the initial supersaturations of the matrix phase, as discussed in Chapter 3.2.4.1. With the conversion factors previously determined, the following simulations are all dimensionalised in regard to space and time, i.e., volumes are expressed in µm³ and time in minutes. Figure 3.42 illustrates an example of the results from a three-dimensional phase-field simulation.

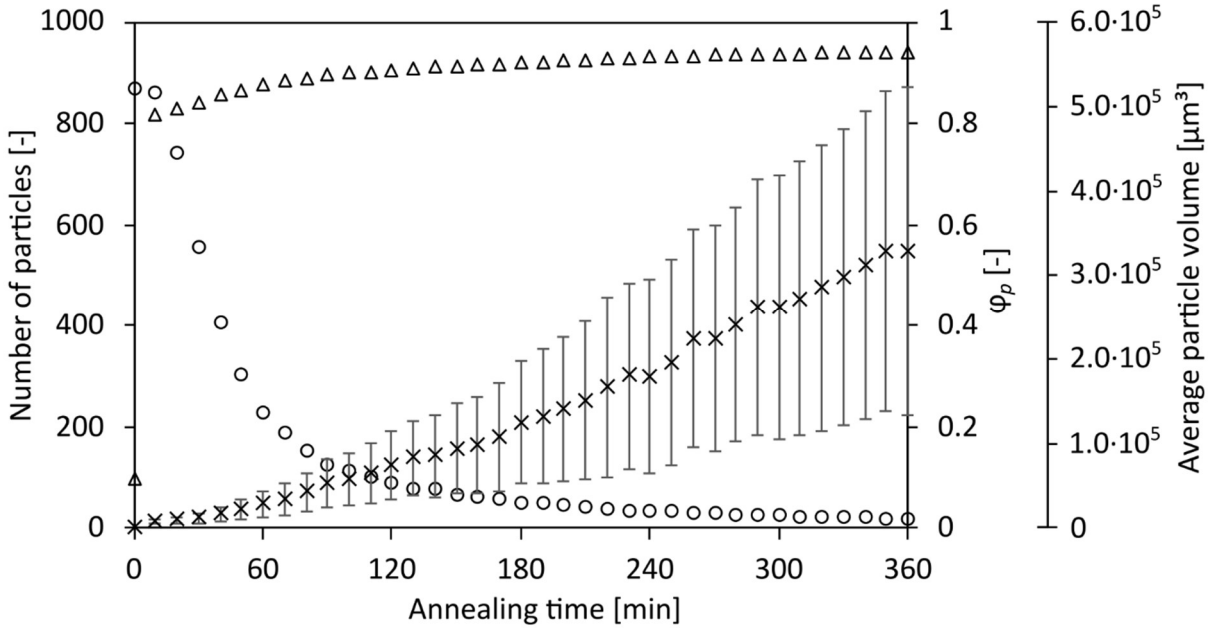

Figure 3.42: Temporal evolution of number of particles (○), volume fraction of particulate phase φ_p (Δ), and the average particle volume (x) with standard deviation (error bars) in the three-dimensional phase-field simulation with *M* = 2.35, *L* = 2.35, c_m^e = 0.539, and *Nx* = 240 gp.

During the annealing simulation, the average particle size continuously increased, and it did not reach a plateau even after t_{sim} = 360 min. Throughout the coarsening process, the standard deviation of the average particle size also increased, indicating an increasing degree of heterogeneity in particle sizes as annealing progressed. Similar to the two-dimensional simulations a lag phase was present, where the volume fraction of the particulate phase showed a rapid increase up to t_{sim} = 10 min while the number of particles remained relatively

constant. During this initial stage, the volume fraction of the particulate phase increased due to supersaturation in the matrix phase, causing all particles to grow until reaching the desired volume fractions determined experimentally in Chapter 3.2.2.2.2. A steady increase in the volume fraction of the particles was observed between t_{sim} = 10 minutes and t_{sim} = 120 minutes as the simulation progressed, particularly when the number of particles decreased rapidly. As with the two-dimensional simulations, this phenomenon is based on the Gibbs-Thomson effect and is related to the curvature of the particles, i.e., the smaller a particle, the greater its curvature and the greater the variation in composition within the particle. Therefore, the volume fraction of the particle increases with coarsening. A description of this phenomenon can be found in Appendix A.

The lag phase observed in the three-dimensional phase-field simulations was notably shorter compared to the two-dimensional simulations. This difference is primarily influenced by two factors. First, the addition of an extra plane of curvature in three dimensions accelerates coarsening, which effectively reduces the lag phase. Secondly, the critical particle size at which dissolution begins differs between two-dimensional and three-dimensional simulations. Specifically, the critical radius for dissolution was determined to be 6 grid points in two-dimensional simulations (representing the radius of a circle) and 7 grid points in three-dimensional simulations (representing the radius of a sphere), as detailed in Appendix A. Consequently, particles in three-dimensional simulations dissolve earlier and coarsen faster, resulting in a shortened lag phase.

The results were also visualised and are shown in Figure 3.43. The steady coarsening of the particulate phase was clearly evident from the three-dimensional visualisations, which also showed an increase in particle size heterogeneity. Moreover, the visualisations underscored that the simulation cannot continue indefinitely. Eventually, particles could grow large enough to span from one boundary to the opposite boundary. This poses a problem as periodic boundary conditions were employed in all simulations. Under these conditions, the left border of the simulation domain effectively continues from the right border, allowing the simulation domain to be conceptually stacked indefinitely from left to right, and similarly from bottom to top and front to back, while preserving the continuity of the internal microstructure.

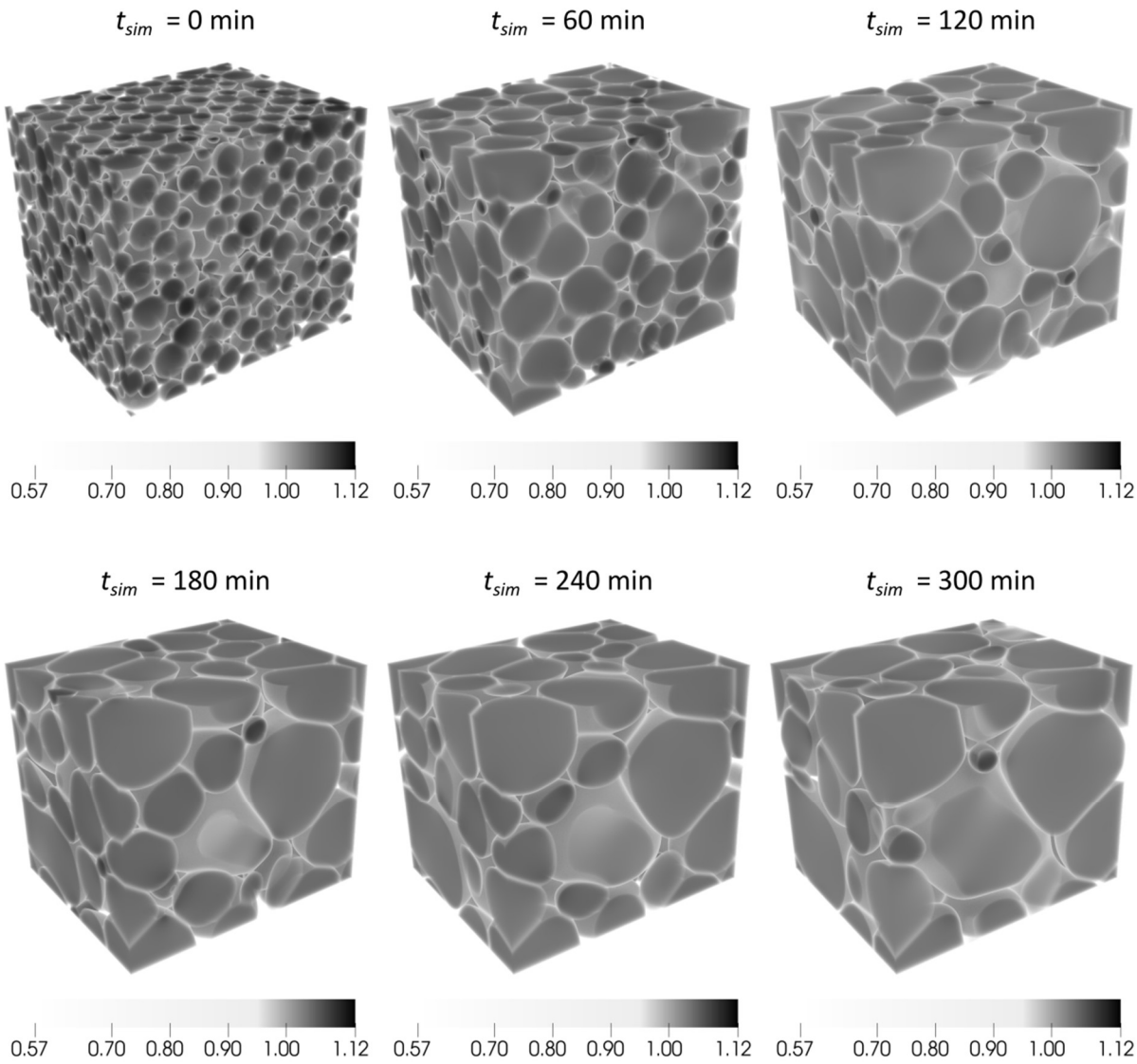

Figure 3.43: Visualisation of the composition field during coarsening in a three-dimensional phase-field simulation with *M* = 2.35, *L* = 2.35, c_m^e = 0.539, and *Nx* = 240 gp.

This also means that a particle growing from any boundary to the opposite side could potentially come into contact with itself, creating an unrealistic scenario if it becomes sufficiently large. This issue is illustrated in Figure 3.44. To address this, all subsequent evaluations were carefully monitored, and simulations were terminated if this issue arose, ensuring the integrity and realism of the simulation results.

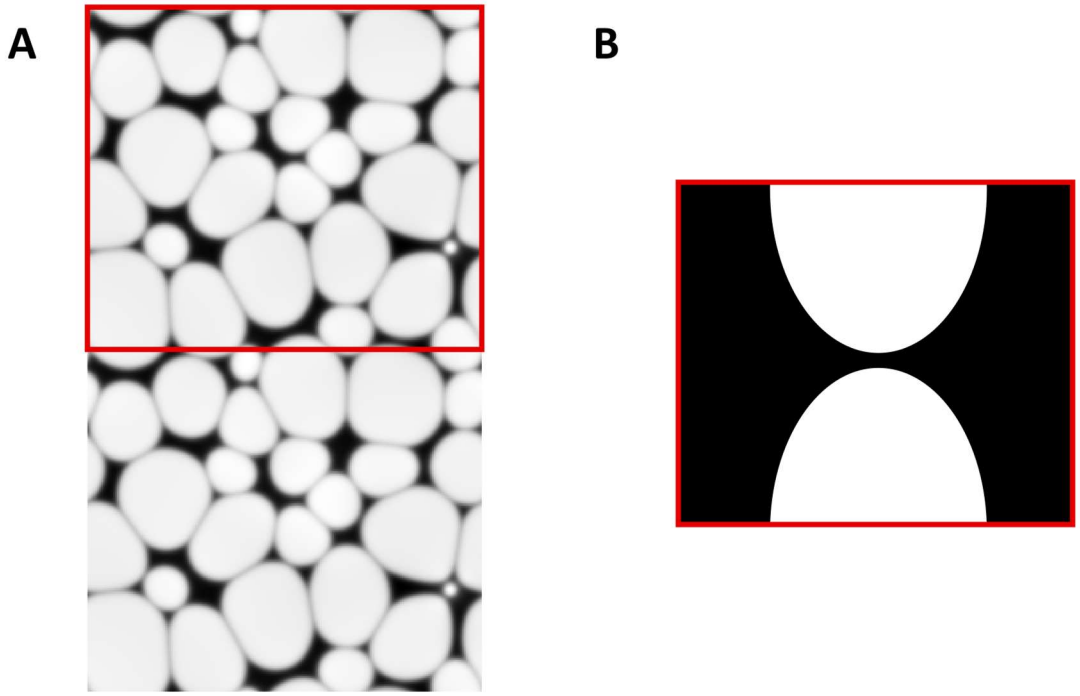

Figure 3.44: Illustration of the periodicity of the simulation domain and the associated problems. The original simulation domain (A, red square) can be replicated and placed at each border due to its periodic boundaries. However, if the particles become too large, there is a risk that a particle will come into contact with itself (B).

3.2.6 Final adjustment of particle volume fractions

In lyophilisation, the sample temperature must be reduced again after annealing to enable the matrix phase to reach its maximum freeze-concentrated state. This step prompts water molecules to precipitate into ice crystals, altering the water-solute ratio in the matrix phase, and consequently affecting its volume fraction in the lyophilisate. It is important to implement this in phase-field simulations to accurately model the particle sizes that correspond to the pores in the lyophilisate.

The adjustment of the volume fractions in the three-dimensional phase-field simulations was achieved by restarting the simulation after the desired annealing step, but with an adjusted matrix equilibrium composition. Elegantly, this is also what happens physically in a real solution. As the temperature decreases, the solubility of the water in the amorphous phase changes and so does its equilibrium concentration. Figure 3.45 shows how the particle volume fraction increases as a result of supersaturation until it reaches the target volume fraction of 0.913, as calculated in Chapter 3.2.2.2.2.

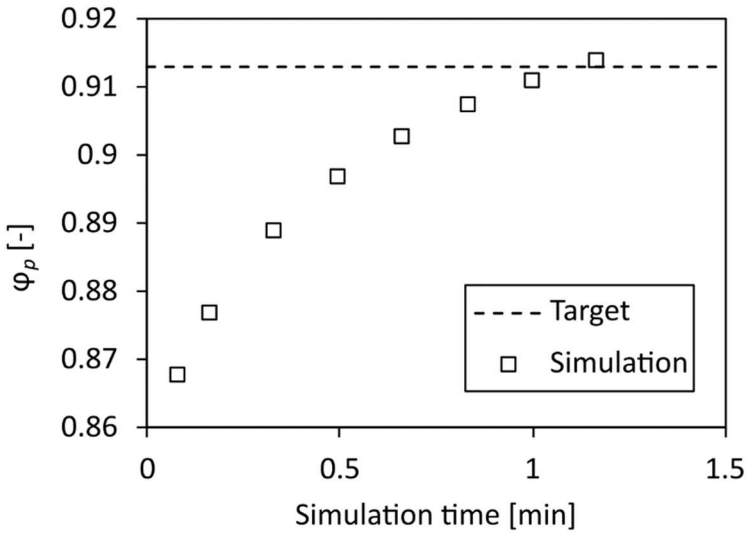

Figure 3.45: Adjustment of the particle volume fraction (φ_p) to the target fraction in the three-dimensional phase-field simulation.

The volume fraction adjustment is proceeding relatively quickly compared to the annealing process, typically requiring about 10 iterations within the simulation to reach the desired target volume fraction. The speed of this adjustment is influenced by the difference between the current matrix composition and the newly adjusted equilibrium matrix composition. This rapid adjustment has both advantages and disadvantages. On the positive side, this rapid adjustment ensures that the simulation completes in a few iterations and does not alter the microstructure, particularly in terms of particle count. However, the downside is that the precision of volume fraction adjustment is constrained by the resolution between simulation iterations. This limitation is evident in Figure 3.45, where the second last data point is below the target volume fraction, but the last one is slightly above.

In the simulations conducted for this work, efforts were made to maintain a constant number of particles throughout the volume fraction adjustment process. Given the minimal difference in the maximum freeze-concentrated states of sucrose ($\varphi_p = 0.913$) and trehalose ($\varphi_p = 0.917$), no distinction was made between these two disaccharides. Achieving such precise differentiation was considered impractical within the constraints of the phase-field model.

3.2.7 Morphological properties in the three-dimensional phase-field model

In the following, the morphological properties of the microstructure and their temporal evolution during annealing were extracted from the three-dimensional phase-field

simulations and subsequently analysed. However, the corresponding properties first had to be defined, as discussed below. These include the size distribution of the ice crystals, the conjunction areas between ice crystals, and the surface area of the matrix phase. In addition, the potential relevance and influence of each morphological property on the overall freeze-drying process were discussed.

3.2.7.1 Description of morphological properties in a porous microstructure

As explained in Chapter 1.4.3, the bulk water that has been separated by freeze-concentration sublimates during primary drying, thereby leaving voids in the lyophilisate, which are referred to as pores in the literature. Assuming that no change occurs in the matrix phase during the sublimation of the bulk water (e.g., micro collapse, shrinkage or cracking), it can be inferred that these voids in the lyophilisate are of a similar size and shape to the ice crystals in the previously frozen solution (see Figure 3.46). This is not entirely accurate, as desorption of water and consequent shrinkage occur to some extent during primary drying [93]. However, for the following considerations, it is assumed that desorption is mainly occurring during secondary drying, and therefore the microstructure remains constant throughout the sublimation of bulk water during primary drying.

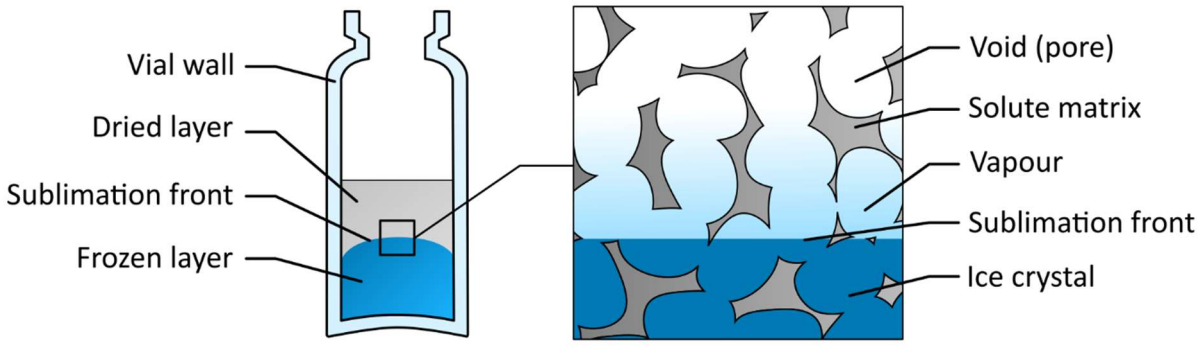

Figure 3.46: Formation of voids in a lyophilisate due to the sublimation of ice crystals during primary drying.

The sublimation rate, i.e., the rate at which frozen water can be effectively removed from samples, is related in the literature to pore size. A simple explanation for this is that larger pores facilitate greater mass flow, thereby enhancing the sublimation rate. However, the experimental determination of pore size is not straightforward, as described in Chapter 1.7. This is partly due to the fact that the definition of pore size in lyophilisation is not standardised. For example, sample preparation for SEM analysis produces a cross section through the

sample which randomly exposes the voids resulting from the removal of bulk water during sublimation. The measured diameter of such voids is highly dependent on the angle and position at which the void was exposed. Thus, each measurement does not determine the average pore size, but only a random length of a void in the lyophilisate. In addition, in most cases, fully dried samples are measured, where the microstructure may have already changed after drying due to shrinkage and cracking, further complicating the correct determination of pore sizes. With porosimetric methods, the basic shape of the pore (e.g. cylindrical or spherical) must be assumed before the pore size can be calculated, introducing additional uncertainty into the determination. For example, the commonly used Washburn equation in mercury intrusion porosimetry presupposes cylindrical pore shapes [157].

In order to be able to quantify the pores from the three-dimensional phase-field simulations, it must first be clarified how exactly a pore should be defined. In the work of Rouquerol et al. (1994), detailed recommendations for the characterisation of porous solids were presented. Figure 3.47 shows the classification of pores for further discussion.

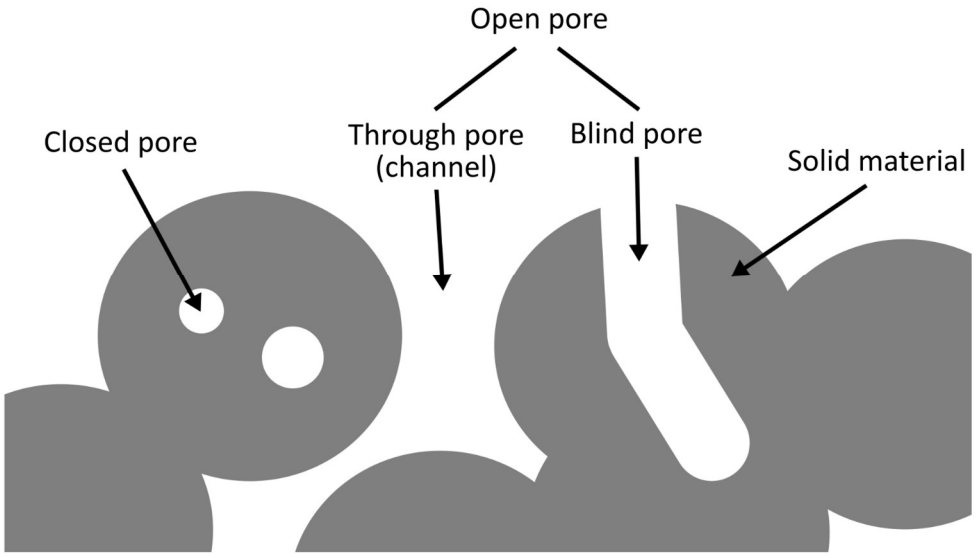

Figure 3.47: General pore categories in porous solids. Adapted from [159].

In general, pores in solids porous materials can be divided into two basic categories, namely open and closed pores. Closed pores are inclusions of voids in a solid and can affect the macroscopic properties of the bulk material, but do not permit processes such as fluid flow through the material. This is different with open pores, which are further divided into blind and through pores. Blind pores end within the material and thus create a dead end for fluid

flow, whereas through pores are channel-like cavities that permit fluid flow and affect it due to their morphological properties.

Although these textbook definitions are useful when describing a lyophilisate experimentally, making definitive statements about individual pores is challenging. Tracing a through pore completely is often not feasible because the observation domain, whether a field of view or simulation domain, is typically too small to capture the entire structure. Consequently, this thesis adopts a definition based on other published works, which is detailed in the following. For all subsequent discussions, a pore is defined as the void created when a single ice crystal sublimates. Hence, the terms ice crystal, particle, and pore are used interchangeably throughout this work. This approach is beneficial as it directly links the ice crystals in the frozen solution to the voids in the dry lyophilisate, and it allows for the quantification of individual void volumes, enabling the derivation of size distributions from simulations. This concept is illustrated in Figure 3.48 for both experiments and simulations.

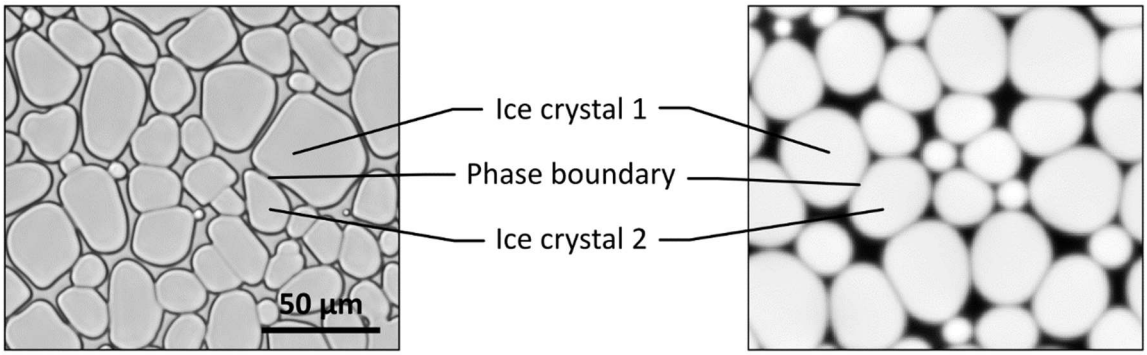

Figure 3.48: Definition of individual ice crystals and subsequent pores in this work for experiments (left) and phase-field simulations (right).

Individual ice crystals may be in direct contact with other ice crystals but are clearly separated by a phase boundary. This does not necessarily mean that there is a layer of matrix phase between the two particles in contact. Instead, the crystallographic orientation of the adjacent particles inhibits fusion/coalescence.

It is crucial to note that the sublimation rate during primary drying is most likely not simply related to a single morphological property such as pore size. It can be assumed that other microstructural properties of the lyophilisate such as tortuosity, porosity, percolation, specific surface area, pore connectivity and pore geometry have an influence on the sublimation rates. The approach of this work represents an initial step towards identifying and quantifying

morphological parameters that can be extracted from phase-field simulations, as well as describing their temporal evolution during annealing. The phase-field model employed is particularly well-suited for determining all properties that can be directly derived from the coarsened particles. First, the pore sizes, as previously defined, correspond to the sizes of the particles after refreezing in the simulation. The size distribution of these pores is the simplest parameter influencing the mass flow rate during sublimation. Secondly, the surface area of the matrix phase may play a role in the drying process, as water molecules interact with the surface of the matrix while migrating through the lyophilisate. In terms of sublimation rate, another potentially significant morphological property are the narrowest gaps in the lyophilisate, which may represent the bottlenecks of mass flow during sublimation. This concept is illustrated in Figure 3.49.

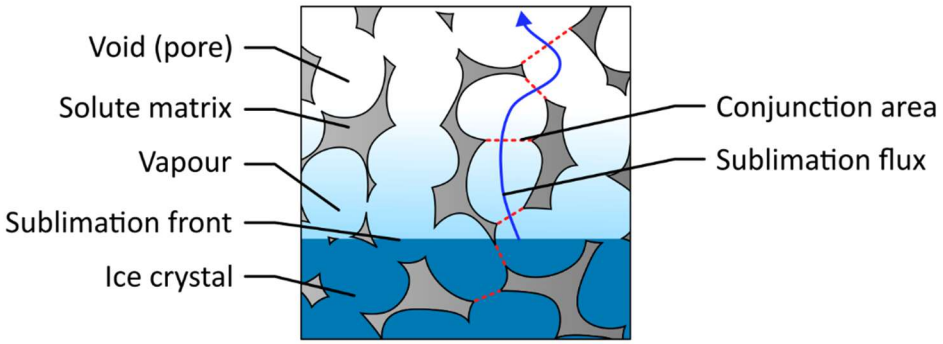

Figure 3.49: Potential bottle neck (red dotted line) of the vapour mass flow (blue line) during sublimation in a porous microstructure.

The narrowest gaps in the microstructure are the result of contact between adjacent particles and will be referred to in the following chapters as the conjunction area. In two-dimensional simulations, a conjunction area is represented by a length, while in three-dimensional simulations, it is represented by an area. While the conjunction area cannot be determined experimentally, the *in silico* determination of such a parameter can provide a detailed understanding of the mass flow and mass transfer resistance in a lyo-cake. Factors such as tortuosity, which are more complex to measure, have not been included in this work. However, it is important to acknowledge that such factors also hold significant relevance for future studies. Some examples will be discussed later in Chapter 4.

3.2.7.2 Ice crystal size distribution

As mentioned in the previous chapter, for the purposes of this work it is assumed that sublimation is the sole process during primary drying and therefore the pores formed are similar in size and shape to the preceding ice crystals. Consequently, the predictions of this model are valid for both ice crystals in the frozen solution and pores in the lyophilisate as long as no shrinkage has occurred. However, as the shape of the ice crystals is not clearly defined, as shown by the freeze-drying microscopy experiments, the diameter has not been used as a measure of size in this work. Instead, the volume of a particle was determined from the simulation, which more accurately captures the size of particles than its sphere equivalent diameter. The volume of a single particle (ice crystal, pore) is given by:

$$V_p = \alpha^3 \cdot \sum_{i=1}^{Nx} \sum_{j=1}^{Ny} \sum_{k=1}^{Nz} \eta_{ijk}\,, \qquad \text{(Eq. 24)}$$

where α is the conversion factor calculated in Chapter 3.2.3, and η_{ijk} is the order parameter containing a single particle from the three-dimensional phase-field simulation.

The first step involved determining the number of individual particles within each order parameter, a necessary measure due to previous efforts to conserve computational resources by placing several particles within one order parameter (see Chapter 3.2.3). Once the number of particles had been determined, the individual particles were separated and the number of grid points that a single particle occupied was counted. Using Equation 24, the size of the particles for each simulation was dimensionalised, with the results displayed in Figure 3.50.

The average size of the ice crystals gradually increased during the annealing simulation and was influenced by both the annealing temperature and the initial particle size. This relationship is logical as larger particles at the start will result in larger particles at the end of the annealing process. To reiterate, the number of particles at the start of each simulation is identical. The size of the particles is altered by the conversion factor α, which means that each grid point is converted to a different physical length for evaluation. This means that the simulations examine different volumes, although their grid sizes are identical. Consequently, these results demonstrate the importance of accurately estimating the initial particle size prior to annealing in shaping the predictions of the simulation.

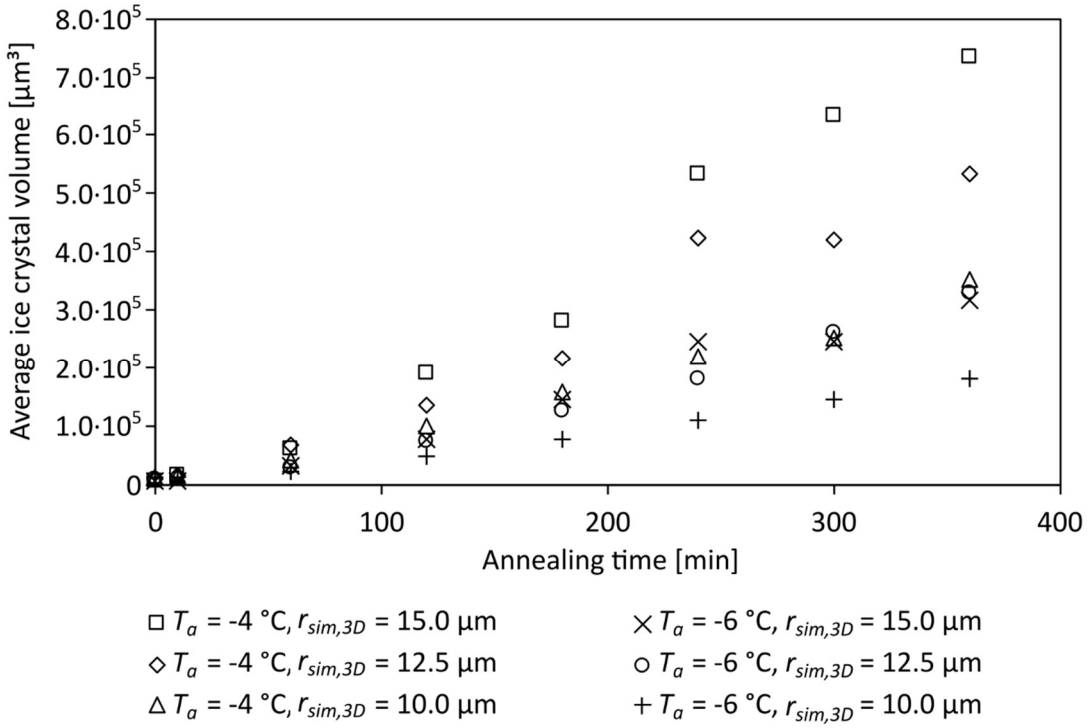

Figure 3.50: Temporal evolution of the average ice crystal size in the three-dimensional phase-field simulation with different initial particle sizes ($r_{sim,3D}$). The standard deviation was omitted for better clarity.

It should be noted that the standard deviation became very high over the course of the simulations and has therefore been omitted from the results for clarity. This phenomenon was observed previously in Figure 3.42 and can be explained by the fact that during coarsening, larger particles tend to continue to increase in size while the rest of the particles continue to shrink until they reach the critical particle radius and dissolve. Therefore, very large and very small particles exist at the same time, which broadens the particle size distribution and increases the heterogeneity in particle size. Notably, the individual data sets do not follow a perfect curve, but tend to "jump" between annealing times. This can be explained by the complete dissolution of particles during the process. This dissolution changes the total number of particles, leading to erratic shifts in the average particle size calculations.

Next, the sphere equivalent radius was calculated with:

$$r_m = \sqrt[3]{\frac{3 \cdot V_p}{4 \cdot \pi}}, \qquad \text{(Eq. 25)}$$

where V_p is the dimensionalised volume of an individual particle.

It must be mentioned that the particles in this simulation were not perfectly spherical, and therefore the sphere equivalent radius is just an approximation of the particle size. However, circle or sphere equivalent radii are commonly used in the literature regarding pore sizes in lyophilisates, and facilitate the comparison with other works. The results are visualised in Figure 3.51.

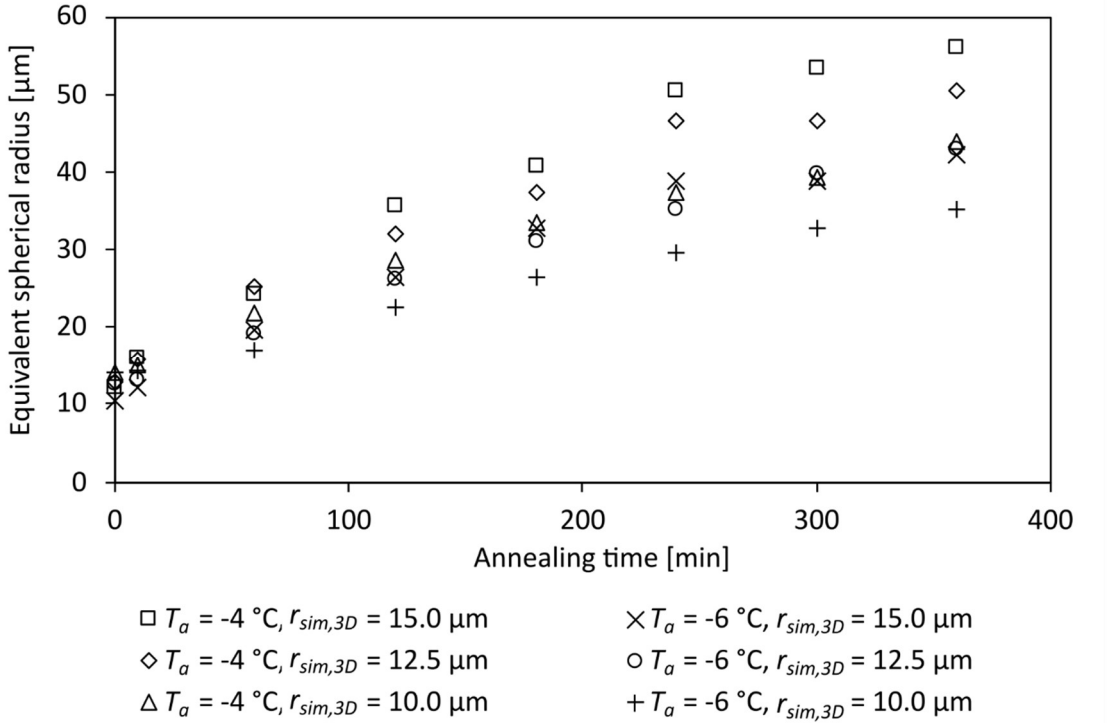

Figure 3.51: Temporal evolution of the sphere equivalent radius in the three-dimensional phase-field simulation with different initial particle sizes ($r_{sim,3D}$) and annealing temperatures (T_a). The standard deviation was omitted for better clarity.

The conversion of the ice crystal volume to the sphere equivalent radius also shows the increase over the annealing period and the dependence of the resulting particle radius on the initial particle size. The increase is not completely linear, and there may be several reasons for this. First, changes in the mass fraction in the matrix phase due to the Gibbs-Thomson effect might play a role, as larger particles exhibit lower compositional values. This phenomenon slightly influences the coarsening behaviour, as the driving force for Ostwald ripening is dependent upon the compositional difference between the particles and the matrix phase. Additionally, the interface may also contribute to the non-linear increase. Given that the interface maintains a fixed thickness, its impact is more pronounced on smaller particles than on larger ones. Consequently, small particles might appear larger in evaluations because the

interface is included in their measurement. As previously demonstrated in Figure 3.42, the standard deviation of particle size increased considerably as annealing progresses. To further illustrate this, the frequency of different particle sizes at various annealing times is depicted in Figure 3.52.

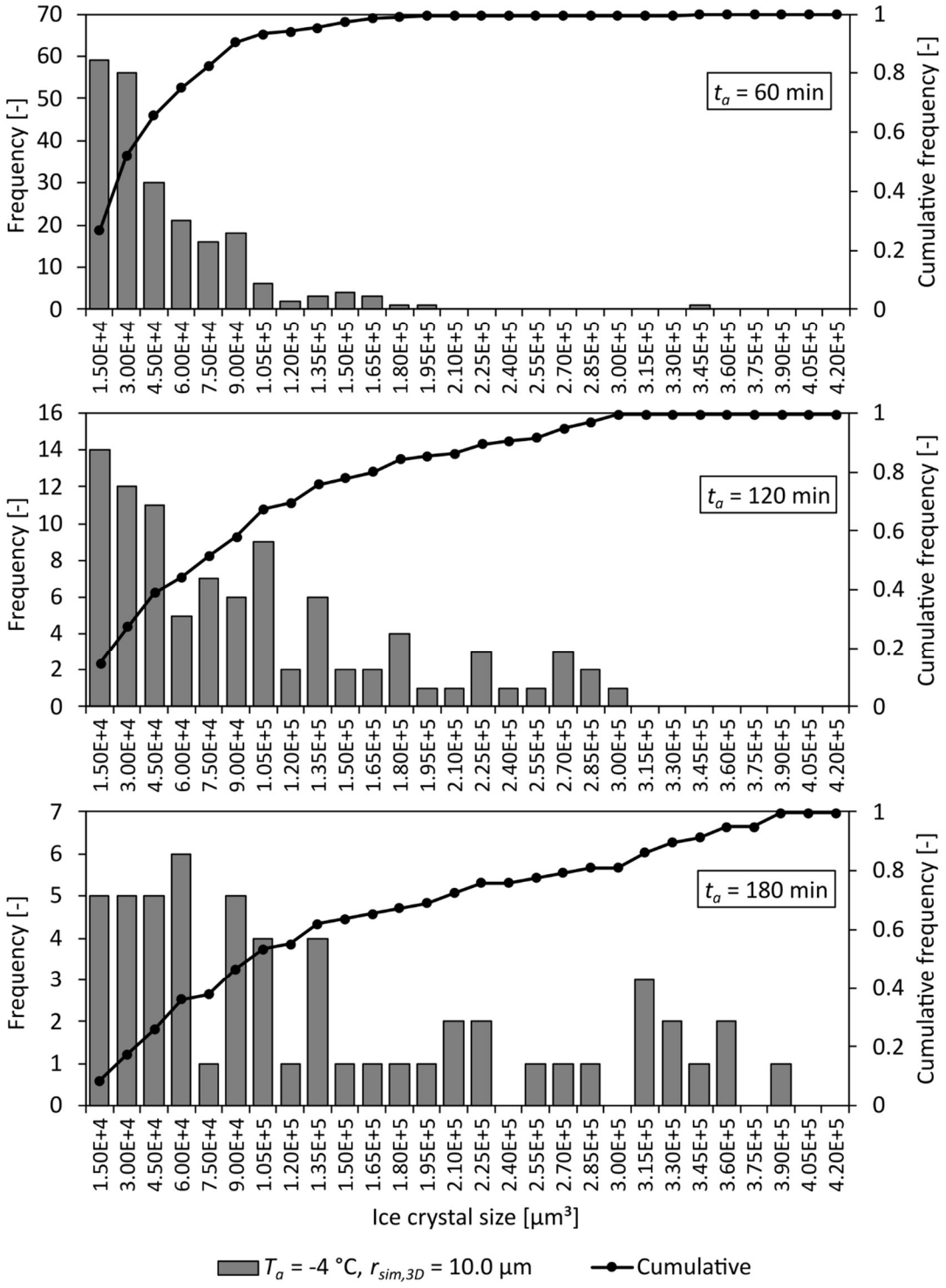

Figure 3.52: Exemplary ice crystal size distributions in the three-dimensional phase-field simulation with T_a = -4 °C and $r_{sim,3D}$ = 10 µm. The frequency alters between the plots.

The flattening of the cumulative frequency of particle volumes, normalised between 0 and 1, clearly indicates a shift towards larger particle sizes. It is important to note that the frequencies depicted in the plots (y-axis) are not consistent across different plots. These results are qualitatively consistent across all sets of simulation parameters and confirm that coarsening in such systems leads to increased heterogeneity in particle sizes.

Furthermore, it can be observed, especially in Figure 3.51, that the average particle radius at the beginning of the simulation is between 10 µm and 15 µm. This indicates that the strategy involving the conversion factor, as detailed in Chapter 3.2.3, was successfully implemented in the three-dimensional simulations and has yielded meaningful results.

3.2.7.3 Conjunction area of ice crystals

The next step involved the determination the conjunction areas as defined in Chapter 3.2.7.1 and their size distributions, or more precisely area distributions. As an intermediate step, the volume resulting from the overlap of the interfaces of two adjacent ice crystals was determined, hereafter referred to as the overlapping volume. The concept of overlapping volumes is illustrated in Figure 3.53 and explained below.

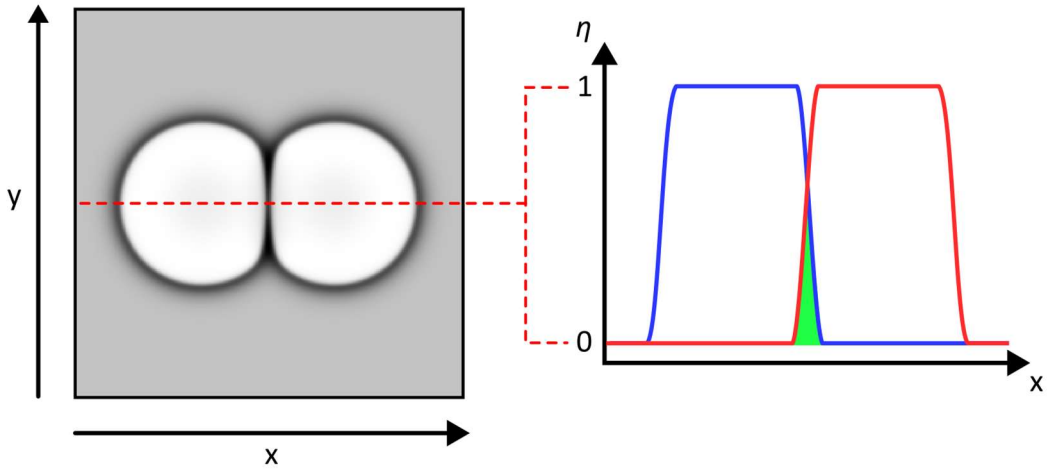

Figure 3.53: Concept of overlapping volume in a two-dimensional domain. The space occupied by the interface of both particles (blue and red) forms an area in two-dimensional space (green) and a volume in three-dimensional space.

The overlapping volume (or area) exists because the interface of the particles exhibit a certain width, which means that some space in the simulation domain can be occupied by two (or even more) particle interfaces simultaneously. Notably, this value depends on how the interfacial width is evaluated. If the interfacial width is defined as the length between two

phases where the values deviate from the equilibrium compositions, then larger widths of 6 to 8 grid points can be measured. Alternative methods, such as in Appendix A, use the inflection point of the interface and determine lower values. Nevertheless, the thickness of the interface, given that gradient energy coefficients are not altered, remains constant.

The overlapping volumes appear as thin and partially curved discs, as shown in Figure 3.54 for three-dimensional simulations. These shapes develop because the interfaces between adjacent particles deform during particle growth and coarsening processes. The total overlapping volume between all particles is given by:

$$V_{o,ij} = \sum_{i=1}^{N_p} \sum_{j \neq i}^{N_p} \eta_i \eta_j \,, \qquad \text{(Eq. 26)}$$

where N_p is the total number of particles, and η is the order parameter.

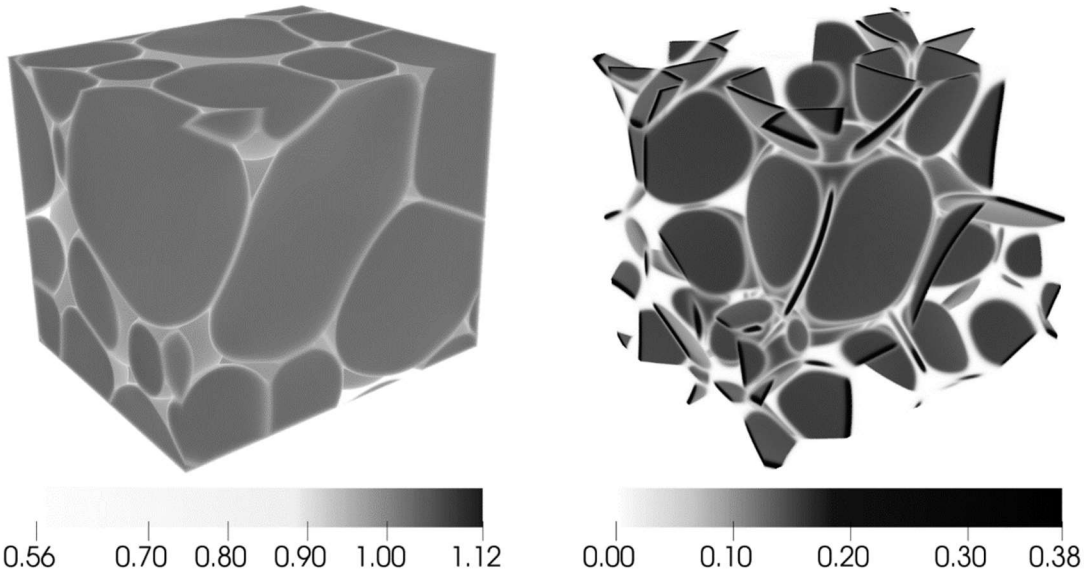

Figure 3.54: Three-dimensional phase-field simulation with an initial particle size of $r_{sim,3D}$ = 10 µm after annealing at T_a = -6 °C for t_a = 360 min. Ice crystals are shown on the left, while the overlapping volumes are visualised on the right.

The conjunction area that corresponds to an overlapping volume approximates about half of its surface are and can be determined with:

$$A_c = \frac{1}{2} A_o \,, \qquad \text{(Eq. 27)}$$

where A_o is the surface area of an overlapping volume.

The concept of conjunction areas is not commonly addressed in the literature concerning the microstructure of lyophilisates. Therefore, in this work, several parameters were initially examined to identify potentially relevant aspects of conjunction areas. Similarly to how ice crystal properties were assessed, the number, average area, and total area of conjunctions were determined. An example of the temporal evolution of these properties is shown in Figure 3.55.

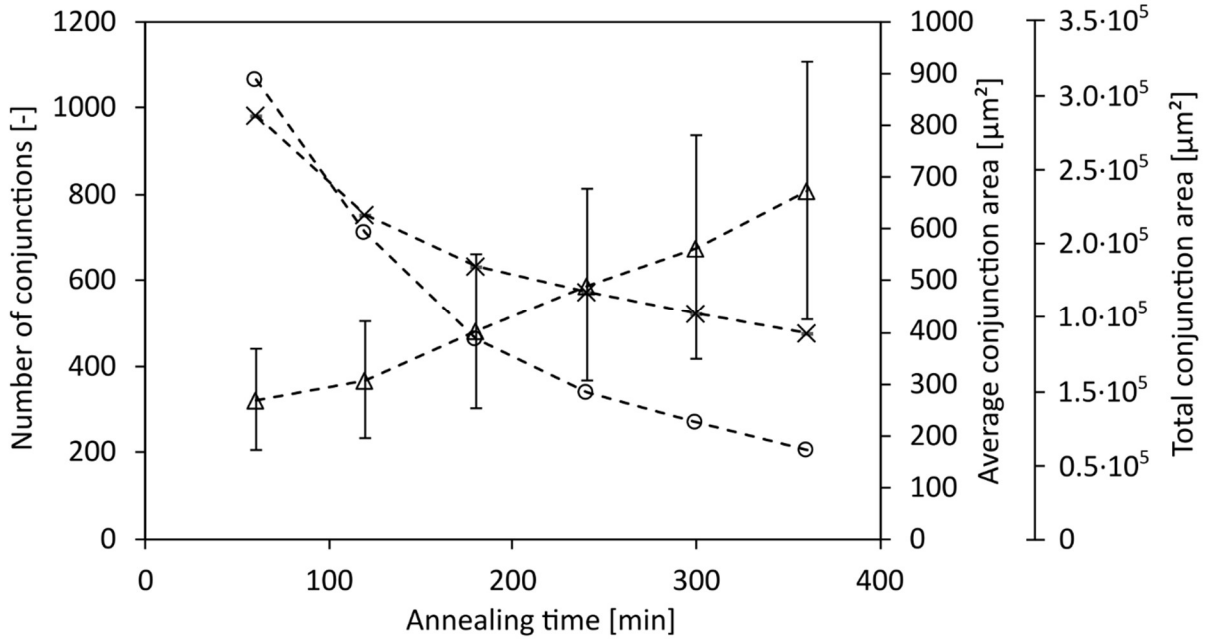

Figure 3.55: Temporal evolution of number of conjunctions (○), average conjunction area with standard deviation (Δ), and total conjunction area (x) during annealing in the three-dimensional phase-field simulation with an initial particle size of $r_{sim,3D}$ = 10 µm after annealing at T_a = -4 °C.

As annealing progressed, the number of conjunctions decreased. This is related to the fact that the number of ice crystals also decreased during coarsening, so that fewer ice crystals were in contact. Meanwhile, an increase in the average conjunction area was observed, which was also accompanied by an increase in its standard deviation. This indicates that, similar to the ice crystals, the system became more heterogeneous in terms of conjunction sizes. Additionally, it was noted that the total conjunction area decreased over the course of the simulation. This decline is consistent with the typical behaviour of coarsening, where surface areas within the system are minimized in favour of larger volumes. The trends in the number of conjunctions for all simulation conditions are depicted in Figure 3.56.

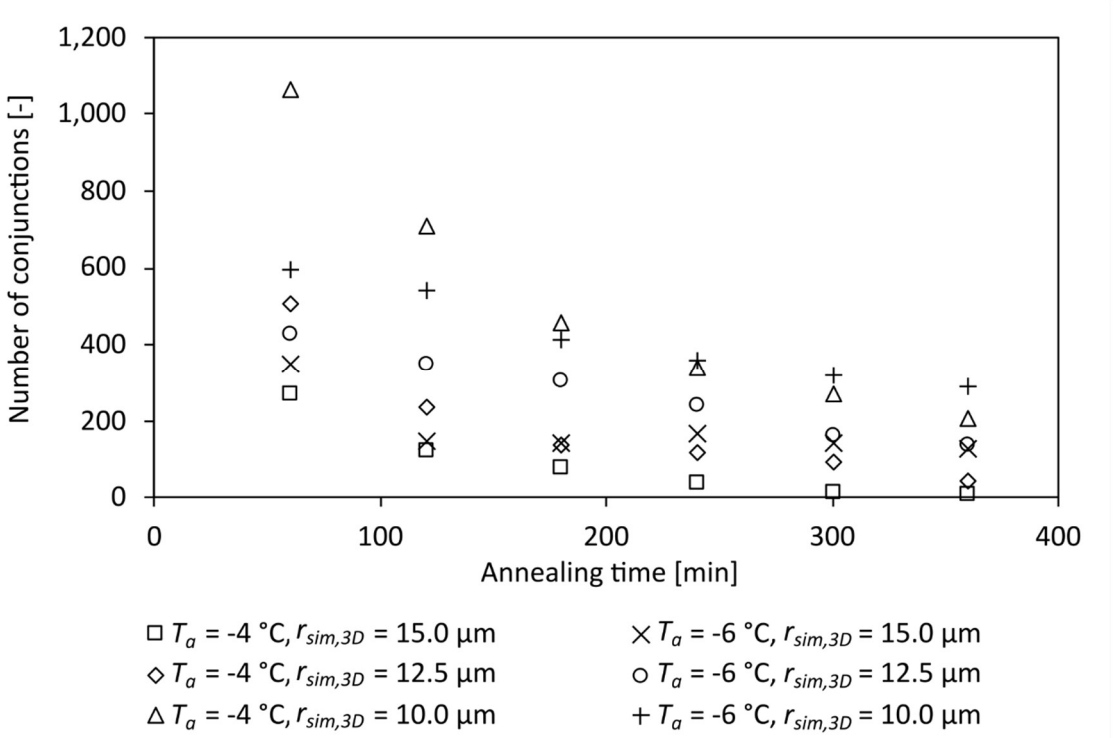

Figure 3.56: Comparison of various simulation parameters on the number of conjunctions in three-dimensional phase-field simulations.

The number of conjunctions decreased more rapidly at higher annealing temperatures, a result of faster coarsening which reduces both the number of particles and their contacts. Furthermore, smaller initial particle sizes resulted in more conjunctions due to the increased frequency of contact among numerous smaller particles. This does not imply a change in the number of conjunctions per particle, but rather indicates that the total number of conjunctions is dependent upon the overall particle count.

Next, the average conjunction area for all simulation conditions was determined with:

$$\hat{A}_c = \frac{\alpha^2 \sum_{i=1}^{N_a} A_{c,i}}{N_a}, \qquad \text{(Eq. 28)}$$

where α is the conversion factor, A_c is the respective conjunction area, and N_a is the total number of conjunctions.

This value is particularly interesting because it describes how narrow, on average, the paths for mass flow of vapour during sublimation can become. The idea is that the narrowest path acts as a bottleneck and potentially limits the total mass flow. The data illustrating this phenomenon is shown in Figure 3.57.

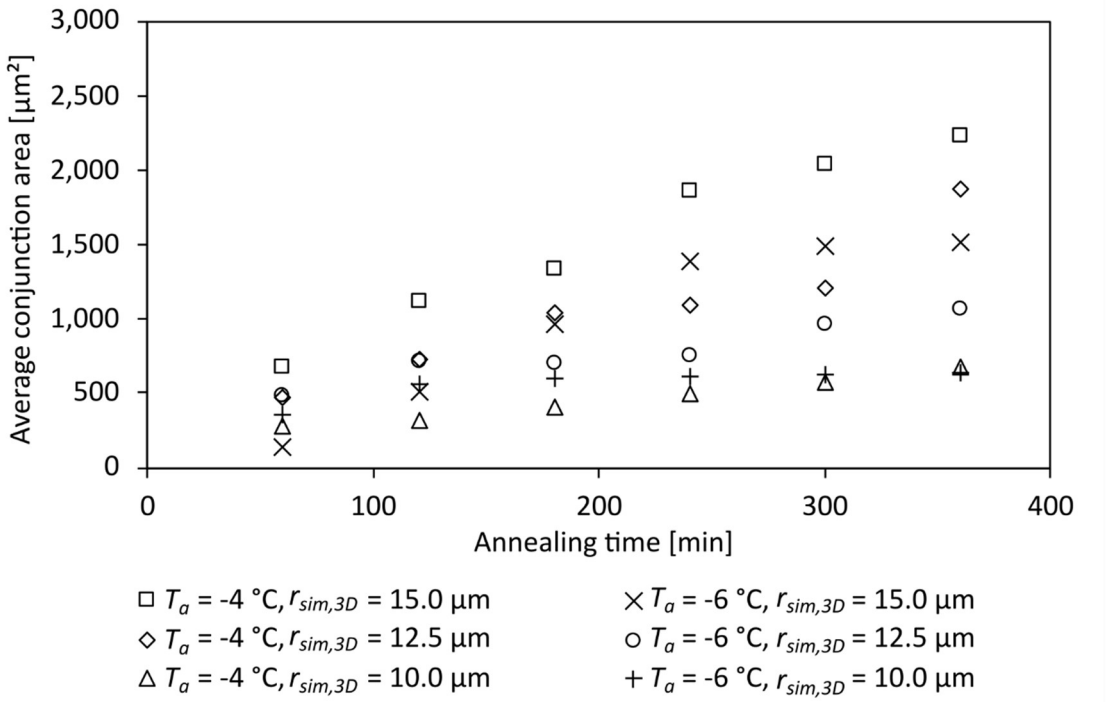

Figure 3.57: Comparison of the impact of various simulation parameters on the average conjunction area in three-dimensional phase-field simulations.

The results demonstrate a clear relationship between the average conjunction area and the initial particle size, which is intuitive as larger particles are likely to have larger contact areas. Additionally, there appears to be a temperature-dependent influence on this relationship. This can be explained by the fact that more rapid coarsening at higher temperatures leads to the formation of larger particles and, consequently, larger conjunction areas. This temperature effect is particularly pronounced for particles with an initial radius of 15 µm, as evidenced by the steeper increases in conjunction area during annealing. Notably, the data shows erratic fluctuations, which are due to the reduction in the number of conjunctions over time. These reductions affect the calculation of the average conjunction area.

Finally, the total conjunction area within the system was examined. It is important to note that the simulations accounted for different total volumes after converting to physical length units, meaning that the distance between grid points varies depending on the applied conversion factor. Therefore, it was crucial to calculate the specific conjunction area to enable meaningful comparisons of the simulation results.

For this purpose, the total volume of a simulation was calculated using:

$$V_{sim} = \alpha^3 \cdot Nx \cdot Ny \cdot Nz\,, \qquad \text{(Eq. 29)}$$

where α is the conversion factor, and *Nx*, *Ny*, and *Nz* are the number of grid points in x, y, and z direction, respectively.

The unit conventionally used in the scientific literature to determine specific surface area is m²/g. This approach is also applicable to simulations, where the physical weight of the simulation domain can be determined by calculating its volume using Equation 29 and then applying the density of the matrix phase. The physical mass of the matrix phase in a simulation is given by:

$$m_{m,sim} = V_{sim} \cdot \left(1 - \varphi_p\right) \cdot \rho_m\,, \qquad \text{(Eq. 30)}$$

where V_{sim} is the physical volume of the simulation domain, φ_p is the volume fraction of the particulate phase, and ρ_m is the density of the matrix phase.

The values for the determination of the physical mass of the matrix phase are summarised in Table 3.8. Since disaccharides such as sucrose and trehalose have similar densities, only the values for sucrose were employed in this analysis. Subsequently, the conjunction area was normalised to the specific conjunction area, defined as:

$$SCA = \frac{\alpha^2 \sum_{i=1}^{N_a} A_{c,i}}{m_{m,sim}}, \qquad \text{(Eq. 31)}$$

where α is the conversion factor, A_c is the respective conjunction area, N_a is the total number of conjunctions, and $m_{m,sim}$ is physical mass of the matrix phase within the simulation domain. The results are depicted in Figure 3.58.

Table 3.8: Conversion values for the calculation of the physical mass of the matrix phase in the simulation domain ($m_{m,sim}$) from the conversion factor (α), the volume of the simulation domain (V_{sim}), the particle volume fraction (φ_p), and the matrix density (ρ_m).

α [µm/gp]	V_{sim} [µm³]	φ_p [cm³/ cm³]	ρ_m [g/cm³]	$m_{m,sim}$ [g]
0.68	3.08 x 10^6	0.913	1.404[1]	3.28 x 10^{-7}
0.85	6.01 x 10^6	0.913	1.404[1]	6.41 x 10^{-7}
1.00	9.78 x 10^6	0.913	1.404[1]	1.04 x 10^{-6}

[1] Lescure (1995)

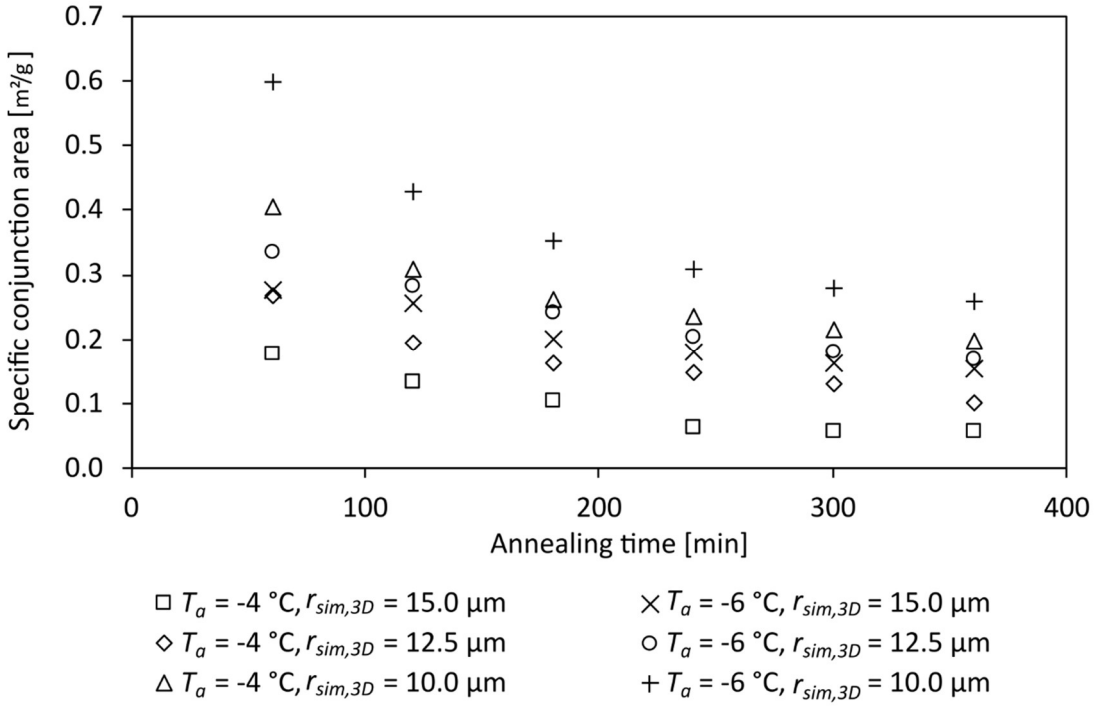

Figure 3.58: Comparison of the impact of various simulation parameters on the specific conjunction area in three-dimensional phase-field simulations.

Generally, the specific conjunction area decreased over the course of annealing, which can be rationalised by considering the fundamental drive to minimise surface areas during coarsening. Interfaces between phases contribute to the enthalpy of the system and are consequently reduced during relaxation processes such as Ostwald ripening. Notably, the specific conjunction area decreased more during annealing when the initial ice crystals were larger and when higher annealing temperatures were used.

3.2.7.4 Surface area of the matrix phase

In the next step, the surface area of the matrix phase was determined. An exemplary visualisation of the surface area is shown in Figure 3.59.

As previously mentioned, it is important to note that the simulation domain corresponds to different physical volumes depending on the set of simulation parameters. This means that analogous to the specific conjunction area, the surface needed to be normalised as well to obtain comparable results between different simulations. Elegantly, the matrix surface area can be determined using values already acquired for particle surface area and conjunction area, as shown in the following.

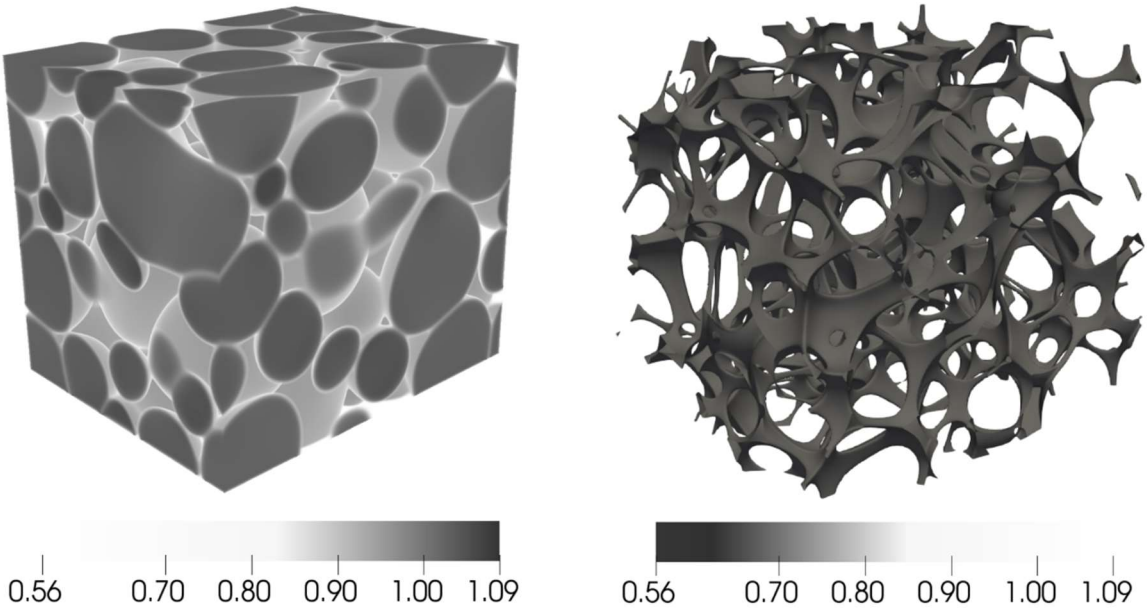

Figure 3.59: Three-dimensional phase-field simulation with an initial particle size of $r_{sim,3D}$ = 15 µm after annealing at T_a = -6 °C for t_a = 360 min. Ice crystals are shown on the left, while the surface area of the matrix phase is visualised on the right.

First, the total surface area of the matrix phase was calculated:

$$A_m = \alpha^2 \cdot \left(\sum_{i=1}^{N_p} A_{p,i} - 2 \sum_{j=1}^{N_p} A_{c,j} \right), \qquad \text{(Eq. 32)}$$

where α is the conversion factor, N_p is the total number of particles, A_p is surface area of an individual particle, and A_c is the conjunction area between two individual particles.

It should be noted that the conjunction area of each contact site must be subtracted twice from the total particle surface area because the total particle surface area was determined separately for each ice crystal, i.e., the contact area between particles is included twice. Subsequently, the specific surface area was calculated with:

$$SSA = \frac{A_m}{m_{m,sim}}, \qquad \text{(Eq. 33)}$$

where A_m is the total surface area, and $m_{m,sim}$ is physical mass of the matrix phase within the simulation domain. The results are shown in Figure 3.60.

The specific surface area (SSA) of the matrix phase decreased during annealing, influenced by both the annealing temperature and the initial particle size. Generally, smaller particles were associated with a larger matrix surface area. Furthermore, higher annealing temperatures

accelerated the reduction in matrix surface area during the annealing process. However, the rate of decrease in SSA slowed over time, eventually stabilising at a plateau, except for an initial particle size of 10 µm at T_a = -6 °C. In this case, the annealing duration was probably too short in order to reach its plateau. This trend was particularly pronounced at annealing temperatures of -4°C, where coarsening occurred faster. Fluctuations during the plateau phase are expected in the phase-field simulation due to the use of the particle surface area as well as the conjunction area in its calculations. Overall, these observations suggest that while annealing effectively reduces the SSA of the matrix phase initially, its impact slows down, leading to diminishing returns with prolonged annealing periods.

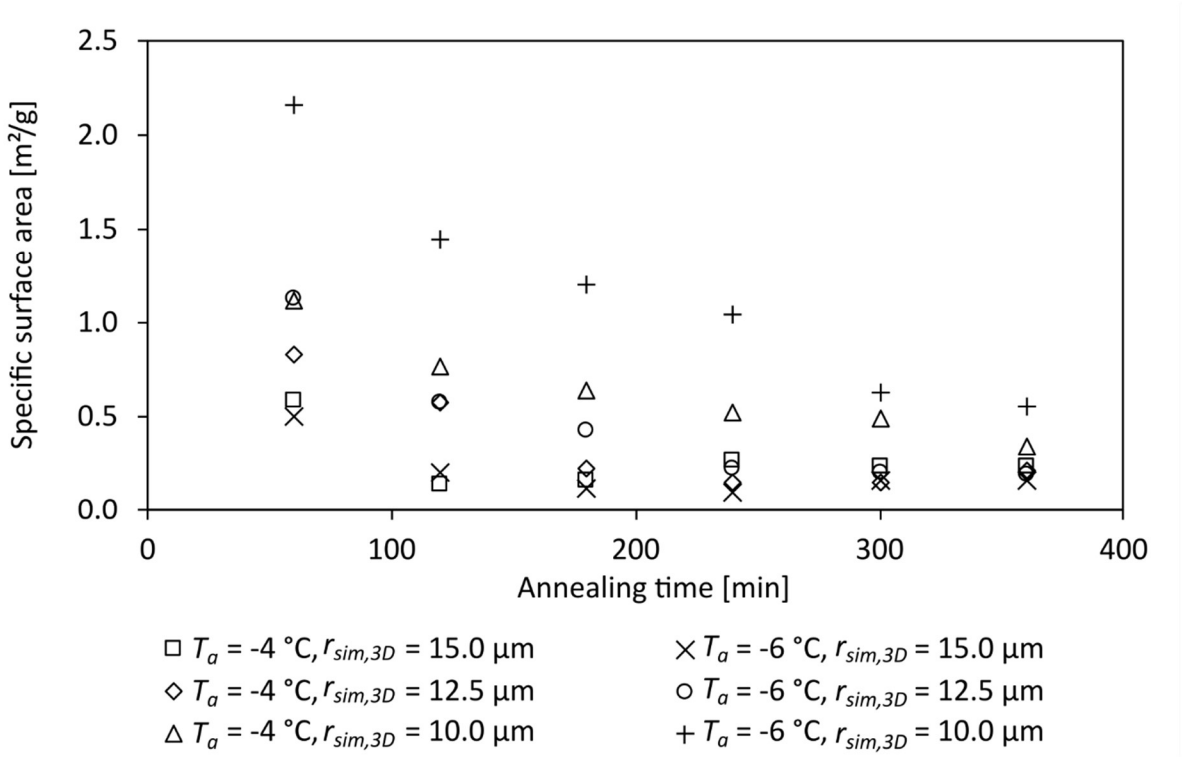

Figure 3.60: Comparison of the impact of various simulation parameters on the specific surface area in three-dimensional phase-field simulations.

To provide an example, Fang et al. (2020) measured a SSA for 5 % (w/w) non-annealed sucrose lyophilisate with different freezing conditions of 0.88 ± 0.00 m²/g and 1.08 ± 0.00 m²/g using mercury intrusion porosimetry. Furthermore, Duralliu et al. (2019) used inverse gas chromatography and determined a SSA of 0.73 ± 0.25 m²/g for a 5 % (w/w) non-annealed sucrose lyophilisate. However, this is not intended to be a direct comparison between simulation and experimental data, but merely to reflect the order of magnitude, because a different solution and different process conditions were used.

3.2.8 General discussion – pore size determination in lyophilisates

In the subsequent discussion, the results from the three-dimensional phase-field model are compared with experimental data from existing literature. Data availability for determining pore sizes in lyophilisates, particularly for annealed samples, is sporadic. In addition to the reasons already summarised in Chapter 1.6, there is a wide variety of solutions and freezing protocols used in different studies. Consequently, the following evaluation should be viewed as a qualitative assessment of the capability of various methods to determine or predict pore size in lyophilisates, rather than a direct comparison of data for a specific process or material. Figure 3.61 presents the average pore sizes observed in experiments by other authors alongside the simulation results from this work.

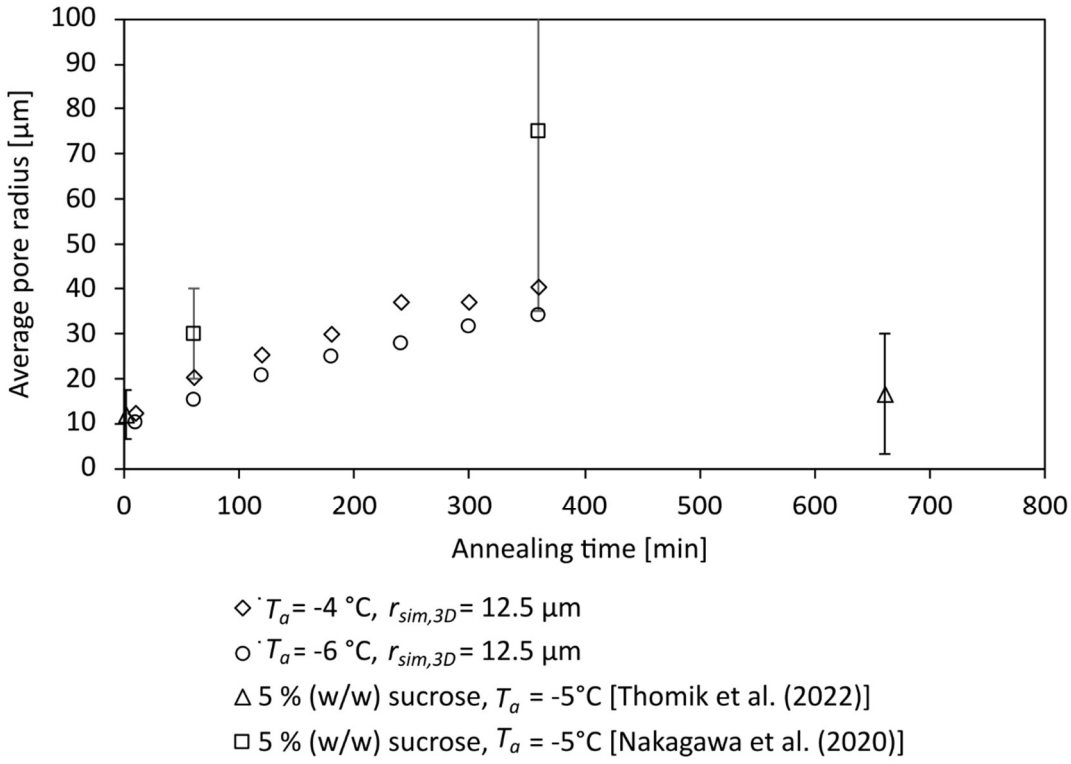

Figure 3.61: Comparison of experimental pore radii from experiments (△, □) with data obtained from three-dimensional phase-field simulations (◇, ○). Standard deviations for the simulation data were omitted for better clarity.

It should be noted that lyophilisates shrink during the drying process and the extent of this shrinkage has been shown to depend on the residual water content in the matrix phase prior to drying [67]. For example, three-dimensional scans of fully dried lyophilisates showed a volume retention of approximately 80 % in the case of a 10 % (w/w) sucrose solution. This

means that after complete drying, lyophilisates of 10 % (w/w) sucrose solution shrink by approximately 20 % compared to the volume of the initial liquid solution. To account for this in the analysis, the particle sizes in the simulations were adjusted by reducing all values by 20 %. Thus, for the following evaluation, it is assumed that shrinkage uniformly reduces the pore sizes by the same proportion as the overall shrinkage of the lyophilisate. This assumption is reasonable since any additional microstructural change would suggest a collapse, which is what a successful lyophilisation process is designed to avoid.

As mentioned, Thomik et al. (2022) used µ-CT to determine pore size, while Nakagawa et al. (2020) used SEM followed by image processing. While the pore sizes for non-annealed samples were comparable, the effect of annealing shows significant discrepancies between the two works, even though the annealing temperature was identical. Thomik et al. (2022) found much smaller pores, while Nakagawa et al. (2020) observed a considerably larger increase in mean pore size after annealing. The simulation results of this work fall between the two experimental evaluations in terms of pore size. Since large differences were found between simulation and experimental data, but also between experimental data from different methods, a detailed discussion of how pore sizes were determined in the case of other works is necessary, in addition to Chapter 1.7. Figure 3.62, from the work of Arsiccio et al. (2019), shows an example of an image segmentation method for the automatic determination of pore sizes from SEM images. The images were taken from an already dried lyophilisate, as is common for SEM analysis.

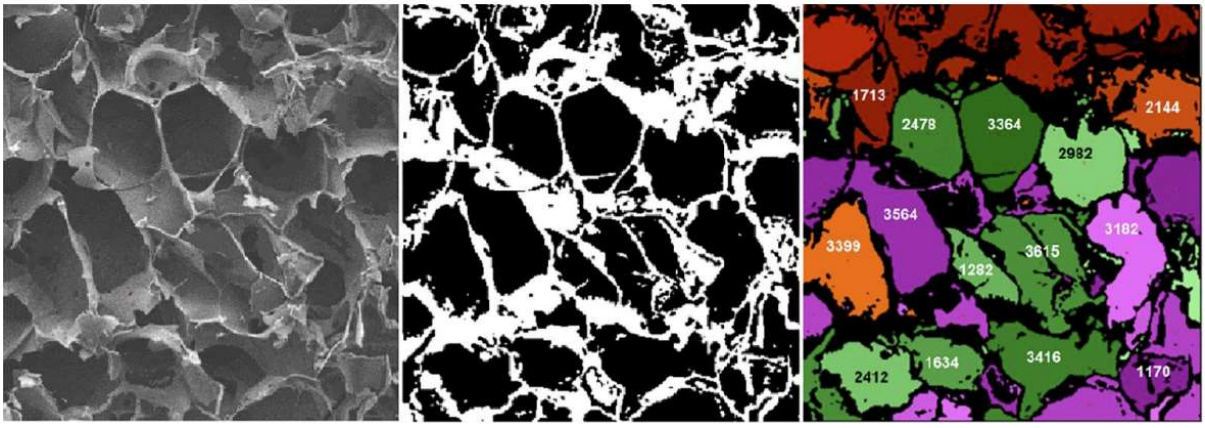

Figure 3.62: Image segmentation in order to determine pore sizes of a lyophilisate. The SEM images of a lyophilisate (left) is pre-processed to a binary image (middle), and then segmented (right). From [108].

The primary purpose of image segmentation is to identify and delineate objects or regions within an image by assigning a label to each pixel. Pixels sharing the same label are grouped based on common characteristics, forming “segments” or “super pixels” that collectively cover the entire image. Several segmentation methods are available, mainly based on the use of binary images [108,122]. The problem here lies not so much with the image segmentation method as with the original SEM image. The voids in the lyophilisate, exposed by a break or cut, do not correspond to a definable size of pore but display a randomly exposed area that may encompass one or several pores. The concept is illustrated in Figure 3.63. Furthermore, the limited perspective provided by SEM of the three-dimensional matrix makes it virtually impossible to clearly distinguish between pores. Therefore, when using SEM to determine pore sizes, it is important to remember that only the order of magnitude of the pores is obtained and by no means an exact pore size.

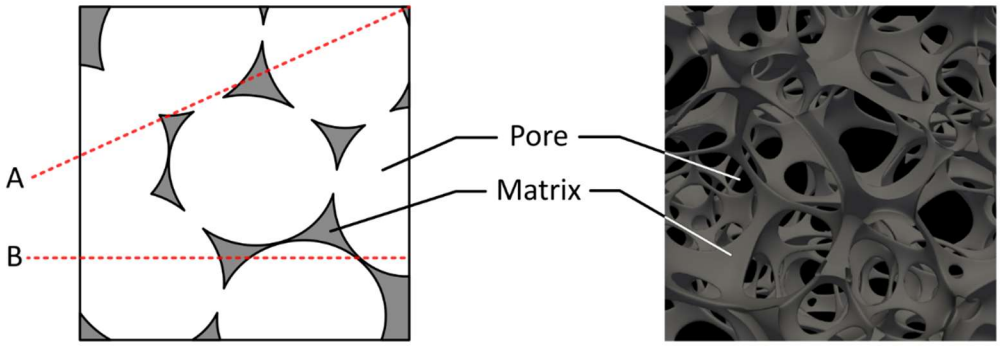

Figure 3.63: Random cuts/breaks through the lyophilisate (A, B) are illustrated on the left in a two-dimensional domain, while difficulties recognising individual pores just visually is demonstrated on a three-dimensional phase-field simulation on the right.

In contrast, reconstructed µ-CT data is more comparable to the results of the phase-field model because both provide a three-dimensional perspective based on either voxels or grid points. Figure 3.64 presents examples of such µ-CT reconstructions. However, as noted by the authors, the resolution is not sufficient to detect small pores. This limitation was evident when Thomik et al. (2022) reported varying porosities for samples with and without annealing. Ideally, porosity should remain relatively unchanged during annealing since the pore volume is merely redistributed, provided the total volume of the lyophilisate stays constant. The authors suggested that undetectable small pores in the lyophilisate, below the µ-CT resolution, might explain these differences. However, this explanation may not be entirely accurate since pores, even in non-annealed samples, are much larger than the typical 1 µm

voxel size of µ-CT. It appears more plausible that the thin-walled matrix, which can be in the sub-micron range, might not be fully captured by the µ-CT, leading to significant data discrepancies.

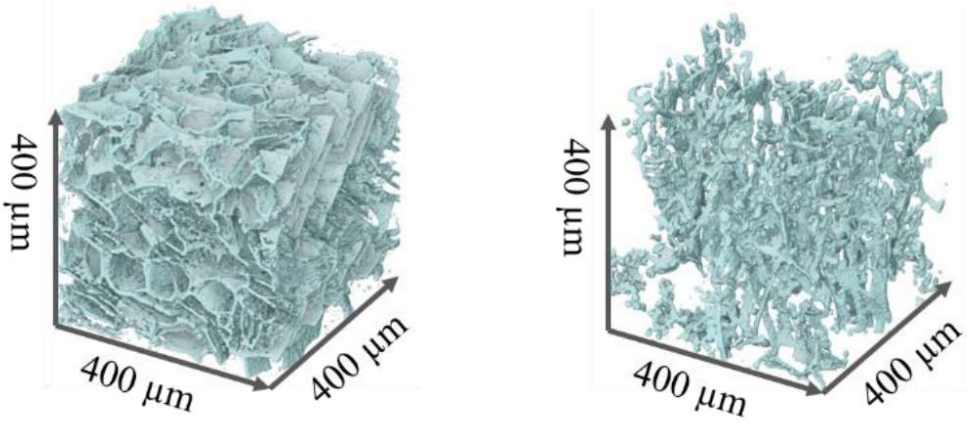

Figure 3.64: Three-dimensional renders from µ-CT scans of 5 % (w/w) sucrose samples without (left) and with (right) annealing. From [71].

In summary, advanced experimental methods like µ-CT and SEM are valuable for making basic observations about the microstructure in lyophilisates. However, the accuracy and comparability of the data remain problematic. SEM data, for example, do not readily yield detailed morphological parameters, and the resolution of µ-CT may not be adequate for its intended purposes. Nevertheless, these experimental methods provide a rough estimation of pore sizes, and are therefore valuable tools to estimate the impact of process conditions on lyophilisates. Simulations, while reliant on assumptions, offer distinct advantages that purely experimental methods cannot match. Once validated, *in silico* methods provide an alternative means to assess the impact of process conditions on the microstructure of lyophilisates, as demonstrated in this work. Particularly, simulations are capable of capturing and quantifying parameters that are difficult or impossible to measure experimentally, such as the conjunction area.

In this thesis different initial particle sizes were used in the simulations reflecting the broad spectrum of values found in the existing literature for non-annealed samples. The results of the three-dimensional annealing simulations in the context of a frozen disaccharide solution can be summarised as follows:

- Annealing leads to an increase in the average size of ice crystals and broadens their size distribution. The increase in ice crystal size during annealing, which later translates into the pore sizes in the dried lyophilisate, aligns with observations that larger pores can enhance the sublimation rate during freeze-drying.
- The specific surface area of the matrix phase decreases over the course of annealing. This phenomenon might play a role in the diffusive and desorption processes during drying. Furthermore, the reduction in surface area is beneficial as it could help minimise protein agglomeration by minimising the available surfaces for protein precipitation, thereby enhancing the stability and quality of the final product.
- During annealing, the number of conjunctions, which form the narrowest gaps in the porous microstructure, decreases. However, the average size of these conjunctions increases, indicating a shift towards fewer but larger channels within the microstructure. Quantifying parameters such as the conjunction area might offer better explanations why annealing effectively reduces primary drying times.
- The phenomena described above depend on both the annealing temperature and the initial ice crystal size. In general, higher annealing temperatures accelerate these processes, while larger initial ice crystal sizes reduce the time required to reach plateaus.

The findings from this research offer practical applications in the field of freeze-drying, specifically through the use of phase-field simulations. By simulating different annealing times and temperatures, it is possible to determine when microstructural changes reach plateau phases. This approach can help optimise freeze-drying process conditions, ensuring that the benefits of annealing (as mentioned above) are achieved efficiently. The goal is to maximise the positive impacts of annealing while minimising the duration of the annealing step, making the process more time-effective and cost-efficient. This methodology allows for a more precise control over the lyophilisation process, potentially leading to better quality products with reduced processing times.

4 Future applications

In the following chapter some ideas for future research are explored, which can be based on the results of this work. These include both experimental and simulation topics.

4.1 Reorganisation kinetics during recalescence and crystallisation

In Chapter 3.1.4, the experimental findings showed that the recalescence and crystallisation phase significantly influences the microstructure formation in a frozen solution. To reiterate, during recalescence and crystallisation, the increased mobility within the partially frozen system led to a reorganisation of the crystalline phase, resulting in the formation of ice crystals resembling grains and approximately matching the sizes of the pores within the lyophilisate. Quantifying this reorganisation event or even understanding its kinetics might be helpful for various reasons.

From a scientific standpoint, it could provide an alternative explanation for the pore sizes in a lyophilisate. This work challenges the common understanding that pores in the lyophilisate directly correspond to stable nuclei formed during freezing. Instead, if the recalescence and crystallisation phase predominantly determines ice crystal size, it is plausible that multiple irregular dendritic ice crystals might coalesce to form each grain-like ice crystal observed. Thus, inferring the number of nuclei solely based on pore size observations may be misleading.

From the perspective of phase-field modeling, understanding the kinetics of this reorganisation event would allow to define the starting point of the subsequent annealing simulation, since initial particle sizes would be known. However, the issue arises on how to observe and quantify such an event. If a freeze-drying microscope is used, the sample thickness of a few micrometres might already be too large for this event to occur in a pseudo-two-dimensional manner, since the initial structures seem to be much finer than the height of the sample. Resolving this challenge might require further reduction in layer thickness or potentially transitioning to a three-dimensional phase-field simulation, where the simulation height matches the distance between the two glass plates. If such a model is calibrated and validated, it would enable the prediction of pore sizes in a lyophilisate when no additional annealing step is performed. Furthermore, it would allow to optimise the freezing step in respect to the homogeneity of the lyophilisate within a vial, or when used with temperature data from the freeze-dryer the homogeneity between individual vials.

4.2 CFD simulations through the porous microstructure

This idea could be used complementary with the simulation output from this work. The three-dimensional phase-field model generates a data object that can be used as a simulation domain for CFD simulations. This integration presents a significant advantage, as fabricating such detailed and complex microstructures using alternative methods would be substantially more challenging. As mentioned in Chapter 3.2.8, the resolution of experimental methods such as µ-CT are simply insufficient to capture the microstructure , especially the thin matrix walls.

The implementation of a robust CFD simulation, fed with the microstructure as a simulation domain, could be used to make predictions about the partial vapour pressure in the pores immediately at the sublimation front.

The Knudsen-Langmuir equation describes the mass flow (sublimation rate) as [161]:

$$\dot{m} = a(p_0 - p_v^b) \cdot \sqrt{\frac{M_v}{2\pi RT}}, \qquad \text{(Eq. 34)}$$

where a is an accommodation coefficient, p_0 is the saturation vapour pressure of the solid phase, p_v^b is the partial pressure in the bulk vapour, M_v is the molecular mass of the vapour, R is the universal gas constant, and T is the interface temperature.
From Equation 34 it can be derived that the purely physical sublimation rate, which does not take geometric features or product resistance into account, depends on three factors:

1) The difference between the equilibrium vapor pressure of the solid phase and the partial vapor pressure in the gas phase.
2) The temperature in the solid phase at the interface.
3) The accommodation coefficient.

The Accommodation coefficient serves as a fundamental physical parameter, describing the interaction of gas or vapour molecules when they collide with the surface of a solid or liquid. The temperature at the interface, on the other hand, emerges as a multifaceted function influenced by several factors. These factors include the heat extracted by the frozen product, heat transferred from surrounding surfaces, heat released during ice crystallisation, and changes in enthalpy arising from the formation of new interfaces.

The pressure terms in this equation indicate that the sublimation rate is slowed down when the partial vapour pressure increases. This means that the total sublimation rate is adjusted to a balance between the pressure reduction due to migration of water vapour away from the interface and the purely physical sublimation rate that is mostly dependent on the temperature at the interface. The pressure reduction term can be assumed to be dependent on the ambient pressure, as well as pore geometry, possibly pore sizes or the smallest conjunction areas (bottleneck principle). Therefore, a CFD simulation could be used to verify if the microstructure predicted from the three-dimensional phase-field model is accurate by comparing the experimental sublimation rate with the balanced sublimation rate from the combination of CFD simulation and the porous microstructure from the phase-field model.

5 Appendices

Appendix A – Validation and stability analysis for the phase-field simulation

The following section describes multiple tests that were conducted to ensure that the simulation had been implemented correctly. On the one hand, care is taken to verify that simulation values correspond to theoretical values (see Gibbs-Thomson effect), but also that the simulation output scales properly with the input parameters (e.g., interfacial width scaling with gradient energy coefficients).

i. Gibbs-Thomson (capillarity) effect on composition

The composition of the phases in a phase-field model are dependent on the curvature of the interface, i.e., the more curved an interface the higher the composition of the corresponding phase. This phenomenon, namely the Gibbs-Thomson effect, is also present in the real world as the curvature-dependent increase of the saturation vapour pressure in sufficiently small particles [162]. The deviation of the composition of a particle with a curved interface is given by [163]:

$$\Delta c_p = \frac{\chi_p \cdot \gamma}{\left(c_p^e - c_m^e\right) \cdot \psi_m}, \qquad \text{(Eq. App. 1)}$$

where χ_p is the mean curvature of the interface, γ is the interfacial energy density, and c_m^e and c_p^e are equilibrium compositions for the *m*- and the *p*-phase, respectively, and ψ_m is a quantity defined as [163]:

$$\psi_m = \left[\frac{\partial^2 f_0}{\partial c^2}\right]_{c_m^e}, \qquad \text{(Eq. App. 2)}$$

where f_0 is the bulk free energy density, and c is the composition.

The impact of the Gibbs-Thomson effect was calculated for the two-dimensional as well as the three-dimensional model. Subsequently, simulations were performed with both models and different initial particle sizes. The results in Figure App. 1 show that simulation output and theoretical calculations agreed, and that both models exhibited a critical particle size. Once the particle radius fell below the critical particle size, the corresponding particle dissolved completely, as can be inferred from the mismatch of simulated and calculated value at 6 grid

points and 7 grid points for the two-dimensional and the three-dimensional simulations, respectively.

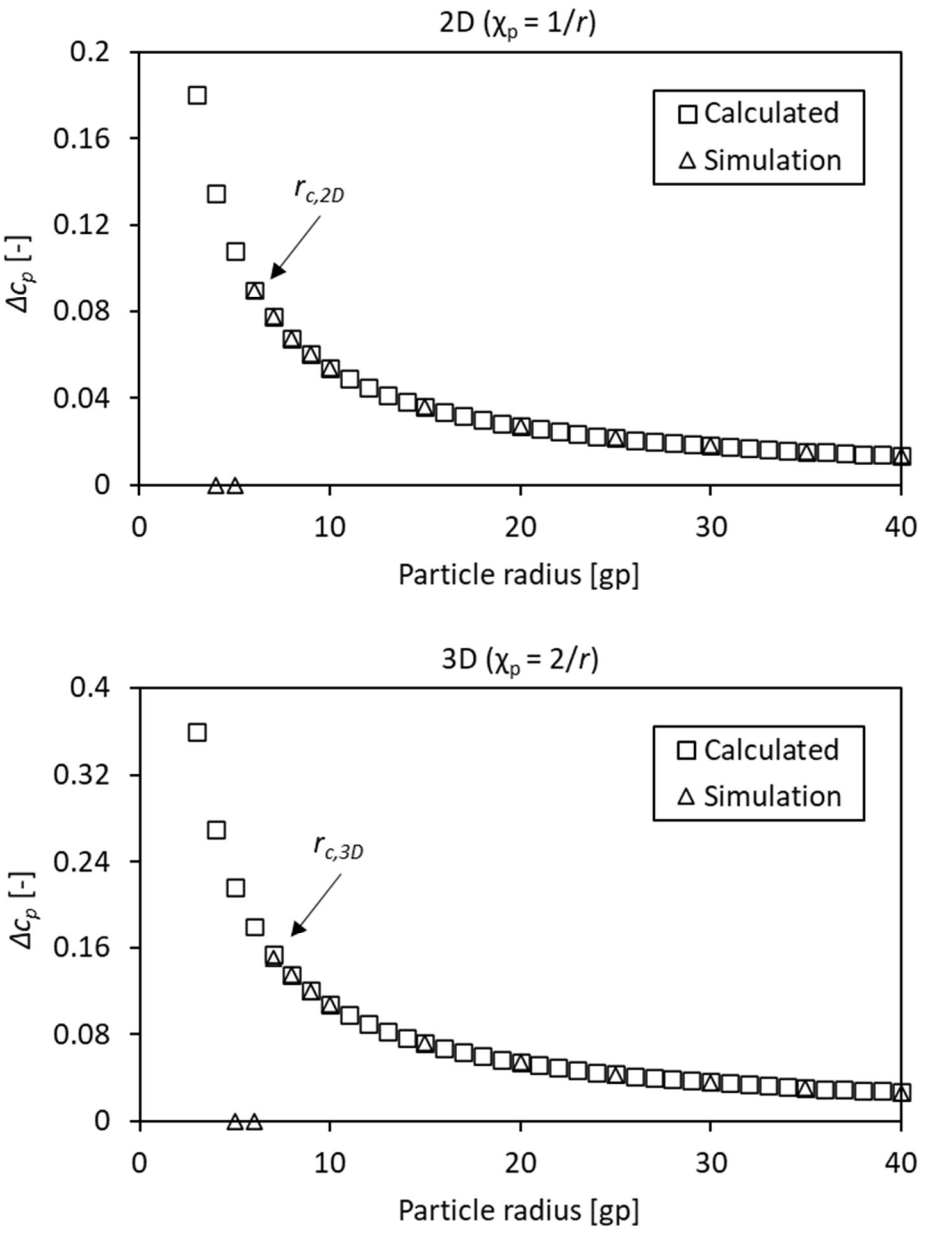

Figure App. 1: Increase of particle composition dependent on particle radius for two-dimensional (top) and three-dimensional (bottom) with critical particle radius (r_c) for dx = 0.9.

ii. Energy barrier coefficient on interfacial free energy

The energy barrier coefficient Q is used in this multiphase-field model to increase the free energy at loci in the simulation domain where the interface of two adjacent particles of differing order parameters come into contact. Consequently, this penalises the overlapping of the interfaces of particles, and therefore promotes phase separation. The addition of such a coefficient allows to increase dt (increment between timesteps), because “moving” interfaces

due to particle growth are already inhibited by their directional expansion early on when close to other interfaces. If *Q* is set to 1, then more overlapping of particle interfaces is necessary to increase the bulk free energy, which in turn means that *dt* has to be low enough to prevent the overlapping from particles from one timestep to the next.

When choosing the energy barrier coefficient, care must be taken that the interfacial free energy σ of the system is not altered, otherwise the simulation results would become dependent on *Q*. In order to identify suitable values for *Q*, a phase-field simulation was set up where interfaces were in contact with each other. Specifically, a single circular particle was placed with a thin ring of another phase separating the particle from the rest of the simulation domain, as shown in Figure App. 2, thereby creating overlapping interfaces.

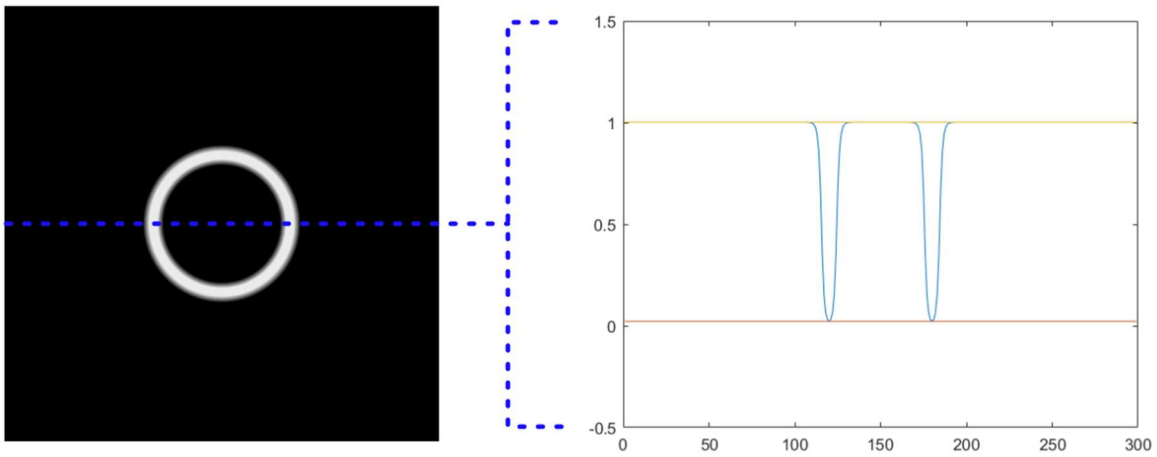

Figure App. 2: two-dimensional simulation domain (left) and cross-section (right) with slightly overlapping interfaces. The particle in the middle and the surrounding phase were both assigned their own order parameter to inhibit fusion.

Next, the energy barrier coefficient *Q* was varied, and the overall interfacial free energy of the cross-section was calculated with:

$$\sigma = \int \left[f(c,\eta_i) + \kappa_c \left(\frac{dc}{dx}\right)^2 + \kappa_\eta \left(\frac{d\eta_i}{dx}\right)^2 dx \right], \qquad \text{(Eq. App. 3)}$$

where $f(c,\eta_i)$ is the bulk free energy density, and κ_c and κ_η are the gradient energy coefficients for composition and order parameter, respectively. The results are depicted in Figure App. 3.

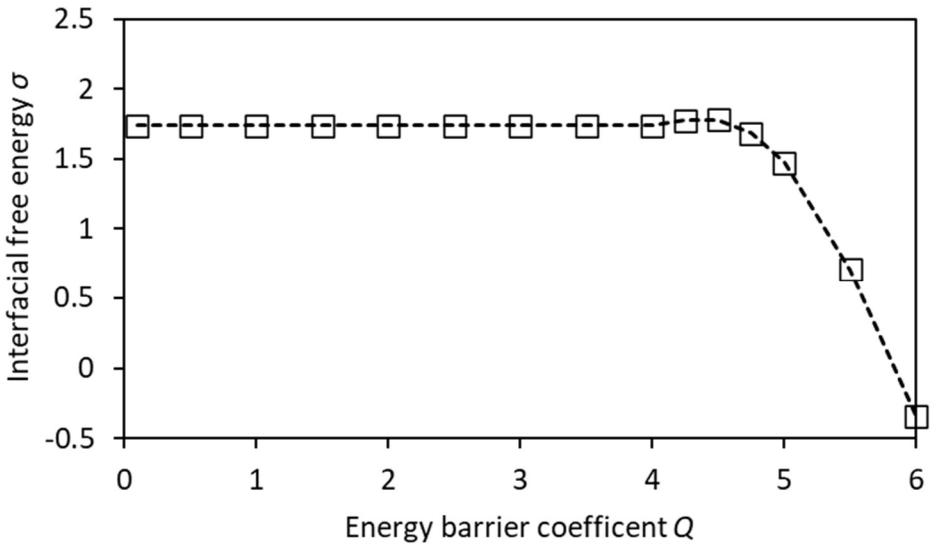

Figure App. 3: Impact of the energy barrier coefficient (*Q*) on the interfacial free energy (*σ*) in the multiphase-field simulation used in this work.

The interfacial free energy *σ* remained constant for values of the energy barrier coefficient *Q* up to 4. If *Q* was further increased, a small increase of *σ* was observed, with a subsequent steep decrease even up to negative values. The results of this test indicate that values for *Q* up to 4 are acceptable without altering the interfacial energy and therefore the simulation results. After some trial and error, a value of 2 was chosen for *Q* as it allowed to sufficiently increase *dt* for all two-dimensional and three-dimensional simulations.

iii. Gradient energy coefficients on interfacial width and interfacial energy

The gradient energy coefficients κ_c and κ_η for composition and order parameter, respectively, both influence the interfacial width ω and the interfacial energy σ in phase-field simulations. In particular, the following expressions must be fulfilled if the phase-field simulation was implemented correctly [164]:

$$\omega \sim \sqrt{\frac{\kappa_i}{\gamma}}, \qquad \text{(Eq. App. 4)}$$

$$\sigma \sim \sqrt{\gamma \cdot \kappa_i}, \qquad \text{(Eq. App. 5)}$$

where γ is a parameter related to the height of the energy barrier between the two phases, and κ_i is the respective gradient energy coefficient.

The interfacial energy was calculated with Equation App. 3, while the interfacial width had to be determined via the inflection point of the interface, as depicted in Figure App. 4.

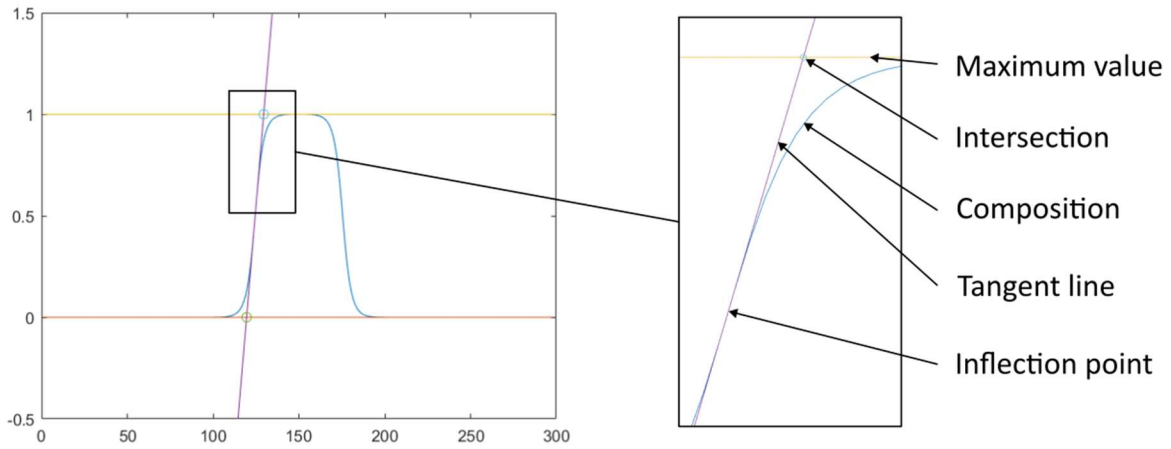

Figure App. 4: Determination of the interfacial width (ω) via a tangent line going through the inflection point of the composition profile.

The determination of the upper and lower limits of the interface was achieved through the identification of the points of intersection between the tangent line and the extrema (maximum/minimum values) of the composition profile. Subsequently, the interfacial width was quantified by measuring the distance between these upper and lower limits. Although alternative methodologies, for example with the derivative of the composition profile, are available, this technique is commonly employed for the estimation of interfacial width due to its simple application. It is noteworthy that, in instances of interfaces exhibiting more width, this method may not encompass the entire interface. Nonetheless, the critical aspect of this procedure is to maintain consistency in the measurement. Next, and the interfacial energy and width were determined for various energy gradient coefficients, as shown in Figure App. 5.

For this test, either κ_c or κ_η or both were varied simultaneously. The results show that the proportionality expressions from Equation App. 4 and Equation App. 5 were fulfilled, as the interfacial width as well as the interfacial energy correlated linearly with the square root of the energy gradient coefficients.

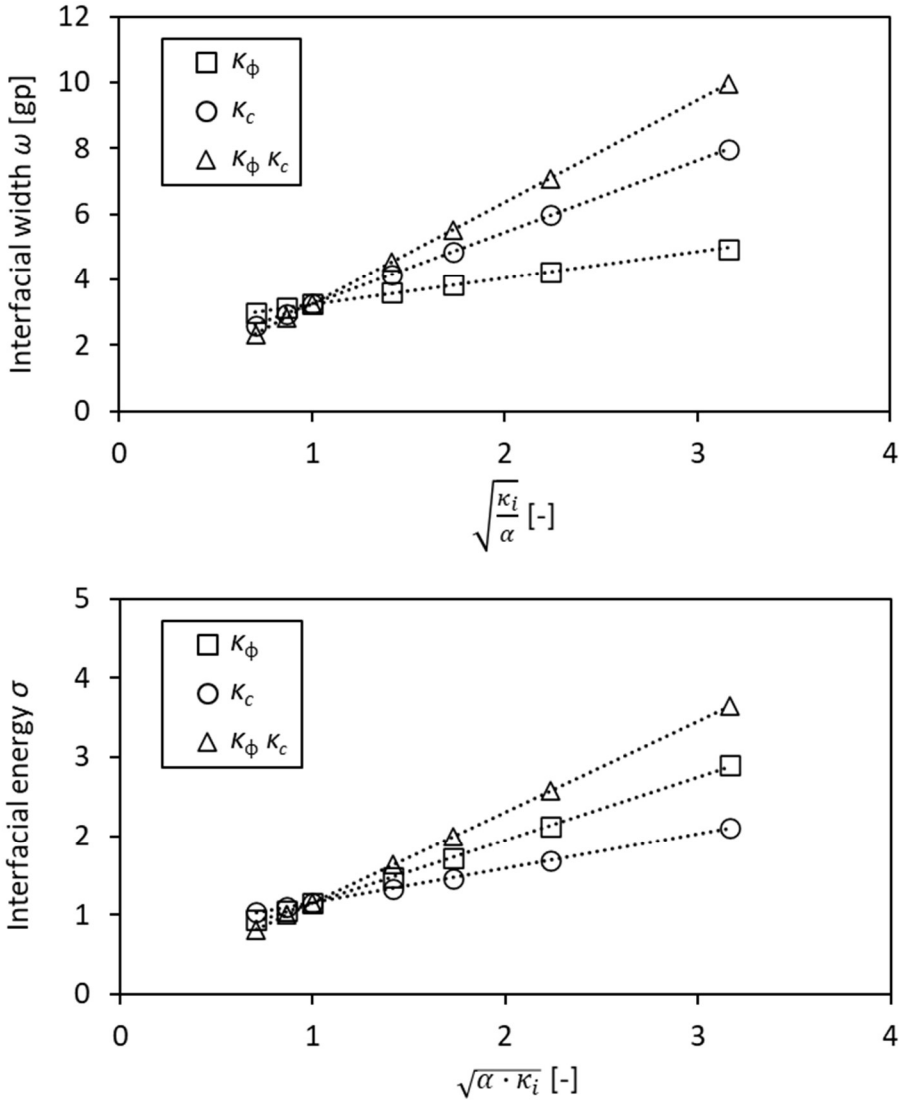

Figure App. 5: Dependency of interfacial width (ω) and interfacial energy (σ) on the gradient energy coefficients with γ = 1. The interfacial width depends on the evaluation method.

Appendix B – Complete data from Chapter 3.1.2

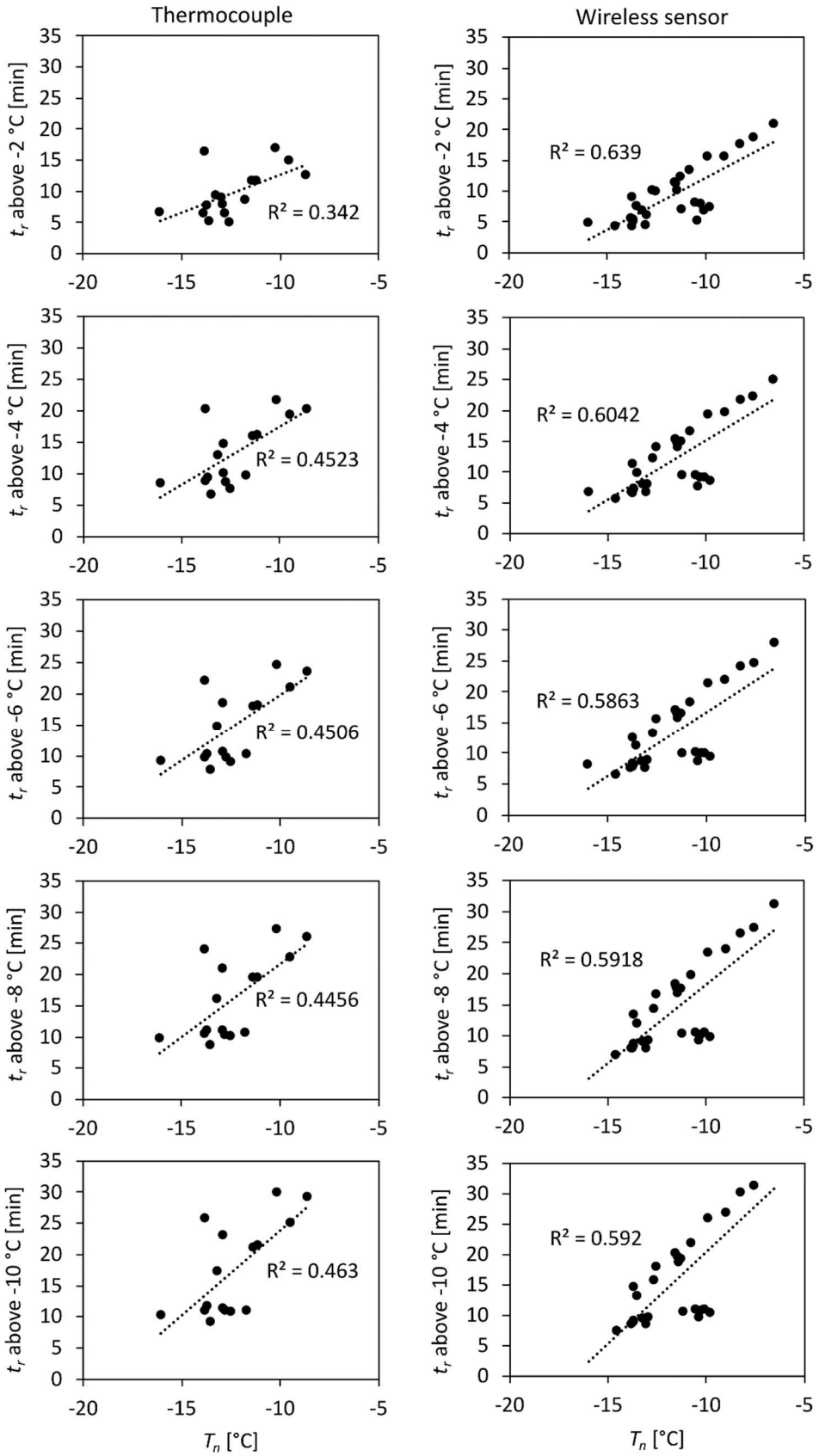

Figure App. 6: Comparison of residence time (t_r) for different temperature limits with the nucleation temperature (T_n) during freezing of a 10 % (w/w) sucrose solution.

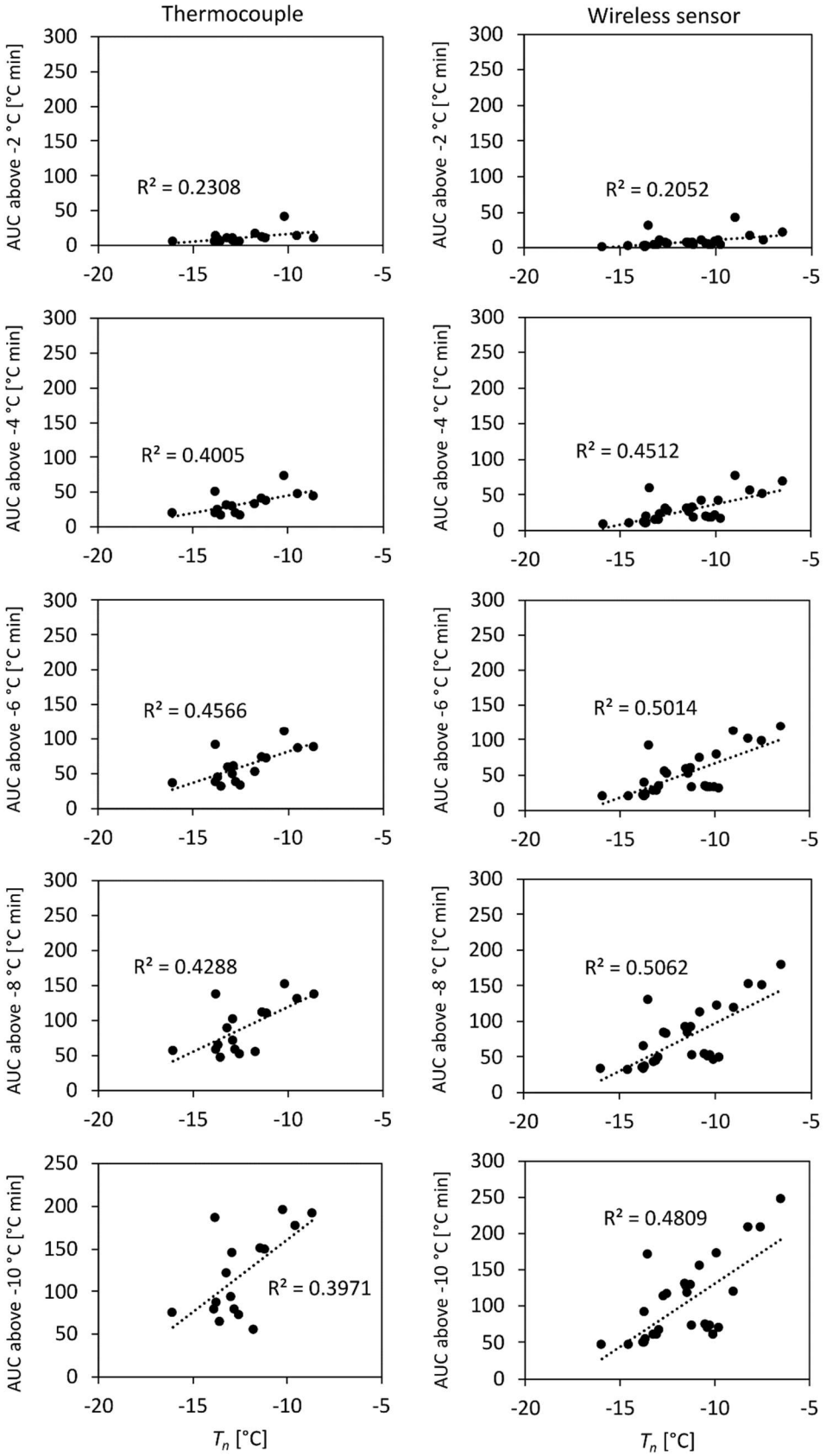

Figure App. 7: Comparison of the area under the curve (AUC) of the recalescence for different temperature limits with the nucleation temperature (T_n) during freezing of a 10 % (w/w) sucrose solution.

Appendix C – List of abbreviations

Abbreviation	Definition
µ-CT	Micro-computed tomography
AUC	Area under the curve
BET	Brunauer-Emmet-Teller
CER	Circle equivalent radius
CER^3	Cube of circle equivalent radius
CFD	Computational fluid dynamics
cryo-SEM	Scanning electron cryomicroscopy
DSC	Differential scanning calorimetry
FDM	Freeze-drying microscopy
gp	Grid points
I_h	Hexagonal ice
LSW	Lifshitz-Slyozov-Wagner
NoP	Number of particles
SEM	Scanning electron microscopy
SI	Système international d'unités (International System of Units)
SSA	Specific surface area
w/w	Weight by weight

Appendix D – Formula symbols

Symbol	Definition
A	Simulation constant
a	Accommodation coefficient
$\bar{A}$	Average ice crystal area
A_0	Surface area of an overlapping volume
A_c	Conjunction area
$\hat{A}_c$	Average conjunction area
A_{total}	Overall area of vision
b	Crystal nucleation order

B	Simulation constant
B_0	Volumetric nucleation rate
c_∞	Solubility of particle material
c_g	Solute concentration
c_g'	Solute concentration at maximum freeze-concentration
c_m^e	Equilibrium compositions for the *m*-phase
c_m^{SS}	Supersaturation in the matrix phase
$c_m^{initial}$	Initial matrix composition
c_p^e	Equilibrium compositions for the *p*-phase
D	Diffusion constant
dt	Duration between two time points
dx	Distance between two grid points in the x-coordinate
dy	Distance between two grid points in the y-coordinate
dz	Distance between two grid points in the z-coordinate
F	Free energy
f	Bulk free energy density
f_c	Chemical free energy density
f_e	External free energy density
f_g	Gradient free energy density
f_m	Mechanical free energy density
f^m	Free energy of the *m*-phase
f^p	Free energy of the *p*-phase
k	Isothermal recrystallisation rate
k_b	Kinetic parameter for crystal nucleation
L	Relaxation coefficient
M	Mobility coefficient
$m_{m,sim}$	Physical mass of the simulation domain
m_s	Mass of solute
M_v	Molecular mass of vapour
m_w	Mass of water
N_a	Number of conjunctions

N_p	Total number of particles
$N_{p,grid}$	Number of grid points occupied from the particulate phase
$N_{total,grid}$	Total number of grid points of the simulation domain
Nx	Number of grid points in the x-coordinate
Ny	Number of grid points in the y-coordinate
Nz	Number of grid points in the z-coordinate
P	Coefficient for the magnitude of the energy barrier between the *m*- and the *p*-phase
p_0	Saturation vapour pressure at solid phase
p_v^b	Partial vapour pressure in bulk vapour
Q	Coefficient for the magnitude of the energy barrier between the *n* particulate phases
r	Radius
R	Ideal gas constant
$\bar{r}$	Mean particle radius
r_0	Initial particle size
r_c	Critical radius
r_e	Circle equivalent diameter
r_{exp}	Experimentally determined circle equivalent radius
R_f	Freezing rate
r_{sim}	Sphere equivalent radius from three-dimensional simulations
T	Temperature
t	Time
T_a	Annealing temperature
t_a	Annealing time
T_c	Collapse temperature
T_{eu}	Eutectic temperature
T_f	Equilibrium freezing temperature
T_g	Glass transition temperature
T_g'	Glass transition temperature at maximum freeze-concentration
T_m	Melting temperature

T_m'	Onset temperature of melting
T_n	Nucleation temperature
t_r	Residence time
t_{sim}	Simulation time
V	Volume
V_f	Filling volume
V_p	Particle volume
V_{sim}	Volume of the simulation domain
W	Interpolation function
ω_w'	Water mass fraction in the maximum freeze-concentrated matrix phase
α	Conversion factor
Δ	Concentration difference between particle surface and liquid phase
ΔG	Gibbs free energy
η	Order parameter
κ_c	Gradient energy coefficients for composition
κ_η	Gradient energy coefficients for the order parameter
μ	Chemical potential
v	Molar volume
ρ	Density
ρ_m	Density of the matrix phase
σ	Surface tension
φ_p	Area or volume fraction of the particulate phase
ω_s	Mass fraction of solute
ω_w	Mass fraction of water
τ	Temporal conversion factor
χ_p	Mean curvature of the interface
γ	Interfacial energy density

Appendix E – Materials

The excipients and the packaging materials used in this work are listed in Table App. 1. All solutions were prepared with purified water and sterile filtered.

Table App. 1: Materials used in this work.

Material	Supplier
D-(+)-sucrose (NF grade)	Merck Millipore, Burlington, USA
D-(+)-trehalose dihydrate (NF grade)	VWR International, Radnor, USA
10R adaptIQ® vials	Schott, Muellheim, Germany
0.22 µm Millex®-GV filters	Merck Millipore, Burlington, USA

References

[1] Ward, Kevin R.; Matejtschuk, Paul (Hg.) (2019): Lyophilization of pharmaceuticals and biologicals. New technologies and approaches. New York, NY: Humana Press (Methods in pharmacology and toxicology).

[2] Rey, Louis; May, Joan Christine (Hg.) (2010): Freeze drying/lyophilization of pharmaceutical and biological products. 3rd ed. New York: Informa Healthcare (Drugs and the pharmaceutical sciences, 206).

[3] Ó'Fágáin, Ciarán (2004): Lyophilization of Proteins 244, S. 309–322. DOI: 10.1385/1-59259-655-x:309.

[4] Bjelošević, Maja; Zvonar Pobirk, Alenka; Planinšek, Odon; Ahlin Grabnar, Pegi (2020): Excipients in freeze-dried biopharmaceuticals: Contributions toward formulation stability and lyophilisation cycle optimisation. In: *International journal of pharmaceutics* 576, S. 119029. DOI: 10.1016/j.ijpharm.2020.119029.

[5] Pardeshi, Sagar R.; Deshmukh, Nilesh S.; Telange, Darshan R.; Nangare, Sopan N.; Sonar, Yogesh Y.; Lakade, Sameer H. et al. (2023): Process development and quality attributes for the freeze-drying process in pharmaceuticals, biopharmaceuticals and nanomedicine delivery: a state-of-the-art review. In: *Futur J Pharm Sci* 9 (1). DOI: 10.1186/s43094-023-00551-8.

[6] Teagarden, Dirk L.; Baker, David S. (2002): Practical aspects of lyophilization using non-aqueous co-solvent systems. In: *European journal of pharmaceutical sciences : official journal of the European Federation for Pharmaceutical Sciences* 15 (2), S. 115–133. DOI: 10.1016/s0928-0987(01)00221-4.

[7] Schneid, Stefan C.; Gieseler, Henning; Kessler, William J.; Luthra, Suman A.; Pikal, Michael J. (2011): Optimization of the secondary drying step in freeze drying using TDLAS technology. In: *AAPS PharmSciTech* 12 (1), S. 379–387. DOI: 10.1208/s12249-011-9600-7.

[8] Wagner, Wolfgang; Saul, A.; Pruss, A. (1994): International Equations for the Pressure Along the Melting and Along the Sublimation Curve of Ordinary Water Substance. In: *Journal of Physical and Chemical Reference Data* 23 (3), S. 515–527. DOI: 10.1063/1.555947.

[9] Liu, W. R.; Langer, R.; Klibanov, A. M. (1991): Moisture-induced aggregation of lyophilized proteins in the solid state. In: *Biotechnology and bioengineering* 37 (2), S. 177–184. DOI: 10.1002/bit.260370210.

[10] Ames, Jennifer M. (1992): The Maillard Reaction, S. 99–153. DOI: 10.1007/978-1-4684-9895-0_4.

[11] Akers, Michael J. (2016): Sterile Drug Products. DOI: 10.3109/9781420020564.

[12] Sadikoglu, H.; Ozdemir, M.; Seker, M. (2006): Freeze-Drying of Pharmaceutical Products: Research and Development Needs. In: *Drying Technology* 24 (7), S. 849–861. DOI: 10.1080/07373930600734018.

[13] Rambhatla, Shailaja; Ramot, Roee; Bhugra, Chandan; Pikal, Michael J. (2004): Heat and mass transfer scale-up issues during freeze drying: II. Control and characterization of the degree of supercooling. In: *AAPS PharmSciTech* 5 (4), e58. DOI: 10.1208/pt050458.

[14] Emteborg, Håkan; Zeleny, Reinhard; Charoud-Got, Jean; Martos, Gustavo; Lüddeke, Jörg; Schellin, Holger; Teipel, Katharina (2014): Infrared thermography for monitoring of freeze-drying processes: instrumental developments and preliminary results. In: *Journal of pharmaceutical sciences* 103 (7), S. 2088–2097. DOI: 10.1002/jps.24017.

[15] Patel, Sajal Manubhai; Nail, Steven L.; Pikal, Michael J.; Geidobler, Raimund; Winter, Gerhard; Hawe, Andrea et al. (2017): Lyophilized Drug Product Cake Appearance: What Is Acceptable? In: *Journal of pharmaceutical sciences* 106 (7), S. 1706–1721. DOI: 10.1016/j.xphs.2017.03.014.

[16] Jennings, Thomas A. (1999): Lyophilization. Introduction and basic principles. New York: Informa Healthcare.

[17] Landi, S.; Held, H. R. (1975): Effect of light on tuberculin purified protein derivative solutions. In: *The American review of respiratory disease* 111 (1), S. 52–61. DOI: 10.1164/arrd.1975.111.1.52.

[18] Gatlin, L. A.; Nail, S. L. (1994): Protein purification process engineering. Freeze drying: A practical overview. In: *Bioprocess technology* 18, S. 317–367.

[19] Jameel, Feroz; Alexeenko, Alina; Bhambhani, Akhilesh; Sacha, Gregory; Zhu, Tong; Tchessalov, Serguei et al. (2021): Recommended Best Practices for Lyophilization Validation-2021 Part I: Process Design and Modeling. In: *AAPS PharmSciTech* 22 (7), S. 221. DOI: 10.1208/s12249-021-02086-8.

[20] Kelley, Brian; Blank, Greg; Lee, Ann (2009): Downstream Processing of Monoclonal Antibodies: Current Practices and Future Opportunities, S. 1–23. DOI: 10.1002/9780470444894.ch1.

[21] U.S. Food and Drug Administration: Inactive Ingredient Field Descriptions. Online available at https://www.fda.gov/drugs/drug-approvals-and-databases/inactive-ingredient-field-descriptions.

[22] Rao, V. Ashutosh; Kim, Jennifer J.; Patel, Dipti S.; Rains, Kimberly; Estoll, Corey R. (2020): A Comprehensive Scientific Survey of Excipients Used in Currently Marketed, Therapeutic Biological Drug Products. In: *Pharmaceutical research* 37 (10), S. 200. DOI: 10.1007/s11095-020-02919-4.

[23] Rayaprolu, Bindhu Madhavi; Strawser, Jonathan J.; Anyarambhatla, Gopal (2018): Excipients in parenteral formulations: selection considerations and effective utilization with small molecules and biologics. In: *Drug development and industrial pharmacy* 44 (10), S. 1565–1571. DOI: 10.1080/03639045.2018.1483392.

[24] Meyer, Jeffrey D.; Nayar, Rajiv; Manning, Mark Cornell (2009): Impact of bulking agents on the stability of a lyophilized monoclonal antibody. In: *European journal of pharmaceutical sciences : official journal of the European Federation for Pharmaceutical Sciences* 38 (1), S. 29–38. DOI: 10.1016/j.ejps.2009.05.008.

[25] US Food and Drug Administration: FDA-approved drugs. Online available at https://www.accessdata.fda.gov/scripts/cder/daf/.

[26] Wang, D. Q.; Hey, J. M.; Nail, S. L. (2004): Effect of collapse on the stability of freeze-dried recombinant factor VIII and alpha-amylase. In: *Journal of pharmaceutical sciences* 93 (5), S. 1253–1263. DOI: 10.1002/jps.20065.

[27] Baheti, Ankit; Kumar, Lokesh; Bansal, Arvind K. (2010): Excipients used in lyophilization of small molecules. In: *Journal of Excipients and Food Chemicals* (1(1)).

[28] Larsen, Bjarke Strøm; Skytte, Jeppe; Svagan, Anna J.; Meng-Lund, Helena; Grohganz, Holger; Löbmann, Korbinian (2019): Using dextran of different molecular weights to achieve faster freeze-drying and improved storage stability of lactate dehydrogenase. In: *Pharmaceutical development and technology* 24 (3), S. 323–328. DOI: 10.1080/10837450.2018.1479866.

[29] Grasmeijer, N.; Stankovic, M.; Waard, H. de; Frijlink, H. W.; Hinrichs, W. L. J. (2013): Unraveling protein stabilization mechanisms: vitrification and water replacement in a glass transition temperature controlled system. In: *Biochimica et biophysica acta* 1834 (4), S. 763–769. DOI: 10.1016/j.bbapap.2013.01.020.

[30] Vilg, Jenny Veide; Undeland, Ingrid (2017): pH-driven solubilization and isoelectric precipitation of proteins from the brown seaweed Saccharina latissima-effects of osmotic shock, water volume and temperature. In: *Journal of applied phycology* 29 (1), S. 585–593. DOI: 10.1007/s10811-016-0957-6.

[31] Wu, Cindy; Shamblin, Sheri; Varshney, Dushyant; Shalaev, Evgenyi (2015): Advance Understanding of Buffer Behavior during Lyophilization, S. 25–41. DOI: 10.1007/978-1-4939-2383-0_3.

[32] Shalaev, Evgenyi Y.; Gatlin, Larry A. (2010): The Impact of Buffer on Solid-State Properties and Stability of Freeze-Dried Dosage Forms. In: Feroz Jameel und Susan Hershenson (Hg.): Formulation and process development strategies for manufacturing biopharmaceuticals. Hoboken, N.J.: Wiley, S. 507–519.

[33] Kannan, Aadithya; Shieh, Ian C.; Fuller, Gerald G. (2019): Linking aggregation and interfacial properties in monoclonal antibody-surfactant formulations. In: *Journal of colloid and interface science* 550, S. 128–138. DOI: 10.1016/j.jcis.2019.04.060.

[34] Lee, Hyo Jin; McAuley, Arnold; Schilke, Karl F.; McGuire, Joseph (2011): Molecular origins of surfactant-mediated stabilization of protein drugs. In: *Advanced drug delivery reviews* 63 (13), S. 1160–1171. DOI: 10.1016/j.addr.2011.06.015.

[35] Jennings, Thomas A. (1999): Effect of formulation on lyophilization.

[36] Kadoya, Saori; Fujii, Kahori; Izutsu, Ken-ichi; Yonemochi, Etsuo; Terada, Katsuhide; Yomota, Chikako; Kawanishi, Toru (2010): Freeze-drying of proteins with glass-forming oligosaccharide-derived sugar alcohols. In: *International journal of pharmaceutics* 389 (1-2), S. 107–113. DOI: 10.1016/j.ijpharm.2010.01.027.

[37] Starciuc, Tatiana; Malfait, Benjamin; Danede, Florence; Paccou, Laurent; Guinet, Yannick; Correia, Natalia T.; Hedoux, Alain (2020): Trehalose or Sucrose: Which of the Two Should be Used for Stabilizing Proteins in the Solid State? A Dilemma

Investigated by In Situ Micro-Raman and Dielectric Relaxation Spectroscopies During and After Freeze-Drying. In: *Journal of pharmaceutical sciences* 109 (1), S. 496–504. DOI: 10.1016/j.xphs.2019.10.055.

[38] Roos, Yrjö H. (2021): Glass Transition and Re-Crystallization Phenomena of Frozen Materials and Their Effect on Frozen Food Quality. In: *Foods (Basel, Switzerland)* 10 (2). DOI: 10.3390/foods10020447.

[39] Handle, Philip H.; Loerting, Thomas; Sciortino, Francesco (2017): Supercooled and glassy water: Metastable liquid(s), amorphous solid(s), and a no-man's land. In: *Proceedings of the National Academy of Sciences of the United States of America* 114 (51), S. 13336–13344. DOI: 10.1073/pnas.1700103114.

[40] Colucci-Mizenko, Lynn M.; Glicksman, Martin E.; Smith, Richard N. (1994): Thermal recalescence and mushy zone coarsening in undercooled melts. In: *JOM* 46 (1), S. 51–55. DOI: 10.1007/bf03222538.

[41] Tavakoli, Faryar; Davis, Stephen H.; Kavehpour, H. Pirouz (2015): Freezing of supercooled water drops on cold solid substrates: initiation and mechanism. In: *J Coat Technol Res* 12 (5), S. 869–875. DOI: 10.1007/s11998-015-9693-0.

[42] Akyurt, M.; Zaki, G.; Habeebullah, B. (2002): Freezing phenomena in ice–water systems. In: *Energy Conversion and Management* 43 (14), S. 1773–1789. DOI: 10.1016/s0196-8904(01)00129-7.

[43] Debenedetti, Pablo G.; Stanley, H. Eugene (2003): Supercooled and Glassy Water. In: *Physics Today* 56 (6), S. 40–46. DOI: 10.1063/1.1595053.

[44] Kasper, Julia Christina; Friess, Wolfgang (2011): The freezing step in lyophilization: physico-chemical fundamentals, freezing methods and consequences on process performance and quality attributes of biopharmaceuticals. In: *European journal of pharmaceutics and biopharmaceutics : official journal of Arbeitsgemeinschaft fur Pharmazeutische Verfahrenstechnik e.V* 78 (2), S. 248–263. DOI: 10.1016/j.ejpb.2011.03.010.

[45] Assegehegn, Getachew; La Brito-de Fuente, Edmundo; Franco, José M.; Gallegos, Críspulo (2019): The Importance of Understanding the Freezing Step and Its Impact on Freeze-Drying Process Performance. In: *Journal of pharmaceutical sciences* 108 (4), S. 1378–1395. DOI: 10.1016/j.xphs.2018.11.039.

[46] Wilson, P. W.; Haymet, A. D. J. (2009): Effect of solutes on the heterogeneous nucleation temperature of supercooled water: an experimental determination. In: *Physical chemistry chemical physics : PCCP* 11 (15), S. 2679–2682. DOI: 10.1039/b817585c.

[47] Fan, Zhongyun; Men, Hua (2022): Heterogeneous Nucleation and Grain Initiation on a Single Substrate. In: *Metals* 12 (9), S. 1454. DOI: 10.3390/met12091454.

[48] Petzold, Guillermo; Aguilera, José M. (2009): Ice Morphology: Fundamentals and Technological Applications in Foods. In: *Food Biophysics* 4 (4), S. 378–396. DOI: 10.1007/s11483-009-9136-5.

[49] Mysak, Lawrence A.; Hamilton, Kevin; Pruppacher, H. R.; Klett, J. D. (2010): Microphysics of Clouds and Precipitation 18. DOI: 10.1007/978-0-306-48100-0.

[50] Sear, Richard P. (2014): Quantitative studies of crystal nucleation at constant supersaturation: experimental data and models. In: *CrystEngComm* 16 (29), S. 6506–6522. DOI: 10.1039/c4ce00344f.

[51] Matsumoto, Masakazu; Saito, Shinji; Ohmine, Iwao (2002): Molecular dynamics simulation of the ice nucleation and growth process leading to water freezing. In: *Nature* 416 (6879), S. 409–413. DOI: 10.1038/416409a.

[52] Flores-Ramírez, Alma J.; García-Coronado, Pedro; Grajales-Lagunes, Alicia; García, Raúl González; Abud Archila, Miguel; Ruiz Cabrera, Miguel A. (2019): Freeze-Concentrated Phase and State Transition Temperatures of Mixtures of Low and High Molecular Weight Cryoprotectants. In: *Advances in Polymer Technology* 2019, S. 1–11. DOI: 10.1155/2019/5341242.

[53] Akamatsu, Silvère; Faivre, Gabriel; Moulinet, Sébastien (2001): The formation of lamellar-eutectic grains in thin samples. In: *Metall Mater Trans A* 32 (8), S. 2039–2048. DOI: 10.1007/s11661-001-0016-y.

[54] Ding, Zongye; Long, Weimin; Jiu, Yongtao; Zhong, Sujuan; Jiang, Danqing; Liu, Chuan et al. (2023): Formation and Morphological Transition of Diversified Eutectic Structures in Ag-Based Brazing Filler Metals with Sn Addition. In: *Crystals* 13 (1), S. 68. DOI: 10.3390/cryst13010068.

[55] Baker, Christopher G. J. (Hg.) (1997): Industrial drying of foods. 1. ed. London: Blackie Academic & Professional.

[56] Xu, Mengjie; Chen, Guangming; Zhang, Cunhai; Zhang, Shaozhi (2017): Study on the Unfrozen Water Quantity of Maximally Freeze-Concentrated Solutions for Multicomponent Lyoprotectants. In: *Journal of pharmaceutical sciences* 106 (1), S. 83–91. DOI: 10.1016/j.xphs.2016.05.007.

[57] Franks, Felix (2009): Freeze-drying of pharmaceuticals and biopharmaceuticals. Principles and practice. Repr. Cambridge: RSC Publishing.

[58] ROOS Y. (1991): Nonequilibrium ice formation in carbohydrate solutions. In: *Cryo-Lett* 12, S. 367–376. Online available at https://cir.nii.ac.jp/crid/1570291225453686784.

[59] Seifert, Ivonne; Bregolin, Alessandro; Fissore, Davide; Friess, Wolfgang (2020): Method development and analysis of the water content of the maximally freeze concentrated solution suitable for protein lyophilisation. In: *European journal of pharmaceutics and biopharmaceutics : official journal of Arbeitsgemeinschaft fur Pharmazeutische Verfahrenstechnik e.V* 153, S. 36–42. DOI: 10.1016/j.ejpb.2020.05.027.

[60] Franks, F. (1998): Freeze-drying of bioproducts: putting principles into practice. In: *European journal of pharmaceutics and biopharmaceutics : official journal of Arbeitsgemeinschaft fur Pharmazeutische Verfahrenstechnik e.V* 45 (3), S. 221–229. DOI: 10.1016/s0939-6411(98)00004-6.

[61] Craig, D. Q.; Royall, P. G.; Kett, V. L.; Hopton, M. L. (1999): The relevance of the amorphous state to pharmaceutical dosage forms: glassy drugs and freeze dried

systems. In: *International journal of pharmaceutics* 179 (2), S. 179–207. DOI: 10.1016/s0378-5173(98)00338-x.

[62] Hedberg, Sarah H. M.; Devi, Sharmila; Duralliu, Arnold; Williams, Daryl R. (2019): Mechanical Behavior and Structure of Freeze-Dried Cakes, S. 327–351. DOI: 10.1007/978-1-4939-8928-7_13.

[63] Doran, Pauline M. (2013): Bioprocess Engineering Principles: Elsevier.

[64] Mubarak, Nabisab Mujawar; Anwar, Mahmood; Debnath, Sujan; Sudin, Izman (Hg.) (2023): Fundamentals of Biomaterials. A Supplementary Textbook. 1st ed. 2023. Singapore: Springer Nature Singapore; Imprint Springer.

[65] Telis, V.R.N.; Telis-Romero, J.; Mazzotti, H. B.; Gabas, A. L. (2007): Viscosity of Aqueous Carbohydrate Solutions at Different Temperatures and Concentrations. In: *International Journal of Food Properties* 10 (1), S. 185–195. DOI: 10.1080/10942910600673636.

[66] Rumble, John R. (Hg.) (2021): CRC handbook of chemistry and physics. 102nd edition 2021-2022. Boca Raton, London, New York: CRC Press.

[67] Kharatyan, Tigran; Igawa, Shunya; Gopireddy, Srikanth R.; Ogawa, Toru; Kodama, Tatsuhiro; Scherließ, Regina; Urbanetz, Nora A. (2023): Impact of post-freeze annealing on shrinkage of sucrose and trehalose lyophilisates. In: *International journal of pharmaceutics* 641, S. 123051. DOI: 10.1016/j.ijpharm.2023.123051.

[68] Kharatyan, Tigran; Gopireddy, Srikanth R.; Ogawa, Toru; Kodama, Tatsuhiro; Nishimoto, Norihiro; Osada, Sayaka et al. (2022): Quantitative Analysis of Glassy State Relaxation and Ostwald Ripening during Annealing Using Freeze-Drying Microscopy. In: *Pharmaceutics* 14 (6). DOI: 10.3390/pharmaceutics14061176.

[69] Tchessalov, Serguei; Maglio, Vito; Kazarin, Petr; Alexeenko, Alina; Bhatnagar, Bakul; Sahni, Ekneet; Shalaev, Evgenyi (2023): Practical Advice on Scientific Design of Freeze-Drying Process: 2023 Update. In: *Pharmaceutical research* 40 (10), S. 2433–2455. DOI: 10.1007/s11095-023-03607-9.

[70] Nakagawa, Kyuya; Tamiya, Shinri; Do, Gabsoo; Kono, Shinji; Ochiai, Takaaki (2018): Observation of glassy state relaxation during annealing of frozen sugar solutions by X-ray computed tomography. In: *European journal of pharmaceutics and biopharmaceutics : official journal of Arbeitsgemeinschaft fur Pharmazeutische Verfahrenstechnik e.V* 127, S. 279–287. DOI: 10.1016/j.ejpb.2018.02.027.

[71] Thomik, Maximilian; Gruber, Sebastian; Kaestner, Anders; Foerst, Petra; Tsotsas, Evangelos; Vorhauer-Huget, Nicole (2022): Experimental Study of the Impact of Pore Structure on Drying Kinetics and Sublimation Front Patterns. In: *Pharmaceutics* 14 (8). DOI: 10.3390/pharmaceutics14081538.

[72] Klinmalai, Phatthranit; Shibata, Mario; Hagiwara, Tomoaki (2017): Recrystallization of Ice Crystals in Trehalose Solution at Isothermal Condition. In: *Food Biophysics* 12 (4), S. 404–411. DOI: 10.1007/s11483-017-9496-1.

[73] Madras, Giridhar; McCoy, Benjamin J. (2003): Temperature effects for crystal growth: a distribution kinetics approach. In: *Acta Materialia* 51 (7), S. 2031–2040. DOI: 10.1016/S1359-6454(02)00621-3.

[74] Chow, T. S. (2000): Glassy—State Relaxation, S. 81–99. DOI: 10.1007/978-1-4612-2108-1_5.

[75] Patapoff, T.W., Overcashier, D.E. (2002): The importance of freezing on lyophilization cycle development. In: *Biopharm* (15(3)), S. 16–21.

[76] Lim, Jun Yeul; Lim, Dae Gon; Kim, Ki Hyun; Park, Sang-Koo; Jeong, Seong Hoon (2018): Effects of annealing on the physical properties of therapeutic proteins during freeze drying process. In: *International journal of biological macromolecules* 107 (Pt A), S. 730–740. DOI: 10.1016/j.ijbiomac.2017.09.041.

[77] Costantino, Henry R.; Pikal, Michael J. (2004): Lyophilization of biopharmaceuticals. Arlington, Va.: AAPS Press (Biotechnology, 2).

[78] Bexiga, N. M.; Bloise, A. C.; Alencar, A. M.; Stephano, M. A. (2018): Freeze-drying of ovalbumin-loaded carboxymethyl chitosan nanocapsules: Impact of freezing and annealing procedures on physicochemical properties of the formulation during dried storage. In: *Drying Technology* 36 (4), S. 400–417. DOI: 10.1080/07373937.2017.1335752.

[79] Krzykowski, Andrzej; Dziki, Dariusz; Rudy, Stanisław; Polak, Renata; Biernacka, Beata; Gawlik-Dziki, Urszula; Janiszewska-Turak, Emilia (2023): Effect of Air-Drying and Freeze-Drying Temperature on the Process Kinetics and Physicochemical Characteristics of White Mulberry Fruits (Morus alba L.). In: *Processes* 11 (3), S. 750. DOI: 10.3390/pr11030750.

[80] Bogdanova, Ekaterina; Fureby, Anna Millqvist; Kocherbitov, Vitaly (2022): Influence of Cooling Rate on Ice Crystallization and Melting in Sucrose-Water System. In: *Journal of pharmaceutical sciences* 111 (7), S. 2030–2037. DOI: 10.1016/j.xphs.2022.01.027.

[81] MacKenzie, A. P. (1977): Non-equilibrium freezing behaviour of aqueous systems. In: *Philosophical transactions of the Royal Society of London. Series B, Biological sciences* 278 (959), S. 167–189. DOI: 10.1098/rstb.1977.0036.

[82] Lim, Jun Yeul; Lim, Dae Gon; Kim, Ki Hyun; Park, Sang-Koo; Jeong, Seong Hoon (2018): Effects of annealing on the physical properties of therapeutic proteins during freeze drying process. In: *International journal of biological macromolecules* 107 (Pt A), S. 730–740. DOI: 10.1016/j.ijbiomac.2017.09.041.

[83] Fang, Rui; Bogner, Robin H.; Nail, Steven L.; Pikal, Michael J. (2020): Stability of Freeze-Dried Protein Formulations: Contributions of Ice Nucleation Temperature and Residence Time in the Freeze-Concentrate. In: *Journal of pharmaceutical sciences* 109 (6), S. 1896–1904. DOI: 10.1016/j.xphs.2020.02.014.

[84] Horn, Jacqueline; Friess, Wolfgang (2018): Detection of Collapse and Crystallization of Saccharide, Protein, and Mannitol Formulations by Optical Fibers in Lyophilization. In: *Frontiers in chemistry* 6, S. 4. DOI: 10.3389/fchem.2018.00004.

[85] Pikal, Michael J.; Shah, Saroj (1990): The collapse temperature in freeze drying: Dependence on measurement methodology and rate of water removal from the glassy phase. In: *International journal of pharmaceutics* 62 (2-3), S. 165–186. DOI: 10.1016/0378-5173(90)90231-r.

[86] Searles, J. A.; Carpenter, J. F.; Randolph, T. W. (2001): The ice nucleation temperature determines the primary drying rate of lyophilization for samples frozen on a temperature-controlled shelf. In: *Journal of pharmaceutical sciences* 90 (7), S. 860–871. DOI: 10.1002/jps.1039.

[87] Amidon, Gordon L.; Lee, Ping I.; Topp, Elizabeth M. (2000): Transport processes in pharmaceutical systems. New York: M. Dekker (Drugs and the pharmaceutical sciences, v. 102). Online available at https://permalink.obvsg.at/.

[88] Nail, Steven; Tchessalov, Serguei; Shalaev, Evgenyi; Ganguly, Arnab; Renzi, Ernesto; Dimarco, Frank et al. (2017): Recommended Best Practices for Process Monitoring Instrumentation in Pharmaceutical Freeze Drying-2017. In: *AAPS PharmSciTech* 18 (7), S. 2379–2393. DOI: 10.1208/s12249-017-0733-1.

[89] Pikal, Michael; Shah, Saroj; Roy, Michael; Putman, Rick (1990): The secondary drying stage of freeze drying: drying kinetics as a function of temperature and chamber pressure. In: *International journal of pharmaceutics* 60 (3), S. 203–207. DOI: 10.1016/0378-5173(90)90074-e.

[90] Kowalski, Stefan Jan; Rajewska, Kinga (2002): Drying-induced stresses in elastic and viscoelastic saturated materials. In: *Chemical Engineering Science* 57 (18), S. 3883–3892. DOI: 10.1016/s0009-2509(02)00307-x.

[91] Ullrich, Sabine; Seyferth, Stefan; Lee, Geoffrey (2015): Measurement of Shrinkage and Cracking in Lyophilized Amorphous Cakes. Part II: Kinetics. In: *Pharmaceutical research* 32 (8), S. 2503–2515. DOI: 10.1007/s11095-015-1639-9.

[92] Ullrich, Sabine; Seyferth, Stefan; Lee, Geoffrey (2015): Measurement of shrinkage and cracking in lyophilized amorphous cakes. Part I: final-product assessment. In: *Journal of pharmaceutical sciences* 104 (1), S. 155–164. DOI: 10.1002/jps.24284.

[93] Ullrich, Sabine (2014): Quantitative measurements of shrinkage and cracking during freeze-drying of amorphous cakes (PhD thesis).

[94] Rambhatla, S.; Obert, J. P.; Luthra, S.; Bhugra, C.; Pikal, Michael J. (2005): Cake shrinkage during freeze drying: a combined experimental and theoretical study. In: *Pharmaceutical development and technology* 10 (1), S. 33–40. DOI: 10.1081/pdt-35871.

[95] Hsu, C. C.; Ward, C. A.; Pearlman, R.; Nguyen, H. M.; Yeung, D. A.; Curley, J. G. (1992): Determining the optimum residual moisture in lyophilized protein pharmaceuticals. In: *Developments in biological standardization* 74, 255-70; discussion 271.

[96] Breen, E. D.; Curley, J. G.; Overcashier, D. E.; Hsu, C. C.; Shire, S. J. (2001): Effect of moisture on the stability of a lyophilized humanized monoclonal antibody formulation. In: *Pharmaceutical research* 18 (9), S. 1345–1353. DOI: 10.1023/a:1013054431517.

[97] Lo Presti, Ken; Frieß, Wolfgang (2021): Adjustment of specific residual moisture levels in completely freeze-dried protein formulations by controlled spiking of small water volumes. In: *European journal of pharmaceutics and biopharmaceutics :*

official journal of Arbeitsgemeinschaft fur Pharmazeutische Verfahrenstechnik e.V 169, S. 292–296. DOI: 10.1016/j.ejpb.2021.10.011.

[98] Colucci, Domenico; Fissore, Davide; Barresi, Antonello A.; Braatz, Richard D. (2020): A new mathematical model for monitoring the temporal evolution of the ice crystal size distribution during freezing in pharmaceutical solutions. In: *European journal of pharmaceutics and biopharmaceutics : official journal of Arbeitsgemeinschaft fur Pharmazeutische Verfahrenstechnik e.V* 148, S. 148–159. DOI: 10.1016/j.ejpb.2020.01.004.

[99] Sanz, E.; Vega, C.; Espinosa, J. R.; Caballero-Bernal, R.; Abascal, J. L. F.; Valeriani, C. (2013): Homogeneous ice nucleation at moderate supercooling from molecular simulation. In: *Journal of the American Chemical Society* 135 (40), S. 15008–15017. DOI: 10.1021/ja4028814.

[100] Crovetto, Rosa; Fernández-Prini, R.; Japas, María Laura (1982): Solubilities of inert gases and methane in H2O and in D2O in the temperature range of 300 to 600 K. In: *The Journal of Chemical Physics* 76 (2), S. 1077–1086. DOI: 10.1063/1.443074.

[101] Blond, G. (1988): Velocity of linear crystallization of ice in macromolecular systems. In: *Cryobiology* 25 (1), S. 61–66. DOI: 10.1016/0011-2240(88)90021-1.

[102] MUHR, A. H.; BLANSHARD, J. M. V. (1986): Effect of polysaccharide stabilizers on the rate of growth of ice. In: *Int J of Food Sci Tech* 21 (6), S. 683–710. DOI: 10.1111/ijfs1986216683.

[103] Theissmann, R.; Fendrich, M.; Zinetullin, R.; Guenther, G.; Schierning, G.; Wolf, D. E. (2008): Crystallographic reorientation and nanoparticle coalescence. In: *Phys. Rev. B* 78 (20). DOI: 10.1103/PhysRevB.78.205413.

[104] Niethammer, Barbara (2008): Effective Theories for Ostwald Ripening, S. 223–243. DOI: 10.1093/acprof:oso/9780199239252.003.0010.

[105] Lifshitz, I. M.; Slyozov, V. V. (1961): The kinetics of precipitation from supersaturated solid solutions. In: *Journal of Physics and Chemistry of Solids* 19 (1-2), S. 35–50. DOI: 10.1016/0022-3697(61)90054-3.

[106] Baldan, A. (2002): Review Progress in Ostwald ripening theories and their applications to nickel-base superalloys Part I: Ostwald ripening theories. In: *Journal of Materials Science* 37 (11), S. 2171–2202. DOI: 10.1023/A:1015388912729.

[107] Beech, Karen E.; Biddlecombe, James G.; van der Walle, Christopher F.; Stevens, Lee A.; Rigby, Sean P.; Burley, Jonathan C.; Allen, Stephanie (2015): Insights into the influence of the cooling profile on the reconstitution times of amorphous lyophilized protein formulations. In: *European journal of pharmaceutics and biopharmaceutics : official journal of Arbeitsgemeinschaft fur Pharmazeutische Verfahrenstechnik e.V* 96, S. 247–254. DOI: 10.1016/j.ejpb.2015.07.029.

[108] Arsiccio, A.; Sparavigna, A. C.; Pisano, R.; Barresi, A. A. (2019): Measuring and predicting pore size distribution of freeze-dried solutions. In: *Drying Technology* 37 (4), S. 435–447. DOI: 10.1080/07373937.2018.1430042.

[109] Aston, Robyn; Sewell, Kim; Klein, Travis; Lawrie, Gwen; Grøndahl, Lisbeth (2016): Evaluation of the impact of freezing preparation techniques on the characterisation

of alginate hydrogels by cryo-SEM. In: *European Polymer Journal* 82, S. 1–15. DOI: 10.1016/j.eurpolymj.2016.06.025.

[110] Vetráková, Ľubica; Neděla, Vilém; Runštuk, Jiří; Tihlaříková, Eva; Heger, Dominik; Shalaev, Evgenyi (2020): Dynamical in-situ observation of the lyophilization and vacuum-drying processes of a model biopharmaceutical system by an environmental scanning electron microscope. In: *International journal of pharmaceutics* 585, S. 119448. DOI: 10.1016/j.ijpharm.2020.119448.

[111] Pang, Tao (2012): An introduction to computational physics. Second edition. New York: Cambridge University Press.

[112] Greiner, David (2021): Numerical Simulation in Physics and Engineering. Lecture Notes of the XVIII 'Jacques-Louis Lions' Spanish-French School. Unter Mitarbeit von María Isabel Asensio und Rafael Montenegro. Cham: Springer International Publishing AG (SEMA SIMAI Springer Ser, v.24). Online available at https://ebookcentral.proquest.com/lib/kxp/detail.action?docID=6533317.

[113] Holz, K.-P. (1978): Simulation of tidal river dynamics 1, S. 145–156. DOI: 10.1007/978-3-642-46416-4_11.

[114] Moon, Min-Yeong; Cho, Hyunkyoo; Choi, K. K.; Gaul, Nicholas; Lamb, David; Gorsich, David (2018): Confidence-based reliability assessment considering limited numbers of both input and output test data. In: *Struct Multidisc Optim* 57 (5), S. 2027–2043. DOI: 10.1007/S00158-018-1900-Z.

[115] Barresi, Antonello A.; Rasetto, Valeria; Marchisio, Daniele L. (2018): Use of computational fluid dynamics for improving freeze-dryers design and process understanding. Part 1: Modelling the lyophilisation chamber. In: *European journal of pharmaceutics and biopharmaceutics : official journal of Arbeitsgemeinschaft fur Pharmazeutische Verfahrenstechnik e.V* 129, S. 30–44. DOI: 10.1016/j.ejpb.2018.05.008.

[116] PETITTI, MIRIAM; Barresi, Antonello A.; Marchisio, Daniele L. (2013): CFD modelling of condensers for freeze-drying processes. In: *Sadhana* 38 (6), S. 1219–1239. DOI: 10.1007/s12046-013-0155-z.

[117] Rosa, Mónica; Tiago, João M.; Singh, Satish K.; Geraldes, Vítor; Rodrigues, Miguel A. (2016): Improving Heat Transfer at the Bottom of Vials for Consistent Freeze Drying with Unidirectional Structured Ice. In: *AAPS PharmSciTech* 17 (5), S. 1049–1059. DOI: 10.1208/s12249-015-0437-3.

[118] Cheng, Chin-Chi; Tsai, Shian-Min; Cheng, Hong-Ping; Chen, Chun-Hung (2014): Analysis for heat transfer enhancement of helical and electrical heating tube heat exchangers in vacuum freeze-drying plant. In: *International Communications in Heat and Mass Transfer* 58, S. 111–117. DOI: 10.1016/j.icheatmasstransfer.2014.08.032.

[119] Zadravec, Matej; Časar, Žiga; Ravnik, Jure; Hriberšek, MatjaŽ (2020): CFD based determination of sublimation mass flux for lyophilization inside a vial. In: *Int. J. CMEM* 8 (1), S. 47–60. DOI: 10.2495/cmem-v8-n1-47-60.

[120] Zhu, Tong; Moussa, Ehab M.; Witting, Madeleine; Zhou, Deliang; Sinha, Kushal; Hirth, Mario et al. (2018): Predictive models of lyophilization process for development, scale-up/tech transfer and manufacturing. In: *European journal of pharmaceutics and biopharmaceutics : official journal of Arbeitsgemeinschaft fur Pharmazeutische Verfahrenstechnik e.V* 128, S. 363–378. DOI: 10.1016/j.ejpb.2018.05.005.

[121] Luo, Chun; Mi, Sha; Zhou, Naijun; Liu, Zhiqiang; Cai, Lingling (2022): Modelling the primary drying stage of the spray freeze drying process based on the non-equilibrium formulation. In: *International Journal of Heat and Mass Transfer* 188, S. 122659. DOI: 10.1016/j.ijheatmasstransfer.2022.122659.

[122] Arsiccio, Andrea; Barresi, Antonello A.; Pisano, Roberto (2017): Prediction of Ice Crystal Size Distribution after Freezing of Pharmaceutical Solutions. In: *Crystal Growth & Design* 17 (9), S. 4573–4581. DOI: 10.1021/acs.cgd.7b00319.

[123] Geslin, Pierre-Antoine; McCue, Ian; Gaskey, Bernard; Erlebacher, Jonah; Karma, Alain (2015): Topology-generating interfacial pattern formation during liquid metal dealloying. In: *Nature communications* 6, S. 8887. DOI: 10.1038/ncomms9887.

[124] Radhakrishnan, Balasubramaniam; Gorti, Sarma B.; Turner, John A.; Acharya, Ranadip; Sharon, John A.; Staroselsky, Alexander; El-Wardany, Tahany (2019): Phase Field Simulations of Microstructure Evolution in IN718 using a Surrogate Ni–Fe–Nb Alloy during Laser Powder Bed Fusion. In: *Metals* 9 (1), S. 14. DOI: 10.3390/met9010014.

[125] Ansari, Talha Qasim; Huang, Haitao; Shi, San-Qiang (2021): Phase field modeling for the morphological and microstructural evolution of metallic materials under environmental attack. In: *npj Comput Mater* 7 (1).

DOI: 10.1038/s41524-021-00612-7.

[126] Biner, S. Bulent (2017): Programming Phase-Field Modeling. Cham: Springer International Publishing.

[127] Zerihun, Nega A.; Steinbach, Ingo (2016): Phase field modeling of intercalation kinetics: a finite interface dissipation approach. In: *MRS Communications* 6 (3), S. 270–282. DOI: 10.1557/mrc.2016.31.

[128] van der Sman, R.G.M. (2016): Phase field simulations of ice crystal growth in sugar solutions. In: *International Journal of Heat and Mass Transfer* 95, S. 153–161. DOI: 10.1016/j.ijheatmasstransfer.2015.11.089.

[129] Fan, Tai-Hsi; Li, Ji-Qin; Minatovicz, Bruna; Soha, Elizabeth; Sun, Li; Patel, Sajal et al. (2018): Phase-Field Modeling of Freeze Concentration of Protein Solutions. In: *Polymers* 11 (1). DOI: 10.3390/polym11010010.

[130] Li, Ji-Qin; Fan, Tai-Hsi (2020): Phase-field modeling of macroscopic freezing dynamics in a cylindrical vessel. In: *International Journal of Heat and Mass Transfer* 156, S. 119915. DOI: 10.1016/j.ijheatmasstransfer.2020.119915.

[131] Li, Ji-Qin; Rahman, Mohsina; Patel, Sajal; Bogner, Robin H.; Fan, Tai-Hsi (2022): Dendritic Morphology and Growth Inhibition of Ice Crystals in Sucrose Solutions. In: *Crystal Growth & Design* 22 (12), S. 6917–6927. DOI: 10.1021/acs.cgd.2c00544.

[132] Mukherjee, R.; Abinandanan, T. A.; Gururajan, M. P. (2009): Phase field study of precipitate growth: Effect of misfit strain and interface curvature. In: *Acta Materialia* 57 (13), S. 3947–3954. DOI: 10.1016/j.actamat.2009.04.056.

[133] Delly, John Gustav (2017): Essentials of polarized light microscopy and ancillary techniques. Drive: Hooke College of Applied Sciences.

[134] Deck, Leif-Thore; Ochsenbein, David R.; Mazzotti, Marco (2022): Stochastic shelf-scale modeling framework for the freezing stage in freeze-drying processes. In: *International journal of pharmaceutics* 613, S. 121276. DOI: 10.1016/j.ijpharm.2021.121276.

[135] Mockus, Linas; LeBlond, David; Basu, Prabir K.; Shah, Rakhi B.; Khan, Mansoor A. (2011): A QbD case study: Bayesian prediction of lyophilization cycle parameters. In: *AAPS PharmSciTech* 12 (1), S. 442–448. DOI: 10.1208/s12249-011-9598-x.

[136] Nakagawa, Kyuya; Hottot, Aurélie; Vessot, Séverine; Andrieu, Julien (2007): Modeling of freezing step during freeze-drying of drugs in vials. In: *AIChE Journal* 53 (5), S. 1362–1372. DOI: 10.1002/aic.11147.

[137] Passot, Stéphanie; Tréléa, Ioan Cristian; Marin, Michèle; Galan, Miquel; Morris, G. John; Fonseca, Fernanda (2009): Effect of controlled ice nucleation on primary drying stage and protein recovery in vials cooled in a modified freeze-dryer. In: *Journal of biomechanical engineering* 131 (7), S. 74511. DOI: 10.1115/1.3143034.

[138] Konstantinidis, Alex K.; Kuu, Wei; Otten, Lori; Nail, Steven L.; Sever, Robert R. (2011): Controlled nucleation in freeze-drying: effects on pore size in the dried product layer, mass transfer resistance, and primary drying rate. In: *Journal of pharmaceutical sciences* 100 (8), S. 3453–3470. DOI: 10.1002/jps.22561.

[139] Petersen, Ansgar; Rau, Guenter; Glasmacher, Birgit (2006): Reduction of primary freeze-drying time by electric field induced ice nucleus formation. In: *Heat Mass Transfer* 42 (10), S. 929–938. DOI: 10.1007/s00231-006-0153-3.

[140] Geidobler, R.; Winter, G. (2013): Controlled ice nucleation in the field of freeze-drying: fundamentals and technology review. In: *European journal of pharmaceutics and biopharmaceutics : official journal of Arbeitsgemeinschaft fur Pharmazeutische Verfahrenstechnik e.V* 85 (2), S. 214–222. DOI: 10.1016/j.ejpb.2013.04.014.

[141] Siódmiak, Jacek; Gadomski, Adam (2022): Spherulites: How Do They Emerge at an Onset of Nonequilibrium Kinetic-Thermodynamic and Structural Singularity Addressing Conditions? In: *Entropy (Basel, Switzerland)* 24 (5). DOI: 10.3390/e24050663.

[142] Libbrecht, Kenneth G. (2005): The physics of snow crystals. In: *Rep. Prog. Phys.* 68 (4), S. 855–895. DOI: 10.1088/0034-4885/68/4/R03.

[143] Chan, Wing S.; Mah, Merlin L.; Voight, Donald E.; Fitzpatrick, Joan J.; Talghader, Joseph J. (2014): Crystal orientation measurements using transmission and backscattering. In: *J. Glaciol.* 60 (224), S. 1135–1139. DOI: 10.3189/2014JoG14J071.

[144] Paskover, Yuri; Xie, Dan; Laforge, François O.; Rabitz, Herschel (2014): Selectively addressing optically nonlinear nanocrystals by polarization-shaped ultrafast laser pulses. In: *J. Opt. Soc. Am. B* 31 (5), S. 1165. DOI: 10.1364/JOSAB.31.001165.

[145] Hsu, C. C.; Nguyen, H. M.; Yeung, D. A.; Brooks, D. A.; Koe, G. S.; Bewley, T. A.; Pearlman, R. (1995): Surface denaturation at solid-void interface--a possible pathway by which opalescent particulates form during the storage of lyophilized tissue-type plasminogen activator at high temperatures. In: *Pharmaceutical research* 12 (1), S. 69–77. DOI: 10.1023/a:1016270103863.

[146] Perez, Michel (2005): Gibbs-Thomson effects in phase transformations. In: *Scripta Materialia* 52 (8), S. 709–712. DOI: 10.1016/j.scriptamat.2004.12.026.

[147] Wang, S.-L.; Sekerka, R. F.; Wheeler, A. A.; Murray, B. T.; Coriell, S. R.; Braun, R. J.; McFadden, G. B. (1993): Thermodynamically-consistent phase-field models for solidification. In: *Physica D: Nonlinear Phenomena* 69 (1-2), S. 189–200. DOI: 10.1016/0167-2789(93)90189-8.

[148] Chen, L. Q.; Shen, Jie (1998): Applications of semi-implicit Fourier-spectral method to phase field equations. In: *Computer Physics Communications* 108 (2-3), S. 147–158. DOI: 10.1016/S0010-4655(97)00115-X.

[149] Chen, C.; Nguyen, T.; Braddock, R. (1990): Relationship Between Freezing Point Depression and Solute Composition of Fruit Juice Systems. In: *Journal of Food Science* 55 (2), S. 566–567. DOI: 10.1111/j.1365-2621.1990.tb06815.x.

[150] Lescure, J. P. (1995): Analysis of sucrose solutions. In: M. Mathlouthi und P. Reiser (Hg.): Sucrose. Properties and Applications. Boston, MA, s.l.: Springer US, S. 155–185.

[151] Blond, Geneviève; Simatos, Denise; Catté, Marianne; Dussap, Claude Gilles; Gros, Jean Bernard (1997): Modeling of the water-sucrose state diagram below 0 °C. In: *Carbohydrate Research* 298 (3), S. 139–145. DOI: 10.1016/s0008-6215(96)00313-8.

[152] Roos, Yrjö (1993): Melting and glass transitions of low molecular weight carbohydrates. In: *Carbohydrate Research* 238, S. 39–48. DOI: 10.1016/0008-6215(93)87004-c.

[153] Miller, D. P.; Pablo, J. J. de; Corti, H. (1997): Thermophysical properties of trehalose and its concentrated aqueous solutions. In: *Pharmaceutical research* 14 (5), S. 578–590. DOI: 10.1023/a:1012192725996.

[154] Slade, L.; Levine, Harry (1988): Non-equilibrium behavior of small carbohydrate-water systems. In: *Pure and Applied Chemistry* 60 (12), S. 1841–1864. DOI: 10.1351/pac198860121841.

[155] Townsend, Adam K.; Wilson, Helen J. (2017): Frictional shear thickening in suspensions: The effect of rigid asperities. In: *Physics of Fluids* 29 (12), Artikel 121607. DOI: 10.1063/1.4989929.

[156] Wu, Yugong (2003): Bulk and interior packing densities of random close packing of hard spheres. In: *Journal of Materials Science* 38 (9), S. 2019–2025. DOI: 10.1023/a:1023597707363.

[157] Abell, A. B.; Willis, K. L.; Da Lange (1999): Mercury Intrusion Porosimetry and Image Analysis of Cement-Based Materials. In: *Journal of colloid and interface science* 211 (1), S. 39–44. DOI: 10.1006/jcis.1998.5986.

[158] Rouquerol, J.; Avnir, D.; Fairbridge, C. W.; Everett, D. H.; Haynes, J. M.; Pernicone, N. et al. (1994): Recommendations for the characterization of porous solids (Technical Report). In: *Pure and Applied Chemistry* 66 (8), S. 1739–1758. DOI: 10.1351/pac199466081739.

[159] Jang, Eun-Suk; Kang, Chun-Won (2022): An experimental study on pore structural changes of ultrasonic treated Korean paulownia (Paulownia coreana). In: *Wood Sci Technol* 56 (3), S. 883–898. DOI: 10.1007/s00226-022-01382-1.

[160] Duralliu, Arnold; Matejtschuk, Paul; Williams, Daryl R. (2019): Measuring the specific surface area (SSA) of freeze-dried biologics using inverse gas chromatography. In: *European journal of pharmaceutics and biopharmaceutics : official journal of Arbeitsgemeinschaft fur Pharmazeutische Verfahrenstechnik e.V* 142, S. 216–221. DOI: 10.1016/j.ejpb.2019.06.026.

[161] Hołyst, Robert; Litniewski, Marek; Jakubczyk, Daniel (2015): A molecular dynamics test of the Hertz-Knudsen equation for evaporating liquids. In: *Soft matter* 11 (36), S. 7201–7206. DOI: 10.1039/c5sm01508a.

[162] Wu, Nanhua; Lu, Xiaohua; An, Rong; Ji, Xiaoyan (2021): Thermodynamic analysis and modification of Gibbs–Thomson equation for melting point depression of metal nanoparticles. In: *Chinese Journal of Chemical Engineering* 31, S. 198–205. DOI: 10.1016/j.cjche.2020.11.035.

[163] M.P. Gururajan (2006): Elastic Inhomogeneity Effects on Microstructures: A Phase Field Study (PhD thesis).

[164] Moelans, Nele; Blanpain, Bart; Wollants, Patrick (2008): An introduction to phase-field modeling of microstructure evolution. In: *Calphad* 32 (2), S. 268–294. DOI: 10.1016/j.calphad.2007.11.003.

Abstract

This work explores the impact of freezing and annealing conditions on the microstructure of lyophilisates, using a combination of experimental techniques, such as freeze-drying microscopy and differential scanning calorimetry, and a theoretical phase-field model.

The research initially focused on how temperature ramps in freeze-dryers influence the recalescence and crystallisation phases, where the temperature in samples rises during freezing due to an exothermic phase transition. Detailed temperature profiling within vials established a correlation between nucleation temperature and the duration of the recalescence and crystallisation phases. Findings indicated that lower nucleation temperatures reduce the period of elevated temperatures, which is crucial during the initial freezing stage.

This study further investigated the variation of recalescence and crystallisation at different heights within a vial by strategically positioning thermocouples. It was determined that the rise in temperature not only depends on the filling volume but also on the measurement height. Typically, larger filling volumes resulted in a more prolonged temperature increase at higher positions within the partially frozen solution, a phenomenon that might contribute to the heterogeneity of pore sizes in lyophilisates.

Moreover, this study examined the microstructural effects of recalescence and crystallisation using a freeze-drying microscope. In cases without a temperature increase, a fine network of crystalline (ice) and amorphous (disaccharides and unfrozen water) phases was observed, complicating phase differentiation. Conversely, samples subjected to controlled temperature increases mimicking in-vial conditions during recalescence and crystallisation showed distinct, grain-like ice crystals, which are comparable to the pores observed in lyophilisates.

To complement experimental observations, a two-dimensional phase-field model was developed, later expanded to three dimensions, to simulate and predict morphological changes within the lyophilisate during annealing. This model was calibrated using data from sucrose and trehalose solutions, gathered from both experiments and literature. The simulations not only provided insights into the dynamics of ice crystal growth and the distribution changes during annealing but also examined additional parameter such as the surface area of the matrix phase, as well as the conjunction areas between neighbouring ice

crystals. Furthermore, the implications of the microstructural changes during annealing on practical freeze-drying were discussed.

In conclusion, this work highlights the complex interplay between processing conditions and microstructural outcomes in lyophilisates. It emphasises the need for further research, driven by both experimental and simulation approaches, to deepen our understanding of these processes. This study serves as a crucial step in bridging the gap between simulation predictions and experimental validations, providing a comprehensive three-dimensional dataset of the microstructure, which lays the groundwork for future analytical and simulation studies in this field.

Zusammenfassung

Diese Arbeit untersucht den Einfluss von Gefrier- und Temperbedingungen auf die Mikrostruktur von Lyophilisaten, wobei eine Kombination aus experimentellen Techniken wie Gefriertrocknungsmikroskopie und Differenzkalorimetrie sowie ein theoretisches Phasenfeldmodell verwendet wird.

Die Untersuchung konzentrierte sich zunächst darauf, wie Temperaturrampen in Gefriertrocknern die Rekaleszenz- und Kristallisationsphasen beeinflussen, in denen die Temperatur in den Proben aufgrund eines exothermen Phasenübergangs während des Einfrierens ansteigt. Detaillierte Temperaturprofile innerhalb der Problenfläschchen deuteten auf einen Zusammenhang zwischen Nukleationstemperatur und der Dauer der Rekaleszenz- und Kristallisationsphasen. Die Ergebnisse zeigten, dass niedrigere Nukleationstemperaturen die Dauer erhöhter Temperaturen verringern, was in der anfänglichen Gefrierphase entscheidend ist.

Die Studie untersuchte weiterhin die Variation von Rekaleszenz und Kristallisation in verschiedenen Höhen innerhalb eines Problenfläschchen, indem Thermoelemente strategisch positioniert wurden. Es wurde festgestellt, dass der Temperaturanstieg nicht nur vom Füllvolumen abhängt, sondern auch von der Messhöhe. Typischerweise führten größere Füllvolumina zu einem längeren Temperaturanstieg in höheren Positionen innerhalb der teilweise gefrorenen Lösung, ein Phänomen, das zur Heterogenität der Porengrößen in Lyophilisaten beitragen könnte.

Darüber hinaus untersuchte diese Studie die mikrostrukturellen Auswirkungen von Rekaleszenz und Kristallisation mit einem Gefriertrocknungsmikroskop. In Fällen ohne Temperaturanstieg wurde ein feines Netzwerk aus kristallinen (Eis) und amorphen (Disaccharide und ungefrorenes Wasser) Phasen beobachtet, was die Phasendifferenzierung erschwerte. Im Gegensatz dazu zeigten Proben, die Temperaturerhöhungen ähnlich der Rekaleszenz und Kristallisation Phasen ausgesetzt waren, deutliche, kornartige Eiskristalle, die mit den in Lyophilisaten beobachteten Poren vergleichbar sind.

Zur Ergänzung der experimentellen Beobachtungen wurde ein zweidimensionales Phasenfeldmodell entwickelt, das später auf drei Dimensionen erweitert wurde, um morphologische Veränderungen innerhalb des Lyophilisats während des Temperns zu

simulieren und vorherzusagen. Dieses Modell wurde unter Verwendung von Daten aus Saccharose- und Trehaloselösungen kalibriert, die sowohl aus Experimenten als auch aus der Literatur stammen. Die Simulationen lieferten nicht nur Einblicke in die Dynamik des Eiskristallwachstums und die Verteilungsänderungen während des Temperns, sondern untersuchten auch zusätzliche Parameter wie die Oberfläche der Matrixphase und die Verbindungsflächen zwischen benachbarten Eiskristallen. Darüber hinaus wurden die Auswirkungen der mikrostrukturellen Veränderungen während des Temperns auf die praktische Gefriertrocknung diskutiert.

Zusammenfassend hebt diese Arbeit das komplexe Zusammenspiel zwischen Prozessbedingungen und mikrostrukturellen Ergebnissen in Lyophilisaten hervor. Sie betont die Notwendigkeit weiterer Forschung, angetrieben durch experimentelle und Simulationsansätze, um das Verständnis dieser Prozesse zu vertiefen. Diese Studie stellt zudem einen entscheidenden Schritt dar, um die Lücke zwischen Simulationsvorhersagen und experimentellen Validierungen zu überbrücken, indem sie einen umfassenden dreidimensionalen Datensatz der Mikrostruktur bereitstellt, der die Grundlage für zukünftige analytische und Simulationsstudien in diesem Bereich legt.

Acknowledgements

Throughout my PhD journey, I have been fortunate to have many people around me who have not only accompanied me but also supported me in various ways. I would like to thank these people, otherwise this thesis would never have been written.

First of all, I would like to thank Professor Regina Scherließ, who gave me the opportunity to take on this project. In addition to accepting me as a PhD student, her continuous guidance and valuable feedback in our numerous meetings have substantially improved my work. Thank you very much.

I would like to Dr. Nora Urbanetz, who also took on the role of my supervisor, whose warm nature and insightful discussions kept my motivation high throughout the project. Her constructive criticism and encouragement were invaluable, and for that I am grateful.

My gratitude goes to Dr. Srikanth Gopireddy, head of the simulation team, for his effective organisation and supportive leadership. His efforts made it possible for me to focus on my research and contributed greatly to my project. Thank you.

Next, I would like to thank Professor Mogadalai Gururajan, who significantly enriched the simulation part of this work with his expertise. His input was crucial in finalising this work and I thank him for that!

Of course, I would also like to thank all my former colleagues at Daiichi Sankyo in Pfaffenhofen an der Ilm, who have actively supported me at all times. Special thanks to Dr. Tobias Keil for his assistance with the technical aspects of the equipment and to Christian Dietrich for his readiness to help whenever needed. I would also like to thank my former Japanese colleagues from Daiichi Sankyo. These include Dr. Toru Ogawa, Dr. Tatsuhiro Kodama, Dr. Hiroshi Nakagawa, Shunya Igawa and Sayaka Osada. Many thanks for the support and the discussions.

Additionally, I am fortunate to have had the company of Dr. Diana Kreitmayer and Shubhangini Awasthi, fellow PhD candidates in the simulation team. Their friendship and mutual support have been very appreciated.

Last but not least, I would like to thank my friends and family for their unconditional support whenever I needed it.

Thank you very much!

Statement in lieu of an oath

Erklärung nach § 8 der Promotionsordnung

Hiermit erkläre ich gemäß § 8 der Promotionsordnung der Mathematisch-Naturwissenschaftlichen Fakultät der Christian-Albrechts-Universität zu Kiel, dass ich die vorliegende Arbeit, abgesehen von der Beratung durch meinen Betreuer, selbstständig und ohne fremde Hilfe verfasst habe. Weiterhin habe ich keine anderen als die angegeben Quellen oder Hilfsmittel benutzt und die den benutzten Werken wörtlich oder inhaltlich entnommenen Stellen als solche kenntlich gemacht. Die vorliegende Arbeit ist unter Einhaltung der Regeln guter wissenschaftlicher Praxis der Deutschen Forschungsgemeinschaft entstanden. Sie wurde weder ganz noch in Teilen an einer anderen Stelle im Rahmen eines Prüfungsverfahrens vorgelegt, veröffentlicht oder zur Veröffentlichung eingereicht. Außerdem versichere ich, dass mir noch kein akademischer Grad entzogen wurde, noch habe ich an dieser oder einer anderen Fakultät einen früheren Promotionsversuch unternommen.

Tigran Kharatyan